University of Tennessee, Knoxville

TRACE: Tennessee Research and Creative Exchange

Doctoral Dissertations

Graduate School

12-2021

A multi-scale homogenization scheme for modeling anisotropic material’s elastic and failure response

Justin Matthew Garrard
jgarrard@utk.edu

Follow this and additional works at: https://trace.tennessee.edu/utk_graddiss

Part of the Applied Mechanics Commons

Recommended Citation

Garrard, Justin Matthew, "A multi-scale homogenization scheme for modeling anisotropic material’s elastic and failure response. " PhD diss., University of Tennessee, 2021.
https://trace.tennessee.edu/utk_graddiss/6986

This Dissertation is brought to you for free and open access by the Graduate School at TRACE: Tennessee Research and Creative Exchange. It has been accepted for inclusion in Doctoral Dissertations by an authorized administrator of TRACE: Tennessee Research and Creative Exchange. For more information, please contact trace@utk.edu.

To the Graduate Council:

I am submitting herewith a dissertation written by Justin Matthew Garrard entitled "A multi-scale homogenization scheme for modeling anisotropic material’s elastic and failure response." I have examined the final electronic copy of this dissertation for form and content and recommend that it be accepted in partial fulfillment of the requirements for the degree of Doctor of Philosophy, with a major in Mechanical Engineering.

Reza Abedi, Major Professor

We have read this dissertation and recommend its acceptance:

Katherine A. Acton, Stephanie C. TerMaath, Trevor M. Moeller

Accepted for the Council:

Dixie L. Thompson

Vice Provost and Dean of the Graduate School

(Original signatures are on file with official student records.)

A multi-scale homogenization scheme for modeling anisotropic material's elastic and failure response

A Dissertation Presented for the
Doctor of Philosophy
Degree
The University of Tennessee, Knoxville

Justin Garrard
December 2021

© by Justin Garrard, 2021
All Rights Reserved.

To my wife Lauren, whose limitless love, support, and dedication made this possible.

Acknowledgments

First and foremost, I want to acknowledge my advisor, Dr. Reza Abedi. His work ethic and dedication to his students is incredible. While I have a full-time career and a family, Dr. Abedi stayed with me throughout multiple career and personal changes, most of which were not advantageous to completing graduate-level research. His encouragement to keep working and finish is the main reason I was able to finish my degree. Dr. Abedi gives everything to his students and his research and I am forever grateful for the time he spent working with me. I consider him not just a colleague, but also a dear friend.

I want to acknowledge my committee members: Dr. Katherine Acton (University of St. Thomas, MN, USA), Dr. Trevor Moeller (UT Space Institute), and Dr. Stephanie TerMaath (UT Knoxville). Each member granted me their time, counsel, and commitment during my research efforts, without which I could not have accomplished this goal.

Next, I was lucky to work with a great research group under Dr. Abedi and want to acknowledge both current and former members who I collaborated with: Dr. Philip Clarke, Wang Hang, and Bahador Bahmani. Each one provided assistance in writing and debugging code, analyzing data, and any other support provided throughout my research.

Thanks to my friends and colleagues at Arnold Engineering Development Complex. I was able to complete this degree through tuition reimbursement support and access to some of the smartest people I've ever met. My work family has been a major inspiration for me to get finished.

One of my biggest motivators throughout my doctoral career has been my father, Dr. Doug Garrard, who also earned his doctorate in Mechanical Engineering through the University of Tennessee. Thank you for being a great father and a great example for me to model my career. I also want to thank my mother and sister for their support throughout this research.

Finally, I would be remiss if I did not acknowledge my wife Lauren, and son, Hudson. I love you so much - without your sacrifices I would not have finished. You two are my entire world and give me inspiration every single day. Thank you for everything you do for me.

Abstract

The effect of small-scale random defects such as microcracks or inclusions are critical to the prediction of material failure, yet including these in a fracture simulation can be difficult to perform efficiently. Typically, work has focused on implementing these through a statistical characterization of the micro- or meso-scales. This characterization has traditionally focused on the spatial distribution of faults, assuming the material is purely isotropic. At the macro-scale, many materials can be assumed to be fully isotropic and homogeneous, but at the small scale may show significant anisotropy or heterogeneity. Other materials may be effectively anisotropic in bulk, such as rock bedding planes.

Statistical volume elements (SVE) are one homogenization methodology used to retain this heterogeneity or anisotropy when characterizing a material. Unlike a Representative Volume Element (RVE), the choice of SVE including size, boundary conditions applied, shape, and type, may affect the given material properties. In addition, the size which an RVE exists is well-studied for homogeneity, but there is less study of the isotropic limit.

This work introduces a multi-scale methodology using SVEs to study material heterogeneity and anisotropy. Results are given for macroscopic fracture simulations using this SVE-based homogenization scheme. In addition, the rate of convergence to the RVE limit for both the homogeneous and isotropic limit of two types of SVE, Regular Square and Voronoi Square, are shown. This methodology shows promise for characterization of both isotropic and anisotropic materials.

Table of Contents

List of Tables

List of Figures

Chapter 1

Introduction

1.1 Motivation

For many engineering applications, the assumption of uniform materials is a useful simplification. Tensors become constant variables. Messy equations requiring computational solvers revert to easily solvable analytical solutions. Yet in nature, truly homogeneous and isotropic materials do not exist. Crystalline grain structures in metals, or minute cracks or inclusions in rock provide weak points distributed spatially in a given material. Bedding planes in rock beds or fibers directionally oriented in a composite provide a strong anisotropic effect which has a large influence on the measured material properties.

Because anisotropy and heterogeneity are the rule instead of the exception, understanding when it is OK to make a simplifying assumption of homogeneity or isotropy is important. The ever present push and pull between computational efficiency and simulation accuracy requires a balancing act when selecting a material as part of the design process for an engineering system. When studying how a given material fails, by performing a fracture simulation for example, we will see the length scale of the subject in question is very important when deciding which level of analysis is required. Much research has been performed to understand the requirements for material heterogeneity. Less research has been done to understand when including anisotropy is required to accurately simulate the material response.

Continuum mechanics relies on the assumption of a material as a continuum – in other words, a uniform body with uniform properties. Inscribed with that assumption is that the material is homogeneous, isotropic, continuous, and behaves independent of any particular coordinate system or boundary condition. But the material microstructure is filled with imperfections - cracks, dislocations, grain boundaries, and other heterogeneities which influence the behavior of the material. Brittle and quasi-brittle materials, characterized as such by the minimal elastic and plastic deformation they experience before reaching failure, have been shown to be greatly influenced by this distribution of flaws contained therein. Even for material samples with the same apparent geometry and under the same loading, the fracture patterns can be completely different [17].

Quasi-brittle materials are defined as materials in which the fracture process zone (FPZ) is not negligible compared to the cross section dimension – in other words, at a small scale the material obeys the theory of plasticity, while at larger scales the linear elastic fracture mechanic model applies. For these materials, the distribution of flaws within the FPZ causes softening damage which occupies the entire nonlinear zone. In comparison, for ductile fracture the FPZ is a point which undergoes plastic yielding rather than damage. If the cross section of a quasi-brittle material becomes much larger than the FPZ size, then the material is essentially perfectly brittle – in other words, it follows the principles of linear elastic fracture mechanics. However, for smaller sections, the material acts as a quasi-brittle material where the softening effect has a greater influence on the failure behavior of the material.

The *size effect* is a well-known phenomenon in material fracture that describes how a given material's strength decreases with increasing size due to the increasing population of microstructural defects which exist in the structure [23, 24]. The seminal work which capped the original development of the statistical theory of the size effect was performed by Weibull [156]. Weibull developed an implicit "weakest link" model for the failure of a chain of links of random strength. Weibull developed a probability distribution which took his namesake which represented the failure probability of the smallest possible *representative volume* of a given material that fails as soon as a macroscopic fracture initiates from a microcrack or other flaw. Weibull theory has been applied successfully for various applications including as part of an interfacial damage model to capture statistical fracture response in rock [5], fracture under dynamic compressive loading [5], and in fragmentation studies [5, 43].

In his review of the size effect, Bazant [24] showed several issues with the direct application of the classical Weibull theory for material failure including the fact that the size effect is a power law implies the absence of a characteristic length which cannot be true for a material which contains sizable heterogeneities. The energy release within a fracture process zone that causes stable crack growth before the maximum stress or strain is reached gives rise to a deterministic size effect which can dominate over the statistical size effect [25]. The classical theory also ignores the differences between structural geometry and the spatial and angular distribution of the given microstructural defects. This has led to experiments which show that for certain quasibrittle materials, the size effect is greater than predicted by Weibull theory [28].

The Weibull theory has been proven effective in capturing the size effect at certain length scales and stochastic variations in fracture response, but the model lacks the direct connection to the material microstructure which truly represents the material behavior. The model is a phenomenological description and not a truly physical representation of the microstructure. To resolve this issue, one could choose to model these heterogeneities explicitly using peridynamic or discrete element methods [146, 109, 82, 55]. The peridynamic method is a nonlocal extension of continuum mechanics which remains valid in the presence of discontinuities by solving the balance of linear momentum using integral equations. Discrete element methods model any mass as a large number of discrete particles which are assigned a given spatial orientation and initial velocity. Material properties such as elasticity are described using a given contact law between each particle. Bonded contacts with a limited resistance are used to represent brittle materials, where an absence of forces between a contact pair can indicate the growth of a crack within a given material. While the explicit representation of defects using either explicit method described above improves the computational accuracy of the given model, doing so for anything except the smallest structures is computationally expensive. While implicit models such as Weibull's do not directly represent the material microstructure, explicit models requires costly computational horsepower.

Homogenization methods address these concerns by averaging the microstructural information within a volume element (VE), retaining the information contained therein without the costly explicit modeling. One type of VE is known as the *Representative Volume Element* (RVE), a smaller volume which is said to be representative (has the same known material properties, behaves the same under the same loading, and so on) of the larger structure. A primary focus of research has been on identifying at what length scales and under what conditions the RVE can be said to exist.

There have been various definitions of the RVE depending on the specific study. Gitman [63] investigated these different definitions which are summarized here:

- the RVE must be structurally entirely typical of the whole mixture on average and contains a sufficient number of inclusions for the apparent moduli to be effectively independent of the surface values of traction and displacement so long as these values are macroscopically uniform [73]
- the RVE should contain enough information on the microstructure [69]
- the response of the RVE must be independent of the boundary condition [118, 136]
- the RVE the smallest material volume element of the composite for which the usual spatially constant (overall modulus) macroscopic constitutive representation is a sufficiently accurate model to represent mean constitutive response [50]
- the RVE is a volume sufficiently large to be statistically representative of the material, *i.e.,* it includes a sampling of all microstructural heterogeneities that occur in the material [83]
- the RVE must ensure a given accuracy of the overall estimated properties obtained by spatial averaging of stress, strain, or the energy fields [83]
- a unit cell in a periodic microstructure [118]
- a volume containing a very large (mathematically infinite) set of microscale elements [118]
- the RVE properties should be statistically homogeneous and ergodic to ensure the RVE is statistically representative of the macro response [118]

All of these definitions imply the same thing: the RVE must be large enough to represent (same properties, same behavior under different boundary conditions, and so on) the macroscopic body on the whole. The RVE size is thus the *minimum* size of the volume element which satisfies this requirement of statistical homogeneity. This lower bound means that volume elements above this size limit behave similarly, while those below do not [33]. Determining this size has been done experimentally using observations of the material microstructures to determine covariance or covariogram of the random set [66, 142]. The size has also been determined analytically using the calculated effective properties such as in [50]. Seb and Nedjar [137] proposed a method using the convergence of the effective properties using multiple realizations of a periodic microstructure. This requires a statistical procedure determine when the property reaches convergence. Examples include Gitman's [63] χ^2 criterion, Monte-Carlo simulations [118], or stochastic stability [64].

But the representative volume element does not retain the statistical variability required for modeling heterogeneous, anisotropic materials. Fracture models which assume homogeneous, isotropic material properties as homogenized at the RVE limit have been shown [153, 48, 31] to be unable to accurately characterize the random heterogeneities that dictate the material fracture pattern. Partitioning the RVE into a collection of smaller *statistical volume elements* (SVE) is one method used to preserve the spatial and angular heterogeneity of the material microstructure. The Hill definition of the RVE above [73] states that the constitutive properties obtained should be independent of the boundary conditions. Because the SVE is below this RVE limit, the definition of the constitutive tensor is not unique and the apparent properties depend on the given boundary condition.

Huet [77] defined a hierarchy of bounds for uniform partitions of a material below the RVE limit. This hierarchy of bounds showed that the effective moduli of the body is bounded by the Hill-Voigt upper bound generated using a kinematically uniform (KUBC) boundary condition and the Hill-Reuss lower bound generated by a statically uniform (SUBC) boundary condition on the volume element. The material converges to the effective RVE value at a rate dependent on the material microstructure as the SVE length scale increases [85]. Additionally, the ensemble average of a property calculated from a population of SVEs using KUBC and SUBC bound the upper and lower limits of the effective modulus of the RVE [77, 72, 71, 168]. Mixed [72, 71] and periodic [81] boundary conditions generate an apparent modulus somewhere between the KUBC and SUBC bounds.

Not only does the size of SVE determine the apparent property, so too does the type and shape of the SVE. Regular SVEs are simple shapes which are used to partition the macroscopic body. This SVE type allows for the intersection of the different phases of the microstructure at the boundary of the volume element, which may result in non-physical stress concentrations at the boundary [15]. To prevent this from occurring, the Voronoi SVE type uses Voronoi tessellation to generate boundaries about the microstructural phases which do not intersect [44, 138]. Voronoi SVEs have been shown to improve the apparent property statistics as they are less sensitive to SVE size variation [138, 15].

The shape of the SVE may introduce spurious anisotropic effects. For example, square SVEs have been shown [14] to introduce a spurious directional bias due to stress concentrations at the corners of the SVE boundary. These stress concentrations can effect elastic and fracture properties. Circular SVEs lack the corner stress concentrations, so anisotropic effects are identified using these SVEs, then the effect should be true material anisotropy. Circular SVEs have been shown to be more suitable to predict elastic [56] and fracture [57] property isotropic or anisotropic responses.

While anisotropy may occur frequently in nature, as a feature it has frequently been ignored in literature, where to date most research has focused on understanding the limit at which a locally heterogeneous material may be represented by a homogeneous representative volume element. But this spatial distribution of microstructural features may also contain an angular component, where a locally anisotropic material may be either isotropic or anisotropic in bulk. As mentioned above, the choice of SVE type or shape may also introduce a non-physical anisotropic modeling bias which should be prevented or removed. Only then can the true material anisotropy at the SVE scale be understood and any model-dependent or approximation errors be prevented from propagating throughout the entire analysis.

This dissertation summarizes research performed to investigate anisotropy contained within material microstructures using an SVE methodology. The effect of SVE type, shape, and boundary condition is shown. The rate of convergence to the RVE limit is studied for both elastic and fracture properties to understand when an analysis can be simplified by making an assumption of homogeneity or isotropy. Fracture is shown to be a more complex, local property which requires including the spatial and angular distribution of the microstructural defects to properly model. Publications and presentations generated over the course of this doctoral research are summarized here.

1.2 Summary of Doctoral Research

1.2.1 Journal Publications

Primary Author

- Garrard, J.M., and Abedi, R., ”Statistical volume element averaging scheme for fracture of quasi-brittle materials, *Computers and Geotechnics*, Elsevier, 117, 103229, January 2020
- Garrard, J.M., and Abedi, R., ”Statistical Volume Elements for the Characterization of Angle-Dependent Fracture Strengths in Anisotropic Microcracked Materials”, *ASCE-ASME Journal of Risk and Uncertainty in Engineering Systems Part B: Mechanical Engineering*, ASME, 6(2), 021008-1 - 021008-18, March 2020
- Garrard, J.M., Yang, M., Abedi, R., Sograhti, S., and Acton, K. ”Elastic and Strength Properties of Statistical Volume Elements: Comparison of Boundary Conditions”, *Submitted to Elsevier Computer Methods in Applied Mechanics and Engineering in November 2021*

Contributing Author

- Garrard, J.M., Abedi, R., and Acton, K.A., ”Elastic and Strength Properties of Statistical Volume Elements: Determination of Isotropic and Homogeneous Size Limits”, *Submitted to Elsevier Journal of the Mechanics and Physics of Solids in November 2021*

- Yang, M., Garrard, J.M., Abedi, R., and Sograhti, S., "Effect of microstructural variations on the failure response of a nano-enhanced polymer: a homogenization-based statistical analysis", *Computational Mechanics*, Springer, 67, 315-340, October 2020
- Acton, K.A., Abedi, R., and Garrard, J.M., "Geometric Partitioning Schemes to Reduce Modeling Bias in Statistical Volume Elements Smaller than the Scale of Isotropic and Homogeneous Size Limits", *Submitted to Elsevier Computer Methods in Applied Mechanics and Engineering in November 2021*
- Clarke, P.L., Wang, H., Garrard, J.M., Abedi, R., and Mudaliar, S. "Space-angle discontinuous Galerkin method for plane-parallel radiative transfer equation", *Journal of Quantitative Spectroscopy and Radiative Transfer*, Elsevier, 233, 87-98, August 2019

1.2.2 Conference Publications and Presentations

Publications

- Garrard, J.M., Abedi, R., and Clarke, P.L., "Random field realization and fracture simulation of rocks with angular bias for fracture strength", *52nd US Rock Mechanics/Geomechanics Symposium*, American Rock Mechanics Assocation, Seattle, Washington, June 2018
- Garrard. J.M., Abedi, R., and Clarke, P.L., "Statistical volume elements for the characterization of angle-dependent fracture strengths", *Proceedings of the ASME 2018 International Mechanical Engineering Congress and Exposition*, American Society of Mechanical Engineers, Pittsburgh, Pennsylvania, November 2018

Presentations

- Garrard, J.M., Clarke, P.L., and Abedi, R., "Random field realization and fracture simulation of rock with angular-bias in microcrack orientation", *Presentation given at the 2018 Engineering Mechanics Institute Conference*, Boston, Massachusetts, May 2018

- Abedi, R., Clarke, P.L., Garrard, J.M., Acton, K.A., Haber, R.B., ”Effects of mesoscale material inhomogeneity on macroscopic dynamic fracture response, *15th U.S. National Congress on Computational Mechanics*, Austin, Texas, July 2019
- Garrard, J.M., Abedi, R., and Haber, R.B., ”Explicit and implicit approaches for characterization and fracture analysis of anisotropic rock, *15th U.S. National Congress on Computational Mechanics*, Austin, Texas, July 2019
- Garrard, J.M., Acton, K.A., and Abedi, R., ”Statistical Volume Element Partioning to Characterize Local Material Anisotropy”, *Presentation given at the 2021 Engineering Mechanics Institute Conference*, Virtual Event, New York, New York, May 2021

1.3 Dissertation Format

The following chapters contain several journal articles which the dissertation author was either primary author or a major contributor. These works summarize the current research towards achieving an understanding of material homogeneity and isotropy using statistical volume elements. Each chapter begins with a short summary of the authors contributions for each work. The author shows that fracture properties are much more complex and localized than elastic properties, and that elastic properties may at certain length scales be considered a homogeneous, isotropic property even for a material which is locally anisotropic. Voronoi SVEs are shown to be more stable across SVE length scales and do not contain spurious angular bias which regular square SVEs contain. Ultimately, the inclusion of anisotropy is an important consideration to properly model material fracture, and the assumption of material isotropy may result in error in the simulation.

Chapter 2

Statistical volume element averaging scheme for fracture of quasi-brittle materials

An original version of the following article was published in Volume 117, published in January 2020, of the Elsevier journal *Computers and Geotechnics*. The article was published under the title ”Statistical volume element averaging scheme for fracture of quasi-brittle materials”. The article was co-authored by Dr. Reza Abedi. My contributions include

- Identified Yuen-Long marble microstructure statistics in [159]. Implemented Weibull statistics for crack-generation into existing microstructure generation code developed by Clarke and Abedi.
- Generated 12 microstructures representing the real Yuen-Long marble example in [159], differing the Weibull shape parameter and crack density to investigate the change in fracture strength based on the material microstructural differences.
- Developed code which implemented circular SVEs for traversing material microstructure. Code calculates fracture strength within each SVE using the sliding wing-crack model which was also used in [159].
- Performed mesoscopic statistical analysis of fracture strength for different microstructures
- Set up and performed macroscopic fracture analysis using Dr. Abedi’s existing aSDG code

This information in this article continues the work performed by Clarke in [40] to generate homogeneous mesoscopic property fields from realistic material microstructures. The primary research contribution of this work was to investigate the effect of changing the shape of the statistical distribution of cracks using the Weibull shape parameter. At $m = \frac{1}{2}$, there is a large amount of small microcracks and some amount of larger cracks within the domain. As the shape parameter increases to a maximum of $m = 4$, the span of microcrack length is reduced such that the crack length is more tightly grouped about the mean. All distributions have the same mean microcrack population length. This work also investigates the effect of varying the microcrack density within the field. Each microstructure was analyzed with four SVE sizes to determine how the properties change as the SVE size approaches the RVE size limit.

2.1 Abstract

To capture the randomness and inhomogeneity of rock at microscale, a statistical volume element (SVE) averaging approach is proposed. The microcrack statistics of a real-world Yuen-Long marble sample is used to realize 2D microcracked domains. The size effect, i.e. the decrease of the mean and variation of homogenized strength field by increasing SVE size, is analyzed. Increasing the crack density is shown to have a similar effect. While smaller SVEs maintain a greater level of inhomogeneity and are preferred for fracture analysis, it is shown that low density of microcracks pose a lower limit on the SVE size. Beside the actual power-law distribution of microcrack length, by varying the Weibull model shape parameter m other domains are created with different microcrack distribution shapes. Macroscopic fracture simulations, by the asynchronous Spacetime Discontinuous Galerkin (aSDG) method, study the effect of m for a uniaxial tensile problem. By increasing m from 0.5 to 4, the length distribution of microcracks become more uniform; this corresponds to a more uniform and stronger mesoscopic strength field, which results to about 3 and 6 times increase to macroscopic tensile strength and toughness, respectively. However, the more uniform length distribution of microcracks is shown to reduce rock brittleness.

2.2 Introduction

Understanding the behavior of rock, including how it is materially constituted, reacts to loading, and fails is vital for critical economic activities such as mining, drilling, tunneling, and construction. While these activities may consider the material in the macro-scale, the behavior of quasi-brittle materials such as rock is heavily influenced by heterogeneity at the meso- and micro-scale [134, 62, 29]. Because brittle materials lack energy dissipative mechanisms, microcrack stress concentrations are not balanced as in more ductile materials and directly influence the material's peek and post-instability response [161]. The distribution of microcracks and voids change the overall response of the system to an applied stress.

These heterogeneities result in crack pattern variability between multiple samples for similar loading [17] and uncertainty in the ultimate fracture strength of the material [86, 161]. The *size effect*, where the sample-to-sample mean and variation of fracture strength of a given material decreases with increasing structure size [30, 29], is a well-known phenomenon for quasi-brittle materials. The size effect for these materials is contributed to the distribution of micro-scale defects and insignificance of plasticity or other mechanisms that could otherwise absorb large energies and significantly redistribute the stress field [62].

Simulating the effect of these heterogeneities can be performed either explicitly or implicitly [107]. *Explicit* models directly incorporate defects greater than some minimum size into the analysis. For example, as in [70, 140, 48, 101] the continuum is simplified as a network of bars or beams with random properties. *Peridynamic* [146], *discrete element methods* [109, 82], and *discrete particle methods* [55] are other examples that can model continuum as a collection of (possibly deformable) particles. Another example is the explicit representation of (micro)cracks in a computational framework.

The explicit representation of defects in general improves the fidelity of computational model. For example, explicit representation of microcracks is important in hydraulic fracturing applications [43]. Moreover, explicit models can even be used to explain highly complex phenomena such as solid- to fluid-like transition in sand dunes [102].

Implementing explicit models is computationally costly; so there is great difficulty in employing these models for anything other than small space and time scales. *Implicit* models represent the microstructure in an averaged or homogenized sense, and have been used to qualitatively explain the size effect. The implicit representation of microstructures makes implicit methods computationally more affordable than explicit ones. A popular implicit model is Weibull's weakest link model [156, 157]. This model has been used to show that realistic fracture patterns can be captured for problems that lack macroscopic stress concentration points, such as fragmentation [5] and dynamic compressive loading [3] problems. The main issue with these models is that while they are able to capture the general phenomenon, they lack a direct physical connection to the material microstructure. Therefore, an approach is necessary that can link the microstructural distribution of defects to the macro-scale, without the computational costs required of explicit models.

Homogenization methods address this concern by averaging the effect of the microstructure in a *volume element* (VE). In continuum mechanics, a *Representative Volume Element* (RVE) acts as a mathematical point of a continuum field approximating the true material microstructure. The equivalent term *Representative Elementary Volume* (REV) is used in rock mechanics. According to [119], RVEs are well-defined for a unit cell in a periodic microstructure and a statistically representative volume containing very large number of microscale elements. In this manuscript, our focus is on the second type of VEs. For a macroscopically homogeneous material with ergodic properties the standard deviation of the homogenized properties follows a power law [105] or model [35, 83] versus the VE size, in that, the variation of homogenized properties tend to zero as the VE size tends to infinity. The RVE size for a given material property of a composite is chosen such that either this standard deviation, or the error in estimating the mean of the homogenized property, falls below a user-specified tolerance for a given number of VE realizations; *cf.* [150, 83, 95, 120] on more detailed discussion on the RVE and the determination of its size.

For a given material property, if the aforementioned condition for the RVE size is not satisfied, the VEs are known as *Statistical Volume Elements* (SVEs). These SVEs are smaller than the corresponding RVE, and simply speaking a large variation is observed in properties homogenized by SVEs. One advantage of SVEs is that they can model spatial and sample-to-sample variation of material properties by using small enough VEs for homogenization. The selected SVE observation window [154, 22], type of boundary conditions [80], and clustering of microstructures [141] all affect the statistics of the homogenized properties.

While RVEs have been used in many studies to homogenize and calibrate various fracture models [152, 76, 143, 115, 97], the use of SVEs provides several advantages for fracture analysis; by maintaining material inhomogeneity in fracture properties, fracture can initiate from material weak points, as opposed to unrealistic fracture initiation from all points under a spatially uniform stress field as shown in [42]. Moreover, by preserving sample-to-sample variations, variations in fracture pattern, ultimate load, and fracture strengths for different samples can be captured when SVEs are used. Finally, it is noted that by homogenizing the effect of microstructure into heterogeneous material property fields, the use of SVEs provides a significant advantage in computational cost over explicit methods.

We have previously used SVEs for fracture analysis of quasi-brittle materials with microcracks in [42, 60, 61]. However, the microcrack statistics were not derived from any known material and instead were simply used to detail the overall analysis process. In addition, no crack interaction was considered. We address these shortcomings in this manuscript; first, a data set [158, 159] which contained the microcrack distribution statistics for a set of six Yuen-Long marble samples was identified for this analysis. As in the paper by Wong *et al.*, a power law distribution was used to match the microcrack length distribution in the simulated Yuen-Long marble RVE domain. Second, a sliding wing crack model was used [19] to take into account the effect of crack interaction caused by crack fields with differing densities and crack distributions. These efforts improve the accuracy of microcrack statistics and the homogenized mesoscopic fracture strength fields.

The distribution of microcrack length can have a significant effect on both homogenized mesoscopic strength fields and macroscopic fracture response. To better analyze such effect, we create synthetic rock samples where crack length follows a Weibull distribution, while the mean of crack length matches that of the original Yuen-Long marble sample data. The Weibull model is used to create very different crack length distributions by simply changing the Weibull shape parameter. Finally, we study the effect of crack density and SVE size on the statistics of homogenized fracture strength fields.

Relating the statistics of microcracks to macroscopic fracture response is the second contribution of this manuscript, which is done by simulating domains with SVE-homogenized fracture strength fields. These fields are simulated using an *asynchronous Spacetime Discontinuous Galerkin method* (aSDG) [6, 7]. The proposed multiscale approach based on the use of SVEs greatly reduces computational cost relative to the direct numerical simulation of rock. At the macroscale, we derive macroscopic strain versus stress responses for a uniaxial tensile problem. The macroscopic simulations are used to demonstrate the effect of initial crack distribution on macroscopic rock strength, toughness, brittleness, and fracture pattern. One general observation is that domains with more uniform crack length distribution can sustain a larger macroscopic stress level, but have a more brittle response.

The remainder of manuscript is structured as follows. In §2.3 the SVE analysis process is described as well as the relevant background material from [159]. Results for the Yuen-Long material crack distribution and differing Weibull crack length model distributions are provided in §2.4. In this section, microcrack statistics are translated to an inhomogeneous mesoscopic fracture strength field, which is subsequently used in §2.5 for dynamic macroscopic fracture analysis. Final discussion of the results and future work are discussed in §3.5.

2.3 Materials and Methods

Figure 1[1] depicts an outline for this section. In [159], the authors consider a 32 mm by 32 mm square domain of Yuen-Long marble to be representative. That is, the size of domain is large enough to contain sufficient number of microcracks and is sufficiently larger than the size of microcracks measured in their experiments. This ensures that properties homogenized on this size demonstrate very small variations from sample to sample. Herein, we refer to a square domain of this size as a *Representative Volume Element* (RVE). In §2.3.1 we describe the process in which we populate microcrack with specific length and angle distributions in the macroscopic domain.

Instead of directly deriving material properties such as fracture strength for RVEs, we are interested in assigning such properties for *Statistical Volume Elements* (SVEs). The use of SVEs ensures that derived properties are no longer uniform for a macroscopically homogeneous rock. Moreover, each SVE maintains sample-to-sample variation for a given property at the same spatial location between different RVEs. As shown in Fig. 1(a), we use circular SVEs of size L_{SVE} to traverse the RVE with spacing S. Figure 1(b) shows a zoomed view of an SVE containing multiple microcracks. The formation of SVEs within the RVE and the characterization of a unique mesoscopic compressive fracture strength per SVE are described in §2.3.2 and §2.3.3, respectively. Once the RVE is traversed with SVEs, at the center of each SVE a unique mesoscopic strength value is assigned. A contour plot generated from grid values of these strengths is shown in Fig. 1(c). Finally, any of such inhomogeneous mesoscopic fields can be used as an input fracture strength field for a macroscopic fracture

---

[1] Please note that all figures in this dissertation are contained within Appendix A

simulation of an RVE. Figure 1(d) shows a sample fracture pattern obtained by the aSDG method.

2.3.1 Distribution of microcracks

While the actual microcrack distribution of the material microstructure for each Yuen-Long marble sample is not given in [159], the provided material properties and microcrack statistics allows us to generate random realizations of the material that accurately represent the material behavior. These realizations contain a field of microcracks with realistic crack length distributions, crack angle distributions, and the correct microcrack density in the domain. The microcrack statistics and material Poisson's ratio and modulus of elasticity were taken from the material sample designated S19 in [159]. The spatial distribution of the individual cracks remains random for each realization. Therefore, this section will describe the statistical distributions used to create the randomly generated domains. While the information contained herein is not original, this section acts as a review of the information required to generate the random domains.

We first discuss the distribution of the length of microcracks. Crack length is indirectly specified by its half length a, as is common in the field of fracture mechanics. From [159] for the given marble, a is shown to follow a power law distribution. Because a power law distribution will blow up with decreasing crack size, a minimum half crack length $a^{'}$ is assigned. Therefore, the cumulative probability for half cracks longer than $a^{'}$ for an elemental volume V_0 is defined as,

$$g(a) = \left(\frac{q^*}{a}\right)^z \tag{2.1}$$

where q^* and Cauchy distribution exponent $z > 1$ are the parameters of the power distribution, subject to the condition,

$$V_0 \int_{a^{'}}^{\infty} g(a)da = 1. \tag{2.2}$$

To ensure this equality, the lower integration limit, $a^{'}$ is defined by,

$$a^{'} = \left[\frac{(q^{*})^{z}V_0}{z-1}\right]^{\frac{1}{z-1}} \tag{2.3}$$

This half crack length distribution was used to create new random crack field realizations with the provided marble properties that are given in [159] and described in §2.4. The angular distribution of the cracks was assumed to follow a uniform distribution, corresponding to a macroscopically isotropic material. The spatial location of cracks is also assumed to follow a uniform distribution, corresponding to a macroscopically homogeneous material. The last descriptor used for realizing microcracked domains is crack density ε_0, defined as the nondimensional sum of the squares of individual crack lengths per unit surface area. To generate a statistically consistent domain such as that shown in Fig. 1(a), individual cracks are created and placed in the domain by a pick-and-place algorithm in which for an individual crack its half length, angle, and spatial location are sampled from their corresponding distribution functions. Individual cracks are placed in the domain until the target crack density is reached.

To investigate how the distribution of half crack length affects fracture response, several additional domains were created with similar material properties as the Yuen-Long marble samples and maintaining the same mean half crack length as that of the power law distribution in [159]. However, rather than using a power law distribution, a Weibull distribution was used due to the ease in changing the shape of the distribution utilizing the shape parameter m. The Weibull cumulative distribution function for a is defined as,

$$g(a) = 1 - e^{-r[\frac{a-\gamma}{\eta}]^{m}} \tag{2.4}$$

As stated previously, the power m is the shape parameter, which controls the shape of the distribution. The Weibull model parameters are calibrated for an elemental volume V_0. The distribution for another elemental volume V is adjusted through the ratio $r := V/V_0$. Moreover, η is the scale parameter and γ, similar to $a^{'}$, controls the minimum half crack length of the distribution. To change the shape of the distribution, several different m values were selected for analysis. To maintain the minimum half crack length, the γ value was set equal to $a^{'}$. Therefore, the only variable which was changed between the given distributions to retain the mean crack length was η.

2.3.2 SVE characterization

The most important aspect affecting material properties homogenized or averaged by SVEs is the size of SVE, L_{SVE}. As L_{SVE} increases toward the RVE size and beyond, the material properties become more uniform; for a macroscopically homogeneous material the values obtained from all SVEs in fact tend to a unique value. The size of SVEs should be chosen considerably smaller than RVE size limit. On the other hand, the SVE size must be sufficiently larger than the microstructural details of the material and ideally contain a sufficient number of them in the SVE to make it representative of the response of the material. For the problem considered herein, microstructure is characterized by microcracks whose length distribution was described in §2.3.1. To ensure SVEs are larger than the typical microstructure size, we require the relative size of SVE by mean crack length, defined by $\beta = L_{SVE}/\mathbb{E}(2a)$, be larger than one. Moreover, to ensure that SVEs are representative, ideally we want to have majority of SVEs to contain some microcracks. For the SVEs which do not contain any cracks, a maximum fracture strength corresponding to minimum allowable crack length of the distributions discussed in §2.3.1 is assigned. As will be shown in §2.4.4, the condition of SVEs containing microcracks further constrains the lower limit of L_{SVE} at low crack densities. In addition, it is shown that the mean and standard deviation of fracture strength decrease as L_{SVE} increases.

The second consideration is the shape of an SVE. In 2D, square and rectangle are typical shapes for SVEs. However, herein we consider circular SVEs for two reasons. First, in [14] it is shown that the square SVEs artificially make the homogenized material anisotropic (even if it is isotropic at macroscale), in that homogenized properties have a nonphysical bias (minimum or maximum value) along 0/90 or 45/135 degrees. While unlike [60, 61], we do not consider angular dependency of the fracture strength, the circular shape still eliminates artificially higher or lower strengths along these angles to be incorporated in the fracture strength of SVEs. Second, the circular shape of an SVE simplifies the algorithm to determine the intersection of a crack with an SVE, as it is needed to determine its strength in §2.3.3.

We use circular SVEs in the context of *moving window* [22, 12, 11] method, wherein overlapping *windows* (volume elements) smaller than RVE scale traverse the domain in the context of *Generalized Method of Cells* (GMC). The square SVEs in [12, 11] and circular ones in present study are overlapping and are centered at the points of a fine structured grid. As shown in Fig. 1(a), the spacing of SVEs, *i.e.,* the center to center distance of consecutive SVEs in horizontal and vertical directions, is denoted by S.

For any given SVE size, we use the spacing $S = L_{SVE}/n$, for a spacing factor n equal or greater than 5. In §2.4.1, we perform a review of several SVE spacing values in order to determine a reasonable value for n. After this review, it was determined that by using the spacing $n = 10$, the characterized inhomogeneous fracture strength field will be of high spatial resolution while retaining computational efficiency; *cf.* Fig. 1(c). For the 32 mm by 32 mm RVE in Fig. 1(a), this corresponds to a $32/S + 1$ by $32/S + 1$ square grid; at each grid point the averaged fracture strength, *cf.* §2.3.3, of an SVE centered at that point is assigned. To ensure the SVEs close to the boundary of the RVE (for example SVE A in Fig. 1(a)) entirely cover the microcracked rock, we need to choose a volume element larger than the RVE size. In this study, a 80 mm by 80 mm volume element is chosen for this volume element.

2.3.3 Mesoscopic fracture strength model

We note that in the present study only fracture strength is considered as an inhomogeneous / random field at the mesoscale, and elastic properties are deemed to be homogeneous. This is consistent with the approach in [158, 159]. In addition, fracture strength has been the field that is considered inhomogeneous in majority of similar studies, see for example [37, 166, 139, 93, 45, 16].

Assigning a fracture strength to an SVE involves two steps.The first step is the determination of uniaxial compressive fracture strength s_c for a single crack contained in a domain with a specific crack density. To ensure consistent strength values with the data set produced by Wong *et al.* [158, 159], the same sliding wing crack strength model for uniaxial compressive strength is utilized in this manuscript. This section summarizes the fracture strength model given in [159] used to calculate the fracture strengths in this manuscript.

The wing crack model relates the compressive failure stress to the critical stress intensity factor, K_{IC}. It considers the tensile stress concentration at the tips of the inclined preexisting cracks of length $2a$. The applied stresses induce a shear traction on the plane of the crack, which if sufficiently high to overcome the frictional resistance along the closed crack, results in stress concentrations that may induce wing cracks to propagate, as shown in Fig. 2. This propagation is characterized by the stress intensity factor K_I at the point of wing crack initiation which is a function of the friction coefficient μ, the angle ψ between the crack and maximum compressive principal stress σ_I, and the applied stress field. While the fracture strength equations for the wing-crack model can be found in [159], we have reproduced the equations (equations 2.5, 2.6, and 2.7) here for clarity.

When the loading is increased, the stress intensity factor K_I approaches the critical value K_{IC} at which point the wing crack grows out of the initial plane along orientations sub-parallel to σ_I. As the stress increases, more cracks distributed throughout the given sample will grow in this form. These cracks will eventually coalesce. One benefit of the wing crack model in [159] is that this complex crack interaction is captured by analytic approximations in the model. So, the given compressive strength is given by,

$$s_{\mathrm{c}} = \frac{K_{IC}}{y\sqrt{\pi a}}, \tag{2.5}$$

where y denotes crack interaction in an averaged sense. In [19] the value of y is derived for a structured grid of parallel wing cracks and was used in [159] to approximately model their interaction for a non-structured network of wing cracks (variable size, angle, and spacing). The value of y is obtained from,

$$y = \frac{\sqrt{1+\mu^2}-\mu}{(1+l_{cr})^{3/2}}[C_3 l_{cr} + \frac{1}{\sqrt{3}(1+l_{cr})^{1/2}}] + \frac{[2\varepsilon_0(l_{cr}+cos\psi)]^{1/2}}{\sqrt{\pi}}. \tag{2.6}$$

In (2.6), μ is the friction coefficient, ψ is the angle between the sliding crack and the maximum principal stress, l_{cr} is the critical normalized crack length, and ε_0 is the crack density. C_3 will be defined as part of the solution for the normalized critical length l_{cr}, which is a positive root of the implicit equation,

$$\frac{C_1}{2(l+cos\psi)^{1/2}}+\frac{C_2}{(1+l)^{3/2}}[C_3-\frac{C_4}{2(1+l)^{3/2}}]-\frac{3C_2}{2(1+l)^{5/2}}[C_3l+\frac{C_4}{(1+l)^{1/2}}]=0 \tag{2.7}$$

where $C_1=\sqrt{2\varepsilon_0/\pi}$, $C_2=\sqrt{1+\mu^2}-\mu$, $C_3=0.23$, and $C_4=0.577$. Although the angle ψ depends on the angle of loading relative to a crack direction, following the work of Wong in [158], an optimal angle of $\psi=(1/2)\tan^{-1}(1/\mu)$ is chosen.

The second step is to determine the compressive strength of an SVE from the strengths of individual cracks contained in it. Within each circular SVE, the microcracks which are contained in or intersect with it are found. These microcracks are shown in Fig. 3. For each of these cracks s_c is obtained from (2.5).

For cracks which are partially contained within the SVE, only the crack length $2a$ contained within the SVE is processed. The minimum fracture strength is then calculated. As mentioned in §2.3.2, the fracture strength of each SVE is assigned to its centroid to form a uniform grid of mesoscopic fracture strengths as shown in Fig. 1(c).

When an SVE contains no microcracks, a maximum fracture strength based on the minimum half crack length $a^{'}$is assigned to the SVE; *cf.* §2.3.1. As will be observed in §2.4, in general this maximum strength is assigned to only a very few SVEs, except when a combination of low crack density and small SVE size is used. The SVEs with the assigned maximum strength are not deemed to greatly influence fracture response, as fracture is mostly affected by regions with lower strength. However, to better represent the strength of these SVEs one could consider failure in the bulk and the effect of microcracks, voids, and defects at scales smaller than those considered herein.

2.3.4 aSDG method and fracture model

The h-adaptive *asynchronous Spacetime Discontinuous Galerkin* (aSDG) method, formulated for elastodynamic problem in [6, 7], is utilized for the dynamic fracture simulations. The aSDG method directly discretizes spacetime using nonuniform grids that satisfy a special causality constraint resulting in unique properties, such as a local and asynchronous solution scheme, arbitrarily high and local temporal order of accuracy, and linear solution scaling versus number of elements.

On fracture surfaces often a cohesive model [52, 21] is employed to represent the process of debonding. In lieu of such models, we employ an interfacial contact and damage model [4], wherein internal parameters including a damage parameter D model the processes of debonding and contact–stick / contact-slip mode transitions. On an arbitrary oriented fracture surface, an *effective stress* scalar value drives damage evolution. The effective stress combines positive normal (*i.e.,* tensile) and shear traction components and is compared against an *effective fracture strength* $\tilde{s}$ at a given point. The strength field $\tilde{s}$ can be inhomogeneous; in §2.5, it will be discussed how it is derived from a mesoscopic uniaxial compressive strength field, such as that shown in Fig. 1(c).

Figure 1(d) shows a sample front mesh (spatial mesh) for a dynamic fracture simulation. For each of the vertices of the front mesh, we check if the effective stress exceeds $\tilde{s}$ for any potential angle of crack propagation, $\theta \in [0, 2\pi]$. If so, a crack is nucleated and propagated in that direction. The same holds for the tips of already propagated cracks. Advanced mesh adaptive operations in spacetime are employed to align inter-element boundaries with the proposed crack direction. To further enhance the accuracy and efficiency of the method, an h-adaptive scheme adjusts element sizes in spacetime to satisfy error indicators in the bulk and on fracture interfaces for controlling the energy dissipation and satisfaction of fracture constitutive relations [8]. The combination of these two sets of mesh adaptive operations and aSDG properties enables accurate representation of very complex fracture patterns for dynamic brittle fracture, as shown in Fig. 1(d). For a review of these mesh adaptive operations for fracture analysis, we refer the readers to [5].

The aforementioned adaptive operations accommodate crack propagation in arbitrary directions, thus providing the same or higher flexibility than other mesh adaptive finite element methods [32, 123, 122, 131], such as the *eXtended Finite Element Methods* (XFEMs) [151, 110, 47] and *Generalized Finite Element Methods* (GFEMs) [34, 149], in accurate numerical modeling of complex crack paths. However, there are several advantages to directly aligning element boundaries with crack direction, rather than having cracks go through elements as in XFEMs and GFEMs. Since the elements containing cracks and crack tips require enrichment functions, the finding of such functions can be challenging for XFEMs and GFEMs. For example, the majority of these methods are based on the *Linear Elastic Fracture Mechanics* (LEFM) theory and using nonlinear models such as cohesive and interfacial damage models (used in this manuscript) is cumbersome, at least in elements containing crack tips. Moreover, geometric complexities such as crack branching, microcracking, and crack intersection are very common in dynamic fracture. Again, specific enrichments should be used for such fracture patterns with XFEMs and GFEMs. In contrast, any fracture model can be used between element boundaries and the aSDG mesh adaptive operations can accommodate aforementioned dynamic fracture patterns. However, as discussed in [10], extension of mesh adaptive methods to 3D for aSDG would be more difficult than XFEMs and GFEMs. Finally, we note that meshless methods such as [167] can be appropriate choices for modeling complex rock fracture problems in 2D and 3D.

2.4 Results for mesoscopic fracture strength homogenization

In this section, the numerical results corresponding to the two scale fracture analysis scheme in Fig. 1 are presented. First, the statistics and initial results from the Yuen-Long marble sample with a Power-Law microcrack distribution and the various generated Weibull distributions with four different shape parameters will be presented in §2.4.1 and §2.4.2. Then, the generated Weibull distributions will be analyzed with a specific focus on SVE size in §2.4.3 and a focus on crack density in §2.4.4. Finally, the dynamic fracture analysis performed utilizing the aSDG method are presented in §2.5. The use of the aSDG method is motivated by employing an interfacial contact-damage model and observing complex fracture intersection patterns, *cf.* Fig. 23; otherwise, as discussed in §2.3.4, these aspects pose challenges to methods such as XFEMs and GFEMs.

2.4.1 Power and Weibull generated domain results

Six Yuen-Long marble samples were analyzed in [159]. For this analysis, the white marble sample statistics from the sample designated S19 were used to generate the simulated Power-Law domain. Table 1[2] summarizes the material properties taken from [159]. These properties include the material density ρ, Poisson's ratio ν, Young's modulus E, mean crack length $2a$, characteristic minimum length $a^{'}$, crack density ε_0, Cauchy distribution exponent z, and power law distribution parameter $q^{*}V_0$. The characteristic minimum length $a^{'}$ is also used in the SVE analysis process to calculate the maximum possible strength associated with the minimum potential crack length.

Several Weibull distributions were created with the same mean crack length $2a$ as the power law distribution domain for the Yuen-Long marble sample, 0.141 mm. The goal of this analysis is to show the effect of changing the crack length probability density function (PDF) on the fracture response of the material. Therefore, a wide variety of PDF shapes were required to provide the desired impact on the fracture response.

Because the Weibull distribution PDF shape changes drastically with increasing shape parameter m, the m values of $\frac{1}{2}$, 1, 2, and 4 were selected to change the shape of the distribution. The value of $m = \frac{1}{2}$ provides a PDF shape that is very close to the power-law distribution, while the shape becomes more bell-shaped and less skewed as higher m values such as $m = 4$ are used.

The minimum crack length $2a$ of 0.015 mm was kept the same, while also reusing the same Young's modulus and Poisson's ratio. Thus, the Weibull distribution parameter γ was set equal to 0.015, while the r factor was set to unity, since the volume element considered is equal to 32 mm × 32 mm square used in [159] for V_0 ($r = V/V_0 = 1$). The scale parameter η was changed for each m value to maintain the mean crack length of 0.141 mm.

To perform a study of the effect of crack density on mesoscopic fracture strength, three different crack densities ε_0 were analyzed using the Weibull distribution, 0.05, 0.243, and 0.75. Thus a total of 12 individual randomly generated microcracked domains similar to Fig. 1(a) were generated for the Weibull model (four m values times three crack densities).

---

[2] Please note that all tables in this dissertation are contained within Appendix B

Finally, to show how small and large SVE sizes capture the heterogeneities in the microcrack-filled domain, we determine macroscopic fracture strength of each of these 12 RVEs with different SVE sizes of L_{SVE} equal to 1, 2, 4, and 8 mm. Thus, the analyses for the Weibull model involves 12 distinct microcracked domain resulting in 48 mesoscopic fields for s_{c}.

As shown in Fig. 1(a) microcracks are formed in a 80 mm×80 mm square domain centered at $(0, 0)$.

Four of the twelve generated Weibull distribution microcrack domains analyzed with ε_0 = 0.243 are shown in Fig. 4. Fig. 5 shows the corresponding crack length probability density functions. For the Weibull distributions, $m = \frac{1}{2}$ most closely approximates the power law distribution. As m increases, the shape changes such that there are less smaller cracks and a more defined bell-curve shape that results in a smaller standard deviation of length for the distribution is formed.

Before performing the SVE analysis process, a reasonable value for SVE spacing, equal to $n = 10$, is determined and detailed next in §2.4.1.

Each domain is then analyzed using SVEs with the proper spacing. For each SVE a uniaxial compressive strength was assigned based on the minimum values of strength calculated for the microcracks in the SVE. For SVEs with no microcrack a crack with minimum length of 0.015 mm is considered; *cf.* the discussion at the end of §2.3.3. The contour plot of strengths for the power law distribution with $L_{SVE} = 1$ and $n = 10$ is shown in Fig. 6(d). After calculating the strength field, the strength field statistics are calculated to provide a better understanding of the general strength trends based on the three different variables that were changed: distribution type and shape, L_{SVE} size, and crack density.

Effect of SVE spacing

As discussed in §2.3.2, in moving window method the RVE is traversed with SVEs with spacing S. In order to determine a reasonable value for this spacing, four values of $n = 1, 2, 5, 10$ were chosen. For lower values of n, the analysis loses spatial resolution, and may not even completely cover the RVE ($n = 1$), leading to gaps that may miss certain cracks entirely. For higher values of n, the statistical distribution of calculated fracture strengths do not vary much with increasing spatial resolution, resulting in a greater computational cost for no apparent gain in creating the mesoscopic fracture strength field. This trend is shown in Fig. 6 in the strength contour plots. The PDFs of strength for various n, and for $L_{SVE} = 1$, in Fig. 7 show that there is not a large difference in strength statistics even with the smallest $n = 1$ is used. The mean strength of the field does change slightly with greater n values, converging to the true value with a smaller spacing between each SVE. For the rest of this manuscript, the value $n = 10$ was selected for calculating the SVE spacing $S = L_{SVE}/n$ as the best trade-off between spatial resolution and computational cost.

2.4.2 Distribution type and shape effect

The goal of this section is to demonstrate how the shape of the distribution of cracks at the microscale affects the statistics of mesoscopic strength field. This is facilitated by using different shape parameters for synthetic Weibull distributions; *cf.* §2.3.1. The data shown in the strength probability density function, found in Fig. 8, is in agreement with the expected trends after reviewing the crack length probability density function in Fig. 5. Despite each domain containing the same mean crack length, the actual mean strength does vary depending on the crack length distribution shape. The variance that results is a function of the fact that the $m = \frac{1}{2}$ and $m = 1$ distributions contain a larger standard deviation, with a larger number of both smaller and larger cracks about the average than the more bell-curve shape crack length distributions for $m = 2$ and 4. This feature can also be shown by reviewing the strength contours themselves for each of various m shapes, as seen in Fig. 9.

Due to a feature of the SVE averaging process wherein any empty SVEs are assigned a strength for a crack of a minimum length, the probability density function that results from this analysis with the smaller L_{SVE} sizes inevitably appears bi-modal with two primary modes: one lower strength mode for the SVEs which contain cracks, and a smaller, higher strength mode for the few SVEs without any crack interaction. As would be expected, utilizing larger SVE sizes removes this feature, as there are fewer SVEs and therefore a reduced number or no SVEs without any cracks containing within the SVEs. This will be detailed in the next section, §2.4.3. For the power law distribution, the calculated mean strength for $L_{SVE} = 1$ is 72.67 MPa, slightly higher than the sample material strength of

55.85 MPa reported in [159]. This is a result of considering both the empty and non-empty SVEs.

It is noted that from the Weibull distribution results, those corresponding to $m = \frac{1}{2}$ are the most realistic, as its microcrack length distribution in Fig. 5 (and consequently s_c in Fig. 8) are closest to that of the power distribution for this Yuen-Long marble sample.

2.4.3 Weibull distribution comparison: SVE size effect

The size of the SVE, L_{SVE}, strongly controls the statistics of the heterogeneous fracture strength field averaged, such as its point-wise *Probability Distribution Function* (PDF).

Recall the parameter β, equal to $L_{SVE}/\mathbb{E}(2a)$, from §2.3.2; as this parameter (*i.e.,* the SVE size) tends to infinity, the material inhomogeneity is lost for this macroscopically homogeneous rock. To show this *size effect*, four different L_{SVE} sizes were used: 1, 2, 4, and 8 mm.

Figure 10 shows the strength contour plots of the same domain ($m = \frac{1}{2}$, $\varepsilon_0 = 0.243$) for each of the various SVE sizes. Each of the four individual subplots utilize the same contour range, which allows for objective comparison of strength fields across each plot. The smaller SVE size, $L_{SVE} = 1$, contains a multitude of high and low strength SVEs. As the SVE size increases, the strength in the field becomes lower and more homogeneous.

The strength PDFs in Fig. 11 show the same trends for each m value for the various Weibull distributions. The change of mean ($\overline{s}_c$) and standard deviation (ς) of strength versus SVE size are also shown in Fig. 12. As m increases, the mean strength generally increases. The only exception is $L_{SVE} = 1$ and $m = \frac{1}{2}$, as shown in Fig. 12(a). This is due to the wide span of crack lengths allowed by this distribution. Generally, the majority of the cracks for this distribution are extremely small. However, larger cracks are allowed, which results in an extremely high standard deviation. Moreover, as shown in Fig. 12(a), $\overline{s}_c$ decreases when L_{SVE} increases. This well-known *size effect* for quasi-brittle materials is contributed to the fact that larger SVEs contain more microcracks thus are more likely to contain longer cracks. This results in lower mean strengths for larger SVEs.

As the size of the SVE increases, the standard deviation ς tends to zero. The decreased variation of the field is shared among all fields homogenized/averaged by SVEs, since as larger SVEs are considered the population of microstructural features (microcracks herein) increases and their statistic converges to that of the macroscopic domain. From Fig. 12(a), the crack length Weibull shape parameter m has no major impact on small values of ς for large SVE sizes. The mean strength $\overline{s}_c$ of the field still strongly depends on the actual crack distribution shape m even at larger SVE sizes, due to the differences in the allowable crack lengths.

Maintaining rock inhomogeneity is advantageous for fracture analysis of quasi-brittle materials, particularly under loading scenarios where there is no macroscopic stress concentration points; *i.e.,* similar to problems considered in §2.5. This analysis shows the importance of maintaining a relatively small SVE size to increase the fidelity of fracture simulations using the corresponding homogenized strength field. Consequently, as long as smaller SVEs are representative, they are preferred for fracture analysis.

2.4.4 Weibull distribution comparison: crack density effect

The actual Yuen-Long marble sample statistics were utilized to generate domains with crack density $\varepsilon_0 = 0.243$ in preceding sections. However, the domains in this section are computationally created with different crack densities to investigate its effect on the statistics of mesoscopic strength. The sliding wing-crack model contains a variable y that attempts to take into account the effect of crack interaction on the fracture strength based on the crack density. A low crack density of $\varepsilon_0 = 0.05$ and a high crack density of $\varepsilon_0 = 0.75$ were selected along with $\varepsilon_0 = 0.243$ for this analysis. Solving equation (2.6) results in $y = 0.37$, 0.64, and 0.96 for $\varepsilon_0 = 0.05$, 0.243, and 0.75, respectively. This modifies the fracture strength in equation (2.5), with a higher crack density resulting in a lower overall strength, as would be expected.

Fig. 13 shows the strength contours for $m = \frac{1}{2}$ with varying ε_0. For low density $\varepsilon_0 = 0.05$, the strength field has a nearly uniform high strength. The (longer) cracks that are placed in the domain are easily seen in the strength contour, as the sampling SVEs at the grid points effectively expand them by a thickness proportional to the SVE size. The resulting PDF in Fig. 14 is bi-modal due to the large number of SVEs that do not contain a crack. Comparatively, the higher density $\varepsilon_0 = 0.75$ is almost uniformly lower in strength. As the crack density increases, this bi-modal feature of the crack field for the SVE averaging process is reduced.

These results show that the crack density affects at what size the SVE can be considered representative, *i.e.,* the majority of sampled SVEs containing cracks. For example, for $\varepsilon_0 = 0.05$ SVEs with $L_{SVE} = 1$ are not appropriate due to the large number of empty SVEs resulting in the bi-modal shape for the PDF in Fig. 13(a). It is noted that the low density of $\varepsilon_0 = 0.05$ is intentionally chosen to better demonstrate that L_{SVE} cannot be set to arbitrarily small values.

For domains with a higher crack density, *i.e.,* experimentally observed $\varepsilon_0 = 0.243$, $L_{SVE} = 1$ is deemed representative and from this perspective even smaller SVEs can be considered to better capture rock inhomogeneity. Finally, it is noted that strength steadily decreases as the crack density increases. This is similar to the effect that increasing SVE size has, because in both cases more cracks are sampled within an SVE, thus reducing the (mean) averaged fracture strength of SVEs.

2.5 Macroscopic fracture analysis

2.5.1 Problem description

As shown in Fig. 1(c), from the averaging scheme discussed in previous sections, a structured grid of s_c is formed for macroscale fracture analysis. To study the effect of changing shape parameter m for the Weibull distribution, four different simulations were performed for each m value. For these simulations we use strength fields obtained by SVE size $L_{SVE} = 1$ since they retain the most heterogeneity. The crack density is $\varepsilon_0 = 0.243$. The four employed fields for s_c are shown in Fig. 9.

Figure 15 shows two different grids employed for storing fracture strengths and fracture analysis. As will be discussed below, the 32 mm × 32 mm RVE shown in Fig. 1(a) is subject to a vertical uniaxial tensile loading. Since the grid spacing is $L_{SVE}/n = 0.1$ ($n = 10$; *cf.* §2.3), fracture strengths in Fig. 9 are stored in a 360×360 structured grid shown in Fig. 15a. The initial spatial mesh for fracture analysis, containing 803 triangular space elements is shown in Fig. 15b. Since the aSDG directly discretizes space and time, for a spatially 2D problem, the computational domain is three dimensional in spacetime. Accordingly, the aSDG method builds a spacetime mesh of tetrahedral elements, by pitching vertices of this mesh in time; *cf.* §2.3.4 and [1, 6]. Mesh adaptive operations adjust the space mesh to first ensure solution is captured with sufficient accuracy and second align element boundaries with proposed crack directions, so that fracture pattern is accurately captured. An intermediate front mesh for a dynamic fracture analysis is shown in Fig. 1(d). As can be seen, the elements in the front mesh are finer close to fractures (blue to red thick lines) in response to the two adaptive operations discussed above.

The spacetime elements of the aSDG method are tetrahedra attached to this spatial front. Since the spatial front adapts in response to the ever evolving fracture pattern, the spatial location of the quadrature points of the spacetime elements varies. As shown in the zoomed view Fig. 15c, a sample quadrature point is spatially contained in one square of the uniform material grid with vertices V_1 to V_4. Fracture strength at this point is obtained by linear interpolation of mesoscopic strength values stored at vertices V_1 to V_4.

If elastic properties were also deemed to be inhomogeneous, they would be stored in the material mesh and obtained by the same process. However, homogeneous and isotropic elastic material properties for rock are taken from Wong [159] for material sample S19: Young's Modulus $E = 65$ GPa , mass density $\rho = 2700\ \frac{\text{kg}}{\text{m}^3}$, and Poisson's ratio $\nu = 0.3$. A 2D plane strain condition is assumed for the analysis. A displacement solution in the form,

$$u_x = axt \tag{2.8a}$$

$$u_y = byt \tag{2.8b}$$

satisfies the elastodynamic equation of motion. The coefficients a and b are normal strain rates in x and y directions, respectively. The solution (2.8) corresponds to the velocity field $v_x = ax$, $v_y = by$ and the strain field $\epsilon_{xx} = at$, $\epsilon_{yy} = bt$, $\epsilon_{xy} = 0$. For all values of a and b, the corresponding stress field is spatially uniform and temporally linearly increasing. This type of loading is typical for fragmentation analysis, *e.g.,* [45, 5]. In fact, for a material with homogeneous fracture properties, a fracture initiation condition is suddenly satisfied across the whole domain once the stress field becomes sufficiently large to satisfy such condition at any point. This response is clearly non-physical and is avoided herein by using mesoscopically inhomogeneous fracture strength fields.

By choosing specific values of a and b, confined and unconfined uniaxial and biaxial tensile and compressive loading conditions can be designed. For an unconfined uniaxial loading in direction y, stress components are,

$$\sigma_{xx} = 0, \qquad \sigma_{yy} = \dot{\sigma} t, \qquad \sigma_{xy} = 0, \tag{2.9}$$

where $\dot{\sigma}$ is a user-specified stress rate. For the plane strain condition, the corresponding coefficients in (2.8) are $a = -\dot{\sigma}\nu(1+\nu)/E$ and $b = \dot{\sigma}(1-\nu)(1+\nu)/E$. Herein, we choose the stress rate $\dot{\sigma} = 10^{11}$ Pa/s. This corresponds to strain rates $a = -0.6$/s and $b = 1.4$/s for $E = 65$ GPa and $\nu = 0.3$. That is, displacement solution in (2.8) corresponds to a spatially uniform and temporally increasing tensile loading ($\dot{\sigma} > 0$) in vertical direction until the very first crack is nucleated in the macroscopic domain.

For plane strain condition, the elasticity constitutive equation in Voigt notation is,

$$\begin{bmatrix} \sigma_{xx} \\ \sigma_{yy} \\ \sigma_{xy} \end{bmatrix} = \mathbf{C} \begin{bmatrix} \epsilon_{xx} \\ \epsilon_{yy} \\ 2\epsilon_{xy} \end{bmatrix} \tag{2.10}$$

where $\mathbf{C}$ is equal to,

$$\mathbf{C} = \begin{bmatrix} C_{11} & C_{12} & C_{13} \\ C_{21} & C_{22} & C_{23} \\ C_{31} & C_{32} & C_{33} \end{bmatrix} = \frac{E}{(1+\nu)(1-2\nu)} \begin{bmatrix} 1-\nu & \nu & 0 \\ \nu & 1-\nu & 0 \\ 0 & 0 & 1-2\nu \end{bmatrix} \tag{2.11}$$

thus, the stress components are given by $\sigma_{xx} = (C_{11}a + C_{12}b)t$, $\sigma_{yy} = (C_{21}a + C_{22}b)t$, and $\sigma_{xy} = 0$. By choosing $a = -\dot{\sigma}C_{12}/(C_{11}C_{22} - C_{12}C_{21})$ and $b = \dot{\sigma}C_{11}/(C_{11}C_{22} - C_{12}C_{21})$, we obtain a stress field in the form,

$$\sigma_{xx} = 0, \qquad \sigma_{yy} = \dot{\sigma} t, \qquad \sigma_{xy} = 0, \tag{2.12}$$

where $\dot{\sigma}$ is a user-specified stress rate; that is, displacement solution in (2.8) corresponds to a spatially uniform and temporally increasing tensile loading ($\dot{\sigma} > 0$) in vertical direction. Herein, we choose the stress rate $\dot{\sigma} = 10^{11}$ Pa/s. This corresponds to strain rates $a = -0.6$/s and $b = 1.4$/s.

The initial and boundary conditions for this problem are set consistent with these solution fields and are shown in Fig. 16. Due to the temporally increasing stress field in (2.12), eventually a crack is nucleated from the weakest point of the sampled fracture strength field, *cf.* Fig. 15a. In subsequent times, the displacement, velocity, strain, and stress solutions presented above no longer hold as the propagation of cracks disrupt them. Consistent with the exact solution prior to nucleation of any cracks, we enforce a traction free boundary condition on the vertical boundaries. On top and bottom surfaces we apply zero tangential stress (frictionless condition) and normal velocity $V_0 = bH/2 = 22.4$ mm/s. This resembles a *displacement-control* loading in quasi-static condition and ensures that we capture the unloading part of the macroscopic strain-stress curve through the process of loading and failure of the RVE.

In simplest form, a crack nucleation/extension criterion compares a scalar *effective* stress s_{eff} formed from the normal t_n and shear t_s components of traction components on a potential crack surface versus an *effective fracture strength* $\tilde{s}$. If at the spatial location $\mathbf{x}$, the condition $s_{\text{eff}}(\mathbf{x}, \theta) \geq \tilde{s}(\mathbf{x}, \theta)$ is satisfied for any potential crack extension angle $\theta \in [0, 2\pi]$ in 2D, a crack is nucleated (or extended if $\mathbf{x}$ is already the tip of a propagating crack), along an angle for which $s_{\text{eff}}(\mathbf{x}, \theta)/\tilde{s}(\mathbf{x}, \theta)$ is maximum (and greater than 1). The dependence of $\tilde{s}$ on $\mathbf{x}$ represents an inhomogeneous strength field, whereas anisotropy of strength is incorporated on the dependence of $\tilde{s}$ on θ, an aspect not considered in the present study.

Since the following fracture simulations are for uniaxial tensile loading, we aim to employ an effective stress model that is more appropriate for such loading. The inhomogeneous fields for effective fracture strength $\tilde{s}$ are obtained from the uniaxial compressive strength fields for s_{c} in Fig. 9. The Mohr-Coulomb failure criterion stipulates a relation between uniaxial tensile and compressive strengths; that is $\tilde{s} = s_{\text{c}}(1 - \sin\phi)/(1 + \sin\phi)$, where $\phi = \tan^{-1}(\mu)$ is the *friction angle*. Similar to [159] we assume the macroscopic friction coefficient to be 0.6

and use the linear relation above to map the compressive strength fields in Fig. 9 to those for $\tilde{s}$.

Finally, a shortcoming of the Mohr-Coulomb failure criterion is that it predicts incorrect fracture angles, thus making it inappropriate for tensile fracture simulations. Instead, we employ the *Maximum Circumferential Stress Criterion* (MCSC) [53], where $s_{\text{eff}} = \langle t_n \rangle_+$ and $\langle . \rangle_+$ is the Macaulay positive bracket, ensuring that only tensile traction ($t_n > 0$) contributes to the effective stress. We refer the reader to [3] for the details on this effective stress model and its use by the aSDG method.

2.5.2 Macroscopic strain versus stress response

The purpose of this example is to demonstrate the great effect of the distribution of microcrack length on macroscopic response. The power law distribution of half crack length for S19 in [159] and all four synthesized Weibull distributions in Fig. 5 have the same mean values. However, they result in different PDFs for mesoscopic strengths in Fig. 8. We use the shape parameter m to demonstrate the great influence of the shape of PDF of microcracks on macroscopic response subsequently. By referring to Fig. 5 and Fig. 8, it is noted that the results for $m = \frac{1}{2}$ would be the most representative for rock sample S19 in [159] with its power law distribution.

We use homogenization boundary integrals [111] to obtain macroscopic strain E and stress Σ tensors for each instant of the loading for different values of m. These homogenized values correspond to averaged stresses and strains that are applied on the boundary of the 32 mm × 32 mm RVE in Fig. 16. Figure 17 shows the histories of Σ_{yy} versus time for all Weibull distribution models for microcrack length; since $\Sigma_{xx} = 0$ and $\Sigma_{xy} = 0$ (as expected from problem description), their histories are not presented.

To discuss important stages of strain versus stress response, we focus on the result for $m = \frac{1}{2}$. As shown, up to time $t = \tilde{t}_i = 46\ \mu\text{s}$, Σ_{yy} linearly increases versus time; *cf.* (2.12). At this time, the first cracks are nucleated in the domain due to the increased stress level, resulting in the degradation of rock. This response continues until the maximum stress $\tilde{\Sigma}_m = 6$ MPa is attained at $t = \tilde{t}_m = 67.2\ \mu\text{s}$. The stress $\tilde{\Sigma}_m$ can be associated with macroscopic tensile strength of this size of RVE for $m = \frac{1}{2}$. Past time $\tilde{t}_m$, cracks (shown later) have propagated in large portions of the domain. This results in stress unloading until Σ_{yy} reaches zero at $t = \tilde{t}_f = 76.7$ μs. Afterwards, some oscillations are observed in stress response due to dynamic nature of the loading and complete failure of the RVE.

The three important points of strain-stress response are: *initiation of nonlinear response*, *maximum stress*, and *failure*. The time ($\tilde{t}$), strain ($\tilde{E}$), stress ($\tilde{\Sigma}$), and energy density ($\tilde{\psi}$) corresponding to these stages are subscripted with i, m, and f, respectively, as observed in the preceding paragraph. Herein, energy refers to the area under the strain-stress curve. Thus, $\tilde{\psi}_f$ is the dissipated energy per unit volume which along with macroscopic the strain-stress response can be used to calibrate a bulk damage model [132].

We compare macroscopically homogenized strain versus stress responses in Fig. 18. Unlike Fig. 17, the portion of response past failure is not depicted to concentrate only on elastic to full damage transition. As mentioned, having a larger variation on initial crack length distribution for $m = \frac{1}{2}$ results in higher variations and generally lower values for averaged mesoscale fracture strengths; *cf.* Fig. 9 and Fig. 12 ($L_{SVE} = 1$). Having smaller minimum strengths ($s_{\rm c}$ and $\tilde{s}$), results in earlier time for failure initiation $\tilde{t}_i$ (thus smaller $\tilde{E}_i$ and $\tilde{\Sigma}_i$) in Fig. 17 and Fig. 18. The smaller minimum and overall strength values for $s_{\rm c}$ also results in a weaker rock compare to other m values, particularly $m = 4$. This is reflected in its much smaller macroscopic tensile strength. Finally, larger standard deviation in microcrack length (and thus mesoscopic strength $\tilde{s}$), results in an expanded time and strain range for transition from the initiation of nonlinear response to maximum stress stages in Fig. 17 and Fig. 18, respectively.

Table 2 compares time, strain, stress, and energy density scales of all Weibull distributions at different stages of macroscopic solution. As discussed above, $m = \frac{1}{2}$ has the lowest nonlinear response initiation time/strain/stress and maximum stress. These trends continue as m increases until the maximum values are realized for $m = 4$. Again, the reason for this trend is the higher minimum and overall mesoscopic fracture strengths $\tilde{s}$ as m increases. Specifically, we observe that nonlinear response in terms of time, strain, and stress starts 4.28 times earlier for $m = \frac{1}{2}$ compared to $m = 4$. In addition, $m = 4$ corresponds to a much stronger rock given that its macroscopic tensile strength ($\tilde{\Sigma}_m$) is 3.30 times of that of $m = \frac{1}{2}$. Higher stress levels for initiation (i) and maximum stages (m) are the main contributors for the $m = 4$ specimen having the highest toughness as well; the ratio of dissipated energy density $\tilde{\psi}_f$ of $m = 4$ to $m = \frac{1}{2}$ solution is 6.22, which is at an even higher value than corresponding ratios for tensile strength and nonlinear initiation stress limit.

Next, we study the effect of m on brittleness. As observed in Fig. 17 and Fig. 18, once the rock's nonlinear response initiates, it takes much less time and strain for $m = 4$ sample to reach failure stage compared to samples with lower m values. That is, there is much less time and a smaller deformation safety zone for this rock once failure initiates. This is reflected in a very high *brittleness factor* $\tilde{t}_i/\tilde{t}_f = \tilde{E}_f/\tilde{E}_i = 0.97$ for $m = 4$ compared to 0.60 for $m = \frac{1}{2}$.

From an energy perspective, $\tilde{\psi}_i/\tilde{\psi}_m$ is the ratio of elastic energy stored up to the initiation of nonlinear response to the energy consumed at the onset of unstable unloading. Moreover, $\tilde{\psi}_m/\tilde{\psi}_f$ represents the ratio of energy at the onset of unloading to the total dissipated energy at failure. These measures are deemed to represent the energy brittleness indicators for the loading and unloading phases. As can be seen from all proposed measures of brittleness, $m = \frac{1}{2}$ and $m = 4$ samples are the least and most brittle ones. In summary, while a higher m corresponds to a higher strength and tougher rock, the tendency of the mesoscopic strength $\tilde{s}$ to a uniform field has the drawback of making the rock more brittle.

2.5.3 Analysis of crack propagation in the RVE

In this section we study the dynamics of crack propagation and analyze the fracture pattern at different stages of solution. Figure 19 shows the total length of propagated crack, L, in the domain over time for each Weibull distribution with shape parameter m. As m increases, more time (and therefore, higher stress) is required to initiate crack propagation. This is in agreement with results in §2.5.2. Interestingly, the result for $m = \frac{1}{2}$ does not depict a rapid growth of L. For $m = \frac{1}{2}$ cracks are nucleated (and propagated) at the weakest points in the domain from $\tilde{t}_i = 46$ μs to around $t = 65$ μs. However, due to the high variability of mesoscopic strength $\tilde{s}$, crack tips may be surrounded by much higher strength rock. About 20 μs time is needed to build up the overall stress field sufficiently high to enable the propagation of a crack through the surrounding area, explaining the rather slow crack growth rate during this period. In contract, for higher m values mesoscopic strength field is more uniform. Thus, once the first cracks are nucleated there is a faster growth of L.

Another observation is the continued growth of L past the failure stage for all m values. For example, for $m = \frac{1}{2}$, $\tilde{t}_f = 76$ μs whereas L growth significantly slows down only at $t \approx 140 - 170$ μs, corresponding to about three full cycles of $\tilde{\Sigma}_{yy}$ oscillations past $\tilde{t}_f$ in Fig. 17. This is due to the dynamic nature of the loading; finite speed cracks and microcracks continue to propagate even past macroscopic failure time $\tilde{t}_f$ until their growth is slowed down at a later time due to ever reducing overall stress level shown in Fig. 17.

To have a better understanding on degradation and energy dissipative role of propagated cracks, beside the total length of cracks we monitor the level of damage parameter D on crack segments. As a crack grows, D evolves over almost all parts of it that are partially debonded. The regions close to the crack tip have the smallest damage value as the damage evolution has just started therein. In contrast, the tails of the larger cracks often experience full damage. The average damage parameter, $\bar{D}$, computed over all crack segments and weighted by their length in the averaging process is a good measure of the overall level of debonding on all crack segments. The time history of $\bar{D}$ is shown in Fig. 20. For $m = \frac{1}{2}$ in the time range of $\tilde{t}_i = 46$ μs to around $t = 65$ μs, we observe a relatively high variation to $\bar{D}$ caused mainly by small length of propagated cracks in Fig. 19. However, for all m values once sufficient length of crack is developed, $\bar{D}$ settles in the range $[0.75,\ 0.82]$. That $\bar{D}$ does not tend to unity, *i.e.,* full damage, for all crack segments is contributed to dynamic nature of loading and microcracking phenomenon (shown in subsequent figures); while major cracks mostly experience full damage, many microcracks emanated from them experience only partial damage as the local damage driving stress magnitudes may subdue faster than the rate at which damage evolves on their surfaces.

The propagation of cracks in the domain are shown in Fig. 21 and Fig. 22. In these figures, each extreme of the Weibull shape parameters, $m = \frac{1}{2}$ and 4 are shown.

The strain energy density is $U := \frac{1}{2}\boldsymbol{\sigma} : \boldsymbol{\epsilon}$, where $\boldsymbol{\sigma}$ and $\boldsymbol{\epsilon}$ are the stress and strain tensors. The kinetic energy density is $K = \frac{1}{2}\rho\mathbf{v}.\mathbf{v}$, where ρ is the mass density and $\mathbf{v}$ is the velocity vector. In Fig. 21 and all subsequent solution visualization U is mapped to color field, where zero to maximum values are mapped to blue-to-purple color range. The unit of U

is $\mathrm{J/m^3} = \mathrm{Pa}$. Similarly, K is mapped to the height field such that regions of high kinetic energy density appear closer.

Different stages of the solutions in these figures are marked in the time history of macroscopic stress in Fig. 17. For both m values, maximum stress $\tilde{\Sigma}_m$ corresponds to early stages of solution, where mainly horizontally propagating cracks have traversed only a part of the domain. Regions of high strain concentration are observed around moving crack tips and on the fronts of propagating elastic waves. Moreover, the stress field relaxes in tail of the cracks as debonding occurs. As shown in Fig. 17, past the failure time $\tilde{t}_f$ the macroscopic stress Σ_{yy} oscillates about zero and is dampened with each successive oscillation from further failure of rock and dissipation of energy on fracture surfaces. This is also reflected in decreased levels of strain energy densities at latter frames of the solutions shown in Fig. 21 and Fig. 22. In comparison of the two sets of solution, fracture initiates later for $m = 4$, involves higher stress values, more abruptly reaches the failure stage, and results in a more widespread and dense network of cracks and microcracks.

Figure 23 shows the aSDG spatial front meshes for the dynamic fracture simulations at $\tilde{t}_m$, the time of maximum stress $\tilde{\Sigma}_{yy}$. As discussed, $\tilde{t}_m$ increases as m increases. Sections of the crack length which have already failed are indicated by a red line; locations where damage is occurring (often close to crack tips) are indicated by lines of varying rainbow color from blue to red, corresponding to $D \in [0,\ 1]$. Generally speaking, each crack distribution appears very similar, containing from one to three zones of mostly horizontal and damaged cracks and ranging in size from only about 10% to 20% of the domain width. These cracks are nucleated from locations of low mesoscopic strength $\tilde{s}$. It is emphasized that all these simulations have started from the relatively coarse spatial mesh (front mesh) shown in Fig. 15b and have resulted in much smaller elements around propagating crack tips; mesh refinement and coarsening operations in spacetime ensure that the differential equations are accurately and efficiently solved on fracture surfaces and in the bulk, and to accommodate arbitrary requested angles of crack propagation.

Finally, Fig. 24 shows the deformed shape of the domain and crack pattern at $\tilde{t}_f$, the time $\tilde{\Sigma}_{yy}$ crosses zero. At failure for all domains except for $m = 1$, the crack has continued to propagate from the initial damage to completely intersect the domain such that the lower half has been completely separated from the upper domain. As discussed before, the more inhomogeneous mesoscopic fracture strength field for $m = \frac{1}{2}$, resulted in an earlier initiation and slower progression for crack nucleation and growth. We believe that the more gradual nature of crack propagation is the cause of the less complex fracture pattern for $m = \frac{1}{2}$. The higher complexity and density of the fracture network for higher m values is contributed to the more sudden process of failure and more homogeneous mesoscopic fracture strength fields.

2.5.4 A compressive rock fracture example

While the preceding examples are for a macroscopic tensile loading problem, rock is often under ambient compressive stress condition. Thus, a fracture problem under uniaxial compressive loading is presented for completeness. The problem description is exactly the same as the tensile examples, with the difference that an opposite loading rate is used in (2.12); that is, $\dot{\sigma} = -10^{11}$ Pa/s, corresponding to strain rates $a = 0.6$/s and $b = -1.4$/s in (2.8).

In rock mechanics Mohr-Coulomb (MC), Hoek-Brown [75], or other *failure criteria* are used for modeling fracture. As detailed in [144, 3], some of these models such as MC are not appropriate for tensile fracture. That was the motivation of using MCSC criterion for tensile fracture in preceding sections; *cf.* §2.5.1. We employ an unmodified MC failure criterion for this problem. The form of the corresponding effective stress model in terms of friction angle ϕ and traction components t_n and t_s is provided in [3].

Another challenge in compressive fracture is that crack surfaces are often closed and crack propagates in mode II, that is through frictional sliding of crack surfaces. We have provided dynamic *Riemann solutions* for contact-stick and contact-slip conditions in [4] and incorporated them into an interfacial contact/fracture model for rock in [2]. These Riemann target values are required for implementing such interface conditions in aSDG and other discontinuous Galerkin methods. The details of the model, including transitions and required regularization between contact and separation, and between stick and slip modes are provided in [2]. In short, computational modeling of rock fracture under compressive loading is generally more challenging and expensive than under tensile loading. This has in part been the motivation for using a tensile loading scenario for more detailed analyses in §2.5.2 and §2.5.3.

Figure 25 shows macroscopically homogenized stress versus time for a domain where mesoscopic fields are obtained for $L_{SVE} = 1$ and Weibull parameter $m = \frac{1}{2}$. We observe that the maximum compressive stress increases by a factor of 4.75, compared to the corresponding tensile value in Fig. 17 (6 MPa vs. 28.6 MPa). The internal and kinetic energy densities for different stages of solutions are shown in Fig. 26. Similar to tensile loading problems, *cf.* Fig. 23, very little damage and crack propagation is observed at the maximum stress stage.

We note that the tensile or compressive macroscopic stress histories are not compared with experimental results. In [159], S19 sample (whose statistics has been the basis of our synthetic microcrack population at the micro-scale) has been used for a computational compressive example. The *Rock Failure Process Analysis* method (based on the linear finite element method) and quasi-static loading regime are used in [159], whereas herein the aSDG method is used for dynamic simulations under low loading rates. Albeit these and other notable differences in terms of computational domain size and loading, there is a reasonable agreement between the results; in [159] a maximum stress of about 40 MPa is obtained for S19 at the macroscale and similar to Fig. 25, there is a rather sharp softening response past the maximum stress. We believe that the use of experimentally measured parameters of interfacial damage model, such as relaxation time and mode mixity parameter [5], and better representation of the experimental setting (boundary conditions, specimen size, and loading rate) would enhance the accuracy of macroscopic simulations. However, a more detailed calibration of the macroscopic model is beyond the scope of this manuscript.

Figure 27 shows four different stages of solution in terms of total solved finite elements. Since the front meshes are asynchronous, the minimum time of the entire front mesh is reported for each stage. Similar to tensile examples, advance mesh adaptive operations enable exact tracking of cracks by refining and aligning element boundaries with crack directions. As shown most cracks propagate from the first nucleated crack in the lower right corner of the domain. The final fracture pattern for this problem is shown in Fig. 28. For a uniaxial compressive loading, the MC criterion predicts the planes with angles $\pm(45^\circ - \phi/2) \approx \pm 29.5^\circ$ with respect to the loading (*i.e.,* vertical) direction to satisfy the failure criterion first [3]. In fact, we observe that many cracks are aligned close to this angle. Finally, it is noted that the spatial front in Fig. 27(d) and Fig. 28 contains 80,850 triangles and 41,884 crack segments with a total length of five meters.

2.6 Conclusion

To incorporate the effect of rock microstructure, we employ a homogenization approach to derive a mesoscopic fracture strength at the center of circular SVEs that traverse a microcracked rock domain. The fracture strength of an SVE is taken as the minimum strength of microcracks contained in or intersecting it; the sliding-wing crack model in [159] is used to compute individual strength of such cracks and take their interaction into account. The homogenization of the effect of microcracks to mesoscale drastically reduces computational cost compared to explicit representation of microcracks and direct numerical simulation of fracture at macroscale. Moreover, by using the microcrack statistics of a real material, Yuen-Long marble from [159], and homogenization by SVEs a direct connection was established between the microscale and the mesoscale fracture strength field.

In [159] microcrack length is assumed to follow a power law distribution. In addition to modeling this distribution, the effect of changing the distribution shape was investigated by using four different shape parameters m for the Weibull distribution; for consistency with the original rock mass, the mean of crack length was kept fixed. Lower values of m result in a larger standard deviation for crack length, which translates to a higher variation and overall lower strengths for the homogenized mesoscopic fracture strength field. We demonstrated that the SVE size has a similar effect, in that by increasing L_{SVE} the mean and standard deviation of mesoscopic strength decrease. This *size effect* was quantitatively analyzed. We also studied the effect of crack density ε_0 on homogenized strength. Due to maintaining a higher level of material inhomogeneity, smaller SVEs are preferred for brittle fracture analysis; however, there is a limit to L_{SVE}. For example, at low crack densities, for small L_{SVE} many SVEs do not contain any cracks and are not representative of the local response.

We use the homogenized mesoscopic fracture strength fields for different Weibull m parameters for a macroscopic uniaxial tensile problem. The SVE size $L_{SVE} = 1$ was chosen as it provides the highest heterogeneity for mesoscopic strength fields without having the problem of being too small for $\varepsilon_0 = 0.243$. Homogenizing the strain and stress tensors at the macroscale revealed that RVE with the highest Weibull parameter $m = 4$ had about 3 times the tensile strength and 6 times the toughness of the RVE with the lowest $m = \frac{1}{2}$. However, the more uniform length distribution of microcracks for higher m values results in a more instantaneous mode of failure, with a more widespread and complex fracture pattern. Therefore, the gains in strength and toughness are offset by a more brittle fracture response. While for all m, the microcracked domains are synthesized and the closest model to the real S19 sample in [159] is for $m = \frac{1}{2}$, this example demonstrates the great impact material microstructure has on its macroscopic response. Thus, accurate characterization and modeling of microstructure is of utmost importance in failure analysis of quasi-brittle materials. Finally, while the macroscopic results, *e.g.,* Figs. 21 to 24, are not compared with any experimental results, we note that the use of an inhomogeneous fracture strength field is crucial in capturing realistic fracture patterns; otherwise, as shown in [42], the use of a homogeneous strength field can result in nonphysical sudden nucleation of cracks almost everywhere in the domain.

We demonstrate the effectiveness of the SVE homogenization approach for modeling rock fracture. There are; however, several areas of improvement for future research. First, the current process assumes a fully isotropic strength field. For rock with bedding planes, fracture strength should be homogenized as an anisotropic field and calibrated to appropriate fracture models, *e.g.,* those in [125, 124]. Second, we acknowledge that the macroscopic fracture results are not validated against experimental results. For more realistic failure analysis, as in [78] other fields such as elasticity tensor should be considered random and inhomogeneous. Experimental results can be used to calibrate both elastic and fracture properties of inhomogeneous rock [128] and calibrate certain parameters of the interfacial damage model that were missing in the present study. Third, by increasing the number of statistical realizations to more than the one considered herein, a more accurate estimation of the statistical variation of the ultimate macroscopic fracture strength is obtained; see for example [103]. Fourth, in §2.5 we used (2.6) for modeling microcrack interaction. More realistic interaction models can either be calibrated from experimental results [127] or the analysis of microcrack propagation and interaction in tensile model. Fifth, microcrack-based bulk damage models [67, 45, 132, 165, 51] can be much more efficient than the interfacial damage model considered herein and can even be employed in accurate hybrid diffuse damage and interfacial cracking approaches [163]. Moreover, for compressive fracture, microcrack propagation and frictional sliding can be homogenized into bulk damage and plasticity models [164]. The calibration and use of these models is especially important when the simulation of many statistical realizations is needed.

Acknowledgements

The authors gratefully acknowledge partial support for this work via the U.S. National Science Foundation (NSF), CMMI - Mechanics of Materials and Structures (MoMS) program grant numbers 1538332 and 1654198.

Chapter 3

Statistical Volume Elements for the Characterization of Angle-Dependent Fracture Strengths in Anisotropic Microcracked Materials

An original version of the following article was published in Volume 6, Number 2, June 2020 edition of the ASME-ASCE journal *Journal of Risk and Uncertainty in Engineering Systems Part B: Mechanical Engineering*. The article was published under the title ”Statistical Volume Elements for the Characterization of Angle-Dependent Fracture Strengths in Anisotropic Microcracked Materials”. This article is a continuation of the previous chapter which extends the work to anisotropic domains and utilizes a loading angle-dependent fracture strength model versus the angle-independent model used in Chapter 2. The article was co-authored by Dr. Reza Abedi. My contributions include

- Generation of isotropic and anisotropic microcrack domains based on Yuen-Long marble statistics found in [159]
- Mesoscopic analysis of fracture strength fields using circular SVEs for four different SVE sizes
- Implementation of several measures of anisotropy
- Generation of correlation and covariance statistics for fracture strength fields
- Administration of dynamic macroscopic fracture analysis aSDG code developed by Abedi for isotropic and anisotropic domains

This work is the first to extend the use of SVEs beyond the analysis of homogeneity for elastic or fracture properties to investigate the effect of material anisotropy in the analysis. A linear elastic fracture model is used to generate the angle-dependent fracture strengths. Both fracture crack density and length distribution are made to match the previous work [58], but the crack angle is varied to be completely isotropic (unbiased) or anisotropic (biased with a triangular distribution about 30 degrees).

3.1 Abstract

Statistical volume elements (SVEs) are used to homogenize fracture strength of rock, based on the microcrack statistics of a real-world Yuen-Long marble sample. The small size of

SVEs enables maintaining inhomogeneities in fracture properties with lower computational cost compared to methods that explicitly model microcracks at macroscale. Maintaining inhomogeneity is important to capture realistic fracture patterns in rock as a quasi-brittle material. Uniaxial tensile, uniaxial compressive, and shear strengths are derived for arbitrary angle for loading and orientation of a single crack by using the linear elastic fracture mechanics (LEFM) method and incorporating frictional effects. Mesoscopic fracture strength fields are generated for different strengths and angle of loading by traversing the spatial domain with circular SVEs. Increasing the SVE size smoothens the spatial inhomogeneity and angular anisotropy of homogenized strengths. Spatial and angular covariance functions of the random fields are obtained to demonstrate how fracture strength varies in space and by changing the angle of loading. Two isotropic and anisotropic rock domains are studied and shown to have very different single- and two-point statistics. Macroscopic fracture simulations by an asynchronous spacetime discontinuous Galerkin (aSDG) method demonstrate that most macroscopic cracks for the anisotropic domain are aligned with the weakest strength planes.

3.2 Introduction

Many common materials used in engineering systems, including rock, concrete, ceramic, and certain composites, are considered quasi-brittle. Understanding their failure mechanisms is vital for using and processing these materials across different size scales. Quasi-brittle materials lack the energy dissipative mechanisms that more ductile materials have [134, 62, 29], resulting in a greater importance to understand the distribution of flaws in the microscale, such as microcracks or inclusions. Crack pattern variability for similar sized samples with equivalent loading [17] has been seen due to these microstructural flaws. The *size effect*, wherein the fracture strength decreases as the size of the material sample increases [30, 29], is a direct result of these microstructural defects. Therefore, characterizing these networks of microcracks is important to understand the behavior of these materials under loading, as very different fracture patterns [17], ultimate strengths [86, 161], and other heterogeneities can be seen for different material samples. Understanding the microstructure of these materials, and its influence on macroscopic fracture, greatly decreases the risk and uncertainty inherent in designs that involve quasi-brittle materials.

Certain material types, such as rock with bedding planes, can contain microstructural defects that are angularly biased, *i.e.,* the microstructure is anisotropic. Depending on the direction of loading, the material strength can be very different. A major increase in risk can be assumed if the engineer only uses a homogeneous, isotropic fracture strength for a given material when designing and modeling an engineering system. To capture these flaws, implicit or explicit methods may be used to introduce these defects into a given model. *Explicit* methods directly incorporate the microstructure, above certain length scale, into the solution scheme. Some examples are lattice modeling [94] and lattice discrete particle modeling [55], which model the flaws as a particle network connected by springs. Because of the small space and time scales required to properly resolve the microstructural defects in larger structures, explicit methods can be very computationally expensive.

Less computationally intensive *implicit* methods incorporate the overall effect of microstructure in the analysis, but do not directly represent them at the macroscale. An example of an implicit method is Weibull's weakest link method [156, 157], which provides a statistical phenomenological characterization of the fracture strength, and has been used successfully by the authors to capture the statistical fracture response of rock in hydraulic fracturing [9], fracture under dynamic compressive loading [3], and in fragmentation studies [5]. While these methods are generally successful in capturing statistical variation for specific properties, they lack the direct connection from the distribution of microstructural defects to macroscopic fracture response.

Therefore, a general method is desired which can link the material microstructure to the meso- and macro-structure that does not require the exorbitant computational costs of explicit methods. To resolve this issue, *homogenization* methods are used to link the material microstructure to the macrostructure by averaging the effect of the microstructure in a *volume element* (VE). Similar approaches have been used to calibrate certain fracture models, see for example [152, 76, 143, 97, 115]. A *Representative Volume Element* (RVE), also known as a *Representative Elementary Volume* (REV) in rock mechanics, is used in homogenization theories to compute bulk material properties of a composite at the continuum level. The RVE should be much smaller than the macroscopic domain size so that the homogenized properties of the RVE can be assigned to a point of the continuum domain. Yet, RVEs should be large enough to be representative; that is, for a given homogenized property there is not much variation if larger VEs are used for homogenization. For a macroscopically homogeneous material with ergodic properties, an RVE is defined [119] such that the homogenized properties only vary within a specific range across different realizations of the RVE [150, 83, 95, 120]; see also [106, 87] for the statistical models that underline the determination of RVE size in preceding references.

A volume element which is smaller than the given size requirements to form a representative volume element is known as a *Statistical Volume Element* (SVE). These elements may be used to capture the statistical variation in material properties caused by the material microstructure. Multiple SVEs may be used to properly characterize the randomness in material properties. Many studies have been performed to determine how the SVE observation window [154, 22], boundary conditions [80], and microstructure defect clustering [141] all effect the given material property statistics. SVEs have been used to capture both the material elastic and fracture properties.

We have used SVEs to homogenize microcracked rocks in [41] to derive an inhomogeneous yet isotropic field for tensile strength. By computing angle-dependent fracture strengths at the SVE level, anisotropic rocks were homogenized in [60]. Herein, we extend the work presented in [60] by using the microcrack statistics of a real-world Yuen-Long marble sample from [159]. In addition, an index is introduced to determine the anisotropy of homogenized fracture strength fields. Finally, following [61], spatial and angular covariance functions of the strength fields are used to analyze how the strengths vary in space and as a function of loading direction, respectively.

Once the anisotropy of fracture strength is considered, there are two main approaches to incorporate the anisotropy into a macroscopic continuum model. First, a second order *microstructure tensor* [125, 124] in addition to commonly used invariants of the stress tensor are used to define a general bulk failure criterion. Second, in contrast to the aforementioned bulk failure models, well-known interfacial models such as Mohr-Coulomb or Hoek-Brown

[75] are made angle-dependent [126, 92, 145] by assigning different tensile strengths or friction coefficients for different angles of loading.

In this work, the latter approach is adopted, such that for any potential angle of loading we characterize different fracture strength parameters. *Linear Elastic Fracture Mechanics* (LEFM) theory is used to derive angle-dependent uniaxial tensile, uniaxial compressive, and shear strengths. The SVE analysis process and angle-dependent strength formulation are derived in the next section. Then, isotropic and anisotropic microcrack-filled domains are generated using real microcrack distribution statistics from Yuen-Long marble [159] and the statistics of the strength fields are analyzed for isotropic and anisotropic domains. Finally, the asynchronous spacetime Galerkin finite element method [6] is used to analyze the fracture response of these domains with the applied random fracture strength fields.

3.3 Formulation

This section defines the statistical volume element approach for defining fracture strength with respect to varying loading angle in a quasi-brittle domain containing microcracks. Section 3.3.1 provides an overview for the anisotropic fracture analysis process in a domain with distributed microcracks using SVEs. The microcrack length and angle distribution will be detailed in §3.3.2. Then, §3.3.3 describes the process to calculate the mesoscopic angular-dependent fracture strength field. Some useful angle-independent strength measures are introduced in §3.3.4. Afterward, a description of the covariance function and its use to determine the correlation of the fracture strength random fields is provided in §3.3.5. Finally, the *asynchronous Spacetime Discontinuous Galerkin* (aSDG) method is detailed in §3.3.7 for performing macroscopic dynamic fracture simulations within the given quasi-brittle domains.

3.3.1 Multi-Scale Anisotropic Fracture Analysis

Figure 29 details the multi-scale model that is described in this work. In step one and at the macroscale, an RVE of the given material is considered. In [159], many samples of Yuen-Long marble were scanned to calculate the statistics of the material microstructure. A 32 mm by 32 mm square domain of Yuen-Long marble was determined to contain a sufficient number of microcracks to be considered representative. The statistics of microcracks demonstrate very low sample to sample variability at this scale. As the size of the RVE decreases, the RVE approaches the SVE regime. The characteristic size of the SVE, l_{SVE}, is smaller than the overall size of the domain of interest and the ratio of the SVE size to the average microcrack length must be small enough that SVE does not approach the RVE limit. As the ratio of l_{SVE} to the average microcrack length approaches infinity, randomness is lost, resulting in a homogeneous material that does not accurately represent the inhomogeneity at the mesoscale due to the existence of microcracks. Several SVE sizes will be studied in §3.4 to show this size effect.

Circular SVEs of diameter L_{SVE} are used to transverse the RVE with spacing $S = L_{SVE}/n$, where n is a grid line spacing variable which was chosen such that the entire domain is sampled with sufficient resolution regardless of SVE size. For this paper, n is equal to 5. Within each SVE, the contained microcracks are processed using LEFM principles, as described in §3.3.3. A loading P is applied at discrete loading angles, θ, and a field of mesoscopic fracture strength is calculated for each angle; *cf.* step 2 in Fig. 29. In step 3, the calculated strength values are assigned at the center points of the SVEs. In Fig. 29, sample uniaxial tensile strength fields are shown for four different angles of loading. Since the SVE size is at an intermediate level between the representative crack and macroscopic domain sizes, the constructed fields are called *mesoscopic strength fields*. Finally, if desired, dynamic fracture analysis can be performed on the same macroscopic domain shown in step 1 without the explicit representation of microcracks. Instead, by using the mesoscopic fracture strength fields, the computational cost is significantly reduced; still, some level of material inhomogeneity is maintained which is important for more realistic fracture simulations.

3.3.2 Microcrack Length and Angle Distributions

Since extensive sampling of rock is difficult or expensive, and detailed microcrack measurements for large domains are scarce, statistical methods are often used to realize microcracked samples that are consistent with the microcrack statistics of the original rock mass. Depending on the method used for realizing samples, different types of statistics of a microcracked domain are used; *cf.* [49] for a few examples. In the *pick-and-place* algorithm, cracks are modeled as discontinuity lines. The distributions of crack center location, length, and angle are sampled for each crack, and a crack with a specific location, length, and angle is inserted in the domain. This process continues until the target crack density ε_0, which is the sum of squares of the microcrack lengths per unit area of the domain, is reached.

While the pick-and-place algorithm can be employed for different microcrack statistics, in this manuscript we use the specific microcrack statistics provided for a Yuen-Long marble sample in [159], given that all specific descriptors required by this method are experimentally measured and reported therein. Specifically, we employ the statistics of sample S19. The spatial location of the centers of microcracks follows a uniform distribution, as the examined Yuen-Long marble is macroscopically homogeneous. A power-law distribution is used, and experimentally verified, to represent the distribution of crack length in [159]. In fact, as discussed in [133], field observations indicate that crack length often follows a power law distribution in rock. For the power-law distribution a minimum value (crack half-length) $a^{'}$ is assigned to ensure the cumulative distribution function to be finite and take the value of one for infinite crack half-length; *cf.* (3.2) below. The cumulative distribution for half-cracks longer than $a^{'}$ for an elemental volume V_0 is defined as,

$$g(a) = \left(\frac{q^*}{a}\right)^z \tag{3.1}$$

where q^* and Cauchy distribution exponent $z > 1$ are the parameters of the power distribution, subject to the condition,

$$V_0 \int_{a^{'}}^{\infty} g(a)da = 1. \tag{3.2}$$

To ensure this equality, the lower integration limit, $a^{'}$ is defined by,

$$a^{'} = \left[\frac{(q^*)^z V_0}{z-1}\right]^{\frac{1}{z-1}} \tag{3.3}$$

The specific model values for sample S19 are reported in §3.4 and used to generate new random crack fields consistent with S19 microcrack length statistics.

The S19 rock sample from [159] is isotropic and crack angle follows a uniform distribution. We will use this actual angle distribution to realize a macroscopically *isotropic rock domain*. Since, one objective of this study is relating the angle distribution of microcracks to anisotropy of the mesoscopically homogenized fracture strength fields, we create a second macroscopically *anisotropic rock domain* where the angle distribution is intentionally non-uniform. A triangular distribution with a peak at $\theta_c = 30$ degrees and a range of $\theta_c =$ 25-35 degrees is used for this synthetic crack angle distribution. The final parameter for defining the microcrack domain is the crack density, where for both rock domains, the crack density of $\varepsilon_0 = 0.243$ of sample S19 is used.

It is noted that the statistics of microcracks plays a crucial role in the homogenized strengths at the mesoscale and macroscopic fracture properties. For example, we have demonstrated that by changing the shape of microcrack length distribution, while keeping the mean length fixed, macroscopic fracture strength can change by a factor of three [59]. Our focus in the remainder of the manuscript will be on the effect of statistics of microcracks on mesoscopic and macroscopic response, rather than validation of the macroscopic response with experimental results. Specific attention is directed to angular dependency of properties at different scales.

3.3.3 Fracture Strength Calculations

Within the SVE, the fracture strength of every microcrack intersecting the element is calculated. As detailed previously, a circular SVE observation window was selected. Cracks that are both completely encircled or only partially intersecting an SVE are considered. For SVEs which contain no microcracks, a maximum fracture strength is assigned based on a crack of minimum length. As all of the intersecting cracks fracture strengths are calculated, the minimum fracture strength is retained and assigned to the center point of the SVE, resulting in a mesh of fracture strengths with uniform spacing in both horizontal and vertical directions. Each mesh point contains a vector of angular-dependent fracture strengths, *i.e.,* the fracture strength calculated for each discrete loading angle.

It it noted that a few SVEs may contain no cracks. For these SVEs, a maximum fracture strength is assigned based on a crack of minimum length to avoid having an infinite strength.

This minimum length is twice the value of minimum allowable half-length crack $a^{'}$ for the power law distribution in (3.3). For the homogenization to be valid, the SVE size should be chosen large enough such that the majority of SVEs are representative of rock microstructure, in that they contain a sufficient number of microcracks. This size depends on the (length) distribution of microcracks and crack density. If the SVE size is too small, the maximum strength based on the minimum crack length is assigned to many SVEs. However, in this manuscript, the SVE sizes are chosen large enough that even for the smallest SVE size, very few SVEs contain no cracks.

For a crack of half-length a, the strength is calculated using LEFM principles. There are three assumptions in calculating fracture strengths. First, the interaction of microcracks is not taken into account. Second, for the microcracks that intersect the boundary of the SVE, the geometric mean of the total microcrack length and the part that is inside the SVE is used for its effective length in LEFM calculations; that is $a^i_{\text{eff}} = \sqrt{a^i a^i_{\text{in}}}$ for microcrack number i in Fig. 29.

Third, as will be described below, the principle of *maximum energy release rate* (MERR) [53] is used to compute fracture strength of individual cracks.

Figure 30 shows the schematic of a single crack with effective half length a_{eff} with angle θ_c and local coordinate system (x', y'). The global Cartesian coordinate system is (X, Y). We are interesting in computing various fracture strengths for a loading angle of θ. As shown, the coordinate system (x, y) for far field loading is at angle θ with respect to the global coordinate system (X, Y). Thus, the relative angle of the crack with respect to x is $\theta_d := \theta_c - \theta$. For computing fracture strengths at angle θ, in-plane stresses are applied in the (x, y) coordinate system. To use LEFM theory, we need to transfer these stresses to the (x', y') coordinate system. This is achieved by Mohr circle transformation of the in-plane components of the stress tensor between the two coordinate systems,

$$\sigma_{x'x'} = \sigma_{xx}\cos^2\theta_d + \sigma_{yy}\sin^2\theta_d + \sigma_{xy}\sin 2\theta_d \tag{3.4a}$$

$$\sigma_{y'y'} = \sigma_{xx}\sin^2\theta_d + \sigma_{yy}\cos^2\theta_d - \sigma_{xy}\sin 2\theta_d \tag{3.4b}$$

$$\sigma_{x'y'} = -\sin 2\theta_d \frac{\sigma_{xx} - \sigma_{yy}}{2} + \sigma_{xy}\cos 2\theta_d \tag{3.4c}$$

The strengths for angle θ correspond to the following stress tensors $\boldsymbol{\sigma} = (\sigma_{xx}, \sigma_{yy}, \sigma_{xy})$ in (x, y) coordinate system,

$$\boldsymbol{\sigma} := (s_{NH}, s_{NH}, 0) \qquad \text{Hydrostatic tensile strength } s_{NH} \tag{3.5a}$$

$$\boldsymbol{\sigma} := (0, s_N(\theta), 0) \qquad \text{Uniaxial tensile strength } s_N \tag{3.5b}$$

$$\boldsymbol{\sigma} := (0, -s_C(\theta), 0) \qquad \text{Uniaxial compressive strength } s_C \tag{3.5c}$$

$$\boldsymbol{\sigma} := (0, 0, s_S(\theta)) \qquad \text{Shear strength } s_S \tag{3.5d}$$

where as mentioned $s_N(\theta)$, $s_C(\theta)$, and $s_S(\theta)$ are positive uniaxial tensile, uniaxial compressive, and shear strengths at angle θ. Note that there is no argument of loading direction for hydrostatic tensile strength since it corresponds to equal principle stresses s_{NH} for all angles of loading. We also observe that uniaxial tensile strength at angle θ corresponds to $\boldsymbol{\sigma} = (0, s_N(\theta), 0)$ rather than $(s_N(\theta), 0, 0)$; for this strength at angle θ, we apply a tensile stress normal to the direction of a hypothetical fracture line with angle θ. This corresponds to only σ_{yy} nonzero in Fig. 30. Finally in (3.5), the form of any of the loadings for angle θ is known, but the factor of stress tensor for which the crack with $2a_{\text{eff}}$ at angle θ_c satisfies an LEFM fracture criterion corresponds to the magnitude of the strength.

The resolvent components of traction $\mathbf{t} = (t_n, t_s)$ acting on the crack plane are,

$$t_n = \sigma_{y'y'} \tag{3.6a}$$

$$t_s = |\sigma_{x'y'}| - k \langle -t_n \rangle_+ \tag{3.6b}$$

where t_n and t_s are the normal and shear components of $\mathbf{t}$, k is the friction coefficient, and $\langle . \rangle_+$ is the Macaulay positive operator. The reason that in (3.6b) the positive operator acts on $-t_n$, is that for the shear stress to induce mode *II* fracture, the far field shear stress $\sigma_{x'y'}$ must be greater than the friction traction $k \langle -t_n \rangle_+$. When under tensile loading, *i.e.,* when $t_n \geq 0$, friction is zero ($k \langle -t_n \rangle_+ = 0$). We model the crack in Fig. 30 in isolation undergoing far field normal stress t_n, corresponding to mode I fracture if $t_n > 0$. The resolvent shear stress t_s results in a mode *II* *stress intensity factor* (SIF) if acting shear stress $|\sigma_{x'y'}|$ can overcome friction $k \langle -t_n \rangle_+$, *i.e.,* when $t_s > 0$. Thus, mode I and *II* SIFs at the crack tips are,

$$K_I = \frac{\langle t_n \rangle_+}{\sqrt{\pi a_{\text{eff}}}} \tag{3.7a}$$

$$K_{II} = \frac{\langle t_s \rangle_+}{\sqrt{\pi a_{\text{eff}}}} \tag{3.7b}$$

There are several criteria such as *maximum circumferential stress criterion* (MCSC), *maximum energy release rate* (MERR), and *minimum strain energy density* (MSED) that can be used to determine whether K_I and K_{II} are large enough to result in propagation at the tips of the crack and at what direction relative to the crack the extension will propagate. For the MERR criterion, to investigate crack propagation at a potential kink angle ψ relative to crack direction, stress intensity factors at the tip of the kink crack extension, $K_I(\psi)$ and $K_{II}(\psi)$, need to be computed from K_I and K_{II} in (3.7) [79]. The crack extends in a direction ψ for which the energy release rate in terms of $K_I(\psi)$ and $K_{II}(\psi)$ is maximum and exceeds the fracture toughness of material [53]. One can show that the corresponding failure criterion in terms of K_I and K_{II} can very accurately be approximated by,

$$K_I^2 + K_{II}^2 = K_c^2 \tag{3.8}$$

where K_c is the critical mode I SIF. For plane stress condition, *i.e.*, for samples with small thickness B, tri-axial stress state is less pronounced than plane strain condition. Thus, K_c is larger than K_{Ic}, its corresponding value for plane stress condition. In general, K_c can be obtained from B and K_{Ic} [18]. While MERR criterion is slightly less conservative than MCSC and MSED criteria, the form of the approximate relation (3.8) greatly simplifies the determination of fracture strengths for a crack with relative angle θ_c to the loading direction.

The process for computing any of the fracture strengths s_{NH}, $s_N(\theta)$, $s_C(\theta)$, and $s_S(\theta)$ is summarized as followed. First, relative crack angle is computed from $\theta_d = \theta - \theta_c$. Second, the stress tensor in (x, y) coordinate system, corresponding to the given strength is chosen from (3.5). Third, the stress tensor is transferred to (x', y') coordinate system from (3.4). Fourth, resolvent traction components t_n and t_s are computed from (3.6). Fifth, SIFs K_I and K_{II} are computed from (3.7). Finally, the magnitude of the given strength, *e.g.*, $s_N(\theta)$, is computed such that the failure criterion (3.8) is satisfied. As will be discussed below, for certain strengths and angles θ_d, one or both of t_n and t_s are negative and (3.8) cannot be satisfied for any magnitude of loading; that is, the given angle-dependent strength is infinite.

Following this process for the four different strengths, the angle-dependent strengths are obtained as,

$$\frac{s_{NH}\sqrt{\pi a_{\text{eff}}}}{K_c} = 1 \tag{3.9a}$$

$$\frac{s_N(\theta)\sqrt{\pi a_{\text{eff}}}}{K_c} = \frac{1}{\cos\theta_d} \tag{3.9b}$$

$$\frac{s_C(\theta)\sqrt{\pi a_{\text{eff}}}}{K_c} = \begin{cases} \frac{1}{-\cos\theta_d(\sin\theta_d + k\cos\theta_d)}, & -\frac{\pi}{2} < \theta_d < -\phi \\ \infty, & -\phi < \theta_d < \phi \\ \frac{1}{\cos\theta_d(\sin\theta_d - k\cos\theta_d)}, & -\phi < \theta_d < \frac{\pi}{2} \end{cases} \tag{3.9c}$$

$$\frac{s_S(\theta)\sqrt{\pi a_{\text{eff}}}}{K_c} = \begin{cases} 1, & -\frac{\pi}{2} < \theta_d < 0 \\ \frac{1}{\cos 2\theta_d - k\sin 2\theta_d}, & 0 < \theta_d < (\frac{\pi}{4} - \frac{\phi}{2}) \\ \infty, & (\frac{\pi}{4} - \frac{\phi}{2}) < \theta_d < (\frac{\pi}{4} + \frac{\phi}{2}) \\ \frac{1}{-\cos 2\theta_d - k\sin 2\theta_d}, & (\frac{\pi}{4} + \frac{\phi}{2}) < \theta_d < \frac{\pi}{2} \end{cases} \tag{3.9d}$$

where $\phi := \tan^{-1}(k)$ is the friction angle. Also, note that the relative crack angle θ_d is taken to in $(-\pi/2, \pi/2]$, given that shifts of π in crack angle does not change the problem description in Fig. 30. Based on (3.9a), the maximum (hydrostatic tensile strength), corresponding on minimum half-length crack a' is $S_{\max} = K_c/\sqrt{\pi a'}$.

The fracture strengths in (3.9) are shown in Fig. 31 for $k = 0.3$. As expected, the hydrostatic tensile strength in angle-independent and takes the value $K_c/\sqrt{\pi a_{\text{eff}}}$. The uniaxial tensile strength takes the lowest value when the loading is normal to the crack; that is for $\theta_d = 0$. As $|\theta_d| \to \pi/2$, a much higher normal stress in y' is needed to result in crack propagation through (3.8). For the compressive strength, the resolvent t_n is always negative and the friction term in (3.6b) is nonzero. Under this loading, crack can propagate only in mode *II* if $|t_s| \geq 0$; *cf.* (3.7b). For relative crack angles $|\theta_d| \leq \phi$, the friction traction $k\langle -t_n\rangle_+$ is higher than $|\sigma_{x'y'}|$. Consequently, crack surfaces cannot slip and have the excess shear stress resulting in mode II crack propagation. For $|\theta_d| > \phi$, slip can occur. The maximum uniaxial compressive strength of $2\cos\phi K_c/(1-\sin(\phi)\sqrt{\pi a_{\text{eff}}}$ is achieved for $|\theta_d| = \phi/2 + \pi/4$. As $|\theta_d| \to \pi/2$, $s_C(\theta)$ tends to infinity.

The only strength whose dependency is not even with respect to θ_d is $s_S(\theta)$. When $\theta_d = -\pi/2$, the stress state (3.5d) results in $\sigma_{y'y'} = s_S(\theta_d = -\pi/4)$ and $\sigma_{x'y'} = 0$ in (3.4)(b-c). Thus, $t_n = s_S(\theta_d = -\pi/4)$ and $t_s = 0$ in (3.6) and the crack is in pure mode I; *cf.* (3.7). On the other hand, for $\theta_d = \pi/4$ we obtain $t_n = -s_S(\theta_d = \pi/4)$ and $t_s = 0$. That is, $\theta_d = -\pi/4$ and $\pi/4$ correspond to pure tension and compression on crack surfaces. Clearly, in the former case, the strength is equal to uniaxial strength, and in the latter case, the crack cannot propagate. This explains the non-symmetric dependency of s_S on θ_d. In short, for $\theta_d < 0$, the resultant t_n is positive and crack can propagate in mixed mode. For $\theta_d > 0$, $t_n < 0$ and crack can only propagate when resolvent shear stress is positive, that is tangential stress $\sigma_{x'y'}$ is larger than friction term $k\left\langle -t_n \right\rangle_+$ in (3.6b). This occurs for $|\theta_d - \pi/4| > \phi/2$.

For a given SVE, the hydrostatic tensile strength S_{NH}, and angle-dependent uniaxial normal $S_N(\theta)$, uniaxial compressive $S_C(\theta)$, and shear $S_S(\theta)$ strengths are defined as,

$$S_\alpha(\theta) = \min\nolimits_{i \in \mathcal{I}_{SVE}} s^i_\alpha(\theta) \tag{3.10}$$

where α refers to one of the strength modes NH, N, C, and S. The minimum of strength is taken over microcracks with index i over $\mathcal{I}_{SVE}$, the set of all microcracks that are in or intersect the SVE; *cf.* Fig. 29(b). That is, for a given loading direction and strength type, the SVE takes the minimum of the corresponding strength of all the cracks that interact with the SVE.

There are three assumptions in using (3.10) as follows. First, the value of $S_\alpha(\theta)$ is capped by $S_{\max}$, the maximum fracture strength based on the value of a'. Since in (3.9), some of these strengths are infinite or tend to infinity, depending on the angle θ_d, for some SVEs $S_\alpha(\theta)$ may take a very large value even if it contains some microcracks. Using the maximum value $S_{\max}$ basically denotes an infinite value for $S_\alpha(\theta)$, corresponding to a situation that none of the microcracks can propagate for the given angle of loading. This is specifically relevant for the anisotropic rock domain as discussed in §3.4.2. Second, it is assumed that all these microcracks are effectively in an infinite domain. This is a reasonable assumption for the majority of SVEs, if the SVE size is sufficiently smaller than the macroscopic domain size. Third, microcrack interaction is not taken into account. Generally, microcrack interaction reduces the strength. In many studies, crack interaction is taken into account by reducing the strength through a non-increasing function of crack density in the form $y(\varepsilon_0)$; see for example [19, 159]. No microcrack interaction model is employed in the present study. This is because we are more interested in spatial variation of strengths, averaged by using SVEs, rather than their absolute values. Moreover, these crack interaction models often can analytically be computed only for simplistic microcrack distributions such as periodic array of parallel cracks with the same size. We believe that full-scale finite element analysis should be employed to accurately model crack interaction for more general distribution of microcracks. However, the computational cost of this approach is prohibitive herein, given than an extremely large number of SVEs are analyzed to study the statistics of homogenized strengths.

3.3.4 Angle-dependency of fracture strength

For an SVE, fracture strengths $S_\alpha(\theta)$, for $\alpha \in \{NH, N, C, S\}$, are angle-dependent. Accordingly, we can define the following angle-independent measures for an SVE,

$$m(S_\alpha) = \min_{\theta\in[0,\pi]} S_\alpha(\theta) \tag{3.11a}$$

$$\bar{S}_\alpha = \text{mean}_{\theta\in[0,\pi]} S_\alpha(\theta) \tag{3.11b}$$

$$A_\alpha = \frac{\bar{S}_\alpha}{\varsigma_{\theta\in[0,\pi]} S_\alpha} \tag{3.11c}$$

where ς stands for standard deviation. If angular dependency of fracture strength is not very high and there is not a specific bias with respect to a given angle, for example rocks with bedding plane, the minimum SVE strength $m(S_\alpha)$ over all angles of loading, can be considered as a reasonable angle-independent fracture strength for the SVE. The mean SVE strength, $\bar{S}_\alpha$, is another (less conservative) alternative for this purpose. The anisotropy index, A_α corresponds to the *coefficient of variance* of the angle-dependent strength S_α. For an SVE with isotropic strength $A_\alpha = 0$. Conversely, it takes higher values as the angular variation of strength increases. In subsequent sections, we use A_α as a measure of fracture strength anisotropy.

3.3.5 Covariance and Correlation Functions

We are interested in studying how the strength fields change spatially and angularly. The strength field S_α, $\alpha \in \{NH, N, C, S\}$, is a function of space-angle coordinate $\xi = (X, Y; \theta)$. The covariance function between two space-angle coordinates ξ_A and ξ_B for strength S_α is denoted by cov_α and is defined as,

$$\begin{aligned}\mathrm{cov}_\alpha(\xi_A, \xi_B) &= \mathbb{E}((S_\alpha(\xi_A) - \mu_A)(S_\alpha(\xi_B) - \mu_B)) \\ &= \mathbb{E}((S_\alpha(\xi_A) S_\alpha(\xi_B)) - \mu_A \mu_B \qquad (3.12)\end{aligned}$$

where $\mathbb{E}$ is the mean value operator and μ_A, μ_B are shorthands for means of S_α at ξ_A and ξ_B; that is $\mu_A = \mathbb{E}(S_\alpha(\xi_A))$ and $\mu_B = \mathbb{E}(S_\alpha(\xi_B))$.

After the covariance function is calculated, the correlation of the two variables can then be calculated. The Pearson correlation coefficient, referred to as *Pearson's r*, is used to calculate how correlated the two variables are. If r is equal to $+1$, then the two variables are completely positively linearly correlated, while if equal to -1 the variables are completely negatively linearly correlated. An r value equal to 0 means that the two variables are not linearly correlated at all. The correlation function for strength S_α between its values at space-angle coordinates ξ_A and ξ_B, is denoted by $\mathrm{corr}_\alpha(\xi_A, \xi_B)$ and is defined by,

$$\mathrm{corr}_\alpha(\xi_A, \xi_B) = \frac{\mathrm{cov}_\alpha(\xi_A, \xi_B)}{\varsigma_A \varsigma_B} \qquad (3.13)$$

where ς refers to the standard deviation and ς_A, ς_B are shorthands for the standard deviation of S_α at points ξ_A and ξ_B, respectively. That is, $\varsigma_A = \sqrt{\mathrm{cov}_\alpha(\xi_A, \xi_A)}$ and $\varsigma_B = \sqrt{\mathrm{cov}_\alpha(\xi_B, \xi_B)}$.

These two covariance and correlation functions are then used to determine how fracture strength fields are related in space and in angle. Homogenizing random fields that are consistent with material microstructure, in this context, is of crucial importance for the resulting *stochastic partial differential equations* for elastodynamic fracture problem.

Investigating how these fields are related provide an interesting look at understanding the fracture strength fields for a given material.

3.3.6 Calculation of mesoscopic field statistics

The statistics of fracture strengths, homogenized at the mesoscale, depend on the statistics of microcracks at the microscale and the size of SVE. As mentioned in §3.3.2, two distinct *isotropic* and *anisotropic* microcrack statistics are used at the microscale. We assume that the mesoscopically homogenized fields are *strongly stationary* in space, in that the *Probability Density Function* (PDF) of $S_\alpha(\xi)$, $\xi = (X, Y; \theta)$, does not depend on its spatial coordinate (X, Y) for all $\alpha \in \{NH, N, C, S\}$; this condition is also referred to as *weakly homogeneous* in homogenization field. This implies that point-wise quantities such as mean $\mathbb{E}(S_\alpha(\xi))$ and variance also only depend on (X, Y). Furthermore, higher order moments such as covariance function will depend on relative spatial distance of the points, not their absolute spatial position. Thus, in §3.4 when the PDFs of S_α are presented, only their angular argument is maintained. Moreover, the spatial dependence of the covariance function in (3.12) is only through $\Delta X = X_B - X_A$ and $\Delta Y = Y_B - Y_A$, the spatial difference of ξ_A and ξ_B, and the function can be expressed as,

$$\begin{aligned} \widetilde{\mathrm{cov}}_\alpha(\Delta X, \Delta Y; \theta_A, \theta_B) &:= \mathrm{cov}_\alpha(0, 0, \theta_A; \Delta X, \Delta Y, \theta_B) \\ &= \mathrm{cov}_\alpha(X_A, Y_A, \theta_A; X_B, Y_B, \theta_B) \end{aligned} \tag{3.14}$$

This will be used in reported covariance functions in §3.4.3.

The second assumption for the mesoscopic fields is their ergodicity, in that the statistical properties can be deduced from a single, sufficiently large realization of these fields. That is, for either of the two isotropic and anisotropic microcrack models, only one rock domain is realized and subsequently homogenized by the SVEs. This simplifies the computation of PDFs of $S_\alpha(\theta)$ in §3.4.1 and §3.4.2, as the spatial domain PDF of S_α over that single realization is computed and used in lieu of ensemble PDF of $S_\alpha(\theta)$ at a fixed spatial location over many realizations. Moreover, the assumption of the ergodicity for the first moments is used to similarly compute covariance function $\widetilde{\mathrm{cov}}$ in (3.14) by moving the base point in one realization, rather than computing the function across many realizations. This assumption is used to compute the covariance (and correlation) functions in §3.4.3.

The spatial stationary condition assumption is justified by the fact that the spatial location of microcracks in sample S19 is reported to follow a uniform distribution [159]; as discussed in §3.3.2, this would result in a uniform spatial distribution of crack center-points in the pick-and-place algorithm. In addition, if the realized rock domain is large enough, based on the details of domain realization scheme and statistics of microcracks, the statistics of mesoscopic fields homogenized by this realization should be representative of the ensemble statistics; this has been the rationale for assuming ergodicity condition for the point-wise PDF and covariance function. Stationarity and ergodicity assumptions are often used in geo-statics [104] and homogenization [83] fields. In is noted that the weaker *wide-sense stationarity* (WSS), *i.e., second-order stationarity*, is also used in homogenization, *e.g.,* [119, 95], where only the mean value and covariance function are stationary. While strong stationarity and the aforementioned ergodicity conditions are used and justified for this study, we emphasize these conditions can be violated in many practical applications; see for example the discussion on the stationary condition for geo-masses in [112].

3.3.7 aSDG Method

The *asynchronous spacetime discontinuous Galerkin* (aSDG) finite element method formulated for elastodynamic [6], is used for the analysis of domains with mesoscopic inhomogeneous and anisotropic fracture strength fields. The method utilizes discontinuous basis functions across all element boundaries, and directly discretizes spacetime using nonuniform grids that satisfy a special causality constraint; the *Tent Pitcher* [1] algorithm advances the solution by consequently solving local *patches* (collections) of spacetime elements, until the entire spacetime domain is filled with tetrahedral elements for 2D problems. Unique properties, such as local and asynchronous solution scheme, arbitrarily high and local temporal order of accuracy, and linear solution scaling versus the number of elements, result in a highly accurate and efficient solution scheme for elastodynamic problem.

An interfacial contact and damage model [2] is used to model the processes of debonding and contact-stick/contact-slip mode transitions in rock. Motivated by a model in [36], an effective stress scalar value, $\breve{s}$, combines positive normal and shear traction components. The effective stress is used for crack nucleation, propagation direction, and damage evolution criteria; a crack is nucleated at a location $\mathbf{X} = (X, Y)$, if the effective stress at $\mathbf{X}$ exceeds the mesoscopic uniaxial tensile strength field at that location for any angle, that is if $\breve{s}(\mathbf{X}, \theta) \geq S_N(\mathbf{X}, \theta)$ for any $\theta \in [0, 2\pi)$. The crack propagation direction requires extension from a crack tip (or a nucleation point) in a direction θ_{ext} for which $\breve{s}(\theta_{\text{ext}})/S_N(\mathbf{X}, \theta_{\text{ext}})$ is a local maximum and is greater than one. Finally, for a point $\mathbf{X}$ on an existing (or extended) crack surface with angle θ_c, damage evolution is governed by the comparison of the corresponding effective stress and strength; that is $\breve{s}(\mathbf{X}, \theta_c)$ and $S_N(\mathbf{X}, \theta_c)$, respectively. Steps 3 and 4 in Fig. 29 show sample mesoscopic strength fields (at four angles) and a macroscopic fracture response obtained by the aSDG method. We refer the reader to [2] and [5] for the overview of the damage model and aforementioned fracture criteria.

Three different sets of error indicators and mesh adaptive operations are used to ensure the accuracy of dynamic fracture problem. First, energy dissipation within individual finite elements is used as an error indicator to ensure the accuracy of the solution of elastodynamic problem. Second, an energy-based error indicator is used on contact/fracture surfaces to measure and control the error in satisfying corresponding interfacial constitutive equations [8]. The h-adaptive scheme in [7] simultaneously refines and coarsen the elements in spacetime to ensure the preceding errors are sufficiently small. Third, the fracture propagation criterion based on macroscopic effective stress, can predict crack propagation in arbitrary directions. Highly advanced mesh adaptive operations in spacetime modify the spatial front mesh used by the aSDG method to align inter-element boundaries with new crack directions [10]. Thus, the method has the flexibility of *eXtended Finite Element Methods* (XFEMs) [151**?**], and *Generalized Finite Element Methods* (GFEMs) [34, 149] without the need to use enriched finite elements. Moreover, for rock fracture, particularly in dynamic regime and in presence of material inhomogeneities, highly complex features such as microcracking, crack branching, and crack intersection are observed that cannot be easily modeled with XFEMs and GFEMs. We refer the reader to [4] for a more thorough discussion on the advantages of the aSDG method to XFEMs and GFEMs.

3.4 Numerical Results

The numerical results for each domain, isotropic and anisotropic, will be presented here. Each domain is rectangular, centered at $\mathbf{X}_{\text{center}} = (0{,}0)$ and spans 40 mm in both X and Y directions, *i.e.,* the domain spans from $[-20, -20]$ to $[20, 20]$. As described in §3.3.2, the microcrack statistics of S19 Yuen-Long marble sample from [159] is used to create the two domains. For the half-crack length power law distribution, the power law Cauchy distribution exponent z is equal to 2.017 and the distribution numerator $q^{*}V_0$ is equal to 0.007. A mean crack length is $2a = 0.141$ mm. The minimum half crack length of $a^{'}$ is defined as 0.0075 mm, or $2a^{'} = 0.015$ mm. This minimum crack length is used to define $S_{\max}$. The crack density is $\varepsilon_0 = 0.243$.

The isotropic domain has a uniform crack angle distribution between $[0, 360]$ degrees and has no angular bias. Crack angle for the anisotropic domain has a triangular distribution with the range of [25,35] degrees and a peak value of 30 degrees. The material Poisson's ratio is 0.25 and Young's modulus is 34.65 GPa . The result of the SVE analysis is shown below for each domain. The generated microcrack domain is shown in Fig. 32 and the given length and angle *Probability Density Functions* (PDFs) are shown in Fig. 33.

3.4.1 Isotropic Domain

As detailed previously, the isotropic domain has a uniform crack distribution of θ_c in $[0, 360]$ degrees. The SVE analysis process was used to process the microcrack domain to develop mesoscopic strength fields using multiple SVE sizes: $L_{SVE} = 1$, 2, 4, and 8 mm. Since fracture strengths are assigned at the centers of the SVEs, the edge size of the square region for which fracture strength is assigned is $40 - L_{SVE}$ mm, with the smallest value of 32 mm for $L_{SVE} = 8$ mm. This explains why larger 40 mm × 40 mm domains are considered in Fig. 32, so that the smallest edge size of the mesoscopic fracture strength fields matches the 32 mm edge size of the VEs in [159]. From here on, all homogenized mesoscopic strength fields are shown in a square with 32 mm edge size.

The loading angle θ was varied between $[0, 180]$ degrees with a discrete angular spacing of 2 degrees within this range, resulting in 90 discrete loading angle strength fields. The minimum uniaxial tensile, uniaxial compressive, shear, and hydrostatic tensile fracture strengths were calculated for every crack in the domain, with the minimum strength retained for each SVE.

At a glance at Fig. 34, there is no discernible trend showing a change of strength depending on the loading angle for an isotropic domain. By calculating the statistics of the mesoscopic strength field, the PDF of the strength field at each discrete loading angle can be compared. From Fig. 35, the PDF for each loading angle confirms that general strength of the domain does not change depending on the loading angle, as there is no bias in the direction of microcracks.

The effect of SVE size on homogenized strengths is shown in Fig. 36. As the SVE size increases, the (spatial) variation of homogenized S_N and its corresponding mean value decrease. This is the well-known *size effect* for quasi-brittle materials [30, 29]. As L_{SVE} increases, the SVE tends to the RVE limit, explaining the decrease in the variation of homogenized strengths. Also, the likelihood of containing larger cracks increases as L_{SVE} increases. This explains the decrease in the overall values of S_N. Again, the PDF of the strength field shown in Fig. 37 agrees with this analysis. As the SVE size increases, the mean strength of the field decreases and the standard deviation of the response becomes smaller.

It is noted that if L_{SVE} were chosen sufficiently smaller than 1 mm, many SVEs would contain no cracks and would be assigned the strength $S_{\max}$, as described in §3.3.3. This would result in a bi-modal PDF for S_N; see for example figure 9 in [60].

We use A_N to study the anisotropy of the homogenized strength field S_N. A field of anisotropy index is constructed by assigning the value of A_N for each SVE at its centroid. While the measure of anisotropy is defined for all angle-dependent strengths in (3.11c), the results are only presented for S_N.

Figure 38 shows the spatial distribution of A_N for different SVE sizes. While for easier comparison of results, the maximum limit of 1 is used in all contour plots, A_N can be arbitrarily high. Since, the distribution of crack angle is uniform in [0, 360] degrees, we expect the macroscopic response of the domain to be isotropic. That is, A_N should tend to zero at all points as L_{SVE} increases toward infinity. This aspect can be observed in the figure. For the smallest SVE size in Fig. 38a, A_N varies with almost the same high spatial frequency that S_N fields varies in Fig. 34. There are several islands of high anisotropy measures that are caused by highly anisotropic distribution of microcrack angles in these regions. Some of the zones with highest values of A_N are framed in the figure. For larger SVE sizes in Figs. 38(b-d), the intensity of the anisotropy index at the peak points decreases and the field is generally smooth. The same argument that is used in the decrease of fracture strength in Fig. 36 and Fig. 37 for larger SVE sizes applies here; for this macroscopically isotropic material, the angle distribution of the most critical (longest) cracks within an SVE tends to its macroscopic uniform distribution of $[0, 360]$ degrees. The spatial variation of this field also decreases, again, because the SVEs tend to the RVE limit. However, for $L_{SVE} = 8$ mm, the same islands of high A_N persist, even though their intensity and sharpness have significantly decreased compared to those in Fig. 38a.

3.4.2 Anisotropic Domain

The anisotropic domain was generated with a triangular distribution in crack angle, with a peak of $\theta_c = 30$ degrees and a range of [25,35] degrees; *cf.* Fig. 33b. Therefore, the lowest fracture strengths should be for loading angles close to $\theta = 30$ degrees, since this loading angle will effectively be pulling the cracks open. The maximum strength of SVEs should be close to $\theta = 120$ degrees, since this is pulling the cracks almost parallel to their direction.

By viewing Fig. 39, the differing trend in strength based on loading angle can be seen. Loading angles of $\theta = 120$ degrees creates a uniform, homogeneous high strength field equal to $S_{\max}$, corresponding to minimum crack length $2a^{'} = 0.015$ mm; since, most cracks are almost parallel to loading angle, *i.e.*, $\theta_d \approx \pi/2$, $s_N(\theta)$ tends to infinity in (3.9b). At 90 degrees apart from this, $\theta = 30$ degrees, a nearly uniform low-strength field is observed in Fig. 39a. This trend is confirmed by the PDF of the strength field by varying the loading angle, as shown in Fig. 40. As the strength gets closer to the θ of minimum strength for the anisotropic domain, the mean strength steadily decreases. When comparing the isotropic PDF shown in Fig. 35 to the anisotropic PDF shown in Fig. 40, the effect of anisotropic crack distributions can be shown clearly. An interesting note to this is that for anisotropic domains, the actual strength of the field can be much higher over a wide range of loading angles compared to isotropic domains. Understanding the anisotropy of a given material can be crucial to whether a given material could be used for a specific application and loading condition.

Figure 41 shows the spatial distribution of the anisotropy measure for the anisotropic domain for different SVE sizes. Since microcrack angles are biased around $\theta_c = 30$ degrees, this domain is anisotropic even when the VE size tends to infinity; the lowest and highest strengths are expected at angles $\theta_d = 30$ and $\theta_d = 120$ degrees, respectively. Overall, as the SVE size increases, the spatial frequency of variations of A_N decreases and the field becomes more uniform. This is because the SVE tends to the RVE size limit.

Another observation is that the averaged fracture strength field S_N is less anisotropic for smaller SVE sizes. As the L_{SVE} increases, there are more microcracks contained in an SVE and very low strengths are expected for θ_d in $[25, 35]$ degrees, particularly for the mode of the crack angle distribution $\theta_d = 30$ degrees. This results in a highly angle-dependent, yet more spatially uniform distribution for S_N, reflected in more uniform and higher values for A_N in Figs. 41(c-d). In contrast, for smaller SVEs, there is a higher variability in angles within $[25, 35]$ degrees that have the longest cracks, thus the lowest strengths, within the SVEs. Thus, the averaged strength field is less anisotropic, yet more spatially variable due to higher variability of the statistics of microcracks within the SVEs. The frames regions in Fig. 41 demonstrate that, similar to Fig. 38, the regions of higher anisotropy are preserved and averaged as the SVE size increases.

To represent this difference in the isotropic and anisotropic domains, four SVEs were selected based on the measure of anisotropy, A_N. Four points, chosen from lowest measure of anisotropy to highest in the isotropic domain, are shown in Fig. 38a and Fig. 41a. While the two domains do not have the same microcrack distribution and are unrelated, the same points were used for both isotropic and anisotropic domain. P2 in the isotropic domain was selected such that it corresponded to the same coordinates as the location of highest anisotropy in the anisotropic domain. The coordinates of each point, measure of anisotropy A_N, and mean strength $\bar{S}_N$ are shown in Table 3, and how the respective uniaxial strength field $S_N(\theta)$ changes in angle is shown in Fig. 42.

For the isotropic domain, as A_N increases, the strength field becomes more anisotropic, dominated by one angle of highest and lowest strength. The standard deviation increases such that the peak and minimum strength are further away from the given mean strength. For the isotropic domain, each SVE contains a different angle of maximum and minimum strength. The measure of anisotropy is a good indicator for the relative dominance of one crack angle contained in that SVE.

The anisotropic domain contains a dominant angle of maximum strength no matter the level of anisotropy. In the anisotropic domain, P2 contains the highest measure of anisotropy. As is expected, the width of the angular band of maximum strength for P2 is also the narrowest, as shown in Fig. 42b. Generally, while the angle of maximum and minimum strength is roughly the same for all SVEs in the anisotropic domain, the measure of anisotropy indicates how narrow the band of maximum and minimum strength is, which is caused by the SVE only containing cracks within a narrow angular distribution.

In short, for the isotropic domain, measure of anisotropy is higher for smaller SVEs and it tends to zero for larger SVEs, as shown in Fig. 38. In contrast, for the anisotropic domain, A_N tends to a finite high value for larger SVEs and it takes lower values for smaller SVEs. For both cases, the homogenized strength fields are more inhomogeneous for smaller SVE sizes. Since, maintaining material inhomogeneity is desirable in fracture analysis, the smaller SVE size $L_{SVE} = 1$ mm is used to produce mesoscopic strength fields for the macroscopic simulations in §3.4.4.

3.4.3 Covariance and Correlation

We first study the dependence of the covariance and correlation functions on space and angle coordinates for S_N. Next, the correlation between different angle-independent strengths derived from S_α, $\alpha \in \{NH, N, C, S\}$ is investigated. In the following, we use the assumed stationarity and ergodicity discussed in §3.3.6 to compute the covariance and correlation functions based on only the single realization for each rock model, and to express the covariance function as a function of spatial distance of the two points; *cf.* (3.14).

Spatial correlation

We first analyze the form of covariance function in space. That is, ξ_A and ξ_B are chosen such that the same loading angle is chosen for both, meaning that $\theta_A = \theta_B$. For this analysis, we use the strength field S_N homogenized by $L_{SVE} = 1$. Moreover, $\theta_A = \theta_B$ is set to zero to focus on spatial correlation of uniaxial tensile strength for zero degree loading direction. This *spatial covariance* function of S_N for zero loading direction is only a function of change of spatial coordinate $(\Delta X, \Delta Y)$ and is denoted and defined by $\mathrm{cov}_{\mathbf{X}N}(\Delta X, \Delta Y) = \overline{\mathrm{cov}}_N(\Delta X, \Delta Y; 0, 0)$. This function can be evaluated from a single homogenized strength field by moving the space position of ξ_A and keeping the spatial difference of ξ_B and ξ_A fixed and equal to $(\Delta X, \Delta Y)$.

Figure 43 shows $\mathrm{cov}_{\mathbf{X}N}$ for both isotropic and anisotropic microcrack statistics. Several observations can be made. First, from the circular contour lines, it is evident that the covariance function is only a function of the relative distance of the two points and not their relative angle. That is the spatial covariance beyond being homogeneous (depending on only on relative spatial difference of ξ_A and ξ_B) is also isotropic (not being a function of relative spatial angle between ξ_A and ξ_B). Second, we observe that the spatial covariance function quickly tends to zero in a spatial range roughly equal to the SVE size. This corresponding to traversing about 5 SVEs as n is chosen equal to 5; *cf.* §3.3.1. Third, the spatial covariance function has an almost identical form for both isotropic and anisotropic microcrack distribution models.

Angular correlation

Next, we analyze the form of the covariance function in angle. That is, ξ_A and ξ_B share the same spatial location (X, Y), but have arbitrary angles $0 \leq \theta_A, \theta_B < \pi$. Again, considering S_N for $L_{SVE} = 1$, this covariance function is defined and denoted by $\mathrm{cov}_{\theta N}(\theta_A, \theta_B) = \overline{\mathrm{cov}}_N(0, 0; \theta_A, \theta_B)$. Similar to the calculation of $\mathrm{cov}_{\mathbf{X}N}$, the spatial stationarity of homogenized strength fields is used to populate the statistics for $\mathrm{cov}_{\theta N}$ by moving (X, Y) in a realization of S_N.

Several observations are made for $\mathrm{cov}_{\theta N}$ of the isotropic domain in Fig. 44a. First, the value of the function along the diagonal line $\theta_A = \theta_B = \theta$ corresponds to $\mathrm{cov}_{\theta N}(\theta, \theta)$, the variance of the uniaxial tensile strength for angle θ. Since the orientation of microcracks is isotropic (uniform in $[0, \pi]$), we expect the statistics of $S_N(X, Y, \theta)$ to be stationary in θ as well; that is, independent of the angle of loading. Consequently, the variance of $S_N(\theta)$ too should be independent of θ, meaning that the value of $\mathrm{cov}_{\theta N}(\theta_A, \theta_B)$ on diagonal $\theta_A = \theta_B = \theta$ should be constant. The small variations of $\mathrm{cov}_{\theta N}$ on this diagonal in Fig. 44a is contributed to numerical errors associated with the finite set of values used in evaluating the covariance function.

Second, again from the stationary condition of S_N in θ, $\mathrm{cov}_{\theta N}(\theta_A, \theta_B)$ should only be a function of the relative difference of the angles $\theta_B - \theta_A$ rather than their individual values. Since $S_N(X, Y, \theta)$ is periodic in θ with period π, $\mathrm{cov}_{\theta N}(\theta_A, \theta_B)$ is a periodic function with the solution in $[0, \pi) \times [0, \pi)$ (the part shown in the figure) repeating in 2D $(\theta_A, \theta_B) \in \mathbb{R}^2$ angle space. Considering these facts, the value of the function only depends on the distance of the point (θ_A, θ_B) from the diagonal $\theta_A = \theta_B$ line. Again, the small deviation of the $\mathrm{cov}_{\theta N}$ from this condition in Fig. 44a, is a consequence of the finite number of points used for computing the covariance function. Finally, we observe that the covariance function tends to zero for an angle difference of about $|\theta_B - \theta_A| = 30$ degrees.

The covariance function in angle for the anisotropic domain is shown in Fig. 44b. Again, the value on the diagonal $\theta_A = \theta_B = \theta$ is the variance of $S_N(\theta)$. For the anisotropic domain, the highest variances of $S_N(\theta)$ are observed at angles about 10 degrees outside the angles corresponding to highest strength around 120 degrees. The observed high variance is a consequence of stipulating a maximum strength corresponding to minimum allowable crack length $2a^{'}$; *cf.* §3.3.2. Overall, we observe a much more complex form for the covariance function of anisotropic domain compared to that in Fig. 44a; specifically, due to the anisotropy of $S_N(\theta)$, $\mathrm{cov}_{\theta N}(\theta_A, \theta_B)$ is no longer only a function of the angle difference $|\theta_A - \theta_B|$.

The angular correlation function, defined by $\mathrm{corr}_{\theta N}(\theta_A, \theta_B) = \mathrm{corr}_N(X_A = X, Y_A = Y, \theta_A; X_B = X, Y_B = Y, \theta_B)$, is shown for isotropic and anisotropic rock domains in Fig. 45. As expected, strengths $S_N(X, Y, \theta_A)$ and $S_N(X, Y, \theta_B)$ are highly correlated as the angle difference tends to zero. In fact, for $\theta_A = \theta_B = \theta$, by definition the correlation is one, given that the two strengths coincide. This corresponds to the value of one on diagonal line $\theta_A = \theta_B$ for both cases in Fig. 45. For isotropic rock, fracture strengths are highly correlated for an angle difference $|\theta_B - \theta_A|$ roughly less than 30 degrees, and the correlation is almost zero for higher angle differences. The zero correlation of fracture strength for this high of an angle difference can be compared to zero correlation between the strength of two points that are roughly 1 mm apart in Fig. 43.

The angular correlation of S_N for the anisotropic domain is vastly different; aside for an about 10 degree range around 120 degrees, the angle corresponding to highest strengths, fracture strength of any two angle of loading are highly correlated. This is due to the fact that the majority of cracks are aligned close to 30 degrees, and in approximate sense, $1/\cos(\theta - 30)$ is the factor that relates strength at angle θ to that for the 30 degrees, *i.e.,* the weakest strength; *cf.* (3.9b) and note that $\theta_d \approx \theta - 30$. Clearly due to the local variation of crack angle in the range $[25, 35]$ degrees, there is not this perfect correlation between S_N at two arbitrary angles; however correlations close to one are observed in Fig. 45b. The zero correlation of high strength angle range and other angles is contributed to assigning $S_{\max}$ for angles around 120 degrees.

Correlation between different strength types

Finally, we study the correlation between different fracture strength fields. To more effectively focus on the type of strength, rather that angle-dependent strengths $S_\alpha(\theta)$, we use the two alternatives of SVE angle-independent strengths proposed in §3.11. The $\bar{S_N}$, $\bar{S_S}$, and $\bar{S_C}$ in (3.11a), provide an overall average angle-independent strength for an SVE. In contrast, $m(S_N)$, $m(S_S)$, and $m(S_C)$ are the most conservative choices by taking the minimum of strengths over all angles of loading in (3.11b). When for a given L_{SVE}, *i.e.,* observation size, strength anisotropy is low, either of these two choices of strength can be used to define a unique isotropic strength for a given spatial location. For example, we have used the mean and min of uniaxial normal strengths for two different types of composites in [16] and [20], respectively. However, in these works only macroscopically isotropic materials were considered and the correlation between different strength types were not studied.

The Pearson correlation coefficient between these six derived angle-independent and inhomogeneous strength fields and the already angle-independent strength S_{NH} are provided in Table 4 for the isotropic domain. Very high correlations are observed between S_N, $\bar{S_N}$, $\bar{S_S}$, and $\bar{S_C}$. The lowest value corresponds to a correlation of 0.847 between S_{NH} and $\bar{S_C}$. This can be contributed to pure mode I and mode II fracture for hydraulic tensile and uniaxial compressive loadings, respectively. In addition, for a single crack s_C is highly anisotropic, and even in the zone for which s_C is finite, its value quickly tends to infinity; *cf.* (3.9c) and Fig. 31. The highly different fracture modes for a single crack, explains the lower correlation between S_{NH} and $\bar{S_C}$, even after the operations (3.10) and (3.11b) are taken into account to derive these angle-independent SVE strengths.

However, if instead of using angular mean of strengths in an SVE, their minimum value is used, a perfect correlation is observed between S_N, $m(S_N)$, $m(S_S)$, and $m(S_C)$. By inspecting Fig. 31 and (3.9), we observe that the angular minimum of all strengths s_N, s_N, s_S, and s_C is the same. Thus, from (3.10) and (3.11a), for all $\alpha \in \{NH, N, C, S\}$, $m(S_\alpha) = K_c/\sqrt{\pi a_{\max}}$, where $a_{\max}$ is the maximum half-length of a crack within an SVE. That is, S_N, $m(S_N)$, $m(S_S)$, and $m(S_C)$ are all equal, explaining their perfect correlation.

From the preceding comparison of $\bar{S}_\alpha$ and $m(S_\alpha)$, it appears that if one aims to simplify the fracture strength fields by eliminating their angular-dependency, the mean value is a more appropriate choice for microcracked domains as it maintains the fundamental differences between different types of strength. Also, as elaborated in [16], the use of angular minimum strengths can be too conservative.

The correlation coefficients for the anisotropic domain are provided in Table 5. As explained, the correlation between all minimum strengths and S_{NH} is one. For the mean strengths, the correlations are considerably higher than those for the isotropic domain, with a minimum value of 0.967. Similar to high correlation of strength between different angles of loading in Fig. 45, this can be contributed to large percentage of cracks being oriented close to 30 degrees and more or less constant factors between different fracture types in (3.9) for $\theta_c \approx 30$ degrees.

From the comparison of the results for isotropic and anisotropic domains, it is suggested that eliminating fracture strengths S_S and S_C in a failure criterion and maintaining only

S_N is a more sensible choice for anisotropic domains. Under such conditions, the other strengths can be approximated as constant factors of uniaxial tensile strength field, without introducing much error. This greatly simplifies several aspects of the proposed multi-scale approach in this manuscript, as we consider a single inhomogeneous strength field for S_N in §3.4.4.

In this section we studied how fracture strengths vary by changing the spatial location, angle of loading, and type of strength. Covariance functions can be used by the Karhunen-Loéve (KL) [84, 96] or other similar methods to generate a large number of random field realizations that are consistent with fields homogenized with a given L_{SVE}. This approach in general is faster than generating domains with an actual microstructure (*i.e.,* the microcracks here) and using the SVEs to homogenize them. Thus, understanding the form of covariance function is of great importance. For the two microcrack distributions considered and for $L_{SVE} = 1$, the corresponding random fields are stationary in space. In addition, the spatial covariance function is spherical and tends to zero at a length scale below L_{SVE}. The angular covariance function is stationary in angle for the isotropic domain and tends to zero for loading angle differences greater than about 20 degrees.

3.4.4 Dynamic Fracture Analysis

For fragmentation and other problems that lack macroscopic stress concentration points, maintaining material inhomogeneity is of great importance. We study the fragmentation of a 32 mm × 32 mm square rock domain (same VE size used in [159]) under bi-axial tensile loading condition. We use the inhomogeneous fracture strength fields for $L_{SVE} = 1$ for both isotropic and anisotropic domains, to maintain the highest level of material inhomogeneity with the SVE sizes considered. Since $n = 5$, *cf.* §3.3.1, any of the fracture strength fields for $S_N(\theta)$ is represented by a 160 × 160 resolution *material property* mesh. The value at each grid point is equal to $S_N(\theta)$ obtained for the SVE centered at that point. Using a step size of 2 degrees for θ, 90 strength fields $S_N(\theta)$ are computed and stored for macroscopic fracture analysis for each of the two rock domains. Four of such meshes for isotropic and anisotropic domains are shown in Fig. 39 and Fig. 34, respectively.

Initial and boundary conditions were applied consistent with a uniform, isotropic tensile field that ramps linearly in time. The components of the displacement field (U, V) are,

$$U(X, Y, t) = \dot{\varepsilon} X t, \qquad V(X, Y, t) = \dot{\varepsilon} Y t \tag{3.15}$$

where (X, Y) and t are space and time coordinates, and $\dot{\varepsilon}$ is the specified normal strain rates for both X and Y directions. Dirichlet boundary conditions, *i.e.,* a prescribed velocity field, is applied on the entire boundary of the domain at all times. This resembles a *displacement control* loading in dynamics and is more appropriate than Neumann boundary condition for capturing the unloading part of macroscopic strain versus stress response. Plane strain conditions were specified with material properties taken from [159]; that is, Young's Modulus $E = 65$ GPa , mass density $\rho = 2700$ kg/m^3, and Poisson's ratio $\nu = 0.3$. The macroscopic fracture simulations are performed by the aSDG method, described in §3.3.7.

Both rock domains are simulated up to time $t = 12$ μs. A strain rate of $\dot{\varepsilon} = 20$/s is used to gradually load them. A spatially uniform and temporally increasing stress response persists until the stress value reaches the minimum tensile strength of $S_N(X, Y, \theta)$ over all spatial points and angles of loading, at location (X_m, Y_m) and for the angle of loading θ_m. At this instant, a crack is nucleated at (X_m, Y_m) and propagated along the direction θ_m. The uniform stress field no longer persists past this instant, and more cracks are nucleated and/or propagated until the square domain completely fails.

We use homogenization boundary integrals [111] to obtain macroscopic strain E and stress Σ tensors for each time $t \in [0, 12\ \mu\text{s}]$. Figure 46 compares the response of the two rock domains in terms of their macroscopic strain versus stress response. The maximum attainable stresses of the isotropic domain are $\max(\Sigma_{XX}) = 19.16$ MPa and $\max(\Sigma_{YY}) = 18.39$ MPa. The corresponding values for the anisotropic rock domain are $\max(\Sigma_{XX}) = 21.82$ MPa and $\max(\Sigma_{YY}) = 21.94$ MPa. Thus, the anisotropic rock domain has a higher macroscopic strength under the bi-axial tensile loading condition. This is due to the fact that over the majority of angles, the fracture strength S_N is much higher than the isotropic domain other than a small angular range about the angle of weakest strength. At time $t = 12$ μs, the isotropic domain has reached failure, but the anisotropic domain has not yet reached failure.

Another interesting feature is that for the anisotropic rock, aside from a small region early in macroscopic failure initiation stages, Σ_{YY} is lower than Σ_{XX} over a zone where significant macroscopic softening and unloading occurs in Fig. 47b. Eventually, however, both stresses take almost the same values once they tend to zero past this zone. Given that for the anisotropic domain, lowest strengths in the homogenized $S_N(X, Y, \theta)$ field are for angles $\theta \in (25, 35)$ degrees, overall the domain is expected to have a lower strength in Y, compared to X, direction. For the single realization of the microcracks with anisotropic angle statistics in Fig. 32b, this happens for the range of strains discussed above. We have repeated the fracture analysis of the same two rock domains under different loading rates $\dot{\varepsilon}$. While the results are not presented for brevity, the same difference between Σ_{XX} and Σ_{YY} for the anisotropic domain is observed for other loading rates. In addition maximum macroscopic stresses of the anisotropic domain consistency remain higher than those of the isotropic domain.

The strain and kinetic energy densities of the two solutions are shown in Fig. 47 for $t = 12\ \mu$s. The strain energy density is mapped to the color field, where blue to magenta color indicates a range of zero to 1000 J/m^3. The kinetic energy is mapped to the height field such that regions of high kinetic energy appear closer. Because the anisotropic domain has not reached failure, higher strain levels are shown in the domain. The isotropic domain shows cracks growing in several directions; however, the anisotropic domain shows the angularly biased crack field where, as expected, the majority of cracks are aligned close to 25 to 35 degrees. The majority of cracks with other orientations connect three to four main cracks that are aligned with the weakest plane of the rock.

Figure 48 depicts the front meshes at the time of failure $t = 12\ \mu$s for the two rock domains. These meshes show the adaptivity of the aSDG method for propagating cracks and controlling solution errors. In addition, the level of interfacial damage parameter is indicated by blue (zero damage) to red (full damage) colors on crack surfaces. For both cases the solution starts with a spatial triangulation containing no cracks. The effect of initial microcracks in the domain is modeled by anisotropic and inhomogeneous mesoscopic fields of S_N as those shown in Fig. 34 and Fig. 39. As the cracks are nucleated with specified propagation directions, the front mesh is continuously adapted to align element boundaries with the specified directions. In addition, adaptive operations ensure that the numerical errors in the bulk and on fracture surfaces is below the user-specified tolerances. This is reflected in finer elements closer to the crack tips in the figure. As a result of these adaptive operations, the front meshes in Fig. 48a and Fig. 48b contain 23,891 and 26,615 triangles, respectively, compared to only 803 triangles in the initial front mesh at $t = 0$.

3.5 Conclusion

An up-scaling approach was proposed in which an angle-dependent inhomogeneous fracture strength field was homogenized from the distribution of cracks at the microscale. The mesoscopic strength field is in turn used for fracture simulations at the macroscale. The computational cost is deemed to be lower compared to direct numerical simulation of the material with explicit representation of its microstructure.

The microcrack statistics of a real material, Yuen-Long marble, as described in [159], was used to generate cracks at the microscale. The proposed multiscale approach can be used to systematically propagate the statistics and randomness of a material at the microscale to uncertainties in its macroscopic failure response.

We use a mixed mode crack propagation criterion, while taking into account the frictional effect for mode II fracture, to derive angle-dependent uniaxial tensile, uniaxial compressive, and shear strengths for arbitrary orientations of the loading and a single crack. These strengths are used to derive corresponding angle-dependent strengths for a circular SVEs, containing potentially multiple cracks. A 2D macroscopic domain is then traversed with overlapping SVEs in X and Y directions. The homogenized fracture strengths of each SVE is assigned to its center point.

Two rock domains with isotropic and anisotropic distribution of microcracks were homogenized with different SVE sizes. Macroscopic fracture responses were consistent with the underlying statistics of microcracks. For example, for the anisotropic domain, the majority of macroscopic cracks were aligned with the weakest directions of the homogenized mesoscopic strength field.

The point-wise and two-point statistics of the random fields were analyzed. As the SVE size increased, the homogenized field became smoother and higher frequency local variations were lost. This corresponded to lower mean and variation of the homogenized strengths for higher SVE sizes. The spatial covariance function of the strength field was shown to only depend on the distance of two points. The angular covariance function of the isotropic rock should be a function of relative angular distance of two points. In contrast, this function was shown to be much more complex for the anisotropic rock domain.

The effectiveness of this method for homogenization and fracture simulation was demonstrated; however, there are several areas of improvement for future research. First, in the present study only fracture properties were assumed to be anisotropic. For more realistic modeling, the elasticity tensor should also be considered inhomogeneous and anisotropic [147], and be homogenized by SVEs. Second, we only presented a single realization of a microcracked domain and its corresponding mesoscopic fracture strength field (for a given SVE size). Many realizations of the microcracked domain (or mesoscopic fracture strength fields) should be generated and analyzed to provide a statistical representation of macroscopic fracture response. Third, the one-point and two-point statistics of the mesoscopic random fields, studied here, can be used to circumvent the microscale domain realization and analysis, and directly generate statistically consistent random fields at the mesoscale. Fourth, finite element analysis can be used at the microscale to accurately model microcrack interaction (not modeled in the present study) and to calibrate computationally more efficient stochastic bulk damage models [98].

Chapter 4

Elastic and Strength Properties of Statistical Volume Elements: Determination of Isotropic and Homogeneous Size Limits

An original version of the following article was submitted for publication in October 2021 to the Elsevier journal *Journal of the Mechanics and Physics of Solids*. The article was submitted under the title ”Elastic and Strength Properties of Statistical Volume Elements:Determination of Isotropic and Homogeneous Size Limits”.

The included article is the second of a two-part journal article collaboration between myself and Dr. Reza Abedi at the University of Tennessee with Dr. Katherine Acton at the University of St. Thomas in St. Paul, Minnesota. The first article, not included in this dissertation, was authored primarily by Dr. Katherine Acton with contributions by myself and Dr. Reza Abedi. The article is titled ”Geometric Partitioning Schemes to Reduce Modeling Bias in Statistical Volume Elements Smaller than the Scale of Isotropic and Homogeneous Size Limits” and was submitted in October 2021 to the Elsevier journal *Computer Methods in Applied Mechanics and Engineering*. The primary research focus of the first journal article was to investigate how the SVE shape (circular or square) and type (regular or Voronoi) can result in modeling bias for the homogenized elastic and fracture property fields. Isotropic and anisotropic domains were used to show how the square regular SVE type introduced an angular bias into the results which was not physical for the isotropic domains.

In the included article, the rate at which the homogenized property fields converge to the isotropic and homogeneous RVE limit is investigated for regular and Voronoi SVE types. My contributions include

- Modification of existing SVE code to improve input of multiple SVE types, add volume fraction and other geometry data, and provide output for Abedi plot tool
- Mesoscopic analysis of elastic and fracture strength fields using regular and Voronoi SVEs using FEA results provided by Dr. Katherine Acton
- Data analysis of mesoscopic results
- Showed optimum location where elastic properties converge to homogeneous, isotropic limit but fracture retains randomness (inhomogeneity, anisotropy) which is needed to accurately capture fracture results

This work is the first to extend the use of SVEs beyond the analysis of homogeneity for elastic or fracture properties to investigate the effect of material anisotropy in the analysis. A linear elastic fracture model is used to generate the angle-dependent fracture strengths. Both fracture crack density and length distribution are made to match the previous work [58], but the crack angle is varied to be completely isotropic (unbiased) or anisotropic (biased with a triangular distribution about 30 degrees).

4.1 Abstract

The use of *Representative Volume Element* (RVE) based effective properties can result in unsatisfactory fracture patterns and dissipated energy, and cannot model statistical sample-to-sample variations. *Statistical Volume Elements* (SVEs) address these problems by approximating random and inhomogeneous apparent material properties. As the SVE size decreases, the accuracy of an SVE-based multiscale model improves at the expense of dealing with more complex apparent material properties and higher computational cost. We examine the trends in which apparent elastic and fracture properties tend to their homogeneous and isotropic effective RVE limit for a two-phase macroscopically homogeneous and isotropic composite. Two different RVE definitions based on 1) vanishing variations of a homogenized property and 2) the convergence of its mean value versus SVE size are proposed. The elastic properties are shown to reach their homogeneous and isotropic limit at much smaller SVE sizes. This is a welcomed effect, as the SVE size can be chosen sufficiently large so that only the apparent fracture strength remains random and inhomogeneous. This not only reduces the computational cost and complexity of an SVE-based multiscale fracture analysis, but also has proven useful in capturing realistic fracture results. Finally, regular SVEs are compared with Voronoi SVEs. For regular SVEs, the intersection of straight SVE edges with inclusions results in a significantly nonphysical size effect for fracture strength, drastically increases anisotropy of apparent properties, and results in 30 to 60 times larger RVEs compared to Voronoi homogenization. All these aspects are further discussed in the context of multiscale SVE-based failure analysis.

4.2 Introduction

Performing accurate fracture simulations heavily relies on the accuracy of the material models. *Direct Numerical Simulation* (DNS) resolves material microstructure to a certain continuum lengthscale such as inclusion or grain characteristic size. While this method is accurate for many failure analyses, its use is generally restricted to very small length and time scales due to high computational costs.

Homogenization methods for *Representative Volume Elements* (RVE), pioneered by [73, 74, 100, 117], have been developed to derive effective material properties without the computational cost of DNS, *i.e.,* explicitly modeling discrete cracks or flaws.

A RVE refers to a large enough *Volume Element* (VE) for which the homogenized effective property can be considered converged. Simulating a material with RVE-derived effective properties is the opposite end of spectrum relative to DNS in terms of model accuracy and solution cost. For example, a material that is inhomogeneous and anisotropic at the microscale, may be represented by homogeneous and isotropic RVE-based effective properties at the macroscale. However, the substantially lower computational cost of using RVE-based effective properties relative to DNS makes RVEs ideal for many applications, for example when linear elastic response of a material is sought at large length scales.

The definition of a RVE has been the subject of much debate in literature [73, 69, 136, 118, 83, 120, 85, 63, 33]. All RVE definitions require enough information about the microstructure to be statistically representative of the macroscopic body independent of any boundary condition [121] or model-related choice. In the context of disordered material, *Statistical Volume Elements* (SVE) refer to VEs that are smaller than RVEs [119]. SVEs are used to partition a macroscopic domain using the method of moving window [22, 65, 66, 11, 12, 13] to calculate the statistics of the material elastic [80, 141, 154] or fracture [57, 59, 160] apparent properties.

Because material fracture is greatly influenced by local heterogeneities [153, 48, 31], accurate characterization of fracture requires capturing statistical variability of the microstructure. The use of RVE-based effective properties is often not appropriate for failure analysis for two reasons. First, since local inhomogeneity of material is lost, such properties can in many cases result in unsatisfactory predictions for macroscopic *Quantities of Interest* (QoIs). For example, in a fragmentation analysis, failure happens at once at almost all points when the applied load reaches the assumed uniform strength of the material [42]. The use of underlying homogeneous material properties has also been attributed to non-convergence issues in fracture pattern [148], and macroscopic dissipated energy from physical [46] and numerical mesh resolution [108] perspectives.

The second problem is the loss of sample-to-sample variations. This stems from using deterministic elastic and fracture properties. Generally, there is little statistical variations in the response of materials in the linear range (for meso and macroscale domains), justifying the use of RVEs for this purpose. However, when failure is considered, small differences in material microstructure can drastically affect the fracture initiation load, subsequent stress concentration points and crack nucleation or coalescence events, and result in significant variations in failure pattern [17] and ultimate load and macroscopic dissipated energy [62, 86]. Clearly, none of these aspects are realistic.

Several phenomenological models, such as the Weibull model [156, 157] in [45, 148, 5, 90, 4], have been used to realize an inhomogenous and non-deterministic fracture strength field and successfully address some of the aforementioned problems. Homogenization of apparent fracture and elastic material properties using SVEs [42, 16, 57, 59] also address these problems by directly resulting in inhomogeneous and random apparent material properties. They may be considered superior to phenomenological models, as physics-based apparent properties can be systematically derived for any material with its particular design at the microscale.

When SVEs are used for homogenization, the effects of boundary conditions, SVE type and SVE size should be clearly understood. With respect to boundary condition type, as the SVE size increases, the Hill-Voigt upper bound generated using a *Kinematic Uniform Boundary Condition* (KUBC) and Hill-Reuss lower bound generated using a *Stress Uniform Boundary Condition* (SUBC) for the effective moduli converge to a unique value [77, 72, 71, 168, 85, 119, 120]. In fact, this condition has been used to define the RVE size in [121] by requiring the KUBC and SUBC results to be close to within a tolerance.

The SVE type also affects the apparent material properties. Regular SVEs allow for microstructural defects or other heterogeneities to cross the boundaries of the SVE, creating stress concentrations at these locations when a uniform boundary condition is applied [14]. These stress concentrations cause inaccurate elastic and strength properties. Danielsson [44] and Salmi [138] showed that Voronoi tessellation can be used to ensure the SVE boundaries do not intersect the different phases of the material microstructure, avoiding these modeling-based stress concentrations.

Finally, SVE size can be viewed as the resolution of the homogenization scheme and acts as a gauge between RVE-based homogenization and DNS in terms of solution accuracy and efficiency. One on hand, when larger SVEs are used, the homogenized apparent material field tends to the effective RVE-based limit inappropriate for many failure simulations as material inhomogeneity and sample-to-sample variation tends to zero. On the other hand, the solution cost increases and various stages of the multiscale stochastic failure analysis become significantly more complex as SVE size decreases. The complexity of the SVE-based multiscale model is specifically related to the anisotropy of apparent properties.

When balancing the competing interests of accuracy and efficiency, often material anisotropy is ignored and only material heterogeneity is considered [37, 45, 16, 166, 139, 93]. However, in the context of SVE homogenization, these two effects are inseparable; even for a macroscopically homogeneous and isotropic material, at small SVE sizes the apparent properties are both inhomogeneous and anisotropic. Handling the anisotropy is specifically difficult in SVE-based multiscale failure analysis. For example, the realization of consistent random fields for the fourth order elasticity tensor is quite challenging [99]; even if possible, the solution of *Stochastic Partial Differential Equations* (SPDEs) arising from the use of SVE-based apparent properties is significantly more expensive when dealing with a fourth order elasticity tensor rather than a random scalar elastic modulus.

The purpose of this work is to determine under what conditions (SVE size and type) a given fracture problem can be greatly simplified by determination that certain elastic and/or fracture properties are homogeneous and/or isotropic. While there have been several anisotropy indices for elastic properties [162, 39, 116, 135, 91, 155, 130, 54], to our knowledge other than [129], there have been no systematic analysis on how SVE-based apparent elastic properties tend to their isotropic limit for a macroscopically isotropic material. We also analyze whether SVE-based apparent fracture strengths become homogeneous and isotropic as the SVE size increases. Finally, regular and Voronoi SVE types are studied to determine if specific modeling choices can introduce spurious anisotropic effects and affect the rate of convergence of various properties to the homogeneous / isotropic RVE limits for elastic and fracture properties.

4.3 Methods

4.3.1 Partitioning of the Macro Domain

A square two dimensional domain was constructed containing circular inclusions with a side length equal to approximately 100 times the diameter of the inclusions d. The domain is isotropic, constructed using Random Sequential Adsorption [38]. The domain is partitioned using SVEs of edge length scale $\mathrm{L} = \delta \cdot d$, where for this work d is set to a unit value. We use the non-dimensional parameter δ to represent the SVE size. Since $d = 1$, the values of L and δ match in this work. The domain is partitioned using two SVE geometry types. Each type of SVE is assured to be a uniform area using square tiles which cover the entire domain. Because both SVE types are space-filling, these SVEs satisfy the Huet hierarchy of bounds [77].

The first SVE type used is the *regular* SVE, which uses a simple square tile geometry to fill the space. This SVE type is one of the most commonly used [120, 83] in the literature to date. The second SVE type is defined as *Voronoi*, which uses a Voronoi tessellation based shape. Voronoi cells are generated with center points about the inclusions in the SVE, ensuring no boundaries intersect a given inclusion, which differs from the regular type. A square grid with sides of length δ is created; those Voronoi cells whose centroids are contained within the grid are assigned to that grid location. This generates an approximately square shape that is produced using Voronoi cells, as shown in Figure 49. Voronoi cell SVEs have been shown [138, 16, 14] to improve the bounds of the apparent material properties, which results in a closer estimate of apparent SVE properties to the effective RVE behavior. This can be used to better characterize material heterogeneity, which is useful for fracture modeling [16], because the Voronoi cell boundaries do not intersect the inclusion boundaries which may cause stress concentrations at these locations.

SVE sizes of δ equal to 3.125, 6.25, 12.5, 25, and 50 are analyzed. The volume fraction of inclusions is approximately 10%. Both the matrix and inclusion Poisson's ratio are 0.3. The ratio of inclusion to matrix elastic modulus is 100:1. In the next section, we will show how we determine the elastic and fracture properties for a given SVE.

4.3.2 Approximation of Apparent Engineering Properties

Elastic material property fields are calculated using the SVEs partitioned with either regular or Voronoi SVEs as detailed in §4.3.1. Unlike an RVE, the SVE-calculated apparent properties are dependent upon the choice of boundary conditions [77]. In this paper, we use a KUBC where an applied uniform displacement boundary condition is imposed in-plane on material samples under a plane strain condition. This boundary condition is applied using the finite element analysis (FEA) method. The SVE elasticity tensor $\mathbf{C}$ in Voigt notation relates engineering strain γ to engineering stress σ through:

$$\sigma = \mathbf{C}\gamma, \text{where } \sigma = \begin{bmatrix} \sigma_{11} \\ \sigma_{22} \\ \sigma_{12} \end{bmatrix}, \ \gamma = \begin{bmatrix} \epsilon_{11} \\ \epsilon_{22} \\ 2\epsilon_{12} \end{bmatrix} \tag{4.1}$$

and $\mathbf{C}$ is the positive definite 3x3 stiffness matrix for the 2D plane strain condition.

To determine $\mathbf{C}$, three uniform displacement boundary conditions corresponding to linearly independent engineering strains are applied on the boundary of the SVEs. Similar to [16], we use hydrostatic (H), pure shear (P), and simple shear (S) strain loadings. For each load case, σ is computed using the average stress of the SVE. By relating these three pairs of strains and stress, $\mathbf{C}$ is computed.

From this stiffness matrix, the given elastic properties can be determined. In this paper the in-plane bulk modulus,

$$\kappa = \frac{1}{S_{11} + S_{22} + 2S_{12}} \tag{4.2}$$

is computed using the components of the compliance matrix $\mathbf{S} = \mathbf{C}^{-1}$. Three other elastic properties (elastic modulus E, shear modulus G, and Poisson's ratio ν) are computed from an isotropic form of $\mathbf{C}$.

The global coordinate system (x_1, x_2) for which $\mathbf{C}$ is originally computed is shown in Figure 50. The rotated stiffness matrix $\mathbf{C}(\theta)$ for the coordinate system (x_1', x_2') shown in Figure 50 can be calculated from $\mathbf{C}$ obtained in the global (x_1, x_2) coordinate system using the fourth order tensor relations. The isotropic $\mathbf{C}^{\mathrm{Iso}}$ tensor can be calculated by integrating the stiffness matrix about θ as shown:

$$\mathbf{C}^{\mathrm{Iso}} = \frac{1}{2\pi} \int_0^{2\pi} \mathbf{C}(\theta) d\theta \tag{4.3}$$

The resulting components of $\mathbf{C}^{\mathrm{Iso}}$ are

$$\mathbf{C}_{11}^{\mathrm{Iso}} = \frac{3}{8}(C_{11} + C_{22}) + \frac{1}{4}C_{12} + \frac{C_{33}}{2} \tag{4.4a}$$

$$\mathbf{C}_{12}^{\mathrm{Iso}} = \frac{1}{8}(C_{11} + C_{22}) + \frac{3}{4}C_{12} - \frac{C_{33}}{2} \tag{4.4b}$$

$$\mathbf{C}_{33}^{\mathrm{Iso}} = \frac{1}{8}(C_{11} + C_{22}) - \frac{1}{4}C_{12} + \frac{C_{33}}{2} \tag{4.4c}$$

where

$$\mathbf{C}^{\mathrm{Iso}} = \begin{bmatrix} \mathbf{C}_{11}^{\mathrm{Iso}} & \mathbf{C}_{12}^{\mathrm{Iso}} & 0 \\ \mathbf{C}_{12}^{\mathrm{Iso}} & \mathbf{C}_{11}^{\mathrm{Iso}} & 0 \\ 0 & 0 & \mathbf{C}_{33}^{\mathrm{Iso}} \end{bmatrix} \tag{4.5}$$

Having $\mathbf{C}^{\mathrm{Iso}}$ we can calculate E, G, and ν. G is equal to $\mathbf{C}_{33}^{\mathrm{Iso}}$. Using the plane strain assumption, ν is calculated by Equation (4.6),

$$\nu = \frac{\mathbf{C}_{12}^{\mathrm{Iso}}}{\mathbf{C}_{12}^{\mathrm{Iso}} + \mathbf{C}_{11}^{\mathrm{Iso}}} \tag{4.6}$$

while E is calculated using ν as,

$$\mathrm{E} = \mathbf{C}_{11}^{\mathrm{Iso}} \frac{(1+\nu)(1-2\nu)}{1-\nu} \tag{4.7}$$

If **C** is isotropic, $\mathbf{C}^{\text{Iso}} = \mathbf{C}$ and E and ν can be unambiguously and directly defined from **C**. Otherwise, if the material is slightly anisotropic $\mathbf{C}^{\text{Iso}}$ can be used to derive quasi-isotropic properties E, ν, and G for general **C**. Below the RVE limit, this calculated **C** is an apparent property of the SVE rather than the effective property of the material. If **C** is highly anisotropic, these isotropic properties are values with limited physical meaning. These elastic properties are analyzed in terms of homogeneity and isotropy at different SVE length scales in §4.4.1.

4.3.3 Approximation of Apparent Strength Properties

Definition of angle-dependent strength

The process for computing normal and shear fracture strengths is taken from [16] and is briefly discussed below. Figure 51 shows a sample SVE under uniaxial tensile ($s_n(\theta)$) and shear ($s_t(\theta)$) loading at angle θ right at the inception of failure. The normal loading corresponds to stress component $\bar{\sigma}_{x_2'x_2'} = 1$ while the other stresses equal zero. For shear loading, $\bar{\sigma}_{x_1'x_2'} = 1$ while the remaining stresses equal zero.

The average stress in the global (x_1, x_2) coordinate system for the tensile strength case is $s_n(\theta)u_n$, where

$$u_n = \begin{bmatrix} (1 - cos(2\theta))/2 \\ (1 + cos(2\theta))/2 \\ -sin(2\theta)/2 \end{bmatrix} \tag{4.8}$$

This corresponds to $\bar{\sigma}_{x_2'x_2'} = s_n(\theta)$ and $\bar{\sigma}_{x_1'x_1'} = \bar{\sigma}_{x_1'x_2'} = 0$. By calculating average stress $\bar{\sigma}^{(k)}$ for the three load cases H,P, and S, we can determine factors where the corresponding linear superposition of the average stresses is equal to u_n. The solution corresponding to loading u_n is known at every nodal point. To calculate $s_n(\theta)$, at every point on the inclusion-matrix interface we determine what load factor is needed to reach the fracture threshold σ^{TH} at each point. $s_n(\theta)$ corresponds to the most critical, *i.e.,* the smallest load factor across all interfaces. The process for calculating shear is similar except u_t is used instead of u_n. For additional details, refer to [16].

There are two primary assumptions in calculating failure strength. First, we assume the failure is initiated at the inclusion-matrix interface. This is a good approximation for many two-phase composites as demonstrated in [20]. As will be demonstrated below, this strength corresponds to a macroscopic stress threshold at which debonding initiates at one interfacial point contained within the SVE. This is called failure initiation strength. Our second assumption is that the failure initiation strength is representative of fracture strength. For quasi-brittle materials, this has been shown [68, 114] to be very close to the ultimate (peak) strength. For more general settings, $s_n(\theta)$ calculated in this way corresponds to the deviation from the elastic/linear response.

Definition of angle-independent strength

For many materials such as rock with bedding planes, fracture properties are highly angle-dependent, and such dependency should be preserved through the explicit representation of properties as a function of loading direction. On the other hand, for the two-phase composite considered here, and many other macroscopically isotropic materials, the angle-independent strengths,

$$S_n = \min_\theta(s_n(\theta)) \tag{4.9a}$$

$$S_t = \min_\theta(s_t(\theta)) \tag{4.9b}$$

provide a reasonably accurate representation of the material after averaging. We will subsequently use S_n and S_t in evaluating the homogeneity of the strength field for this material, with the capital S indicating the strength is angle-independent.

4.3.4 Anisotropy Indices

With the definition of both elastic and fracture property fields, the spatial distribution of these properties may be used to determine if each respective field is inhomogeneous. In order to determine whether the field is isotropic; however, additional considerations are needed. Anisotropy measures have been developed to describe the extent of anisotropy within a given material. Many such measures exist for the elasticity tensor [162, 91, 130, 135, 116] as the degree of anisotropy is a key index for describing the directionality of the elastic properties. As an anisotropy measure may be used to investigate the difference in anisotropy between different materials, so too may it be used to describe SVE anisotropy at different length scales and boundary types. For this work, the anisotropy measure developed by [54] is used to describe elastic anisotropy. This anisotropy measure is defined as the maximum and minimum strain energy calculated by rotating the elasticity tensor of the given material element over all possible strain loadings,

$$A^{\text{Gao}} = \max_{\gamma}\left(\frac{\max_{R_\gamma}[\frac{1}{2}(R_\gamma\gamma)^T\mathbf{C}(R_\gamma\gamma)]}{\min_{R_\gamma}[\frac{1}{2}(R_\gamma\gamma)^T\mathbf{C}(R_\gamma\gamma)]}\right) - 1 \tag{4.10}$$

The tensor γ takes the entire space of possible strain loadings and R_γ is the rotation matrix of strain. We refer the reader to [54] for more detail. As the length scale of the VE increases, a material which is truly isotropic would be expected to converge to an A^{Gao} of zero. Materials which are macroscopically anisotropic would reach a homogeneous value at the RVE limit greater than zero.

anisotropy measures for strength are defined as the ratio of the difference between the maximum and minimum apparent normal $s_n(\theta)$ or tangential $s_t(\theta)$ material fracture strength over the span of loading θ (0-180 degrees) for each SVE, as shown in *Equations* (4.11) and (4.12):

$$A^{s_n} = \frac{s_n^{\text{Max}} - s_n^{\text{Min}}}{s_n^{\text{Min}}} \tag{4.11}$$

$$A^{s_t} = \frac{s_t^{\text{Max}} - s_t^{\text{Min}}}{s_t^{\text{Min}}} \tag{4.12}$$

As with the elastic anisotropy measures, for an isotropic material the value of the strength anisotropy measures should tend towards zero as the observation scale increases.

4.3.5 Size Effect Relations and RVE Size

Here we consider a macroscopically homogeneous material with stationary and ergodic properties. For a given apparent field f, an RVE is defined [119] such that the homogenized effective properties only vary within a specific range across different realizations of the RVE [150, 83, 63, 95, 120, 33] either within the same sample at different locations or in the same location across different sample realizations; see also [106, 87, 88, 89] for the statistical models that underline the determination of RVE size in preceding references.

A schematic representation of the dependency of an apparent property f versus the normalized VE size δ in terms of its (nominal) mean $\bar{f}$ and standard deviation D_f is shown in Figure 52. By nominal, we refer to the numerically computed mean or variation from a finite number of realized VEs as opposed to their mathematically converged values in the limit of infinite VEs for the given size. We adopt two different perspectives in examining such convergence to an effective homogeneous (and deterministic) RVE limit for a given apparent property f based on the behavior of $\bar{f}$ and D_f (versus δ). The first perspective, shown in Figure 52a, refers to *variation-based* RVE convergence where the variation (standard deviation D_f or normalized coefficient of variation c_f) of the property f converges as δ increases. This convergence may be independent of the mean value $\bar{f}$, which means that the mean value may be unstable. We will describe this in convergence in more detail in §4.3.5. The second perspective, shown in Figure 52b, refers to *mean-based* RVE convergence where the mean value $\bar{f}$ of the property f converges to a terminal value as δ increases, independent of the property variation D_f. This convergence is shown in §4.3.5. Ultimately, while the mean value may have converged, the variation calculated from the population of SVEs may still be large. The more conservative approach requires both mean-based and variation-based criteria, which is shown in Figure 52c. Both criteria are used in this paper.

Variation-based RVE size

For the variation-based RVE convergence, the examination of RVE condition is only carried out among VEs of the same size. For example, RVE can be chosen as a large enough VE for which the nominal computed mean value (from one or larger number of VE realizations) is equal to the actual mean of the property for that property over all VEs of the same size [83, 95]. This warrants using the computing nominal mean value as the RVE-based homogenized property. Another example is requiring that the variation (or normalized variation by using coefficient of variation) of the homogenized property over the population of VEs of the same size is small enough. This perspective is useful when the VE-homogenized values are used in constructing underlying material property field for f as in [42, 16]. If the variations are small enough the field can be considered homogeneous (and deterministic). Otherwise, it should be modeled as a random field. We will adopt this latter notation as the *variation-based* definition of RVE. While the two definitions convey different interpretations, one can show that the mathematical expressions to determine RVE size are equivalent.

As detailed in [83], the variance of a property f for a 2D volume of edge length L tends to zero as $L \to \infty$ under certain conditions. When f is ergodic and stationary, the standard deviation D_f across the domain for a VE of edge length L can be expressed using the power relation,[1]

$$D_f = \frac{A}{L^\alpha} \tag{4.13}$$

For additive properties such as the inclusion volume ratio or density, the value of the power α, also known as the rate of convergence, has been shown [105, 88] to be equal to 1. Numerical results demonstrate that the same power relation holds for non-additive properties such as bulk modulus [83, 95, 89] and they generally have a smaller convergence rate than the additive properties ($\alpha < 1$).

Herein, the standard deviation D and coefficient of variation c are used as measures of variations of homogenized values across SVEs of the same size. The coefficient of variation is defined as the standard deviation of the field f divided by its mean $\bar{f}$; that is, $c_f = D_f/\bar{f}$. Both D_f and c_f are fit to a power relation in the form of Equation (4.13), with left hand sides of D_f and c_f. If $\bar{f} \neq 0$, the power relations of c_f and D_f have the same convergence rate α. These parameters are used to determine when the corresponding *variation-based* RVE size Δ^{c_f} is reached, based on the reduction of the variation to a tolerance ϵ as δ increases for a given field f. The upper-case Δ will be used throughout to indicate that the size of the volume element has reached the RVE limit. The c superscript in the aforementioned variation-based RVE size formula is updated to either D or c depending on whether the standard deviation or coefficient of variation are used, respectively. These measures are shown in standard deviation form in Equation (4.14a) and coefficient of variation form in

---

[1] In [83] the equation relates variance (D_f^2) to the volume of the VE. By taking the square root of such relation in 2D and relabeling terms we obtain Equation (4.13).

Equation (4.14b),

$$D_f = \left(\frac{\delta_{D_f}}{\delta}\right)^{\alpha_{D_f}} \rightarrow \Delta^{D_f} = \frac{\delta_{D_f}}{\epsilon^{(1/\alpha_{D_f})}} \tag{4.14a}$$

$$c_f = \left(\frac{\delta_{c_f}}{\delta}\right)^{\alpha_{c_f}} \rightarrow \Delta^{c_f} = \frac{\delta_{c_f}}{\epsilon^{(1/\alpha_{c_f})}} \tag{4.14b}$$

where → denotes convergence to the RVE Δ. The rate of convergence α_{D_f} or α_{c_f} is determined by curve fitting the numerical results with power relations. For quantities such as bulk modulus that have a physical dimension, c_f is used to determine convergence to the RVE. For example, for κ the RVE size is defined as,

$$\Delta^{c_\kappa} = \frac{\delta_{c_\kappa}}{\epsilon^{(1/\alpha_{c_\kappa})}} \tag{4.15}$$

Otherwise, for nondimensional properties such as Poisson ratio, the standard deviation is already non-dimensional and appropriate to represent its variation. For such properties, Equation (4.14a) is used to determine the variation-based RVE size.

Mean-based RVE size

Next, we examine how the (nominal mean) of the apparent property f varies versus VE size. In the *mean-based* RVE size, one requires that the (nominal) mean of the effective property changes to only within a narrow tolerance for that VE size and larger ones. That is, it requires the mean value to have converged to its terminal (infinite volume element size) limit (if it exists). For bulk modulus, one can show that such limit exists and that KUBC and SUBC boundary conditions tend to this limit from above and below as δ tends to infinity. In fact, the definition of elastic RVE size by requiring KUBC and SUBC mean elastic (bulk) properties to be within a tolerance [121] is based on having such unique terminal value and can be compared with the aforementioned mean value-based RVE size definition. We discuss the mean value-based RVE size in §4.3.5.

In addition to the variance, this work proposes that the mean of a homogenized field also follows a power relationship, as seen in Figure 52. For any given field f we will examine the relation,

$$\bar{f}(\delta) = \bar{f}_\infty[1 \pm (\frac{\delta_{\bar{f}}}{\delta})^{\alpha_{\bar{f}}}] \tag{4.16}$$

The over-bar is used to indicate the nominal mean value, and ∞ indicates the limiting value of f as the SVE size δ tends to infinity. The plus and minus signs correspond to the cases where the apparent property decreases and increases versus size, respectively, as for example for bulk modulus for KUBC and SUBC, respectively. We also note that the equation is considered for sufficiently large δ, for which deriving apparent properties is justified; that is, the equation does not apply to the limit $\delta \to 0$. The RVE is defined as the size beyond which the homogenized value does not change substantially,

$$\left|\frac{\bar{f} - \bar{f}_\infty}{\bar{f}_\infty}\right| = \epsilon \;\to\; \Delta^{\bar{f}} = \frac{\delta_{\bar{f}}}{\epsilon^{(1/\alpha_{\bar{f}})}} \tag{4.17}$$

where $\to$ denotes convergence to the RVE Δ. For cases where the field is non-dimensional or the terminal value is zero (such as anisotropy measures for isotropic fields), we use the absolute difference $(f - f_\infty)$ rather than the relative difference in seeking a power relation and defining the mean value-based RVE size. When the terminal value is found to be zero, f_∞ is set to zero and only $\delta_{\bar{f}}$ and $\alpha_{\bar{f}}$ are sought; that is, $\bar{f}(\delta) = (\delta_{\bar{f}}/\delta)^{\alpha_{\bar{f}}}$. For example, for A^{Gao} anisotropy index of a macroscopically isotropic material (as in this paper), we use,

$$\bar{A}^{\text{Gao}}(\delta) = (\frac{\delta_{\bar{A}^{\text{Gao}}}}{\delta})^{\alpha_{\bar{A}^{\text{Gao}}}} \qquad \to \qquad \Delta^{\bar{A}^{\text{Gao}}} = \frac{\delta_{\bar{A}^{\text{Gao}}}}{\epsilon^{(1/\alpha_{\bar{A}^{\text{Gao}}})}} \tag{4.18}$$

In short, the variation-based RVE size is useful in determining whether the effective property for a given VE size can be considered homogeneous and deterministic (and at the same time, whether the nominal mean is close to the actual mean of the field). In the mean value-based definition, the concern is more on whether the computed mean value has stabilized and is close enough to its terminal value (if it exists). The question is more on the existence of a unique effective property independent of the VE size beyond a certain size. It is based on this viewpoint that in [63, 113] the existence of RVE-based fracture properties for quasi-brittle materials is challenged. We will use these RVE size definitions to discuss the homogeneity of elastic and fracture properties. Moreover, the same definitions will be applied to anisotropy measures to examine the anisotropy of the SVE-based homogenized fields.

4.3.6 Homogeneous and Isotropic Limits

Using the methodology described in §4.3.5, we seek to determine at what volume element size a material property has reached either a homogeneous or isotropic limit. While the variation-based definition from 4.3.5 guarantees that VEs of corresponding RVE size or larger result in homogeneous fields, there is no guarantee that the mean values are stable, *i.e.,* converged, as larger VEs are considered. If we consider the maximum of variation-based and mean value-based RVE sizes, for VEs larger than this value, the sampled values will not only be homogeneous and deterministic, but also insensitive to the VE size. This motivates the definition of more stringent RVE size limit,

$$\Delta^{f} = \max(\Delta^{\mathrm{c}_f}, \Delta^{\bar{f}}) \tag{4.19}$$

This definition is important in a numerical setting; for example, in finite element analysis we deal with a range of element sizes. If homogeneous elastic fields are to be used in this context, the elements (or characteristic distance between quadrature points) should be larger than Δ^{f} for the bulk modulus, for example.

After consideration of the field homogeneity, next we consider whether the given elastic or fracture property is isotropic or not. For the composite considered, the apparent fields will become isotropic as δ increases. To claim that a given field f has reached its isotropic, we can require that the maximum anisotropy index of all SVEs beyond the corresponding isotropy RVE size are below a certain threshold. Alternatively, we can achieve a similar condition by requiring the variations of anisotropy index to tend to zero and its mean value also be close to its terminal value of zero. That is, definition (4.19) of the anisotropy index of the elastic / fracture field is suitable to determine its isotropic limit for this macroscopic isotropic composite. The summary of homogeneity / isotropy RVE limits for elastic / fracture properties are summarized in Table 6.

The purpose of this analysis is to determine if there is a range of SVE size for which the elastic properties can be considered homogeneous and isotropic, while the fracture properties retain some level of heterogeneity. This range is ideal as maintaining inhomogeneity of the strength field is critical in capturing key aspects of quasi-brittle fracture such as realistic fracture pattern and sample-to-sample variations while ideally circumventing the complex fourth order tensor elasticity random field or even scalar elastic modulus random field. In the next sections, Voronoi and regular SVEs will be compared in terms of the homogeneous and isotropic limits as described in this section. In §4.5, the proper volume element size is determined for the example material.

4.4 Results

4.4.1 Elastic Properties

Angle-independent properties and inhomogeneity

In this section, elastic results for the regular and Voronoi SVE types are evaluated for convergence to the homogeneous RVE limit. Each SVE is loaded as described in §4.3.2. Figure 53 shows the mean, minimum, and maximum values for the respective elastic fields κ, G, E, and ν over the range of SVE sizes. The stiffness ratio of inclusion to matrix is 100:1, and the elastic modulus of the matrix is 1 GPa. The values shown can be viewed as nondimensional properties relative to the elastic modulus of the matrix. We adopt this interpretation in the remainder of this paper.

The regular SVE has a much greater range of values than the Voronoi SVE for smaller SVE sizes, which is representative of a field which is more heterogeneous. As δ increases, the mean value for each field converges to a terminal value $\bar{f}_\infty$, which is represented in Table 7. This value is calculated by fitting the data with a curve using the power law Equation (4.16).

The bulk modulus κ has been shown in [16] to converge to an effective property which is a upper bound result due to the boundary condition applied as established by the hierarchy of bounds in [77] for both regular and Voronoi SVE types. Both types converge to approximately the same effective property as δ increases. The primary difference in mean value at a given length scale comes from the choice of boundary type. Especially at smaller δ, this causes the regular SVEs to be stiffer than the Voronoi SVEs. For the smallest δ regular SVE, κ is 39% larger for regular SVEs than Voronoi SVEs.

This also holds true for the other elastic properties, as shown in Figure 53. Poisson's ratio ν converges from below to a value close to 0.3. This is expected as the Poisson ratio is 0.3 for both the matrix and the inclusion for this specific composite material. Voronoi SVE models exhibit less heterogeneity, and are more stable across the entire size range with lower variation. To verify the applicability of the power law distribution for both the mean-based and variation-based models, the relative convergence to the Δ limit for the mean value and variation are shown in $Figures$ s54 and 55, as defined by reaching the tolerance ϵ. In these figures the horizontal green lines at ordinate -2 corresponds to the chosen $\epsilon = 0.01$ and represent attainment of the corresponding RVE size.

The power law relation in Equation (4.14b) is expressed as a straight line in the log-log plot of Figure 55. Similarly, the power law relation Equation (4.16) is expressed in log-log scale. After subtracting the estimated terminal value, the closer the data points are to the best-fit straight line, the better the power fit is. The same applies for the convergence of measures of variation in Equation (4.14). One method to compare the linear correlation of the best-fit power law model to the data is the Pearson's correlation coefficient, which should be equal to -1 or 1 if the model perfectly fits the decreasing or increasing data, respectively. All fields shown in this section have a coefficient close to -1 (1 for the mean convergence of ν) with a maximum value of -0.995 for the convergence to $\Delta^{\bar{f}}$ and -0.945 for the convergence to Δ^{c_f}, nearly a perfect fit. This demonstrates the applicability of the proposed power law relation Equation (4.16) to SVE-homogenized values.

The Voronoi SVE type converges to the RVE limit much faster than the regular SVE type for the mean-based RVE definition $\Delta^{\bar{f}}$ as shown in Figure 54. Regular SVEs exhibit much more heterogeneity and in fact, none of the four elastic properties converge within the given SVE δ range. The variation-based results converge with a rates close to 1 for Voronoi and 1.5 for regular SVE types. Voronoi SVEs converges to Δ^{c_f} at a smaller size δ than regular SVEs as shown in Figure 55. The variation for regular SVEs are much greater than Voronoi, especially at smaller SVE sizes. For Voronoi SVEs, Poisson ratio is effectively homogeneous even for the smallest SVEs considered.

Table 7 summarizes the convergence results to mean-based $\Delta^{\bar{f}}$ and variation-based Δ^{c_f} RVEs. The final column $\Delta = \max(\Delta^{\bar{f}}, \Delta^{c_f})$ is the more stringent measure for RVE size. The rows for the bulk modulus κ are highlighted and will be described here in more detail. The second column indicates whether the SVE is regular (R) or Voronoi (V). Columns three through five provide the curve fit information for Equation (4.16). As can be seen, both SVE types are converging to approximately the same terminal value $\bar{f}_\infty$ for all elastic properties, within a few thousandths. The rate of convergence $\alpha_{\bar{f}}$ is slightly higher for the Voronoi case, 1.290 compared to 1.056. Columns six and seven provide the same curve fit parameters for Equation (4.14b), with the overall rate α_{c_f} higher for the Regular SVE than Voronoi for this field. However, the Voronoi SVE has lower variance at smaller SVE sizes as represented by the δ_{c_f} value.

Columns eight and nine show the mean-based and variation-based RVE sizes, respectively. In both cases, the Voronoi SVE is much more homogeneous and reaches Δ at much smaller sizes. It is noted, however, that unlike regular SVEs, for Voronoi type, the mean value (in Column 8) converges to its terminal value first, in in fact at very small SVE sizes ($\delta \approx 3$ - 8). This is a major advantage of Voronoi SVEs, in that by the analysis (and computation of the mean value) of a sufficient number of even very small SVEs, the RVE limit effective property can accurately be approximated.

Anisotropy

The anisotropy of the elastic field at different SVE sizes δ is analyzed using the anisotropy measure introduced by [54] and detailed in §4.3.4. Figure 56 shows the mean, minimum, and maximum A^{Gao} for both regular and Voronoi SVE types versus SVE size δ. For both SVE types A^{Gao} tends to zero as δ increases. That is, the domain is isotropic at the macroscale, which is fully expected from having no angular bias in geometric and material property description of the microstructure. The small number of inclusions contained in smaller SVEs result in a more anisotropic elastic response. This explains a higher anisotropy index value for both SVE types as δ decreases.

At smaller SVE sizes, regular SVEs display much higher levels of anisotropy than Voronoi SVEs. Each SVE type converges to zero. The primary difference in the predicted mean values is the choice of SVE boundary. The larger anisotropies for the regular type are caused by excessive stress concentrations generated by the application of displacement boundary condition, and the straight boundaries of an SVE potentially cutting through inclusions. Unlike the naturally higher anisotropy of composites at smaller length scales (as explained above), the additional anisotropy of the regular SVE type is considered a direct nonphysical consequence of SVE boundary and loading type.

The accuracy of power relations for capturing the convergence of the mean and standard deviation of A^{Gao} to zero are investigated in *Figures* 57(a,b). Because the anisotropy measure is non-dimensional, the standard deviation is used rather than the coefficient of variation in definition of the variation-based RVE size; *cf.* Equation (4.14). Table 8 summarizes the convergence data for the power law model fit to the SVE data in Figure 57. The A_{∞}^{Gao} column is not shown, since in all cases A_{∞}^{Gao} takes the value of 0. As in §4.4.1, the power law model fits the A^{Gao} data closely. The Pearson's correlation coefficient is close to -1 for all fields with a maximum value of -0.992 for the mean-based convergence to $\Delta^{\bar{A}^{\text{Gao}}}$ and -0.997 for the variation-based convergence to $\Delta^{D_{A^{\text{Gao}}}}$, again demonstrating the excellent fit of the data to proposed power relations. For the mean-based results, the regular SVE curve has a power greater than 1 (1.131), while the power for Voronoi SVE curve is less than 1 (0.826). For the variation-based results, the regular SVE curve has a power close to 1.5, while the power for the Voronoi SVE curve is approximately 1; both of these values agree with the elastic field data.

Voronoi SVEs reach isotropic limits $\Delta^{\bar{A}^{\text{Gao}}}$ and $\Delta^{D_{A^{\text{Gao}}}}$ at $\delta = 7.65$ and 4.21, from mean- and variation-based criteria. The isotropy limits for regular SVE type are much larger; a domain nearly twice the size of the selected domain would be needed to reach the (zero) mean-based isotropy limit at $\Delta^{\bar{A}^{\text{Gao}}} = 152.0$ and the variation-based isotropic limit is reached at a lower size $\Delta^{D_{A^{\text{Gao}}}} = 45.4$. As discussed in §4.3.6, the maximum of the corresponding RVE sizes $\Delta^{A^{sn}} = \max(\Delta^{\bar{A}^{\text{Gao}}}, \Delta^{D_{A^{\text{Gao}}}})$ are considered for all cases to ensure that the population of SVEs tend toward the isotropic limit. Thus, the elastic fields can be considered isotropic for δ larger than $\Delta^{A^{\text{Gao}}}$ equal to 7.7 and 152.0 for Voronoi and regular SVE types, respectively.

4.4.2 Fracture Properties

Angle-independent properties and inhomogeneity

In this section, fracture strength results for the regular and Voronoi SVE types are compared with respect to convergence to the homogeneous RVE limit. Each SVE is loaded as described in §4.3.3. Figure 58 shows the mean, minimum, and maximum angle-independent strengths S_n and S_t, *cf.* §4.3.3. As the SVE size increases, the mean and variation of fracture strengths decrease, consistent with size effect for fracture strength described by [30]. For this composite, the stress concentrations are influenced by the distance between inclusions. Herein, there is an minimum allowable distance between inclusions. As δ increases, for all SVEs the minimum sampled distance tends to this minimum limit. This explains both the smaller variation of strengths for larger SVEs and the tendency of strength to some terminal value, as seen in Figure 58. This is in contrast to some size effect models, *e.g.,* Weibull and Weibull-Gaussian models [28, 27**?** , 26], that predict the tendency of fracture strength to zero as δ tends to infinity.

The regular SVEs have a greater variation than the Voronoi SVEs for all SVE sizes, which is representative of a field which is more heterogeneous. In addition, the mean is less stable for the regular SVE type and the minimum is lower for all sizes δ and the maximum is higher for the smallest δ sizes. As δ increases, the strength decreases at a higher rate for regular SVEs than Voronoi SVEs. Because the morphology of the inclusions is what reduces strength, for Voronoi we quickly reach SVE sizes that are close to the minimum inclusion distance.

For regular SVEs; however, there are more likely to be high stress concentrations, as the boundaries can intersect inclusion points. This results in SVEs which are outliers from the remaining population for those where small slivers of inclusion overlap. This issue has been found to be prevalent in this analysis. To resolve this issue, during the FEA, each inclusion was approximated by a 50-node polygon. If more than one node was inside the regular region, it was left in the analysis. in other words, if only one node was located within the regular region then the inclusion was rejected.

This metric performed reasonably well at removing any outliers, as only one SVE needed to be rejected from the analysis at the post-processing stage. This SVE had a different issue where the inclusion was very close to the SVE boundary without overlapping, resulting in a sliver of matrix material which the FEA program could not generate a regular, properly formed mesh. The conclusion is that the regular SVE type is prone to problematic edge geometry. This geometry forces the FEA program to generate irregular, badly formed meshes, or causes non-physical stress concentrations where the displacement controlled boundary condition is applied, or both. These non-physical outliers should be rejected to produce a more accurate statistical characterization of the material, which may require a larger population of SVEs to analyze. Regular SVEs may also have higher strengths for smaller SVE sizes, because it is possible to get an SVE which does not contain or barely contains any inclusions. Voronoi cells within the Voronoi SVE are always constructed around one or more inclusions.

The convergence to both $\Delta^{\bar{S}_n}$ and $\Delta^{c_{S_n}}$ for S_n is shown in Figure 59. Because both S_n and S_t follow the same general trends, only S_n is shown. Table 9 provides the curve fit data for S_n and S_t. For the mean value-based convergence to $\Delta^{\bar{S}_n}$, the power law relation in Equation (4.16) is quite accurate, manifested by Pearson coefficients around -0.99 for both regular and Voronoi SVEs. The variation-based results also fits the power relation in Equation (4.14b) accurately with Pearson coefficients around -0.79. As an indication of the highly nonphysical effect of the intersection of SVE edges with inclusions for regular SVEs (discussed above), we observe that the terminal values of strengths are four to five times smaller for regular SVEs compared to Voronoi SVEs for both S_n and S_t.

The rate of convergence for mean value-based curves is approximately 0.7, resulting in about 50 to 200 times larger mean-based RVE sizes for the strengths compared to elastic RVE sizes in Table 8. The variation-based RVEs are even further larger for fracture strengths; this is due to considerably smaller rates of convergence of 0.3 for Voronoi and 0.1 for regular SVEs. These slow convergence rates result in $\Delta^{c_{S_n}} = 9139$ and $\Delta^{c_{S_t}} = 5490$ for Voronoi type and $\Delta^{c_{S_n}} = 10^{17}$ and $\Delta^{c_{S_t}} = 10^{21}$ for regular type. Clearly the use of such variation-based RVE values at the macroscale is highly questionable even for the Voronoi type, given their exceptionally large sizes. The 10 to 20 times larger variation-based versus mean value-based

Voronoi type RVEs for fracture strength is a direct consequence of lower convergence rate of 0.3 versus 0.7 in Table 9.

In contrast, for elastic properties, convergence rates of both mean- and variation-based quantities are around 1 for Voronoi type in Table 7. That is, for this composite elastic properties converge as fast as additive properties to the RVE limit; *cf.* discussion pertained to Equation 4.13. As a result, for elastic fields mean- and variation-based RVEs are very close (related by factors less than 4). The slower convergence rate and larger RVE size of fracture strengths are attributed to the local nature of fracture properties and are consistent with results in [83], where constitutive parameters with more complex underlying physics had larger RVE sizes. In short, for this material fracture strengths cannot be considered homogeneous for any practical VE homogenization size.

Anisotropy

The anisotropy of the fracture strength field at different SVE sizes δ is analyzed using the anisotropy indices in *Equations* (4.11) and (4.12). Again, as the trend is the same for both A^{s_n} and A^{s_t}, only A^{s_n} is shown in the following figure. In general, the regular SVE type has greater anisotropy than the Voronoi type, with the mean values of A^{s_n} being approximately 0.2-0.3 for Voronoi SVEs and over 1.5 for regular SVEs. In comparison, for elastic fields, the anisotropy indices reach 0.03 and 0.002 for regular and Voronoi types, respectively, for the largest VE size in Figure 56. That is, fracture properties are significantly more anisotropic than elastic properties.

The same conclusion can also be drawn by comparing respective convergence rates and RVE sizes for normal strength; the mean-based convergence rate is extremely small, around 0.17 for regular SVEs and 0.1 for Voronoi SVEs. The corresponding variation-based convergence rates are around 0.32 and 0.46 for regular and Voronoi SVEs, respectively. The values combined with other power relation parameters result in $\Delta^{A^{s_n}} = \max(\Delta^{\bar{A}^{s_n}}, \Delta^{D_{A^{s_n}}}) \approx$ 6978 for Voronoi type. For the regular SVE type, $\Delta^{A^{s_n}} \approx 10^{14}$, which essentially means that the apparent strength fields are never isotropic for the regular SVE type. Finally, in addition to exceptionally large isotropic RVE sizes and low convergence rates for strength fields, as shown in Figure 60 the power relations do not fit this data as accurately as the preceding data. This is reflected in the respective Pearson coefficients of -0.7 versus values around ±0.99 for the preceding properties.

From a physical perspective, having isotropy in strength requires that the minimum distance of inclusions for any angle of loading is more or less the same. This property is local and convergence to this state is slow, especially as it implies reaching the state where the realized inclusion distances are almost uniform in all directions. This macroscopically isotropic composite eventually tends to this isotropic limit, but this limit is achieved at exceptionally large RVE sizes compared to elastic fields, given the highly local nature of fracture (initiation) response. This situation is exacerbated by the regular SVE type, as stress concentrations generated from the intersections of inclusions at the boundary of the SVE greatly influence the computed initiation strengths, resulting in higher anisotropy values compared to Voronoi SVEs.

To elaborate on the nature of anisotropy in fracture strength, Figure 61 shows the minimum, maximum, and mean values of $s_n(\theta)$ for all the SVEs of size $\delta = 12.5$, for varied loading angle $\theta \in [0, 180°]$. It is evident that there is no specific angular bias, especially for the mean curve. This implies that while each individual SVE can be highly anisotropic in its apparent fracture strength, their collective behavior is isotropic; for example the angle of the lowest strength, used in the definitions S_n and S_t in Equation (4.9), must follow a uniform distribution. This is opposed to inherent anisotropy of various materials such as rock with bedding plane, wherein fracture strength is highly anisotropic both at the meso (SVE) and macro scales. Our prior work [42] demonstrates that ignoring local inhomogeneity of fracture strength results in highly inaccurate fracture patterns for fragmentation problems. In contrast, as long as local anisotropy of fracture strength does not result in anisotropic bias angles, as in Figure 61, the use of isotropic instead of the actual anisotropic SVE-homogenized fracture strength fields will not affect the accuracy of a macroscopic failure simulation. We plan to examine this simplification in subsequent works.

4.5 Discussion

In this section, the inhomogeneity and anisotropy of elastic and fracture fields are summarized and further elaborated in terms of their use for macroscopic fracture simulations. Figure 62 shows the homogeneity size effect of elastic and fracture fields through angle-independent bulk modulus κ and normal strength S_n, respectively. For anisotropy, A^{Gao} and A^{s_n} are used. The corresponding RVE sizes are summarized in Table 10. As mentioned before. for the regular SVE type, fracture strengths do not reach either homogeneous or isotropic limits.

In the moving window method [**?** 65, 66, 11, 12, 13], a macroscopic domain is traversed with SVEs and an inhomogeneous field is constructed by assigning the value homogenized by each SVE to its entire area or center. In the aforementioned works, an inhomogeneous elastic modulus field is constructed. We denote this by $E(\mathbf{x})$, where dependence on spatial coordinate $\mathbf{x}$ denotes the inhomogeneity of E. As demonstrated in §4.4.1, when δ tends to zero the elastic field can no longer be expressed as an isotropic field and the correct representation of this anisotropic / inhomogeneous elastic field is $\mathbf{C}(\mathbf{x})$. For normal fracture strength, inhomogeneous isotropic and anisotropic fracture strength fields are represented by $S_n(\mathbf{x})$ and $s_n(\mathbf{x}, \theta)$, respectively, where the loading direction θ denotes the anisotropy of s_n. As the SVE size increases, both $\mathbf{C}$ and E reach their homogeneous limit at homogeneous RVE size. Beyond this size, the dependence on $\mathbf{x}$ is dropped.

Figure 63 shows that how the complexity of SVE-homogenized fields changes as the SVE size used for homogenization increases. For regular type, the inhomogeneous/anisotropic elastic field $\mathbf{C}(\mathbf{x})$ first tends to its homogeneous/anisotropic limit $\mathbf{C}$ at $\delta = 33.8$, shortly followed by tending to its homogeneous/isotropic limit E at $\delta = 45.4$. Fracture strengths can be considered inhomogeneous/anisotropic for all practical SVE sizes. For Voronoi type, first, at the very small size of $\delta = 4.2$, the inhomogeneous/anisotropic elastic field becomes inhomogeneous/isotropic $E(\mathbf{x})$. Shortly beyond $\delta = 18.5$, the elastic field can be considered to be homogeneous and isotropic. For fracture strength, the homogeneity and isotropy limits are rather indistinguishable; the inhomogeneous/anisotropic field $s_n(\mathbf{x}, \theta)$ switches to homogenous/isotropic limit S_n at exceptionally large size of $\delta \approx 10000$.

The trends observed above are extremely important when SVE-based homogenized values are used in statistical failure analysis of composites. In this context, the statistics of elastic and/or fracture fields are used to construct statistically consistent random fields that can subsequently be used for the solution of corresponding *statistical partial differential equations* (SPDEs). As mentioned in the introduction, SVE-based homogenization can be viewed as an intermediate stage between RVE-based homogenization and DNS of the microstructure in terms of accuracy and solution efficiency. The smaller δ is, the closer the response of the corresponding SPDEs to DNS in terms of macroscopic fracture pattern and other QoIs such as dissipated energy, and the better is sample-to-sample variation captured.

However, decreasing SVE size has its own disadvantages. The smaller the SVE, the more terms are needed in expansion of the underlying random fields, for example using the Karhunen-Loève (KL) method [84, 96] as in [42]. As observed, when δ decreases elastic and fracture fields also tend to become anisotropic and inhomogeneous, thus further increasing the total number of components of random fields, *e.g.,* 6 for 2D elasticity stiffness $\mathbf{C}$ versus 1 for E. Moreover, as detailed in [99], generating consistent random fields for the fourth order elasticity tensor is extremely challenging. Thus, one wants to avoid using small SVEs that result in $\mathbf{C}(\mathbf{x})$; maintaining only the inhomogeneity of fracture field(s) is even further beneficial because the elastic field may be treated as a homogeneous / isotropic field (E) if large enough SVEs are used for homogenization.

The outcomes of this analysis are quite valuable. It is demonstrated that whether Voronoi or regular SVEs are used, there are large enough SVEs (δ greater than 18.5 and 45.4, respectively) for which the elastic field can be considered homogeneous/isotropic, while the fracture field is still inhomogeneous. As demonstrated in [37, 166, 139, 93, 45, 16**?**], maintaining such inhomogeneity in fracture strength is generally sufficient to capture many aspects of quasi-brittle fracture. This analysis not only shows such assumption is realistic (*e.g.,* if material is homogenized with large enough VEs), but also provides a systematic means to determine preferable δ for homogenization; for example $18.5 < \delta \lesssim 10000$ for Voronoi types; as smaller SVEs are used in this range, the results of corresponding microstructures tend to DNS and the computational cost increases. We defer the sensitivity analysis of macroscopic QoIs and solution cost of a macroscopic simulation to the underlying

SVE size used for homogenization to future works. Finally, the Weibull model is used to construct various forms of inhomogeneous fracture strength fields [45, 148, 5, 90, 4, 2**?**] and assumed forms of random fracture strength fields are used in the solution of SPDEs [78**?**]. SVE-based homogenization can provide a more specific and accurate fracture strength field than the Weibull model and can also provide a more physics-based input random strength field for the solution of SPDEs.

4.6 Conclusions

The important contributions of this paper can be discussed through the effect of SVE size and type on derived apparent properties. For the size effect, as the SVE size increased, the elastic field eventually reached its effective homogeneous and isotropic limit, far before similar limits for fracture fields. That is a welcomed effect as the corresponding inhomogeneous random fracture strength field along with homogeneous (and isotropic) elastic field lends itself to efficient and accurate quasi-brittle fracture analysis; *cf.* §4.5.

For the SVE type effect, Voronoi SVEs are much better than regular SVEs for the following reasons. First, regular SVEs reached the RVE limit at much larger sizes, and for fracture strengths no realistic RVE size was obtained. Even when only RVE-limit material properties are sought, Voronoi VEs can provide them at much lower computational cost. Second, highly nonphysical size effect relations are obtained for fracture strengths when regular SVEs are used. For the regular SVE type the mean fracture strength decreases much more rapidly than Voronoi SVEs; this is reflected in 87% versus only 15% reduction in mean normal strength from its maximum value at the smallest SVE size to its mean terminal value, for regular and Voronoi SVEs respectively. A consequence of this is about 4 to 5 times smaller terminal fracture strengths for regular versus Voronoi SVE type. It is worth noting that, in contrast, for elastic properties both SVE types resulted in almost the same terminal value. Third, apparent properties homogenized by regular SVEs are significantly more anisotropic than those homogenized by Voronoi SVEs, by an average factor of about 50 for elastic and 10 for fracture properties.

All of these problems, especially nonphysical fracture size effect and higher anisotropy of apparent properties of regular SVEs, are deemed to stem from the straight boundaries of a regular SVE cutting through inclusions and producing nonphysical stress concentrations therein. In fact, several regular SVEs were intractable to mesh in FEA due to sliver-like inclusion or matrix features inside an SVE. Otherwise, in this work and other application of regular VEs for deriving apparent material properties, all the aforementioned problems are even further exacerbated. In future work, the authors plan to apply Voronoi type homogenization to more complex composites and further investigate the role of SVE size by using SVE-based apparent properties for macroscale failure analysis as in [42]. Also, the authors plan to investigate what should be done when Voronoi partitioning is impossible or impractical.

Bibliography

[1] Abedi, R., Chung, S.-H., Erickson, J., Fan, Y., Garland, M., Guoy, D., Haber, R., Sullivan, J. M., Thite, S., and Zhou, Y. (2004). Spacetime meshing with adaptive refinement and coarsening. In *Proceedings of the Twentieth Annual Symposium on Computational Geometry*, SCG '04, pages 300–9, Brooklyn, New York, USA. ACM. 31, 61

[2] Abedi, R. and Clarke, P. L. (2019). A computational approach to model dynamic contact and fracture mode transitions in rock. *Computers and Geotechnics*, 109:248–271. 39, 61, 62, 104

[3] Abedi, R., Haber, R., and Elbanna, A. (2017a). Mixed-mode dynamic crack propagation in rocks with contact-separation mode transitions. In *Proceeding: 51th US Rock Mechanics/Geomechanics Symposium*, San Francisco, California, USA. ARMA 17-0679. 13, 34, 39, 40, 47

[4] Abedi, R. and Haber, R. B. (2018). Spacetime simulation of dynamic fracture with crack closure and frictional sliding. *Advanced Modeling and Simulation in Engineering Sciences*, 5(1):22. Equal contribution authorship. 23, 39, 62, 81, 104

[5] Abedi, R., Haber, R. B., and Clarke, P. L. (2017b). Effect of random defects on dynamic fracture in quasi-brittle materials. *International Journal of Fracture*, 208(1-2):241–268. 2, 13, 23, 31, 40, 47, 62, 81, 104

[6] Abedi, R., Haber, R. B., and Petracovici, B. (2006a). A spacetime discontinuous Galerkin method for elastodynamics with element-level balance of linear momentum. *Computer Methods in Applied Mechanics and Engineering*, 195:3247–73. 15, 22, 31, 49, 61

[7] Abedi, R., Haber, R. B., Thite, S., and Erickson, J. (2006b). An h–adaptive spacetime–discontinuous Galerkin method for linearized elastodynamics. *Revue Européenne de Mécanique Numérique (European Journal of Computational Mechanics)*, 15(6):619–42. 15, 22, 62

[8] Abedi, R., Hawker, M. A., Haber, R. B., and Matouš, K. (2009). An adaptive spacetime discontinuous Galerkin method for cohesive models of elastodynamic fracture. *International Journal for Numerical Methods in Engineering*, 1:1–42. 23, 62

[9] Abedi, R., Omidi, O., and Clarke, P. (2016). Numerical simulation of rock dynamic fracturing and failure including microscale material randomness. In *Proceeding: 50th US Rock Mechanics/Geomechanics Symposium*, Houston, Texas, USA. ARMA 16-0531. 47

[10] Abedi, R., Omidi, O., and Enayatpour, S. (2018). A mesh adaptive method for dynamic well stimulation. *Computers and Geotechnics*, 102:12–27. 24, 62

[11] Acton, K. and Graham-Brady, L. (2009a). Fitting an anisotropic yield surface using the generalized method of cells. In *Advances in mathematical modeling and experimental methods for materials and structures*, pages 27–41. Springer. 20, 80, 102

[12] Acton, K. and Graham-Brady, L. (2009b). Meso-scale modeling of plasticity in composites. *Computer Methods in Applied Mechanics and Engineering*, 198(9):920–932. 20, 80, 102

[13] Acton, K. and Graham-Brady, L. (2010). Elastoplastic mesoscale homogenization of composite materials. *Journal of engineering mechanics*, 136(5):613–624. 80, 102

[14] Acton, K., Sherod, C., Bahmani, B., and Abedi, R. (2019). Effect of volume element geometry on convergence to a representative volume. *ASCE-ASME Journal of Risk and Uncertainty in Engineering Systems, Part B: Mechanical Engineering*, 5(3):030907. 6, 19, 82, 83

[15] Acton, K. A., Baxter, S. C., B., B., Clarke, P. L., and Abedi, R. (2018a). Voronoi tessellation based statistical volume element characterization for use in fracture modeling. *Computer Methods in Applied Mechanics and Engineering*, 336:135–155. 6

[16] Acton, K. A., Baxter, S. C., Bahmani, B., Clarke, P. L., and Abedi, R. (2018b). Voronoi tessellation based statistical volume element characterization for use in fracture modeling. *Computer Methods in Applied Mechanics and Engineering*, 336:135–155. 20, 70, 71, 81, 82, 83, 84, 86, 90, 94, 103

[17] Al-Ostaz, A. and Jasiuk, I. (1997). Crack initiation and propagation in materials with randomly distributed holes. *Engineering Fracture Mechanics*, 58:395 – 420. 2, 13, 46, 81

[18] Anderson, T. L. (2017). *Fracture mechanics: fundamentals and applications*. CRC press, New York, USA. 55

[19] Ashby, M. and Hallam, S. (1986). The failure of brittle solids containing small cracks under compressive stress states. *Acta Metall.*, 34(3):497–510. 15, 21, 58

[20] Bahmani, B., Yang, M., Nagarajan, A., Clarke, P. L., Soghrati, S., and Abedi, R. (2019). Automated homogenization-based fracture analysis: Effects of SVE size and boundary condition. *Computer Methods in Applied Mechanics and Engineering*, 345:701–727. 70, 87

[21] Barenblatt, G. I. (1962). The mathematical theory of equilibrium of cracks in brittle fracture. *Advanced Applied Mechanics*, 7:55–129. 23

[22] Baxter, S. and Graham, L. (2000). Characterization of random composites using moving-window technique. *Journal of Engineering Mechanics*, 126(4):389–397. 14, 20, 48, 80

[23] Bazant, Z. (1984). Size effect in blunt fracture: Concrete, rock, metal. *Journal of Engineering Mechanics*, 110:518 – 535. 2

[24] Bazant, Z. (1999). Size effect on structural strength: a review. *Archive of Applied Mechanics*, 69:703 – 725. 2, 3

[25] Bazant, Z. (2005). Role of deterministic and statistical length scales in size effect for quasibrittle failure at crack initiation. In *Proceedings of the 9th International Conference on Structural Safety and Reliability*, pages 411–415. 3

[26] Bazant, Z. and Le, J. (2012). Size effect on strength and lifetime probability distributions of quasibrittle structures. *Sadhana*, 37(1):17–31. 98

[27] Bazant, Z. and Novak, D. (2000). Probabilistic nonlocal theory for quasibrittle fracture initiation and size effect- I: Theory. *Journal of Engineering Mechanics*, 126(2):166–174. 98

[28] Bazant, Z. and Planas, J. (1998). *Fracture and Size Effect in Concrete and Other Quasibrittle Materials*. CRC Press, Boca Raton, FL. 3, 98

[29] Bazant, Z. P. and Le, J.-L. (2017). *Probabilistic Mechanics of Quasibrittle Structures: Strength, Lifetime, and Size Effect*. Cambridge University Press. 12, 13, 46, 64

[30] Bazant, Z. P. and Planas, J. (1997). *Fracture and size effect in concrete and other quasibrittle materials*, volume 16. CRC press. 13, 46, 64, 98

[31] Biner, S. and Hu, S. (2009). Simulation of damage evolution in composites: a phase-field model. *Acta Materialia*, 57(7):2088–2097. 5, 80

[32] Bouchard, P.-O., Bay, F., and Chastel, Y. (2003). Numerical modelling of crack propagation: automatic remeshing and comparison of different criteria. *Computer methods in applied mechanics and engineering*, 192(35-36):3887–3908. 23

[33] C. Pelissou, J. Baccou, Y. M. and Perales, F. (2009). Determination of the size of the representative volume element for random quasi-brittle composites. *International Journal of Solids and Structures*, 46:2842–2855. 5, 80, 89

[34] CA, D., I, B., and TJ, O. (2000). Generalized finite element methods for three-dimensional structural mechanics. *Computers and Structures*, 77(2):215–232. 23, 62

[35] Cailletaud, G., Jeulin, D., and Rolland, P. (1994). Size effect on elastic properties of random composites. *Engineering computations*, 11(2):99–110. 14

[36] Camacho, G. T. and Ortiz, M. (1996). Computational modelling of impact damage in brittle materials. *International Journal of Solids and Structures*, 33:2899–2938. 61

[37] Carmeliet, J. and Hens, H. (1994). Probabilistic nonlocal damage model for continua with random field properties. *Journal of Engineering Mechanics*, 120(10):2013–2027. 20, 82, 103

[38] Chiu, S. N., Stoyan, D., Kendall, W. S., and Mecke, J. (2013). *Stochastic geometry and its applications*. John Wiley. 83

[39] Chung, D. and Buessem, W. (1967). The elastic anisotropy of crystals. *Journal of Applied Physics*, 38(5):2010–2012. 82

[40] Clarke, P. (2018). *A statistical approach for fracture property realization and macroscopic failure analysis of brittle materials*. PhD thesis, University of Tennessee. 11

[41] Clarke, P. and Abedi, R. (2017). Fracture modeling of rocks based on random field generation and simulation of inhomogeneous domains. In *Proceeding: 51th US Rock Mechanics/Geomechanics Symposium*, San Francisco, California, USA. ARMA 17-0643. 48

[42] Clarke, P., Abedi, R., Bahmani, B., Acton, K., and Baxter, S. (2017). Effect of the spatial inhomogeneity of fracture strength on fracture pattern for quasi-brittle materials. In *Proceedings of ASME 2017 International Mechanical Engineering Congress & Exposition IMECE 2017*, page V009T12A045 (9 pages). 14, 15, 42, 81, 90, 101, 103, 105

[43] Clarke, P. L. and Abedi, R. (2018). Modeling the connectivity and intersection of hydraulically loaded cracks with in-situ fractures in rock. *International journal for numerical and analytical methods in geomechanics*, 42(14):1592–1623. 2, 13

[44] Danielsson, M., Parks, D. M., and Boyce, M. C. (2007). Micromechanics, macromechanics and constitutive modeling of the elasto-viscoplastic deformation of rubber-toughened glassy polymers. *Journal of the Mechanics and Physics of Solids*, 55(3):533–561. 6, 82

[45] Daphalapurkar, N., Ramesh, K., Graham-Brady, L., and Molinari, J. (2011). Predicting variability in the dynamic failure strength of brittle materials considering pre-existing flaws. *Journal of the Mechanics and Physics of Solids*, 59(2):297–319. 20, 31, 43, 81, 82, 103, 104

[46] Dimas, L., Giesa, T., and Buehler, M. (2014). Coupled continuum and discrete analysis of random heterogeneous materials: Elasticity and fracture. *Journal of the Mechanics and Physics of Solids*, 63(1):481–490. 81

[47] Dolbow, J., Moës, N., and Belytschko, T. (2000). Discontinuous enrichment in finite elements with a partition of unity method. *Finite elements in analysis and design*, 36(3-4):235–260. 23

[48] Doltsinis, I. and Dattke, R. (2005). Numerical experiments on the rupture of brittle solids - variation of microstructure, loading and dimensions. *International Journal of Solids and Structures*, 42(2):565–579. 5, 13, 80

[49] Dowd, P., Xu, C., Mardia, K., and Fowell, R. (2007). A comparison of methods for the stochastic simulation of rock fractures. *Mathematical Geology*, 39(7):697–714. 50

[50] Drugan, W. and Willis, J. (1996). A micromechanics-based nonlocal constitutive equation and estimates of representative volume element size for elastic composites. *Journal of the Mechanics and Physics of Solids*, 44(4):497–524. 4, 5

[51] Dubey, V., Abedi, S., and Noshadravan, A. (2018). Multiscale modelling of microcrack-induced mechanical properties in shales. In *52nd US Rock Mechanics/Geomechanics Symposium*. American Rock Mechanics Association. 43

[52] Dugdale, D. S. (1960). Yielding of steel sheets containing slits. *Journal of the Mechanics and Physics of Solids*, 8:100–104. 23

[53] Erdogan, F. and Sih, G. (1963). On the crack extension in plates under plane loading and transverse shear. *Journal of basic engineering*, 85(4):519–525. 34, 53, 55

[54] Fang, Y., Wang, Y., Imtiaz, H., Liu, B., and Gao, H. (2019). Energy-ratio-based measure of elastic anisotropy. *Physical review letters*, 122(4):045502. 82, 88, 96

[55] Fascetti, A., Bolander, J. E., and Nisticó, N. (2018). Lattice discrete particle modeling of concrete under compressive loading: Multiscale experimental approach for parameter determination. *Journal of Engineering Mechanics*, 144(8):04018058. 3, 13, 47

[56] Firooz, S., Saeb, S., Chatzigeorgiou, G., Meraghni, F., Steinmann, P., and Javili, A. (2020). A systematic study on homogenization and the utility of circular simplified rve. *Mathematics and Mechanics of Solids*, 117. 6

[57] Garrard, J. and Abedi, R. (2019). Statistical volume elements for the characterization of angle-dependent fracture strengths in anisotropic microcracked materials. *ASCE-ASME Journal of Risk and Uncertainty in Engineering Systems, Part B: Mechanical Engineering*. 6, 80, 81

[58] Garrard, J. and Abedi, R. (2020a). Statistical volume element averaging scheme for fracture of quasi-brittle materials. *Computers and Geotechnics*, 117. 45, 79

[59] Garrard, J. M. and Abedi, R. (2020b). Statistical volume element averaging scheme for fracture of quasi-brittle materials. *Computers and Geotechnics*, 117:103229. 52, 80, 81

[60] Garrard, J. M., Abedi, R., and Clarke, P. L. (2018a). Modeling of rock inhomogeneity and anisotropy by explicit and implicit representation of microcracks. In *Proceeding: 52nd US Rock Mechanics/Geomechanics Symposium*, Seattle, Washington, USA. ARMA 18-151-0228-1094 (10 pages). 15, 19, 48, 64

[61] Garrard, J. M., Abedi, R., and Clarke, P. L. (2018b). Statistical volume elements for the characterization of angle-dependent fracture strengths. In *ASME 2018 International Mechanical Engineering Congress and Exposition*, pages V009T12A045–V009T12A045. American Society of Mechanical Engineers. 15, 19, 48

[62] Genet, M., Couegnat, G., Tomsia, A., and Ritchie, R. (2014). Scaling strength distributions in quasi-brittle materials from micro- to macro-scales: A computational approach to modeling nature-inspired structural ceramics. *Journal of the Mechanics and Physics of Solids*, 68(1):93–106. 12, 13, 46, 81

[63] Gitman, I., Askes, H., and Sluys, L. (2007). Representative volume: existence and size determination. *Engineering fracture mechanics*, 74(16):2518–34. 4, 5, 80, 89, 92

[64] Gitman, I., Gitman, M., and Askes, H. (2006). Quantification of stochastically stable representative volumes for random heterogeneous materials. *Archive of Applied Mechanics*, 75:79–92. 5

[65] Graham, L. and Baxter, S. (2001). Simulation of local material properties based on moving-window GMC. *Probabilistic Engineering Mechanics*, 16(4):295–305. 80, 102

[66] Graham, S. and Yang, N. (2003). Representative volumes of materials based on microstructure statistics. *Scripta Mater*, 48:269–274. 5, 80, 102

[67] Graham-Brady, L. (2010). Statistical characterization of meso-scale uniaxial compressive strength in brittle materials with randomly occurring flaws. *International Journal of Solids and Structures*, 47(18-19):2398–2413. 43

[68] Graham-Brady, L. and Liu, J. (2013). Upscaling crack propagation and coalescence through a stochastic damage micromechanics model. pages 191 – 193, New York, NY, United states. Computationally efficient;Constitutive relationships;Elasto-plastic properties;Finite-element approach;Microstructural descriptors;Multi-scale mechanics;Probabilistic approaches;Simplifying assumptions;. 87

[69] Hashin, Z. (1983). Analysis of composite materials - a survey. *Journal of Applied Mechanics*, 50:481–505. 4, 80

[70] Hassold, G. and Srolovitz, D. (1989). Brittle fracture in materials with random defects. *Physical Review B (Condensed Matter)*, 39(13):9273–9281. 13

[71] Hazanov, S. and Amieur, M. (1995). On overall properties of elastic heterogeneous bodies smaller than the representative volume. *International Journal of Engineering Science*, 33(9):1289–1301. 6, 81

[72] Hazanov, S. and Huet, C. (1994). Order relationships for boundary conditions effect in heterogeneous bodies smaller than the representative volume. *Journal of the Mechanics and Physics of Solids*, 42(12):1995–2011. 6, 81

[73] Hill, R. (1963). Elastic properties of reinforced solids: some theoretical principles. *Journal of the Mechanics and Physics of Solids*, 11(5):357–372. 4, 5, 80

[74] Hill, R. (1972). On constitutive macro-variables for heterogeneous solids at finite strain. *Proceedings of the Royal Society A: Mathematical, Physical, and Engineering SCiences*, 326:131–147. 80

[75] Hoek, E. and Brown, E. T. (1980). *Underground excavations in rock*. CRC Press. 39, 49

[76] Homand-Etienne, F., Hoxha, D., and Shao, J. (1998). A continuum damage constitutive law for brittle rocks. *Computers and Geotechnics*, 22(2):135–151. 14, 47

[77] Huet, C. (1990). Application of variational concepts to size effects in elastic heterogeneous bodies. *Journal of the Mechanics and Physics of Solids*, 38(6):813–841. 5, 6, 81, 83, 84, 94

[78] Hun, D.-A., Guilleminot, J., Yvonnet, J., and Bornert, M. (2019). Stochastic multi-scale modeling of crack propagation in random heterogeneous media. *International Journal for Numerical Methods in Engineering*. 42, 104

[79] Hussain, M., Pu, S., and Underwood, J. (1974). Strain energy release rate for a crack under combined mode I and mode II. In *Fracture analysis: Proceedings of the 1973 national symposium on fracture mechanics, part II*. ASTM International. 55

[80] Huyse, L. and Maes, M. (2001). Random field modeling of elastic properties using homogenization. *Journal of Engineering Mechanics*, 127(1):27–36. 14, 48, 80

[81] Jiang, M., Alzebdeh, K., Jasiuk, I., and Ostoja-Starzewski, M. (2001). Scale and boundary conditions effects in elastic properties of random composites. *Acta Mechanica*, 148(1-4):63–78. 6

[82] Jing, L. and Stephansson, O. (2007). *Fundamentals of discrete element methods for rock engineering: theory and applications*, volume 85. Elsevier. 3, 13

[83] Kanit, T., Forest, S., Galliet, I., Mounoury, V., and Jeulin, D. (2003). Determination of the size of the representative volume element for random composites: statistical and numerical approach. *International Journal of solids and structures*, 40(13):3647–79. 4, 14, 48, 61, 80, 83, 89, 90, 100

[84] Karhunen, K. and Selin, I. (1960). *On linear methods in probability theory.* Rand Corporation. 72, 103

[85] Khisaeva, Z. and Ostoja-Starjewski, M. (2006). On the size of rve in finite elasticity of random composites. *Journal of Elasticity*, 85:153–173. 5, 80, 81

[86] Kozicki, J. and Tejchman, J. (2007). Effect of aggregate structure on fracture process in concrete using 2D lattice model. *Archives of Mechanics*, 59(4-5):365–84. 13, 46, 81

[87] Lantuejoul, C. (1991). Ergodicity and integral range. *Journal of Microscopy*, 161(3):387–403. 48, 89

[88] Lantuejoul, C. (2002). *Geostatistical Simulation: Models and Algorithms.* 89, 90

[89] Lantuéjoul, C. (2013). *Geostatistical simulation: models and algorithms.* Springer Science & Business Media, Berlin. 89, 90

[90] Le, J.-L. and Eliáš, J. (2016). A probabilistic crack band model for quasibrittle fracture. *Journal of Applied Mechanics*, 83(5):051005. 81, 104

[91] Ledbetter, H. and Migliori, A. (2006). A general elastic-anisotropy measure. *Journal of Applied Physics*, 100(6):063516. 82, 87

[92] Lee, Y.-K. and Pietruszczak, S. (2008). Application of critical plane approach to the prediction of strength anisotropy in transversely isotropic rock masses. *International Journal of Rock Mechanics and Mining Sciences*, 45(4):513–23. 49

[93] Levy, S. and Molinari, J. (2010). Dynamic fragmentation of ceramics, signature of defects and scaling of fragment sizes. *Journal of the Mechanics and Physics of Solids*, 58(1):12–26. 20, 82, 103

[94] Li, J. (2000). Debonding of the interface as 'crack arrestor'. *International Journal of Fracture*, 105(1):57–79. 47

[95] Liu, W. K., Siad, L., Tian, R., Lee, S., Lee, D., Yin, X., Chen, W., Chan, S., Olson, G. B., and Lindgen, L.-E. (2009). Complexity science of multiscale materials via stochastic computations. *International Journal for Numerical Methods in Engineering*, 80(6-7):932–978. 14, 48, 61, 89, 90

[96] Loéve, M. (1977). *Probability theory*. Springer, New York. 72, 103

[97] Lu, Y., Elsworth, D., and Wang, L. (2013). Microcrack-based coupled damage and flow modeling of fracturing evolution in permeable brittle rocks. *Computers and Geotechnics*, 49:226–44. 14, 47

[98] Malyarenko, A. and Ostoja-Starzewski, M. (2019). Towards stochastic continuum damage mechanics. *International Journal of Solids and Structures*. 76

[99] Malyarenko, A. and Ostoja-Starzewski, M. (2020). Tensor random fields in continuum mechanics. *Encyclopedia of Continuum Mechanics*, pages 2433–2441. 82, 103

[100] Mandel, J. (1966). Contribution theorique aletude de l'ecrouissage et des lois de l'ecoulement plastique. *Applied Mechanics*, pages 502–509. 80

[101] Manzato, C., Alava, M., and Zapperi, S. (2014). Damage accumulation in quasibrittle fracture. *Physical Review E-Statistical, Nonlinear, and Soft Matter Physics*, 90(1). 13

[102] Marteau, E. and Andrade, J. E. (2018). A model for decoding the life cycle of granular avalanches in a rotating drum. *Acta Geotechnica*, 13(3):549–555. 13

[103] Mashhadian, M., Abedi, S., and Noshadravan, A. (2018). A probabilistic multiscale approach for modeling poromechanical properties of shales. In *52nd US Rock Mechanics/Geomechanics Symposium*. American Rock Mechanics Association. 42

[104] Matheron, G. (1971a). *The Theory of Regionalized Variables and its Applications*. CRC Paris School of Mines publications. 61

[105] Matheron, G. (1971b). The theory of regionalized variables and its applications, vol. 5. *Paris: École National Supérieure des Mines*, 211. 14, 90

[106] Matheron, G. (1989). *Estimating and Choosing. An Essay on Probability on Practice.* Springer, Berlin. 48, 89

[107] Matouš, K., Geers, M. G., Kouznetsova, V. G., and Gillman, A. (2017). A review of predictive nonlinear theories for multiscale modeling of heterogeneous materials. *Journal of Computational Physics*, 330:192–220. 13

[108] Molinari, J.-F., Gazonas, G., Raghupathy, R., Rusinek, A., and Zhou, F. (2007). The cohesive element approach to dynamic fragmentation: the question of energy convergence. *International Journal for Numerical Methods in Engineering*, 69(3):484–503. 81

[109] Munjiza, A. (2004). *The combined finite-discrete element method*, volume 32. Wiley Online Library. 3, 13

[110] N, M., J, D., and T, B. (1999). A finite element method for crack growth without remeshing. *International Journal for Numerical Methods in Engineering*, 46(1):131–150. 23

[111] Nemat-Nasser, S. and Hori, M. (1993). *Micromechanics : overall properties of heterogeneous materials*. Elsevier, Amsterdam ; New York. 34, 73

[112] Neuman, S. P., Riva, M., and Guadagnini, A. (2008). On the geostatistical characterization of hierarchical media. *Water Resources Research*, 44(2). 61

[113] Nguyen, V. P., Lloberas Valls, O., Stroeven, M., and Sluys, L. (2010). On the existence of representative volumes for softening quasi-brittle materials - a failure zone averaging scheme. *Computer Methods in Applied Mechanics and Engineering*, 199(45-48):3028–38. 92

[114] Nguyen, V. P., Lloberas-Valls, O., Stroeven, M., and Sluys, L. J. (2011a). Homogenization-based multiscale crack modelling: From micro-diffusive damage to macro-cracks. *Computer Methods in Applied Mechanics and Engineering*, 200(9):1220–36. 87

[115] Nguyen, V. P., Stroeven, M., and Sluys, L. J. (2011b). Multiscale continuous and discontinuous modeling of heterogeneous materials: a review on recent developments. *Journal of Multiscale Modelling*, 3(04):229–270. 14, 47

[116] Nye, J. (1985). *Physical properties of crystals: their representation by tensors and matrices*. Oxford university press. 82, 87

[117] Ogden, R. (1974). On the overall moduli of non-linear elastic composite materials. *Journal of the Mechanics and Physics of Solids*, 22:541–555. 80

[118] Ostoja-Starzewski, M. (1998). Random field models of heterogeneous materials. *International Journal of Solids and Structures*, 35(19):2429–2455. 4, 5, 80

[119] Ostoja-Starzewski, M. (2002). Microstructural randomness versus representative volume element in thermomechanics. *Journal of Applied Mechanics-Transactions of the ASME*, 69(1):25–35. 14, 48, 61, 80, 81, 88

[120] Ostoja-Starzewski, M. (2006). Material spatial randomness: From statistical to representative volume element. *Probabilistic Engineering Mechanics*, 21(2):112 – 132. 14, 48, 80, 81, 83, 89

[121] Ostoja-Starzewski, M., Du, X., Khisaeva, Z., and Li, W. (2007). Comparisons of the size of the representative volume element in elastic, plastic, thermoelastic, and permeable random microstructures. *International Journal for Multiscale Computational Engineering*, 5(2). 80, 81, 91

[122] Park, K. S., Paulino, G. H., Celes, W., and Espinha, R. (2012). Adaptive mesh refinement and coarsening for cohesive zone modeling of dynamic fracture. *International Journal for Numerical Methods in Engineering*, 92(1):1–35. 23

[123] Paulino, G. H., Park, K., Celes, W., and Espinha, R. (2010). Adaptive dynamic cohesive fracture simulation using nodal perturbation and edge-swap operators. *International Journal for Numerical Methods in Engineering*, 84(11):1303–1343. 23

[124] Pietruszczak, S., Lydzba, D., and Shao, J. (2002). Modelling of inherent anisotropy in sedimentary rocks. *International Journal of Solids and Structures*, 39(3):637–648. 42, 48

[125] Pietruszczak, S. and Mroz, Z. (2000). Formulation of anisotropic failure criteria incorporating a microstructure tensor. *Computers and Geotechnics*, 26(2):105–112. 42, 48

[126] Pietruszczak, S. and Mroz, Z. (2001). On failure criteria for anisotropic cohesive-frictional materials. *International Journal for Numerical and Analytical Methods in Geomechanics*, 25(5):509–524. 49

[127] Pourahmadian, F., Guzina, B., et al. (2016). Active ultrasonic imaging and interfacial characterization of stationary and evolving fractures in rock. In *50th US Rock Mechanics/Geomechanics Symposium*. American Rock Mechanics Association. 42

[128] Pourahmadian, F. and Guzina, B. B. (2018). On the elastic anatomy of heterogeneous fractures in rock. *International Journal of Rock Mechanics and Mining Sciences*, 106:259–268. 42

[129] Ranganathan, S., Murshed, M., and Costa, L. (2018). Heterogeneous anisotropy index and scaling in two-phase random polycrystals. *Acta Mechanica*, 229(6):2631–2646. 82

[130] Ranganathan, S. and Ostoja-Starzewski, M. (2008). Universal elastic anisotropy index. *Physical Review Letters*, 101(5):055504. 82, 87

[131] Rangarajan, R. and Lew, A. J. (2014). Universal meshes: A method for triangulating planar curved domains immersed in nonconforming meshes. *International Journal for Numerical Methods in Engineering*, 98(4):236–264. 23

[132] Ren, X., Chen, J.-S., Li, J., Slawson, T., and Roth, M. (2011). Micro-cracks informed damage models for brittle solids. *International journal of solids and structures*, 48(10):1560–1571. 35, 43

[133] Renshaw, C. E. (1999). Connectivity of joint networks with power law length distributions. *Water Resources Research*, 35(9):2661–2670. 51

[134] Rinaldi, A., Krajcinovic, D., and Mastilovic, S. (2007). Statistical damage mechanics and extreme value theory. *International Journal of Damage Mechanics*, 16(1):57–76. 12, 46

[135] Rychlewski, J. and Zhang, J. (1989). Anisotropy degree of elastic materials. *Archives of Mechanics*, 41(5):697–715. 82, 87

[136] Sab, K. (1992). On the homogenization and the simulation of random materials. *European Journal of Mechanics A - Solids*, 11:585–607. 4, 80

[137] Sab, K. and Nedjar, B. (2005). Periodization of random media and representative volume element size for linear composites. *C.R. Mecanique*, 333:187–195. 5

[138] Salmi, M., Auslender, F., Bornert, M., and Fogli, M. (2012). Apparent and effective mechanical properties of linear matrix-inclusion random composites: Improved bounds for the effective behavior. *International Journal of Solids and Structures*, 49(10):1195–1211. 6, 82, 83

[139] Schicker, J. and Pfuff, M. (2006). Statistical modelling of fracture in quasi-brittle materials. *Advanced Engineering Materials*, 8(5):406–410. 20, 82, 103

[140] Schlangen, E. and Garboczi, E. (1997). Fracture simulations of concrete using lattice models: computational aspects. *Engineering Fracture Mechanics*, 57(2-3):319–332. 13

[141] Segurado, J. and LLorca, J. (2006). Computational micromechanics of composites: The effect of particle spatial distribution. *Mechanics of Materials*, 38(8-10):873–883. 14, 48, 80

[142] Shan, Z. and Gokhale, A. (2002). Representative volume element for non-uniform microstructure. *Computational Material Science*, 24:361–379. 5

[143] Shao, J. and Rudnicki, J. (2000). A microcrack-based continuous damage model for brittle geomaterials. *Mechanics of Materials*, 32(10):607–619. 14, 47

[144] Sharpe, J., Labuz, J., et al. (2017). Failure of rock under tensile-compressive loading. In *51st US Rock Mechanics/Geomechanics Symposium*. American Rock Mechanics Association. 39

[145] Shi, X., Yang, X., Meng, Y., and Li, G. (2016). An anisotropic strength model for layered rocks considering planes of weakness. *Rock Mechanics and Rock Engineering*, 49(9):3783–92. 49

[146] Silling, S. A. and Askari, E. (2005). A meshfree method based on the peridynamic model of solid mechanics. *Computers & structures*, 83(17-18):1526–1535. 3, 13

[147] Staber, B. and Guilleminot, J. (2017). Stochastic modeling and generation of random fields of elasticity tensors: A unified information-theoretic approach. *Comptes Rendus Mécanique*, 345(6):399–416. 76

[148] Strack, O. E., Leavy, R., and Brannon, R. M. (2015). Aleatory uncertainty and scale effects in computational damage models for failure and fragmentation. *International Journal for Numerical Methods in Engineering*, 102(3-4):468–495. 81, 104

[149] Strouboulis, T., Babuška, I., and Copps, K. (2000). The design and analysis of the generalized finite element method. *Computer Methods in Applied Mechanics and Engineering*, 181:43–69. 23, 62

[150] Suquet, P. (1997). Continuum micromechanics. *CISM Courses and Lectures*, 272. 14, 48, 89

[151] T, B. and T, B. (1999). Elastic crack growth in finite elements with minimal remeshing. *International Journal for Numerical Methods in Engineering*, 45(5):601–620. 23, 62

[152] Taylor, L. M., Chen, E.-P., and Kuszmaul, J. S. (1986). Microcrack-induced damage accumulation in brittle rock under dynamic loading. *Computer Methods in Applied Mechanics and Engineering*, 55(3):301 – 320. 14, 47

[153] Tomar, V. and Zhou, M. (2005). Deterministic and stochastic analyses of fracture processes in a brittle microstructure system. *Engineering Fracture Mechanics*, 72(12):1920–1941. 5, 80

[154] Tregger, N., Corr, D., Graham-Brady, L., and Shah, S. (2006). Modeling the effect of mesoscale randomness on concrete fracture. *Probabilistic Engineering Mechanics*, 21(3):217–225. 14, 48, 80

[155] Wang, L.-F. and Zheng, Q.-S. (2007). Extreme anisotropy of graphite and single-walled carbon nanotube bundles. *Applied physics letters*, 90(15):153113. 82

[156] Weibull, W. (1939). A statistical theory of the strength of materials. *R. Swed. Inst. Eng. Res.*, page Res. 151. 2, 13, 47, 81

[157] Weibull, W. (1951). A statistical distribution function of wide applicability. *Journal of Applied Mechanics*, 18:293–297. 13, 47, 81

[158] Wong, R. H., Chau, K., and Wang, P. (1996). Microcracking and grain size effect in yuen long marbles. *Int. J. Rock Mech. Min. Sci. & Geomech. Abstr.*, 33(5):479–485. 15, 20, 22

[159] Wong, T.-F., Wong, R. H., Chau, K., and Tang, C. (2006). Microcrack statistics, weibull distribution and micromechanical modeling of compressive failure in rock. *Mechanics of Materials*, 38:664–681. x, 11, 15, 16, 17, 18, 20, 21, 25, 28, 31, 33, 34, 40, 41, 42, 45, 48, 49, 51, 52, 58, 61, 63, 72, 73, 75, 177

[160] Yang, M., Garrard, J., Abedi, R., and Soghrati, S. (2021). Effect of microstructural variations on the failure response of a nano-enhanced polymer: a homogenization-based statistical analysis. *Computational Mechanics*, 67(1):315–340. 80

[161] Yin, X., Chen, W., To, A., McVeigh, C., and Liu, W. (2008). Statistical volume element method for predicting microstructure-constitutive property relations. *Computer Methods in Applied Mechanics and Engineering*, 197(43-44):3516–3529. 12, 13, 46

[162] Zener, C. (1948). *Elasticity and anelasticity of metals.* University of Chicago press. 82, 87

[163] Zhao, L., Zhu, Q., and Shao, J. (2018a). Analysis of localized cracking in quasi-brittle materials with a micro-mechanics based friction-damage approach. *Journal of the Mechanics and Physics of Solids*, 119:163 – 187. 43

[164] Zhao, L., Zhu, Q., and Shao, J. (2018b). A micro-mechanics based plastic damage model for quasi-brittle materials under a large range of compressive stress. *International Journal of Plasticity*, 100:156 – 176. 43

[165] Zhao, L., Zhu, Q., Xu, W., Dai, F., and Shao, J. (2016). A unified micro-mechanics-based damage model for instantaneous and time-dependent behaviors of brittle rocks. *International Journal of Rock Mechanics and Mining Sciences*, 84:187 – 196. 43

[166] Zhou, F. and Molinari, J. (2004). Stochastic fracture of ceramics under dynamic tensile loading. *International Journal of Solids and Structures*, 41(22-23):6573–6596. 20, 82, 103

[167] Zhuang, X., Augarde, C., and Mathisen, K. (2012). Fracture modeling using meshless methods and level sets in 3d: framework and modeling. *International Journal for Numerical Methods in Engineering*, 92(11):969–998. 24

[168] Zohdi, T. and Wriggers, P. (2005). Introduction to computational micromechanics, volume 20 of lecture notes in applied and computational mechanics. 6, 81

Appendices

A Figures

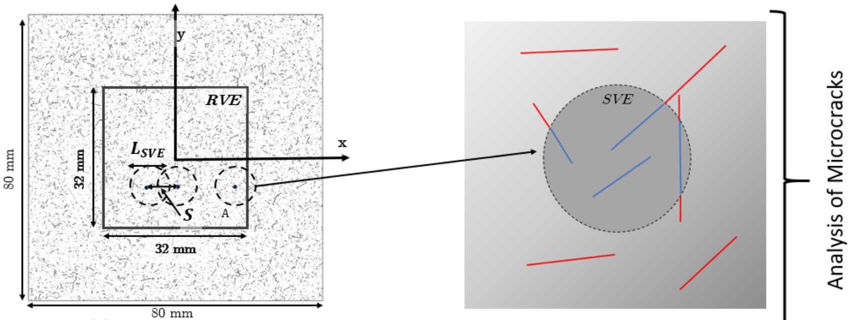

(a) Representative Volume Element (**RVE**)

(b) Statistical Volume Element (**SVE**)

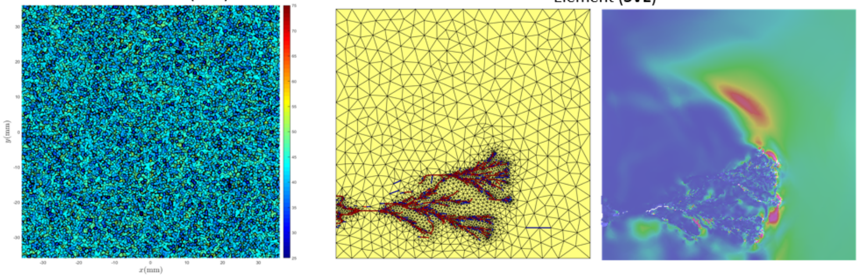

(c) Mesoscopic Strength Field

(d) Macroscopic Fracture Analysis

Figure 1: A multi-scale model for fracture analysis of microcracked rock.

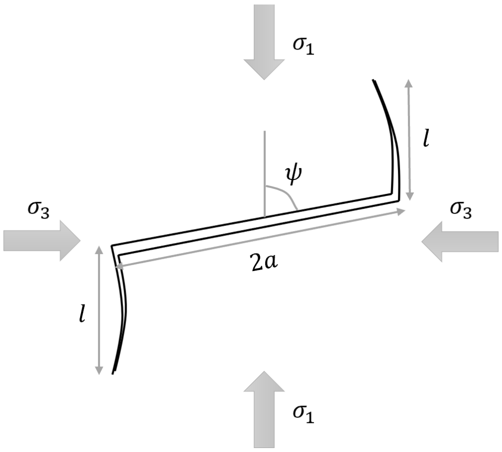

Figure 2: Sliding wing crack model with orientation of wings relative to principal compressive stresses σ_1 and σ_3

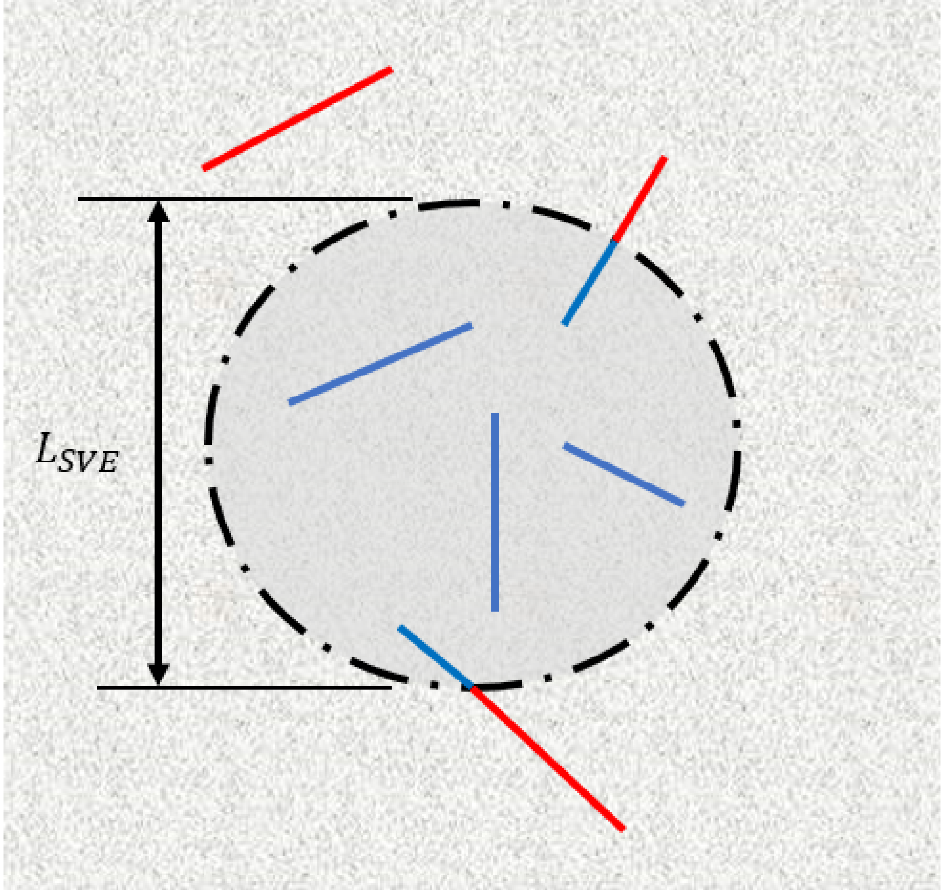

Figure 3: SVE containing cracks for fracture analysis (Red lines are considered crack segments external to SVE, Blue lines are considered crack segments internal to SVE).

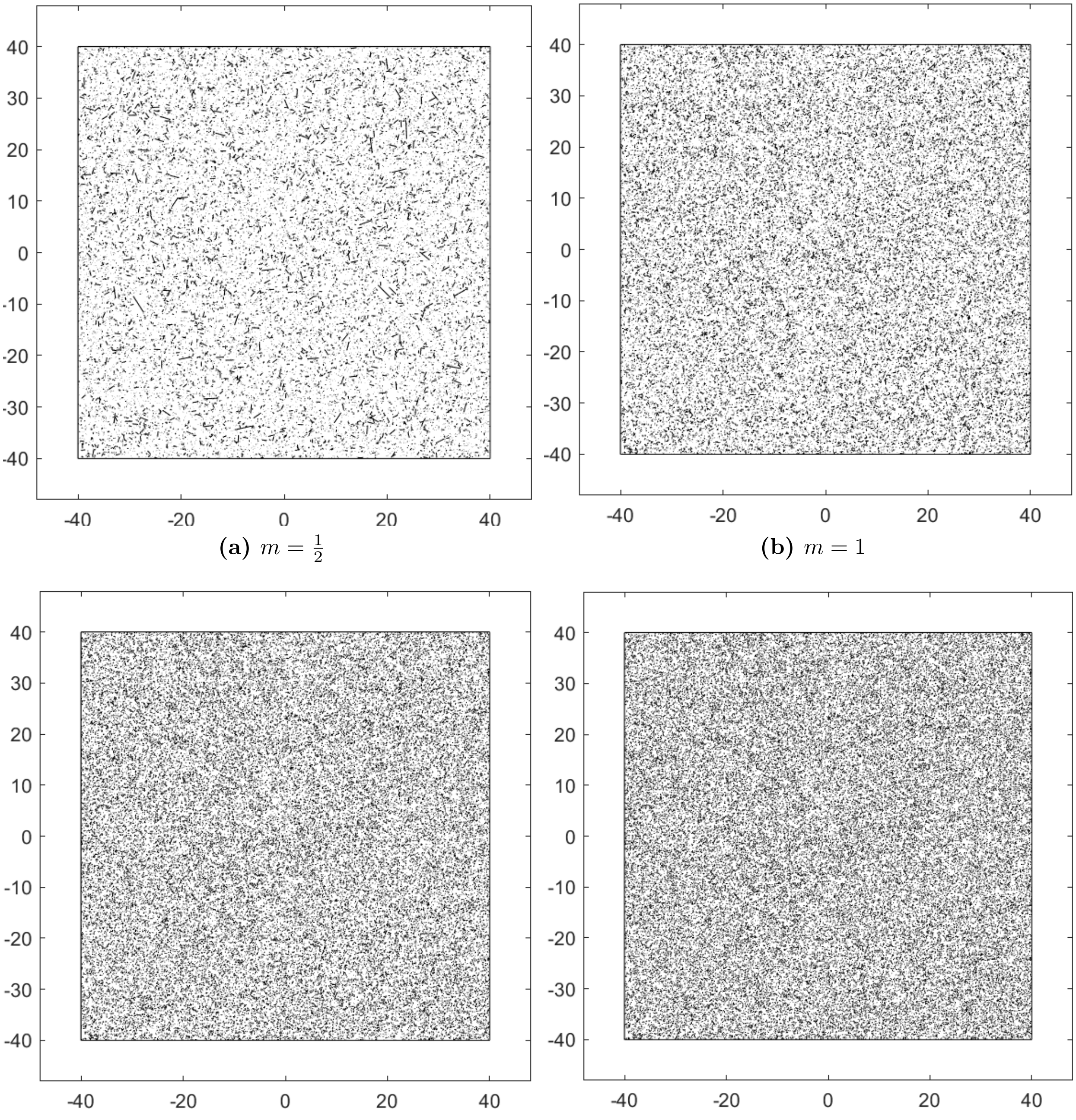

(a) $m = \frac{1}{2}$ **(b)** $m = 1$

(c) $m = 2$ **(d)** $m = 4$

Figure 4: Representative generated microcrack domains for various m Weibull crack length distributions for $\varepsilon_0 = 0.243$

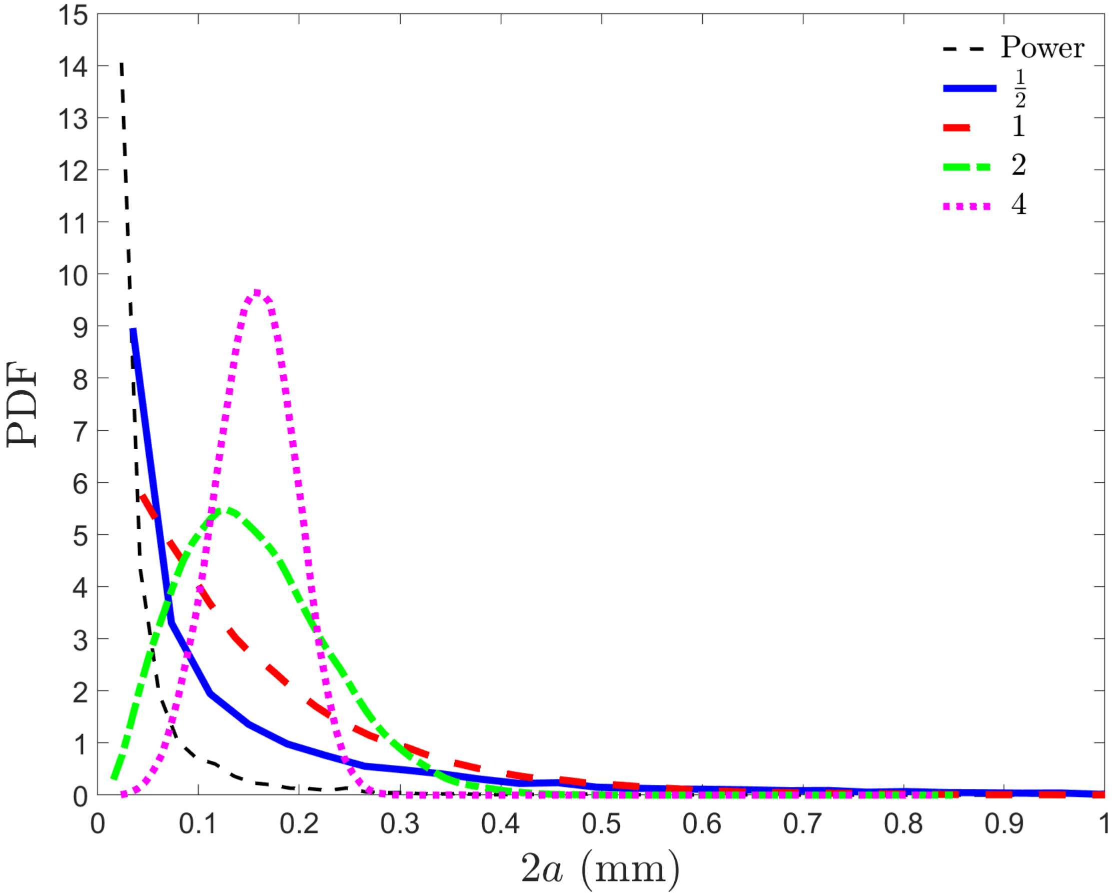

Figure 5: Probability density function of crack length $2a$ for generated power distribution and Weibull domains with $\varepsilon_0 = 0.243$

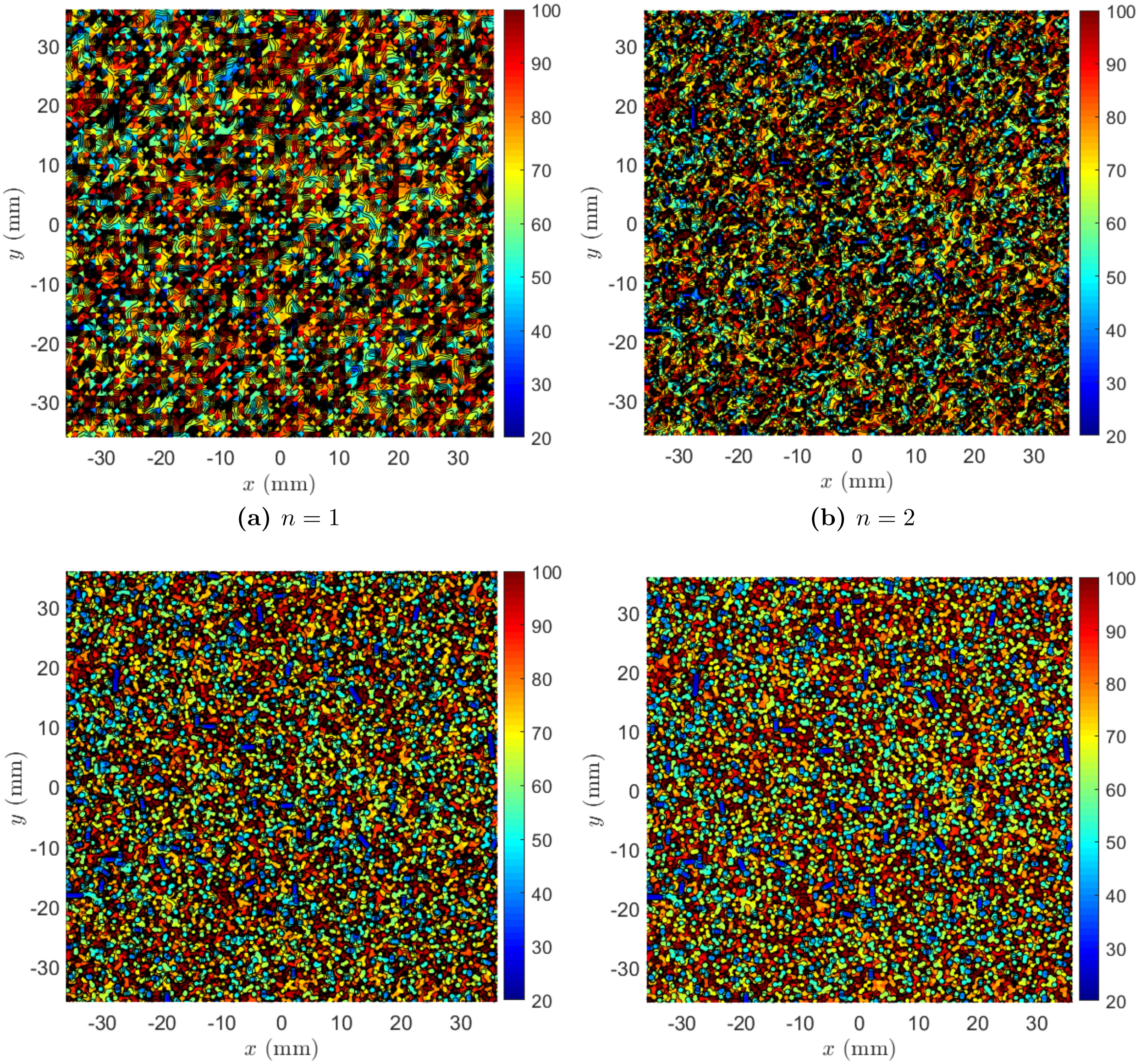

(a) $n = 1$ **(b)** $n = 2$

(c) $n = 5$ **(d)** $n = 10$

Figure 6: The effect of SVE spacing n on mesoscopic strength contours s_c for $L_{SVE} = 1$ and $\varepsilon_0 = 0.243$

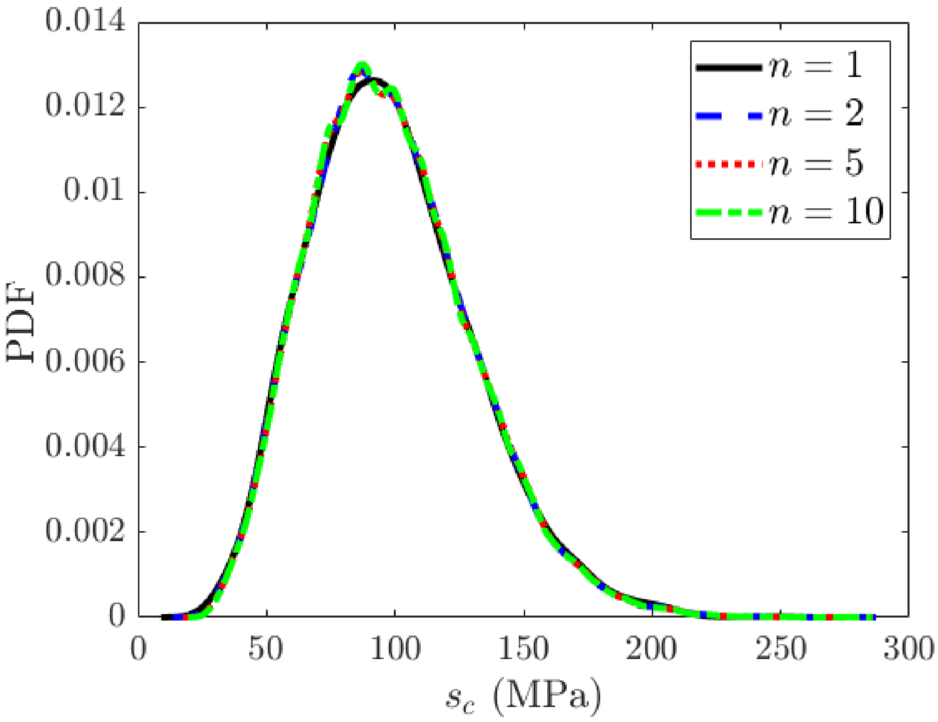

Figure 7: Mesoscopic strength s_c (MPa) PDF for various SVE spacing n ($L_{SVE} = 1$ and $\varepsilon_0 = 0.243$)

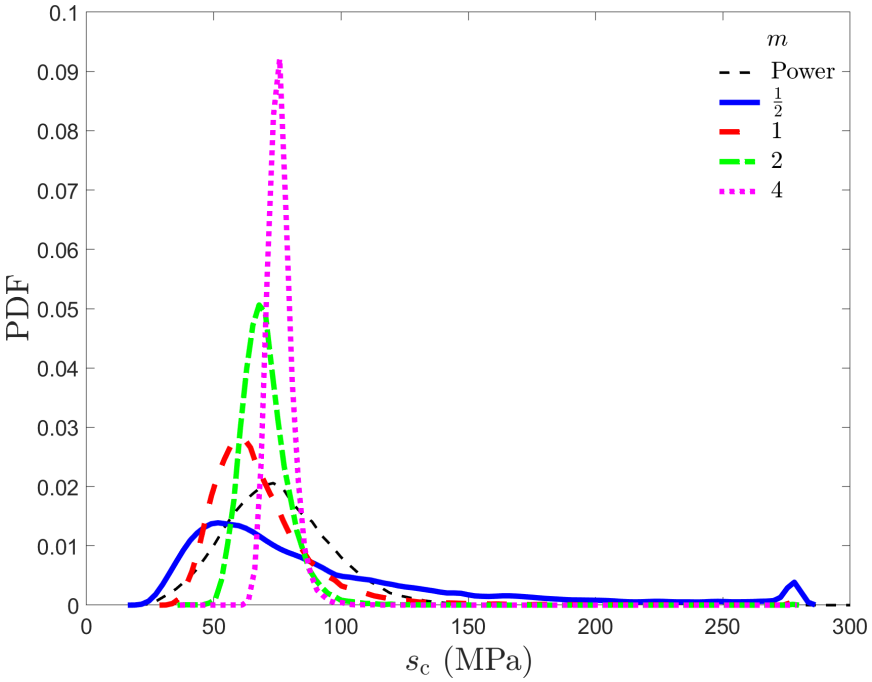

Figure 8: Mesoscopic strength s_c (MPa) probability density function for power and Weibull distribution domains with $L_{SVE} = 1$ and $\varepsilon_0 = 0.243$

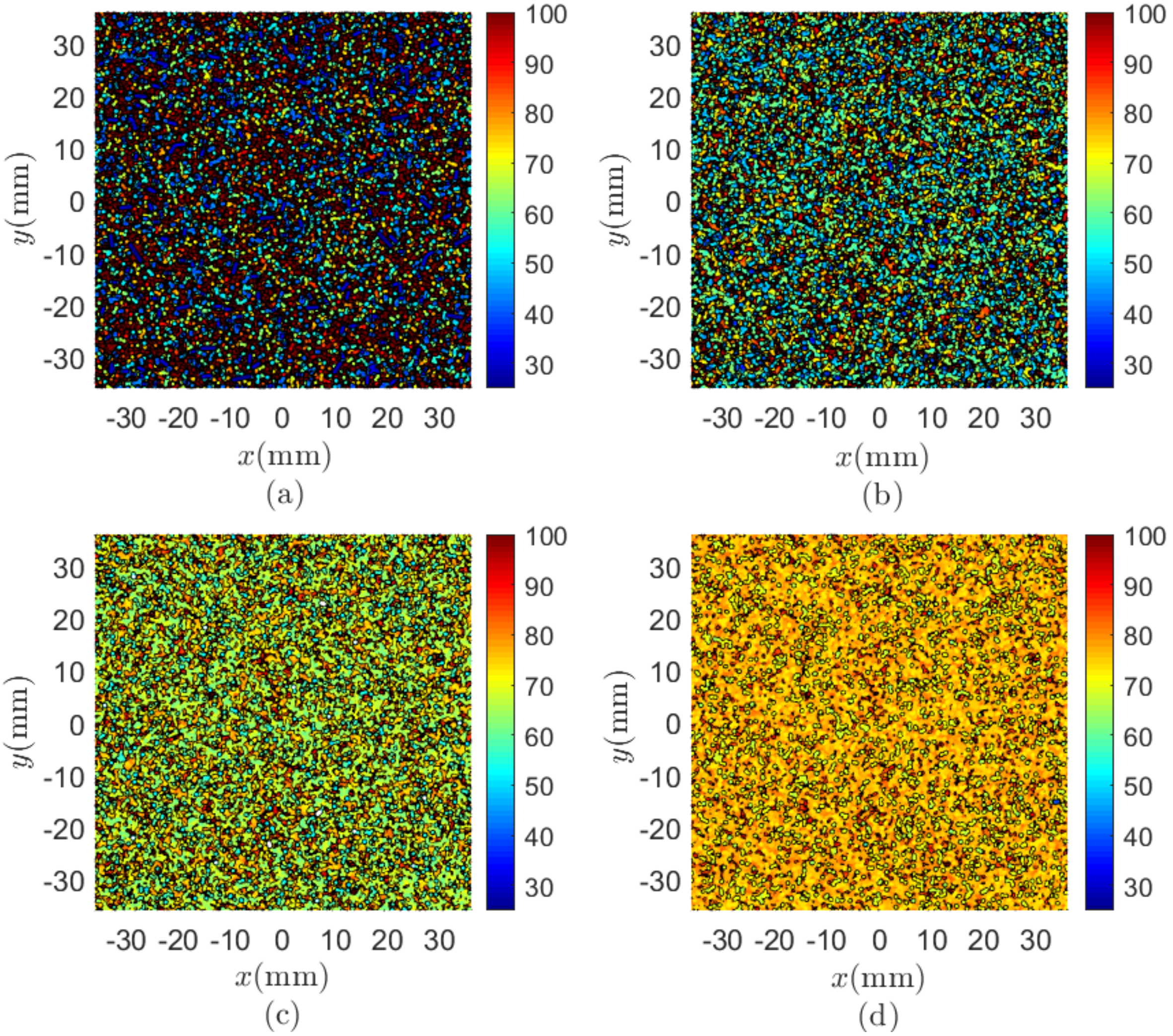

(a)

(b)

(c)

(d)

Figure 9: Mesoscopic strength contour s_c (MPa) for $\varepsilon_0 = 0.243$, $L_{SVE} = 1$, and Weibull shape parameters (a) $m = \frac{1}{2}$, (b) $m = 1$, (c) $m = 2$, and (d) $m = 4$

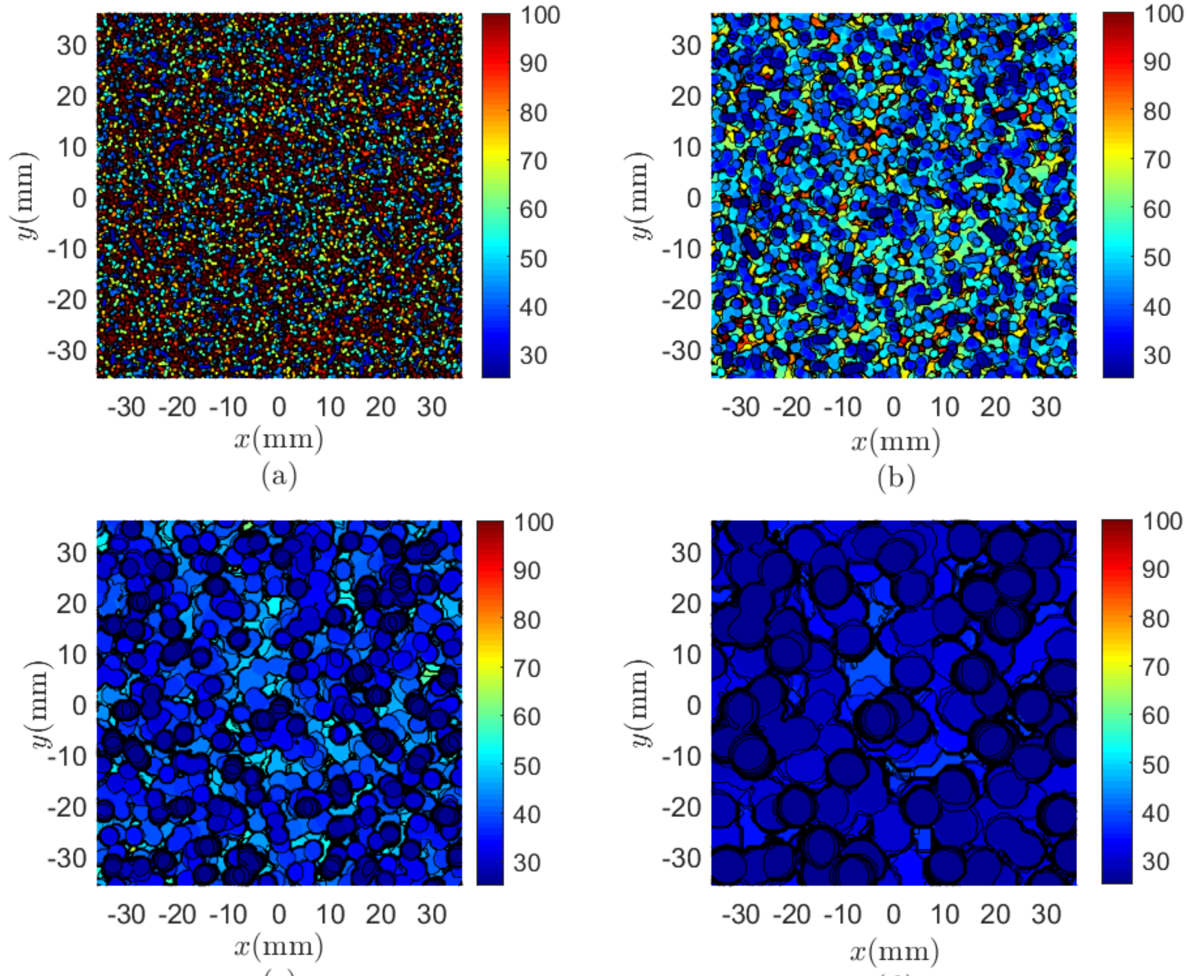

(a)

(b)

(c)

(d)

Figure 10: Mesoscopic strength contour s_c (MPa) SVE size effect comparison for $\varepsilon_0 = 0.243$, $m = \frac{1}{2}$, with (a) $L_{SVE} = 1$, (b) $L_{SVE} = 2$, (c) $L_{SVE} = 4$, and (d) $L_{SVE} = 8$

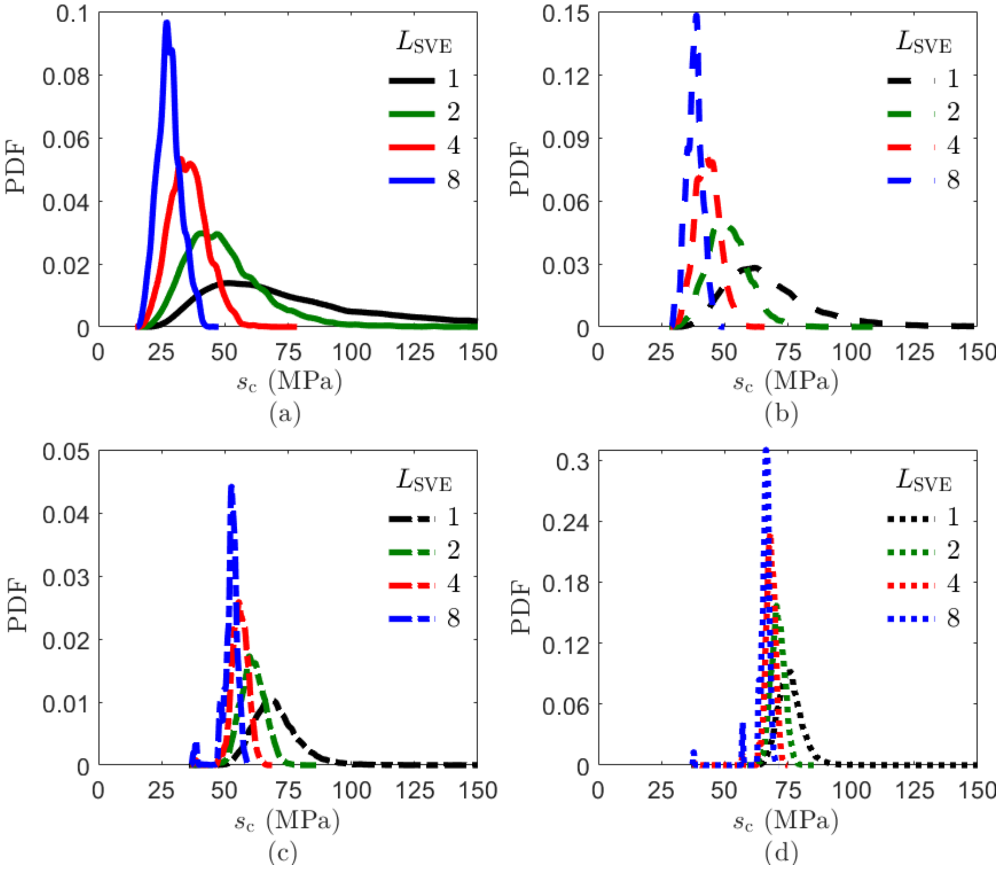

Figure 11: Strength probability density function and SVE size effect comparison for $\varepsilon_0 = 0.243$, with (a) $m = \frac{1}{2}$, (b) $m = 1$, (c) $m = 2$, and (d) $m = 4$

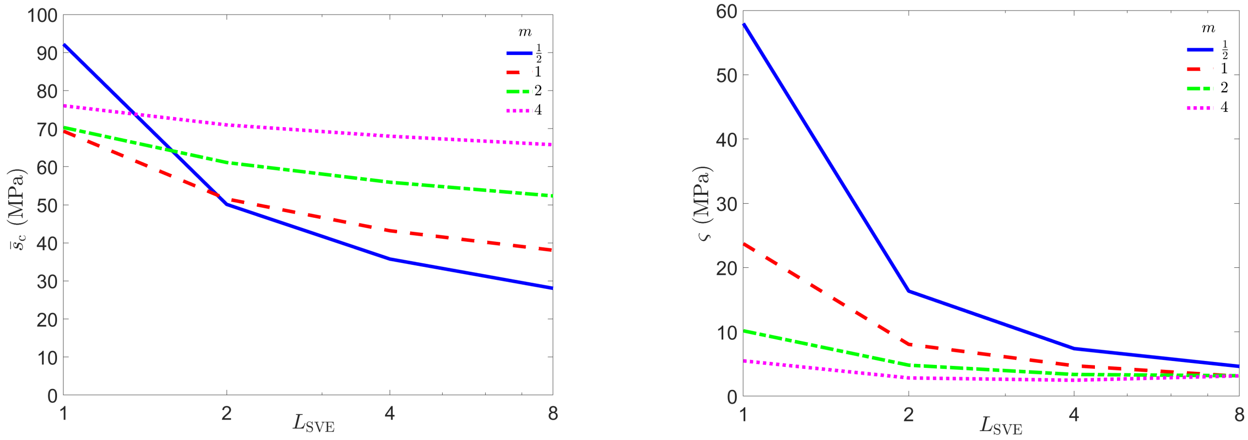

(a) $\bar{s}_c$ **(b)** ς

Figure 12: Mean strength $\bar{s}_c$ and standard deviation ς for $\varepsilon_0 = 0.243$

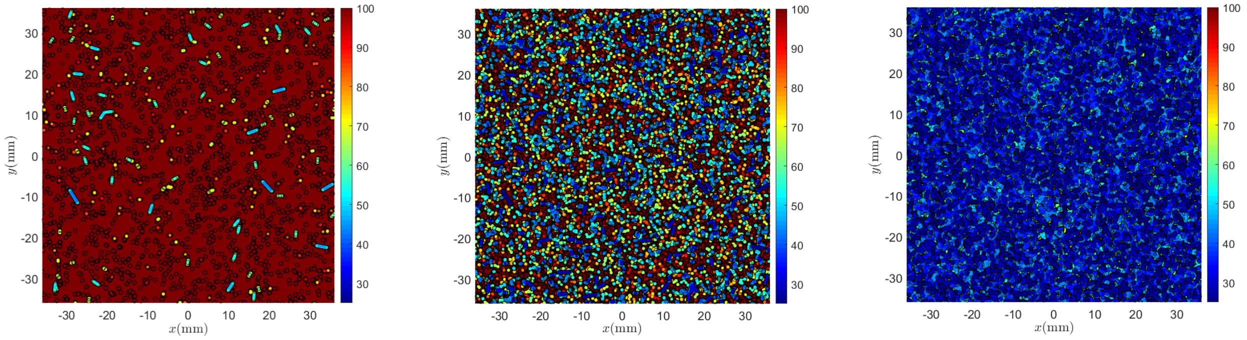

(a) $\varepsilon_0 = 0.05$ **(b)** $\varepsilon_0 = 0.243$ **(c)** $\varepsilon_0 = 0.75$

Figure 13: Mesoscopic strength s_c contours for $m = \frac{1}{2}$, (a) $\varepsilon_0 = 0.05$, (b) $\varepsilon_0 = 0.243$, and (c) $\varepsilon_0 = 0.75$

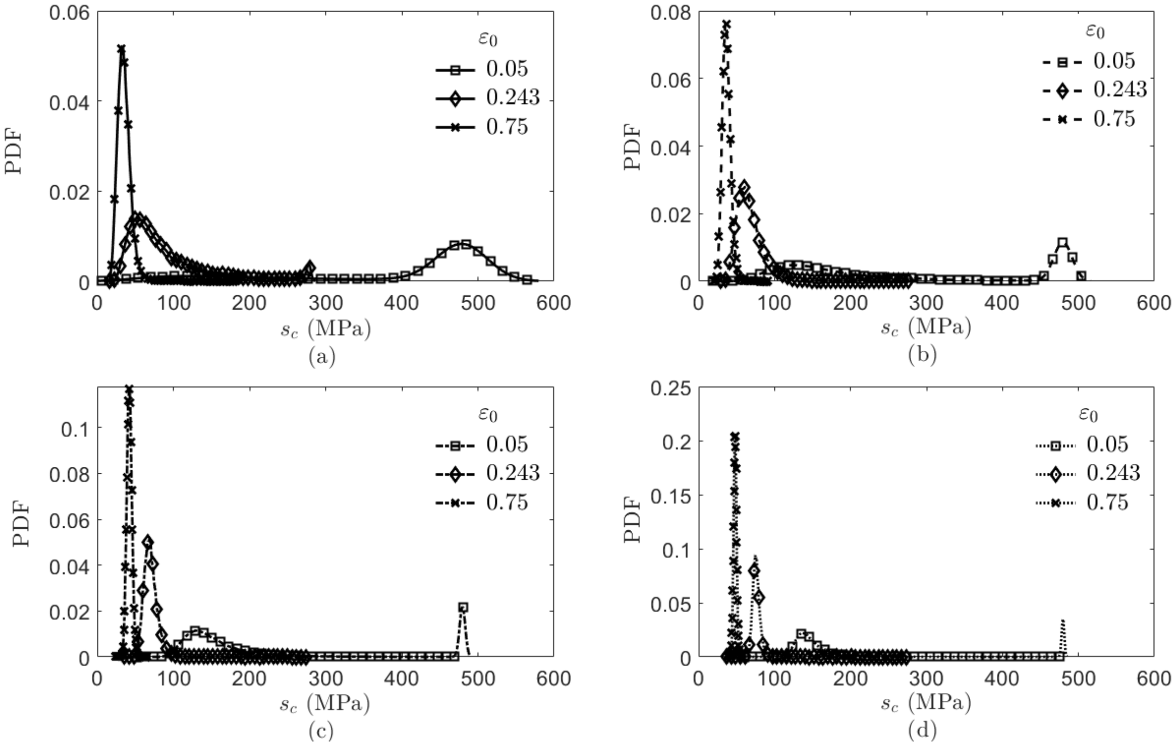

Figure 14: Strength probability density function comparison for various crack densities and Weibull distribution shape parameters for $L_{SVE} = 1$, (a) $m = \frac{1}{2}$, (b) $m = 1$, (c) $m = 2$, and (d) $m = 4$

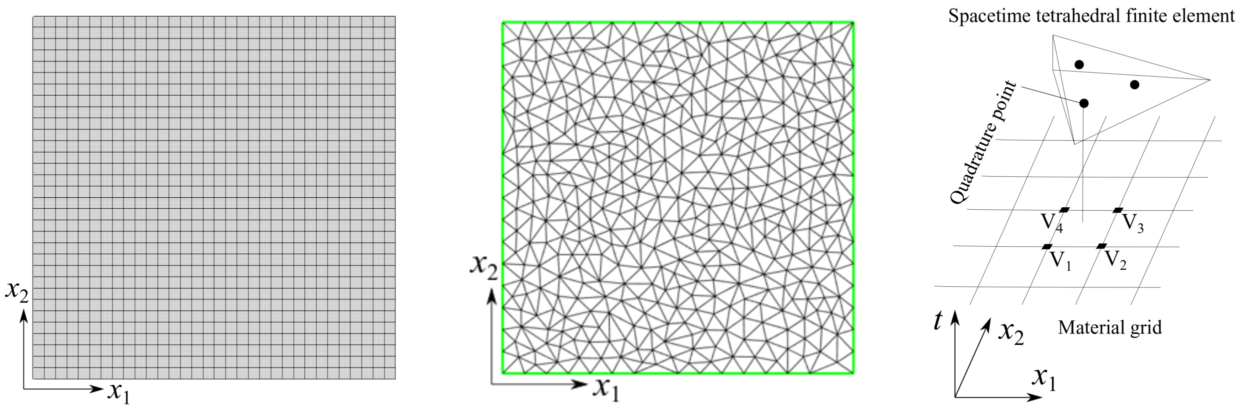

(a) Structured 360 × 360 grid for fracture strength

(b) Initial unstructured spatial mesh for aSDG fracture analysis

(c) Interpolation of properties at quadrature points

Figure 15: Distinct discrete grids for material properties and fracture analysis.

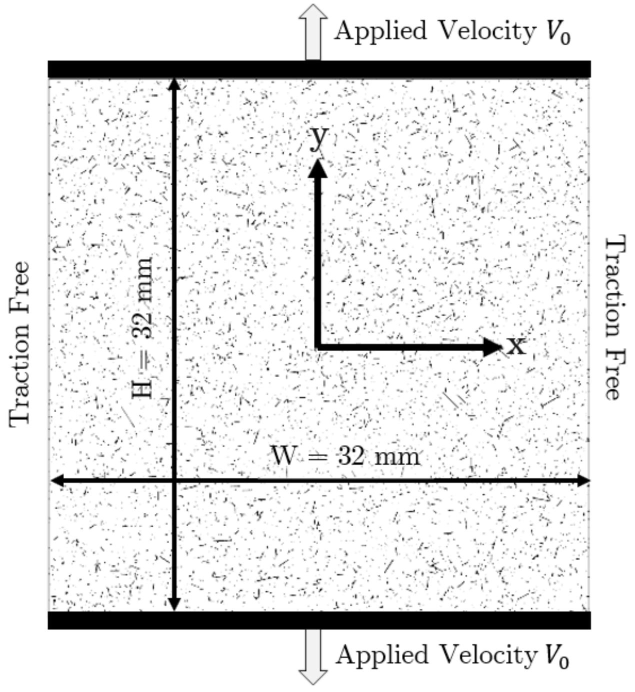

Figure 16: Applied boundary conditions for aSDG dynamic fracture analysis

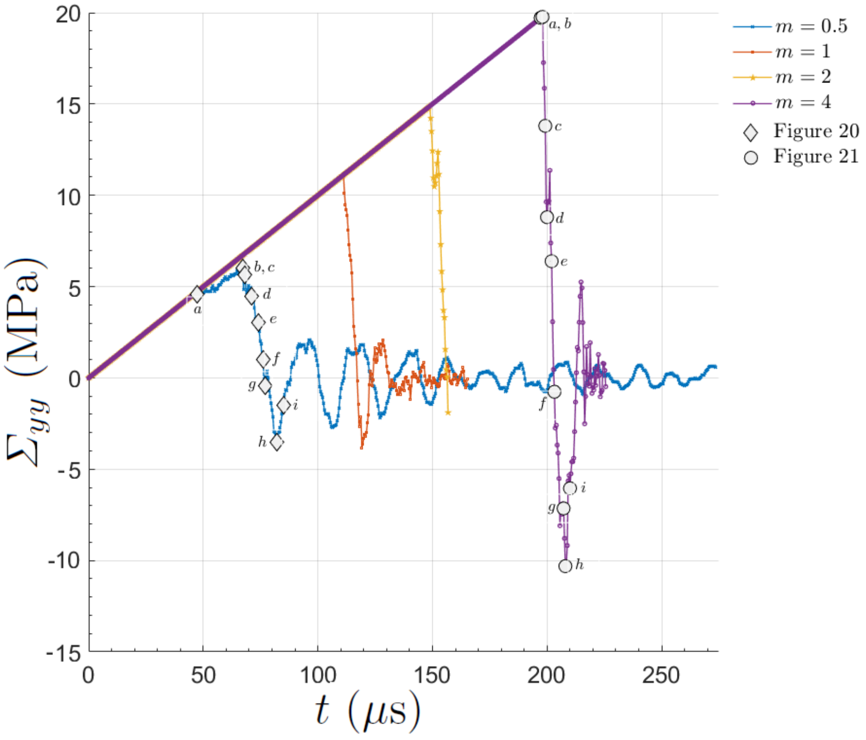

Figure 17: Macroscopically homogenized stress Σ_{yy} versus time for all Weibull distributions. The detailed solution for different stages of solutions for $m = \frac{1}{2}$ and 4 are shown in Fig. 21 and Fig. 22, respectively

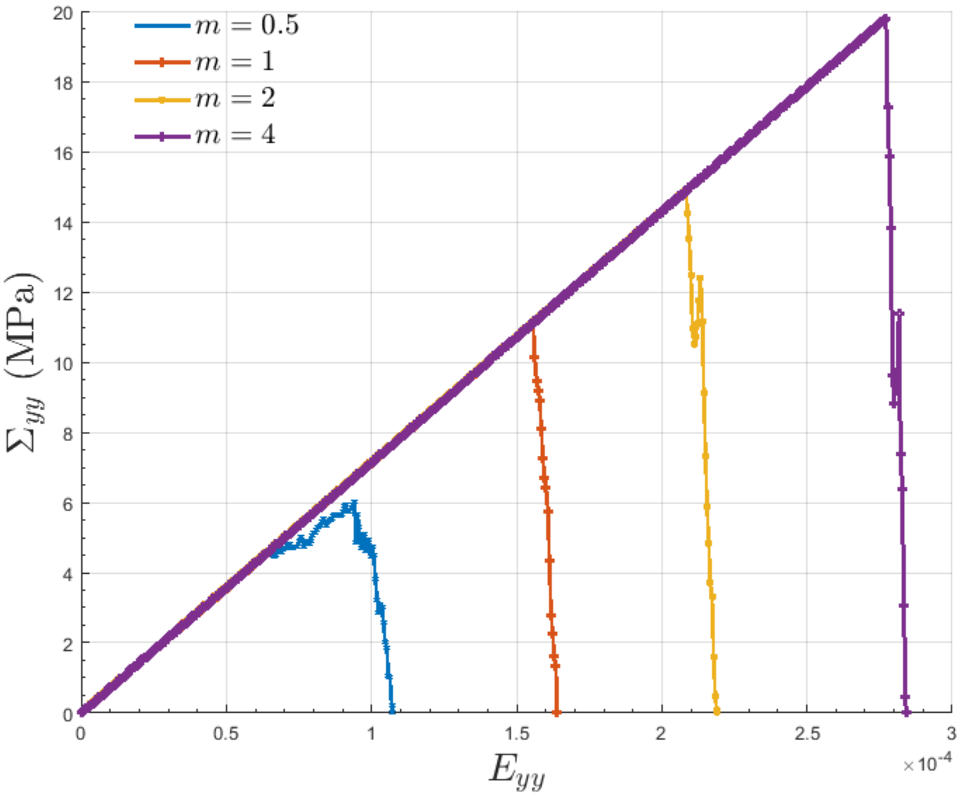

Figure 18: Macroscopically homogenized strain E_{yy} versus stress Σ_{yy} for all Weibull distributions

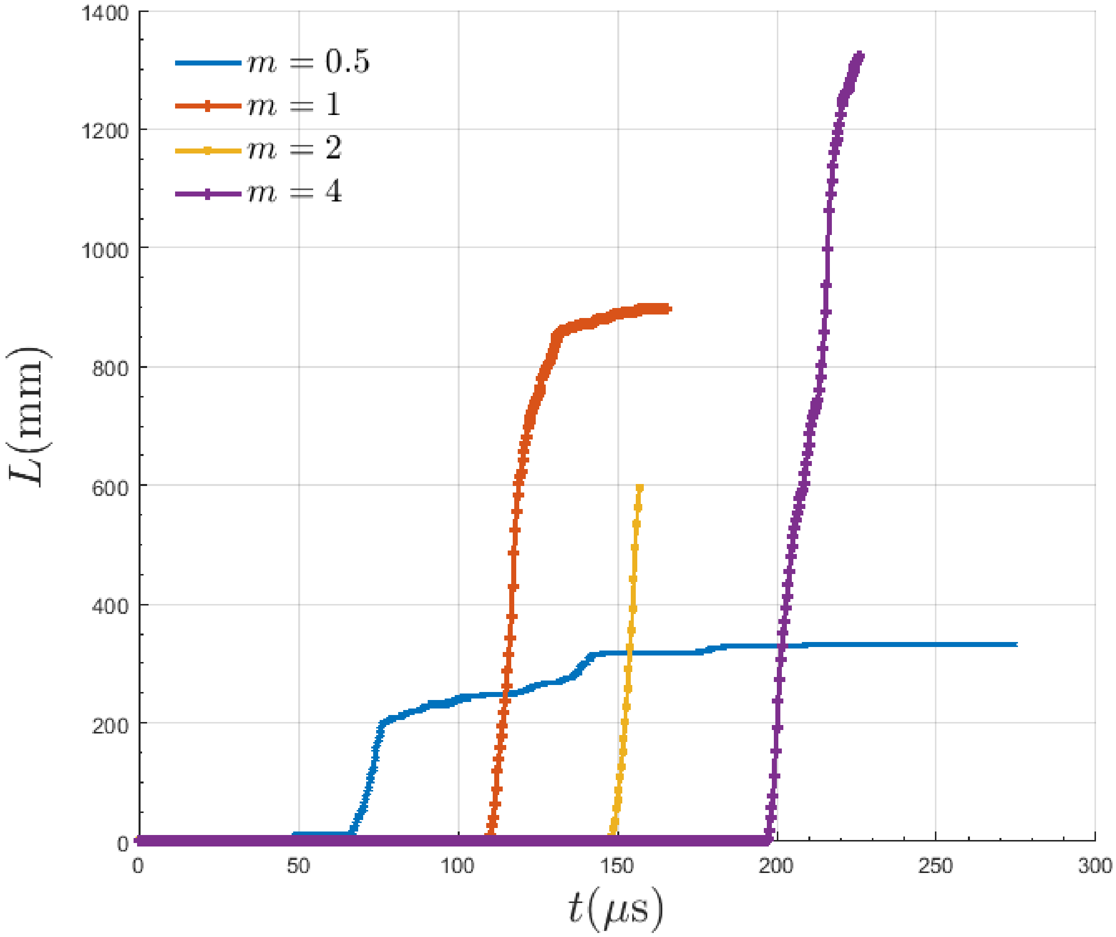

Figure 19: Total crack length L versus time for all Weibull distributions

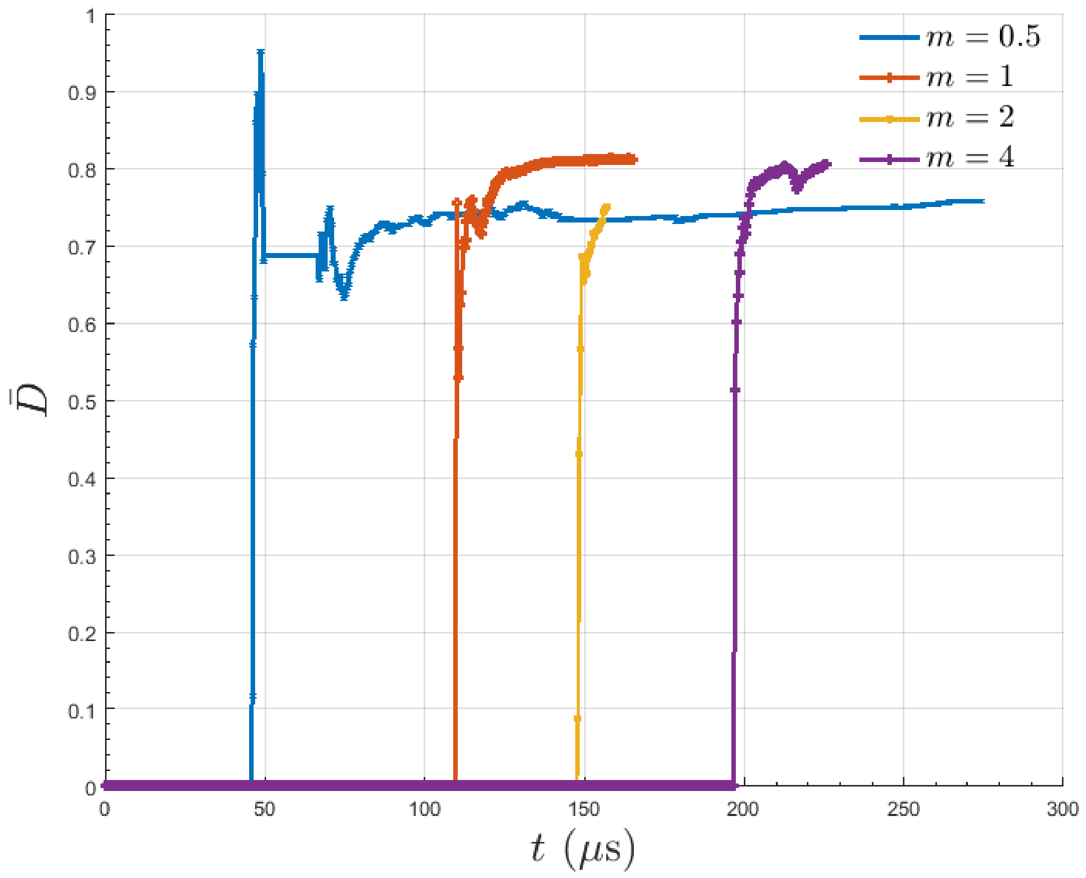

Figure 20: Averaged damage parameter $\bar{D}$ versus time for all Weibull distributions

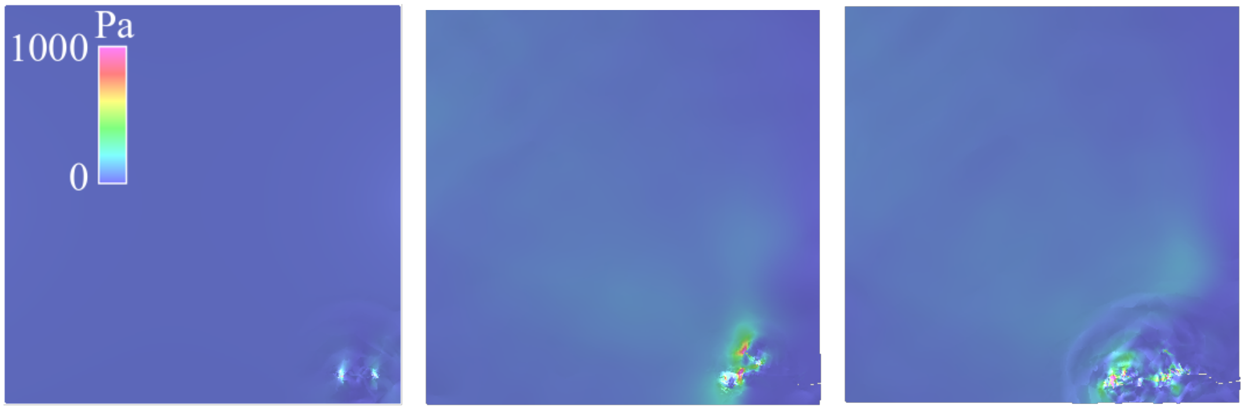

(a) t = 47 μs, Initial Crack Propagation **(b)** t = 67 μs, Maximum Loading **(c)** t = 68 μs, Post-Maximum Loading

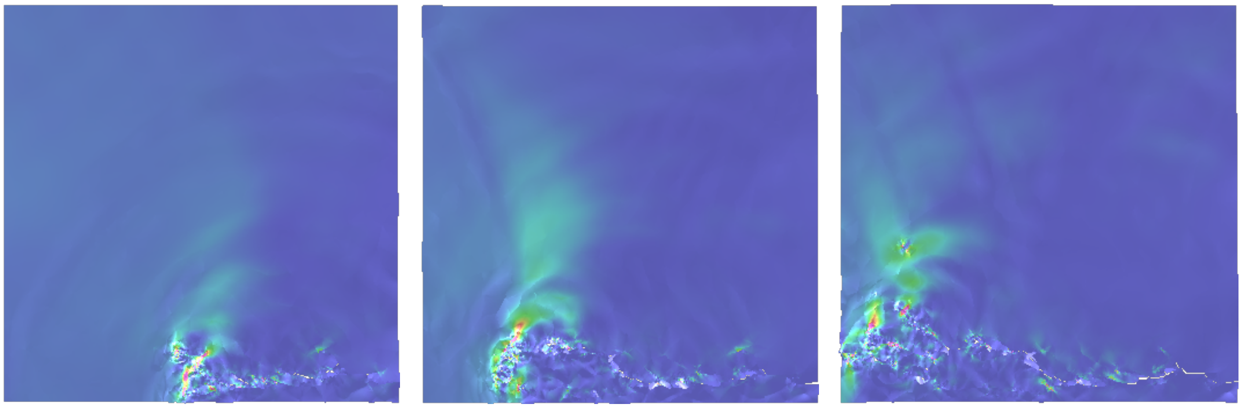

(d) t = 71 μs, Before Material Failure **(e)** t = 74 μs, Before Material Failure **(f)** t = 76 μs, Material Failure

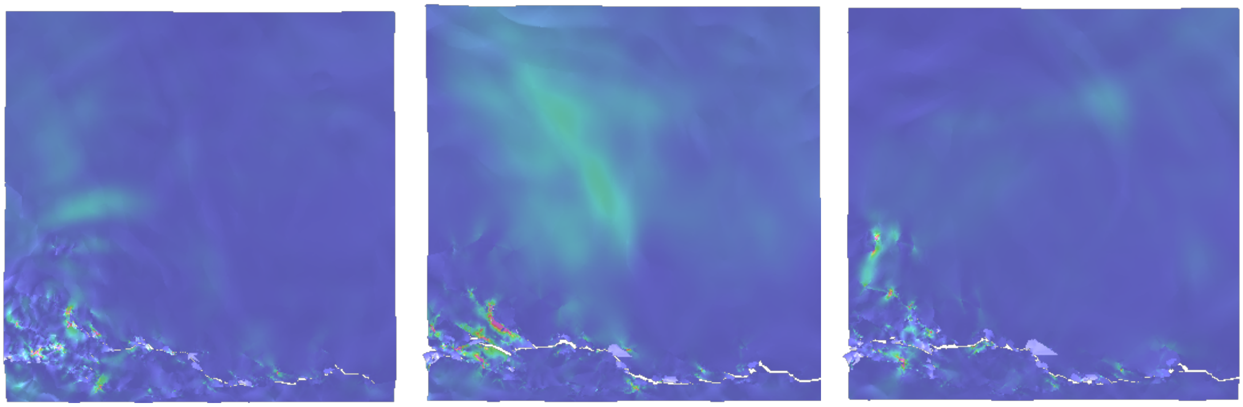

(g) t = 77 μs, Post Material Failure **(h)** t = 82 μs, Minimum Stress **(i)** t = 85 μs, Post-Minimum Stress

Figure 21: aSDG solution visualization for Weibull shape parameter $m = \frac{1}{2}$. Color and height fields depict internal and kinetic energy densities, respectively

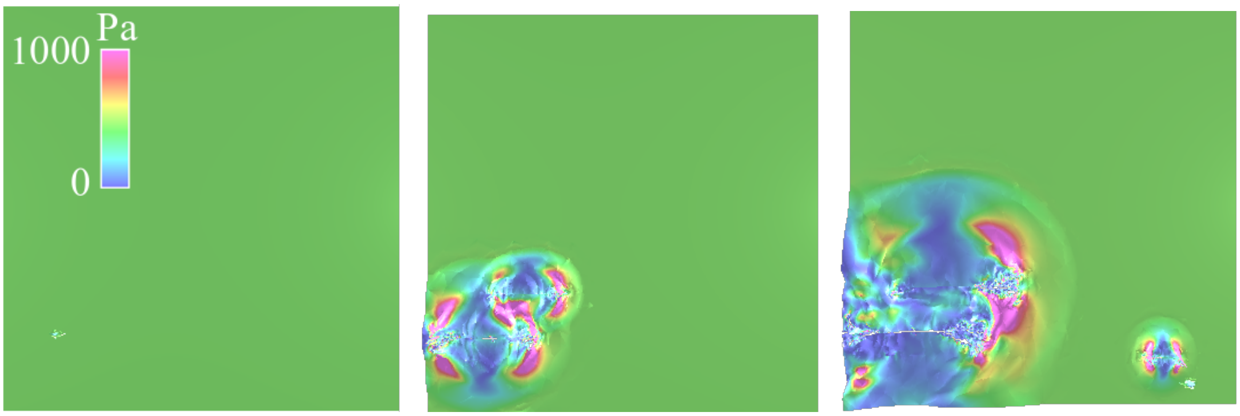

(a) t = 197 μs, Initial Crack Propagation **(b)** t = 198 μs, Maximum Loading **(c)** t = 199 μs, Post-Maximum Loading

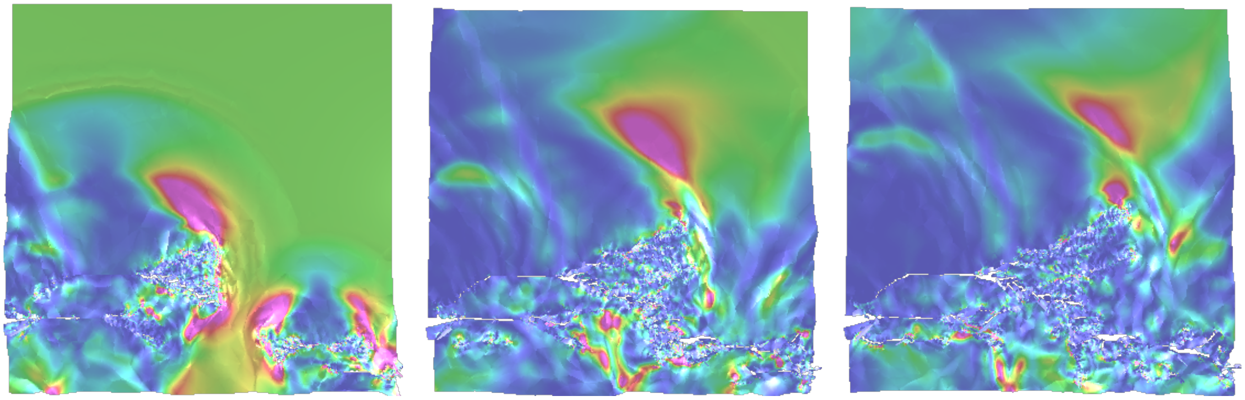

(d) t = 200 μs, Before Material Failure **(e)** t = 202 μs, Before Material Failure **(f)** t = 203 μs, Material Failure

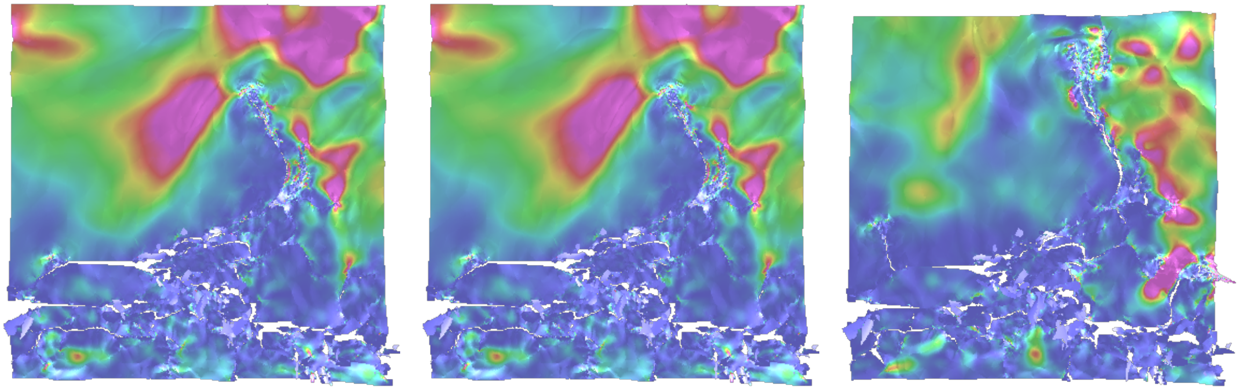

(g) t = 207 μs, Post Material Failure **(h)** t = 208 μs, Minimum Stress **(i)** t = 210 μs, Post-Minimum Stress

Figure 22: aSDG solution visualization for Weibull shape parameter $m = 4$. Color and height fields depict internal and kinetic energy densities, respectively

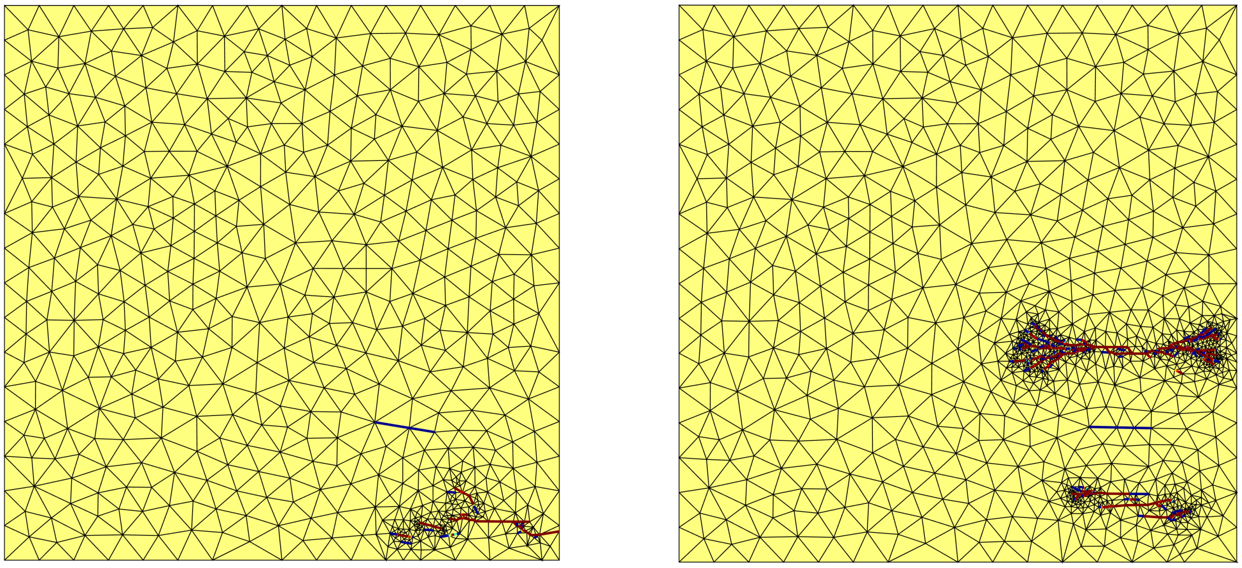

(a) $\tilde{t}_m = 67.2\ \mu\text{s}$ for $m = \frac{1}{2}$

(b) $\tilde{t}_m = 111.2\ \mu\text{s}$ for $m = 1$

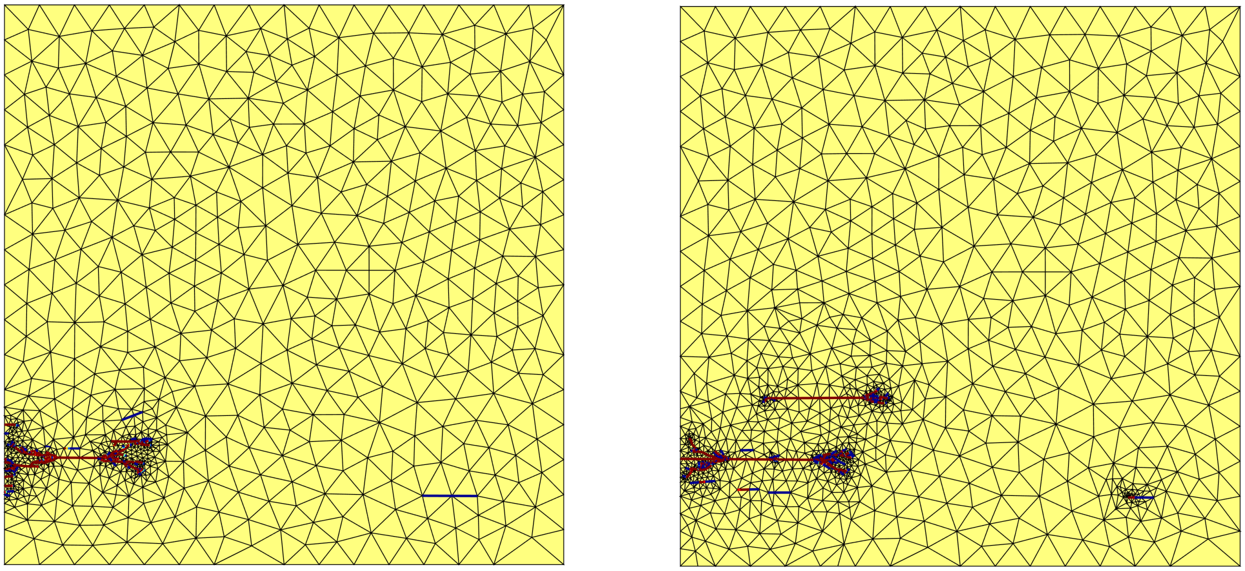

(c) $\tilde{t}_m = 148.8\ \mu\text{s}$ for $m = 2$

(d) $\tilde{t}_m = 198\ \mu\text{s}$ for $m = 4$

Figure 23: aSDG front meshes for Weibull distributions at maximum stress stage

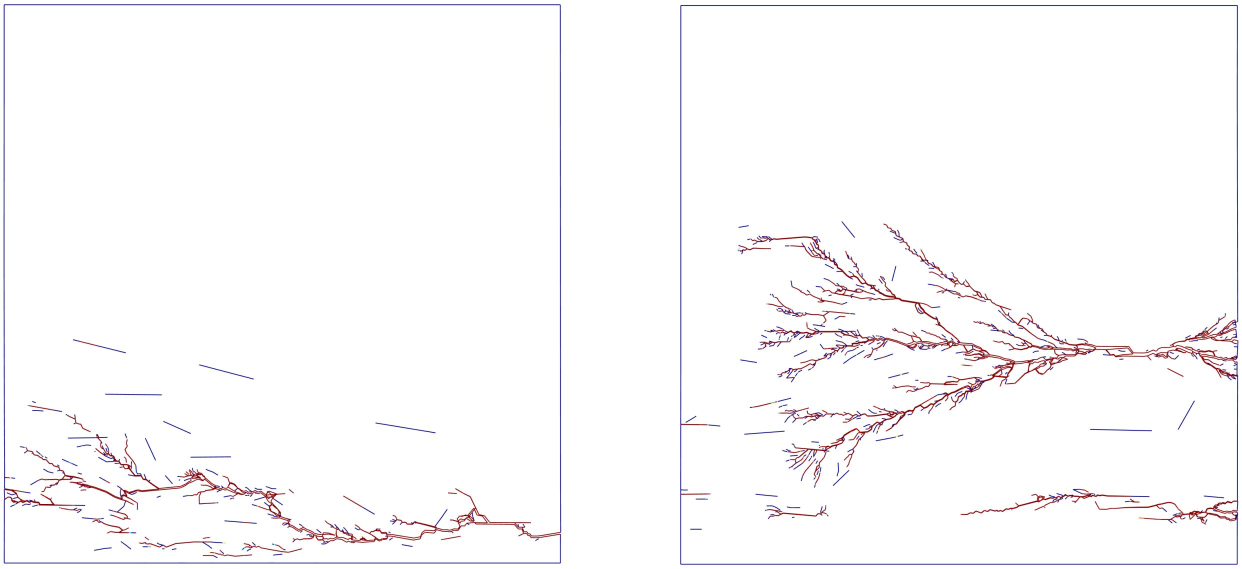

(a) $\tilde{t}_f = 76.7\ \mu\text{s}$ for $m = \frac{1}{2}$ **(b)** $\tilde{t}_f = 117.2\ \mu\text{s}$ for $m = 1$

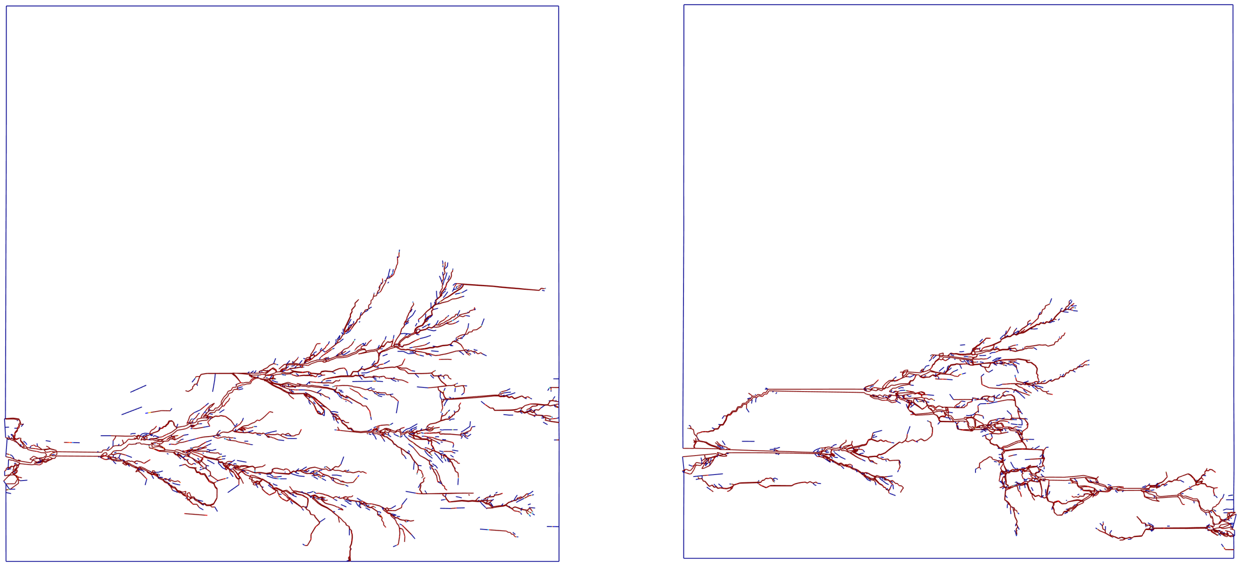

(c) $\tilde{t}_f = 156.4\ \mu\text{s}$ for $m = 2$ **(d)** $\tilde{t}_f = 203.0\ \mu\text{s}$ for $m = 4$

Figure 24: aSDG deformed shape for Weibull distributions at failure stage

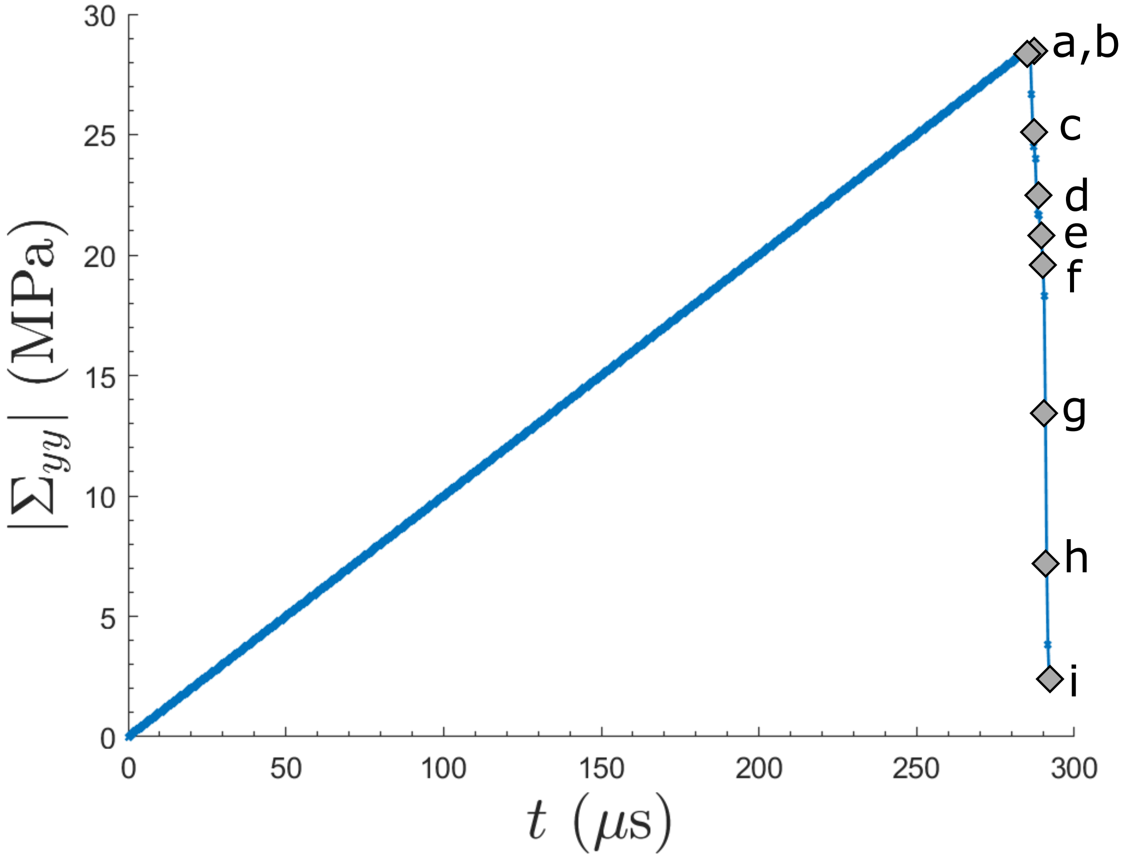

Figure 25: Macroscopically homogenized stress $|\Sigma_{yy}|$ versus time for the compressive loading example. The detailed solution for different stages of solutions are shown in Fig. 26

(a) t = 285.62 μs, (28 MPa), After Initial Crack Propagation
(b) t = 286.0 μs, (28.61 MPa), Maximum Loading
(c) t = 286.8 μs, (25.21 MPa), Post-Maximum Loading

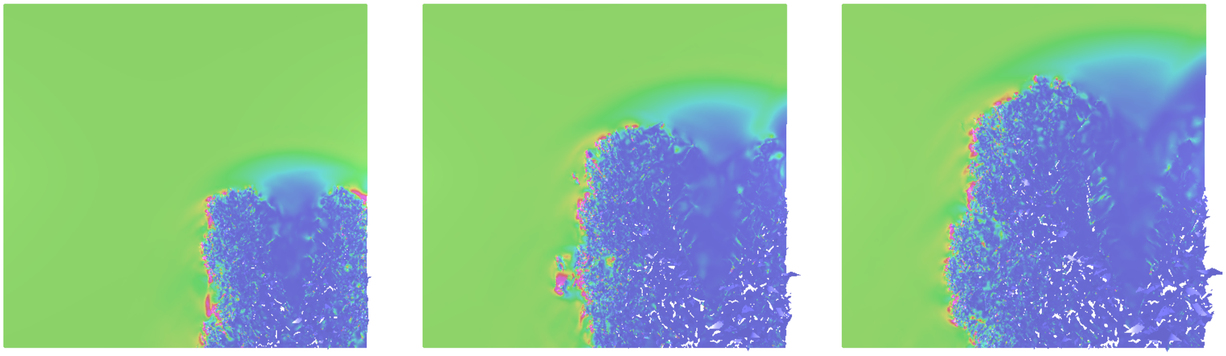

(d) t = 288.0 μs, (22.40 MPa), Before Material Failure
(e) t = 289.2 μs, (20.95 MPa), Before Material Failure
(f) t = 290.0 μs, (19.66 MPa), Before Material Failure

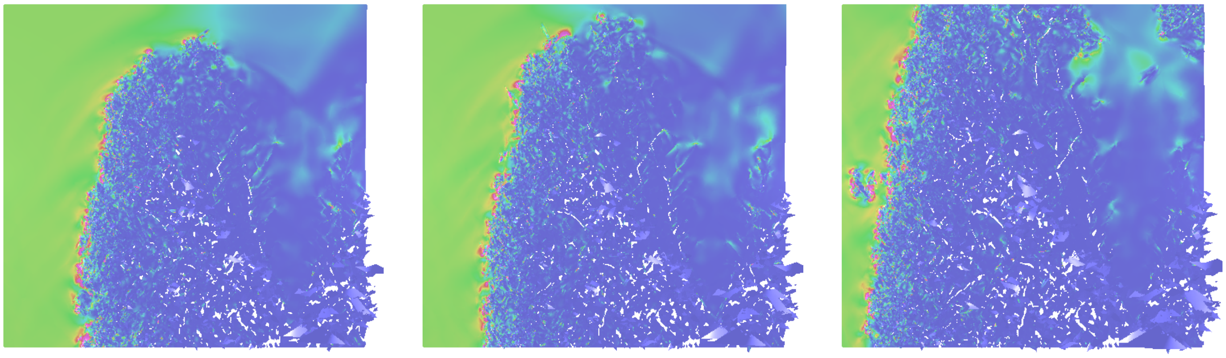

(g) t = 290.8 μs, (13.50 MPa), Before Material Failure
(h) t = 291.2 μs, (7.29 MPa), Before Material Failure
(i) t = 292.0 μs, (2.46 MPa), Material Failure

Figure 26: aSDG solution visualization for the compressive loading example. Color and height fields depict internal and kinetic energy densities, respectively. Numbers in parentheses are $|\Sigma_{yy}|$

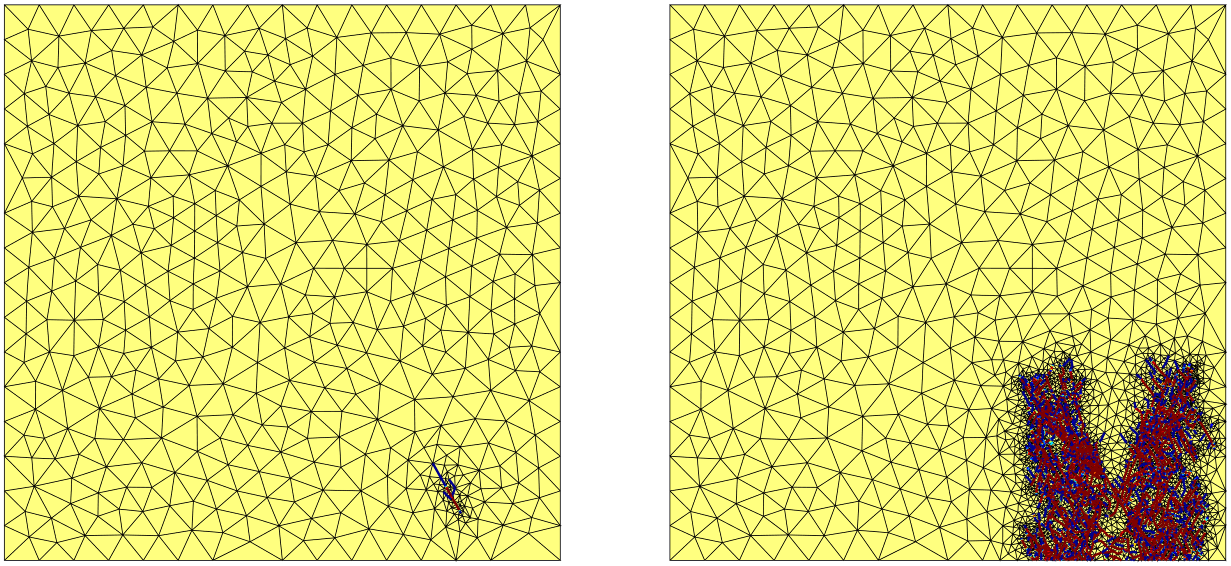

(a) 5.6 million elements, $t \approx 285.6$ μs **(b)** 9.0 million elements, $t \approx 287.2$ μs

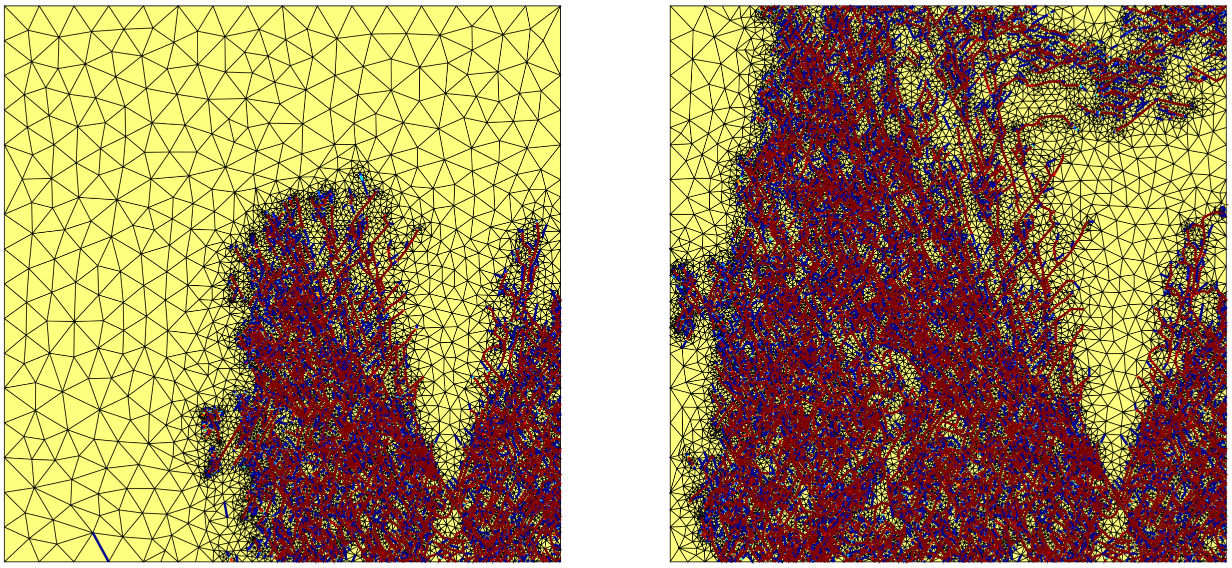

(c) 30.5 million elements, $t \approx 289.2$ μs **(d)** 105.8 million elements, $t \approx 292.0$ μs

Figure 27: aSDG front meshes for the compressive loading example at different solution times

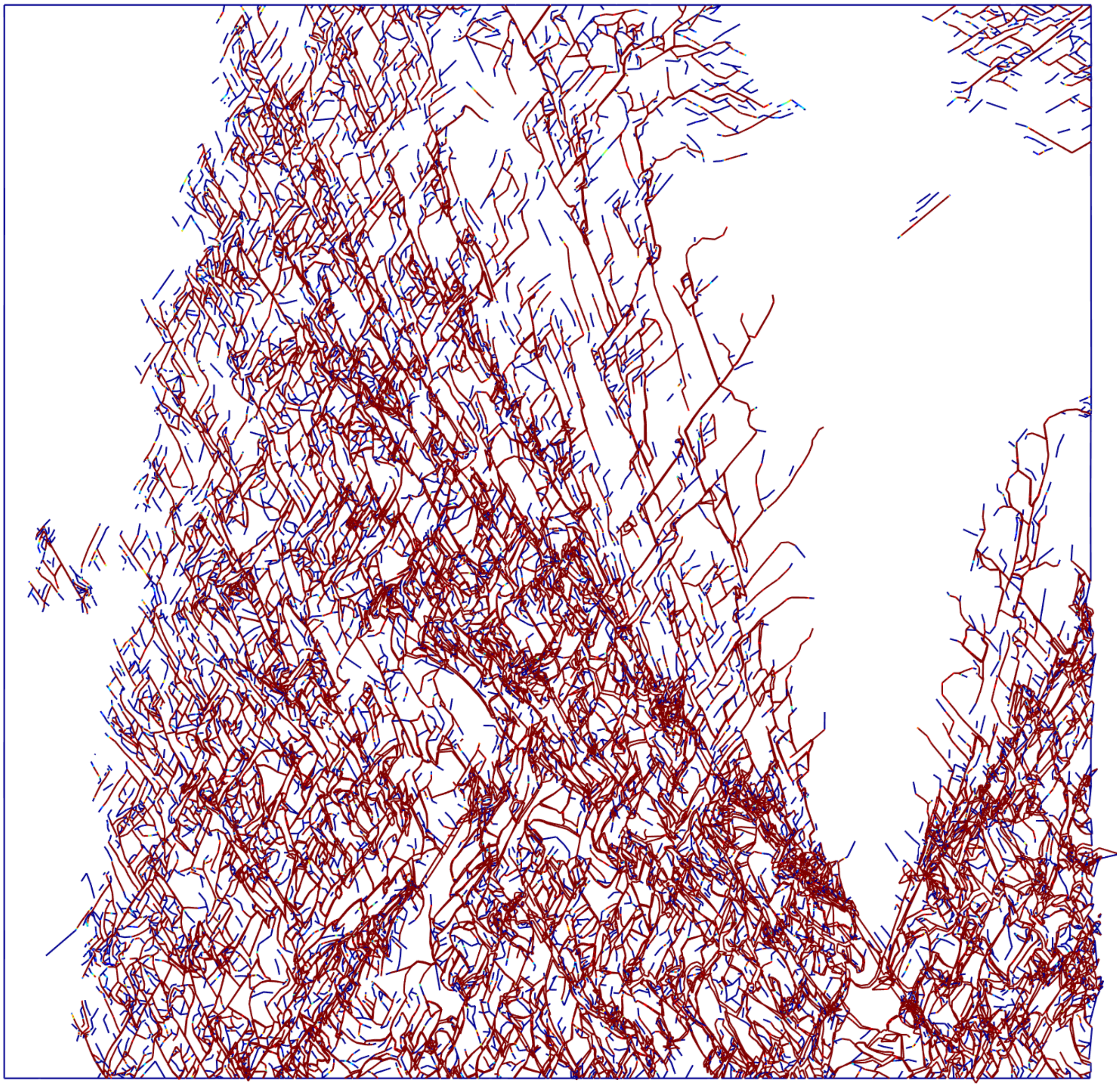

Figure 28: aSDG deformed shape for the compressive loading example at $t = 292.0\ \mu$s

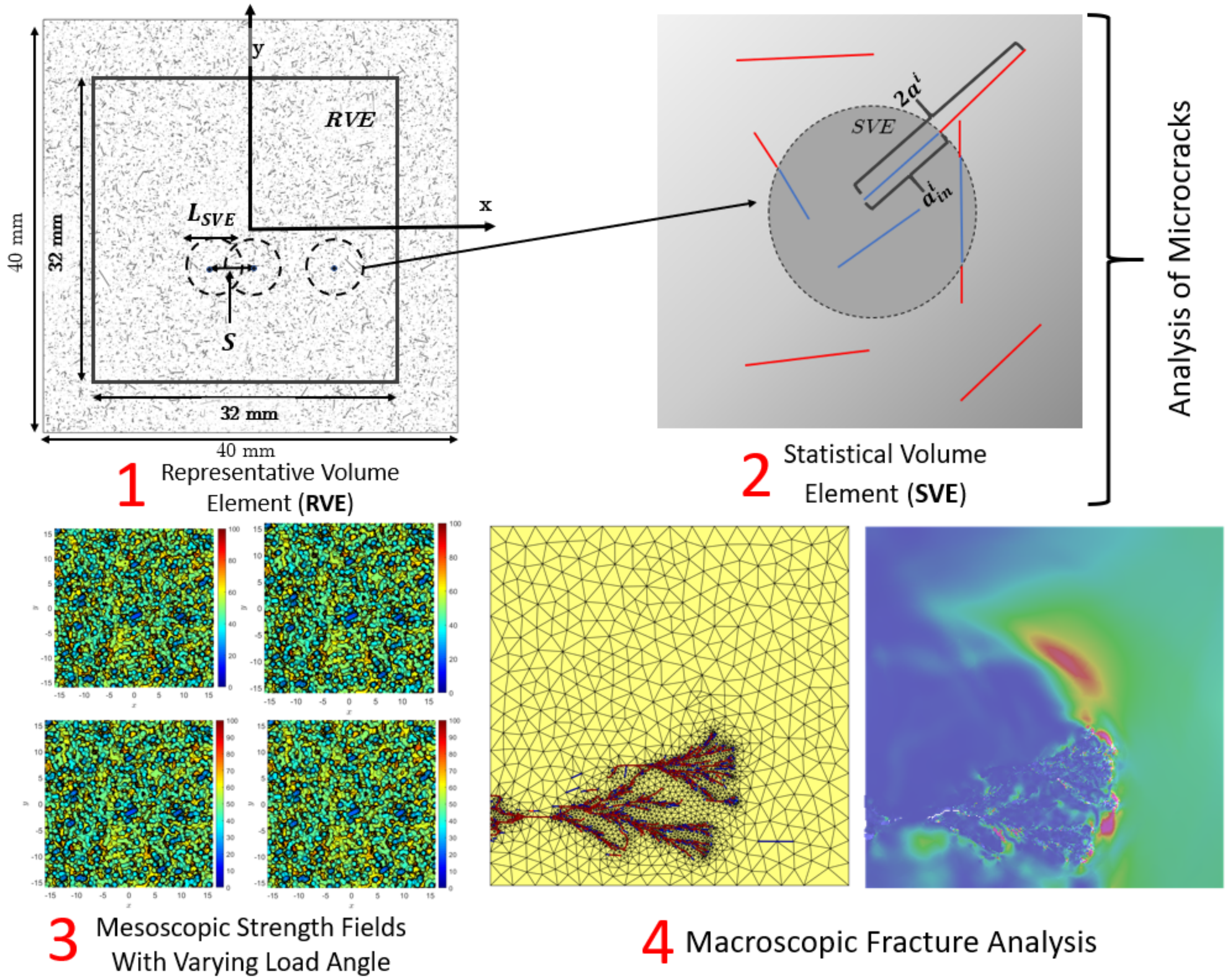

Figure 29: A multi-scale model for anisotropic fracture analysis of microcracked rock.

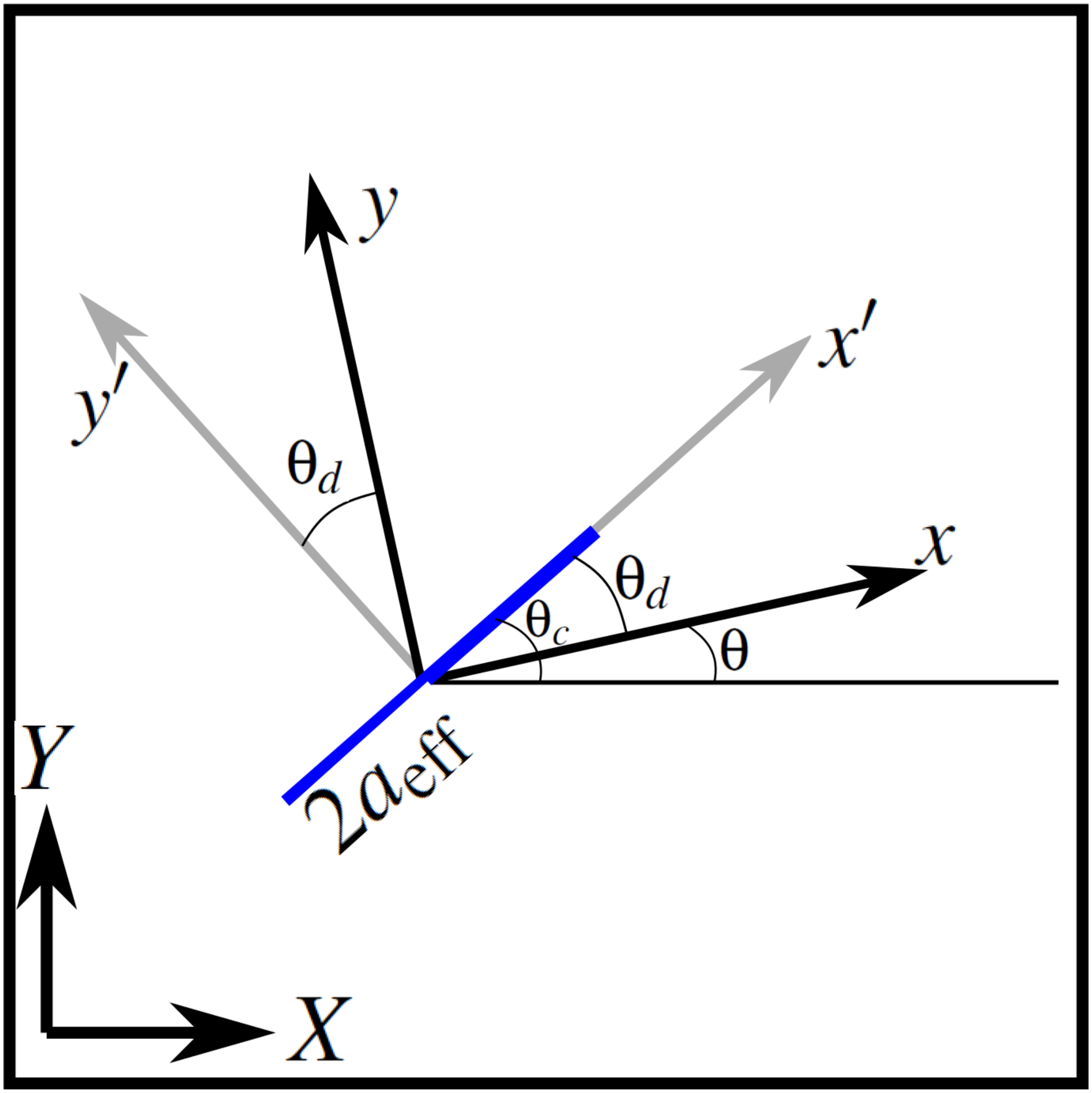

Figure 30: Crack Angle θ_c and Loading Angle θ

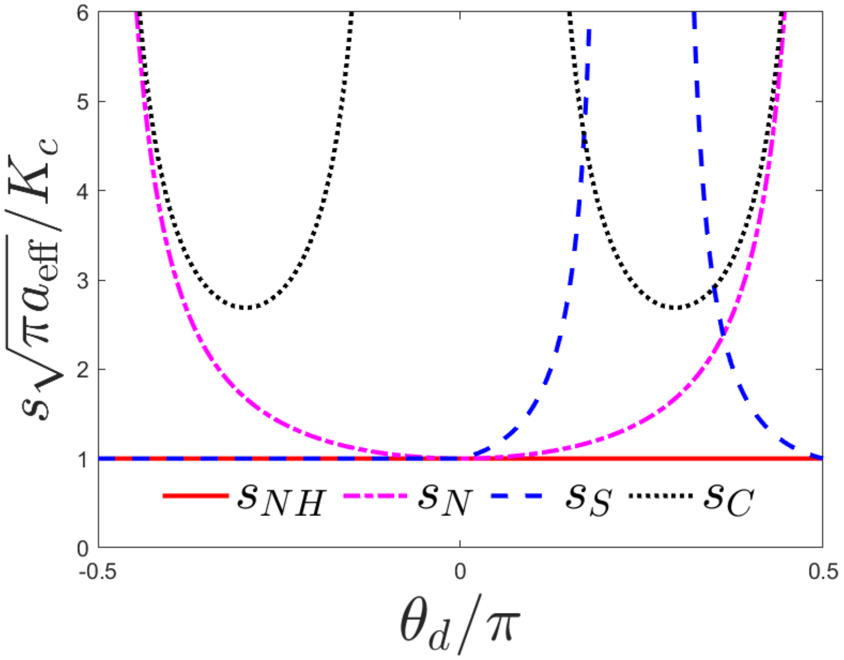

Figure 31: Different fracture strengths for the crack in Fig. 30 as a function of relative crack angle θ_d for $k = 0.3$.

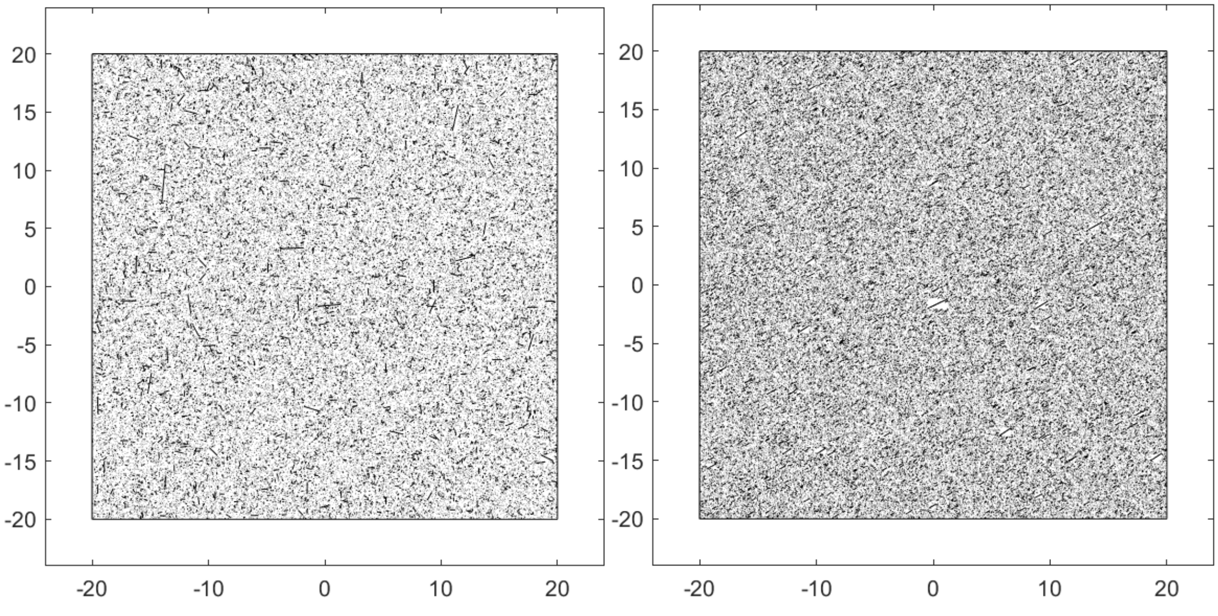

(a) Isotropic domain **(b)** Anisotropic domain

Figure 32: Generated microcrack domains

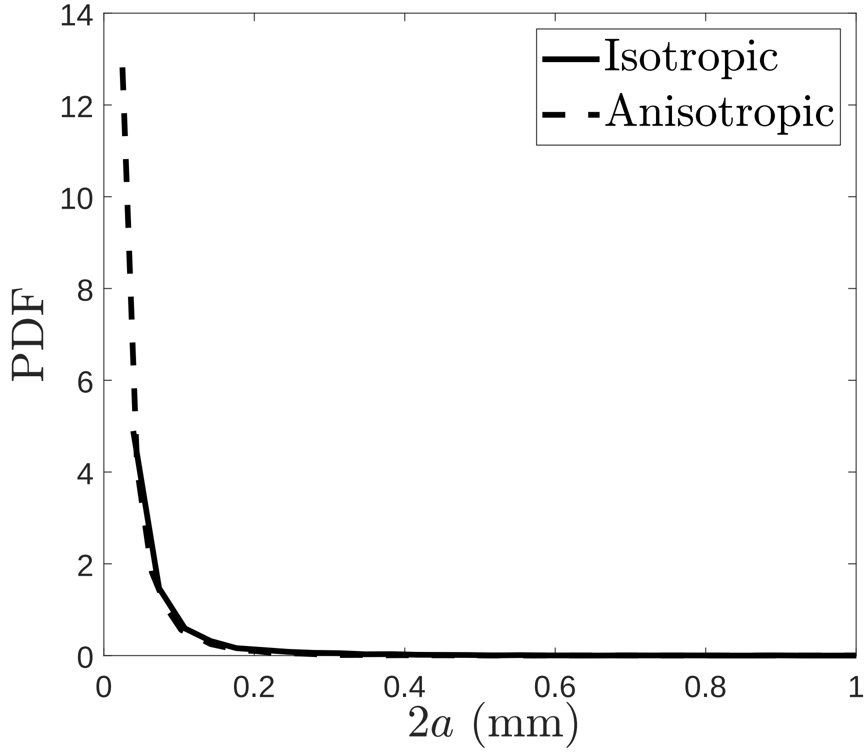

(a) Length $2a$ (mm)

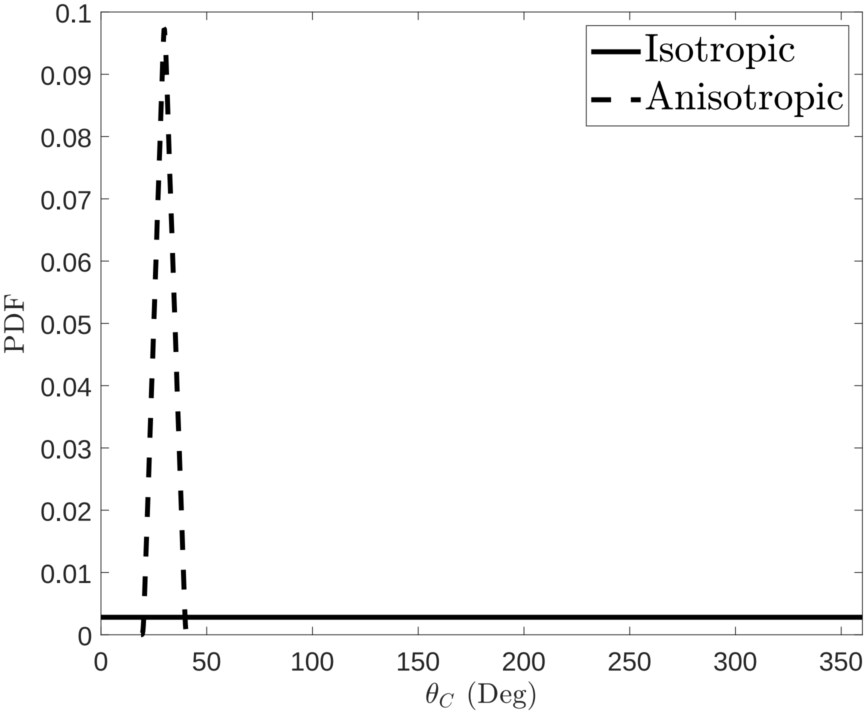

(b) θ_c (degrees)

Figure 33: Generated microcrack domain crack PDFs

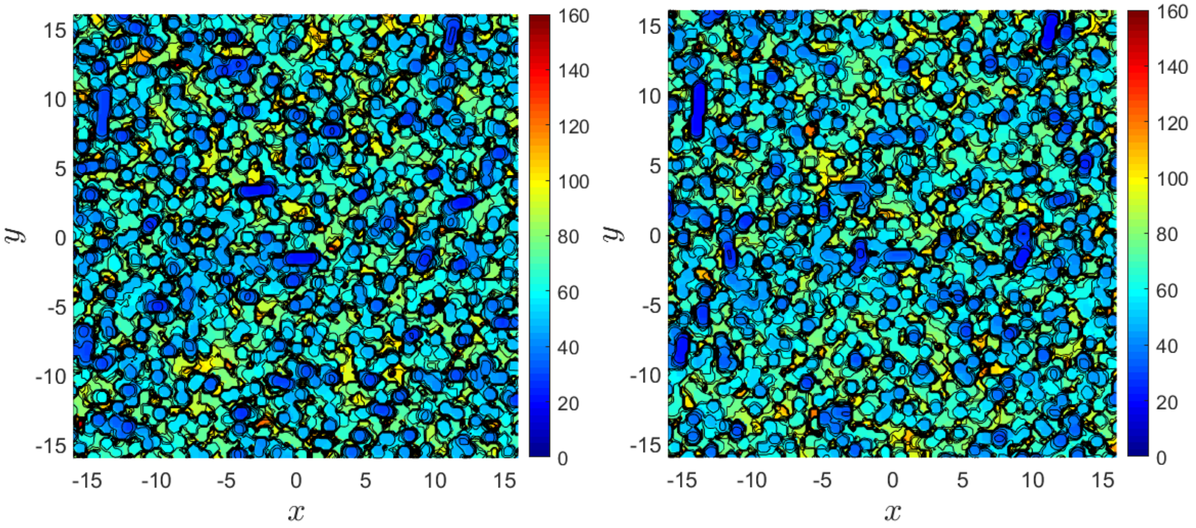

(a) $\theta = 30$ Degrees

(b) $\theta = 60$ Degrees

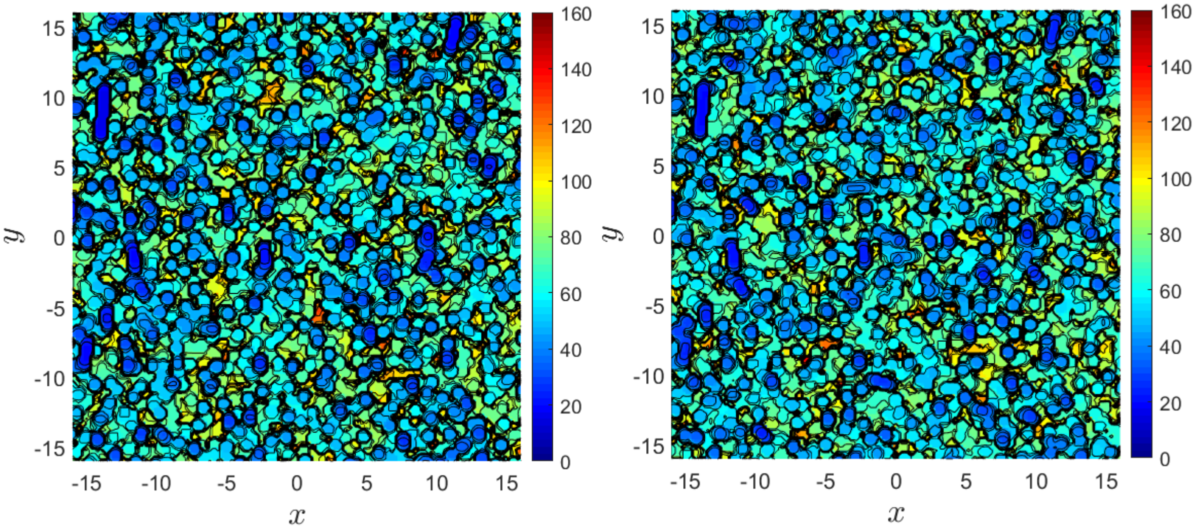

(c) $\theta = 90$ Degrees

(d) $\theta = 120$ Degrees

Figure 34: $S_N(\theta)$ mesoscopic isotropic strength fields ($L_{SVE} = 1$ mm) at various θ

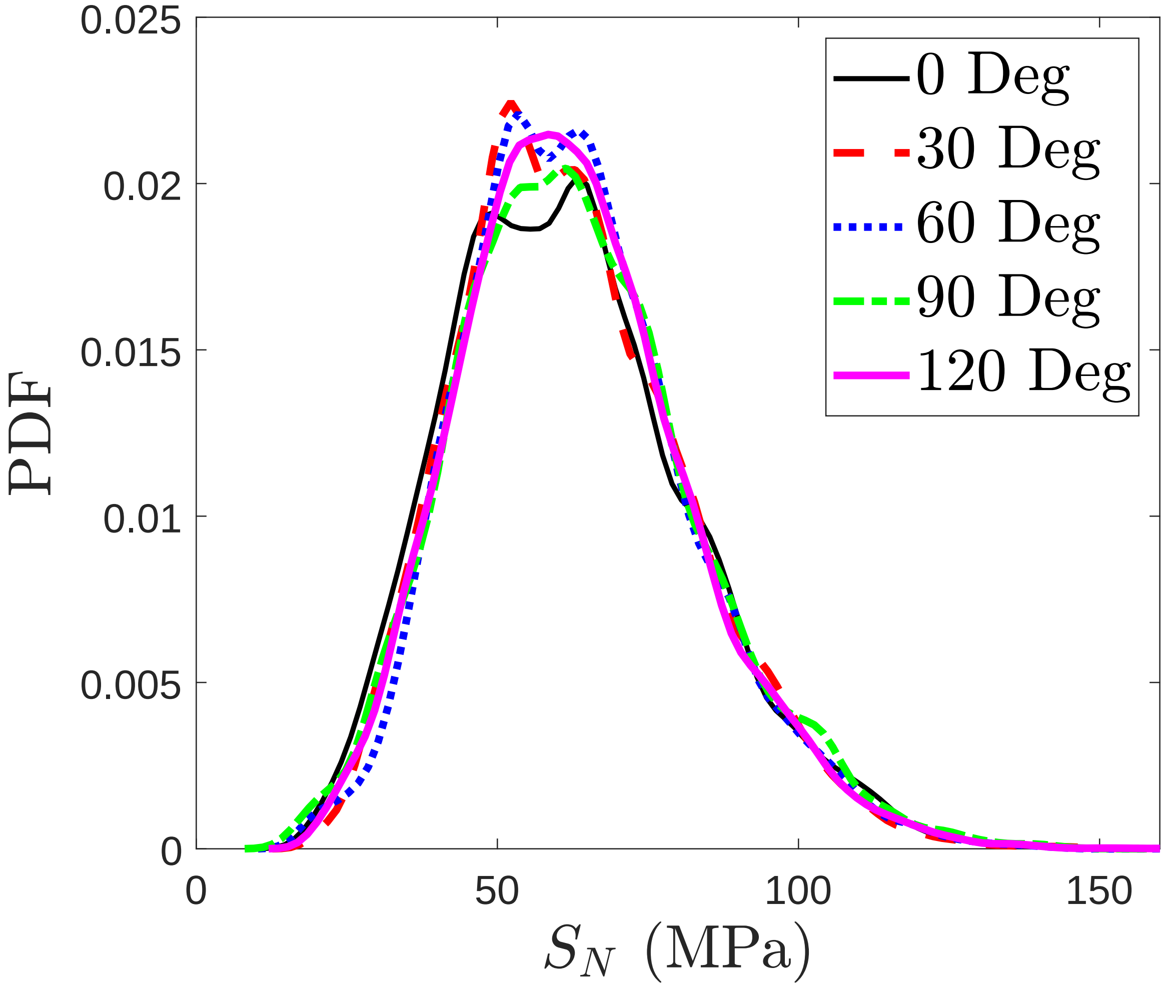

Figure 35: Isotropic $S_N(\theta)$ PDF for varying θ

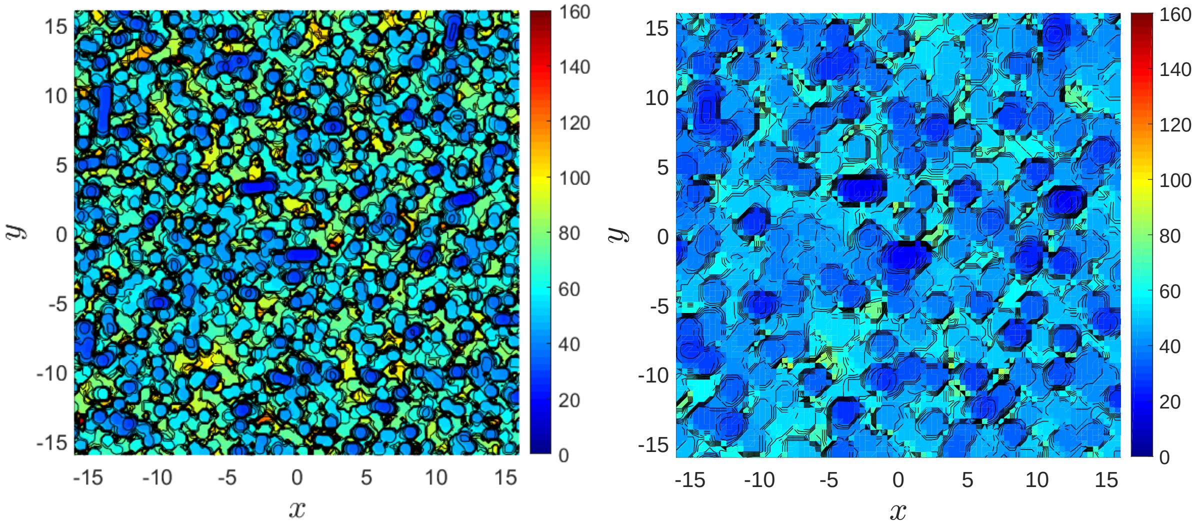

(a) $L_{SVE} = 1$ mm **(b)** $L_{SVE} = 2$ mm

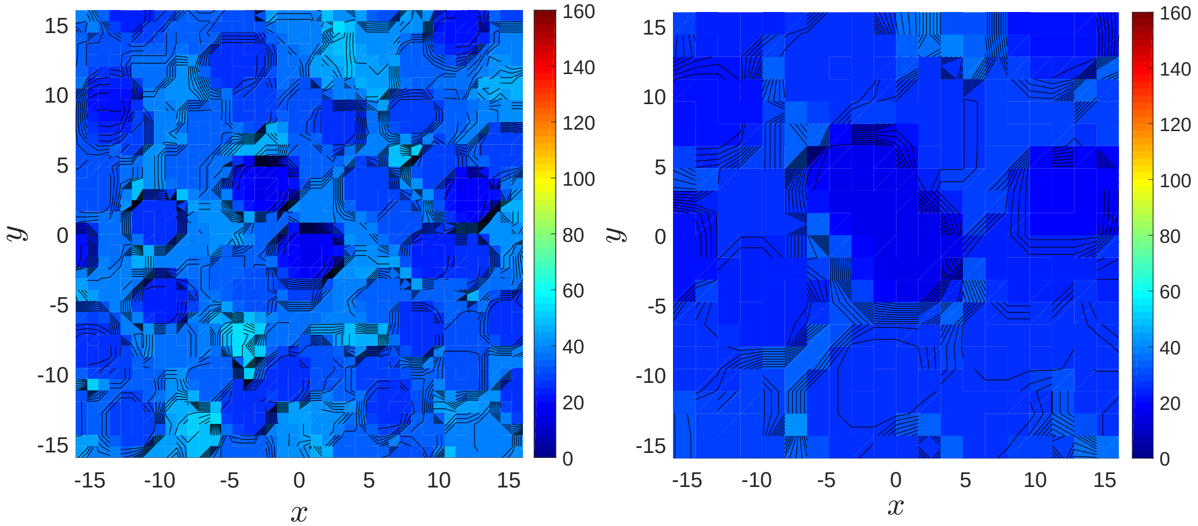

(c) $L_{SVE} = 4$ mm **(d)** $L_{SVE} = 8$ mm

Figure 36: $S_N(\theta)$ mesoscopic isotropic strength fields ($\theta = 0$ deg) for different SVE sizes

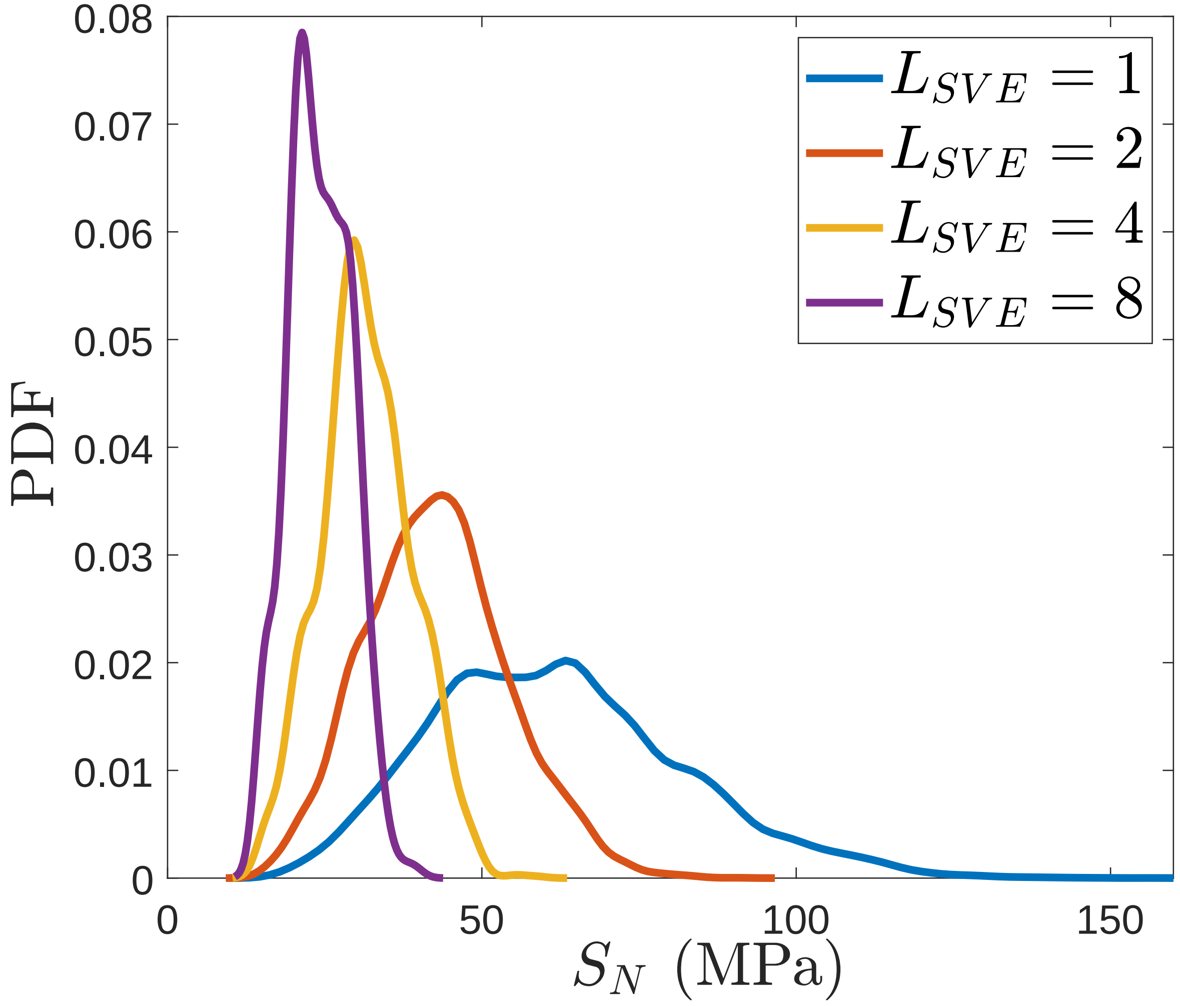

Figure 37: Isotropic S_N PDF for varying SVE size L_{SVE}

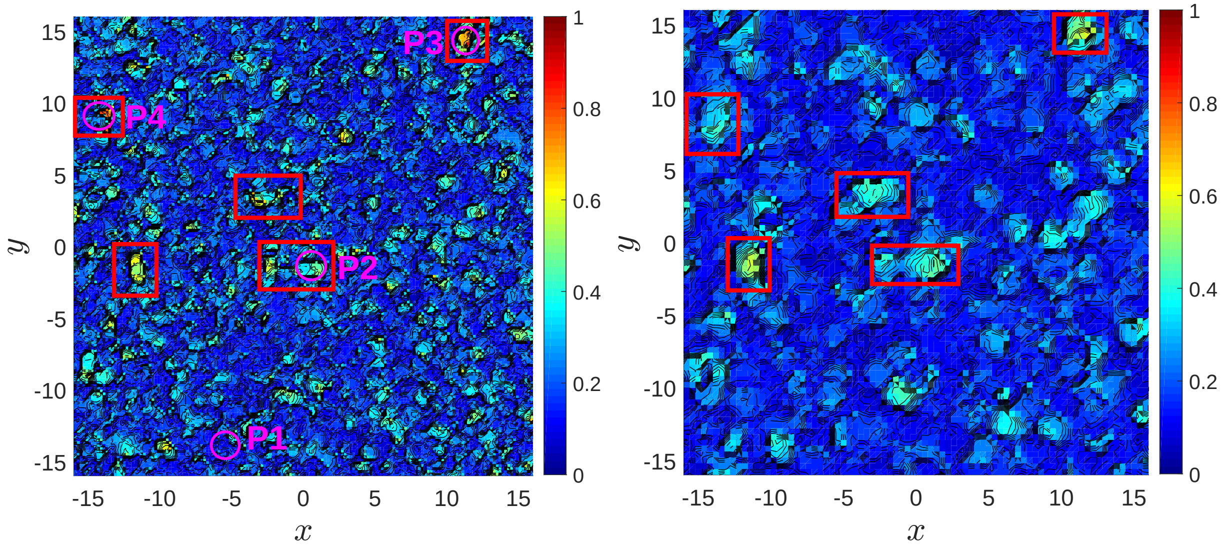

(a) $L_{SVE} = 1$ mm **(b)** $L_{SVE} = 2$ mm

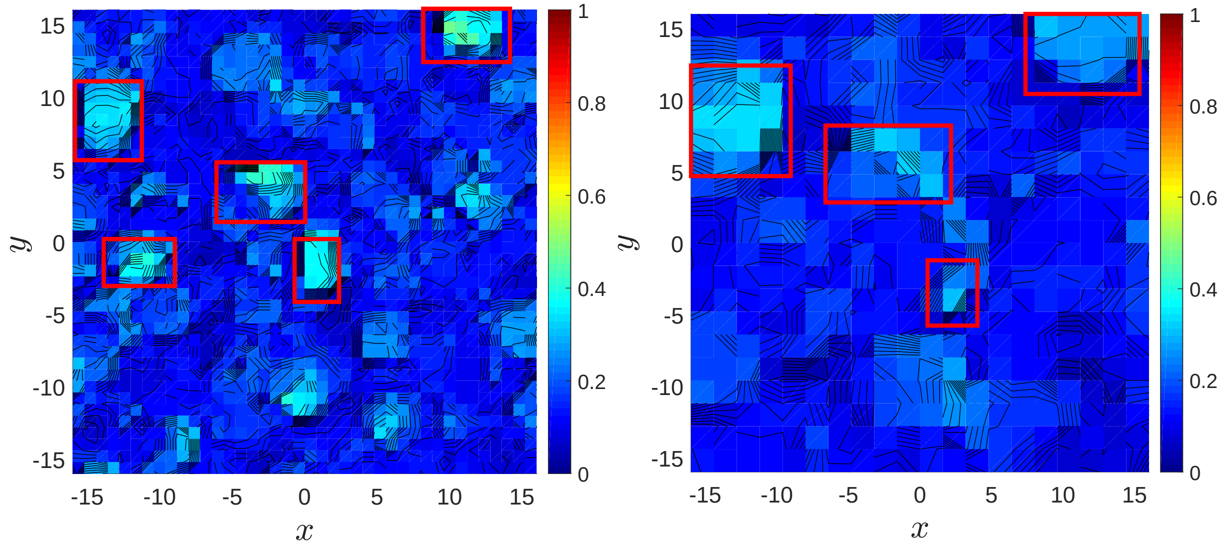

(c) $L_{SVE} = 4$ mm **(d)** $L_{SVE} = 8$ mm

Figure 38: Measure of anisotropy, A_N, for the macroscopically isotropic domain for different SVE sizes

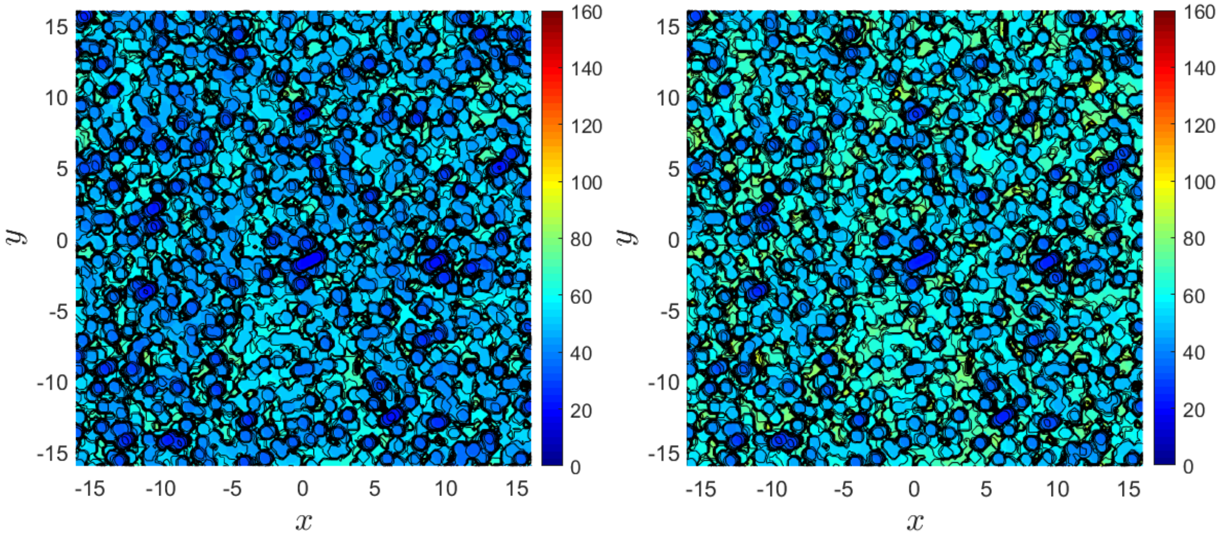

(a) $\theta = 30$ degrees **(b)** $\theta = 60$ degrees

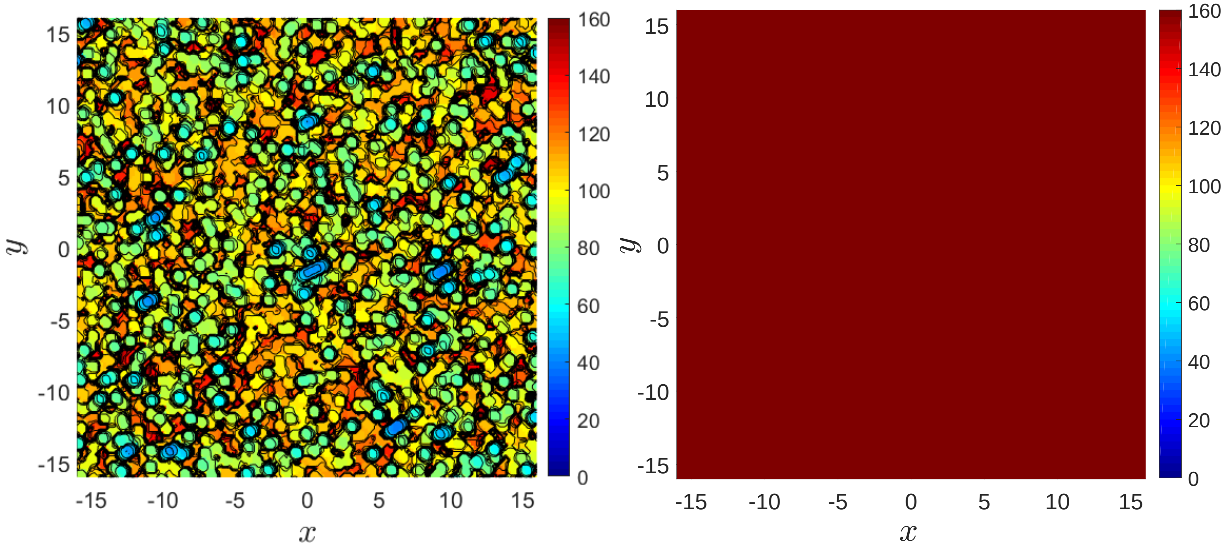

(c) $\theta = 90$ degrees **(d)** $\theta = 120$ degrees

Figure 39: S_N mesoscopic anisotropic strength fields ($L_{SVE} = 1$ mm) at various loading angles

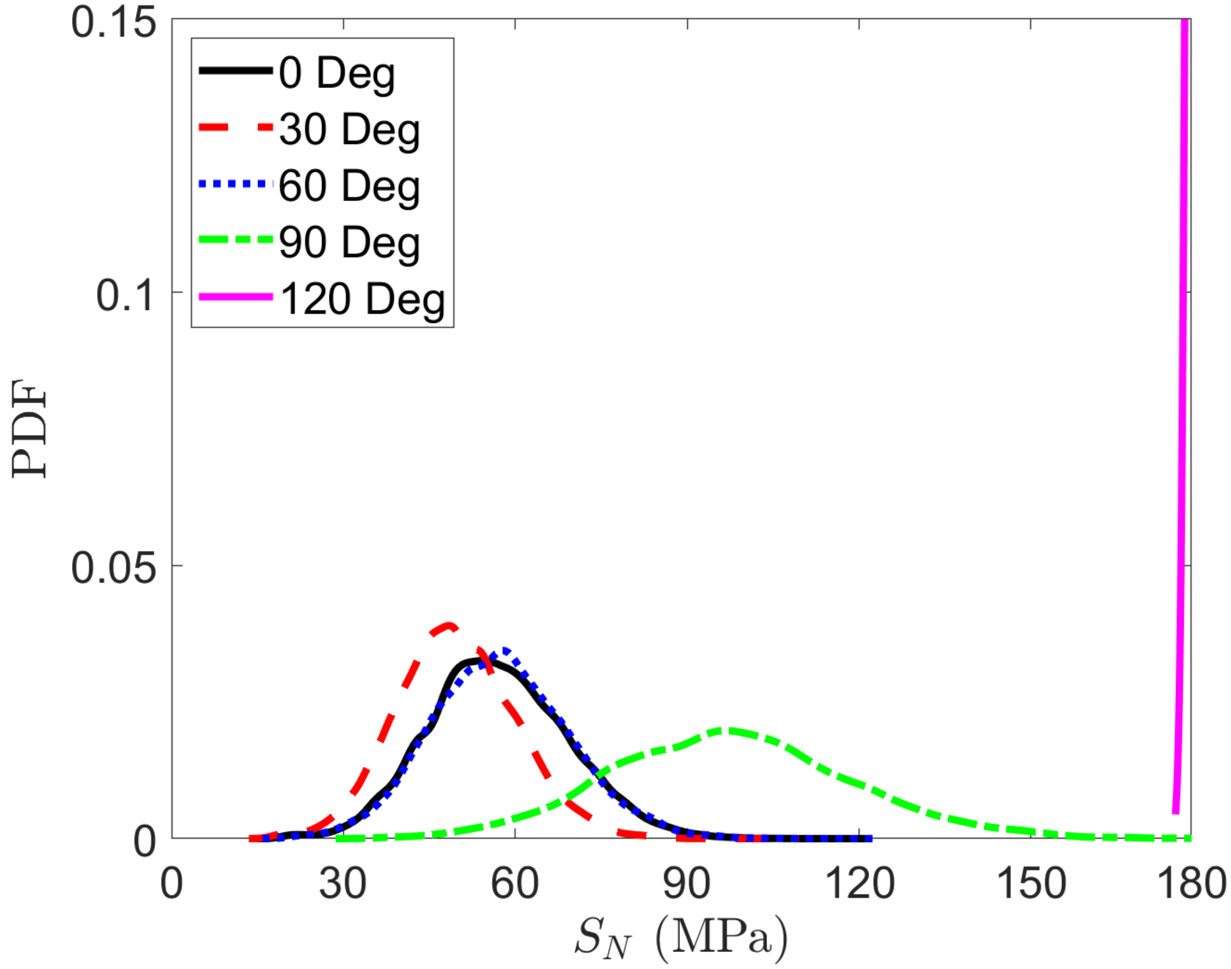

Figure 40: Anisotropic S_N PDF for varying θ

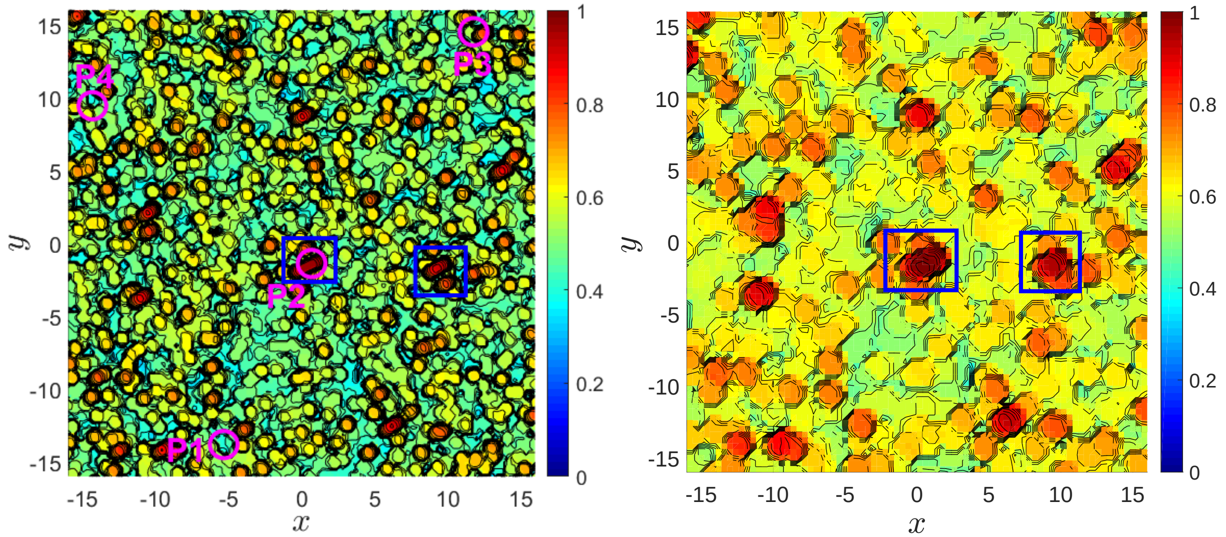

(a) $L_{SVE} = 1$ mm **(b)** $L_{SVE} = 2$ mm

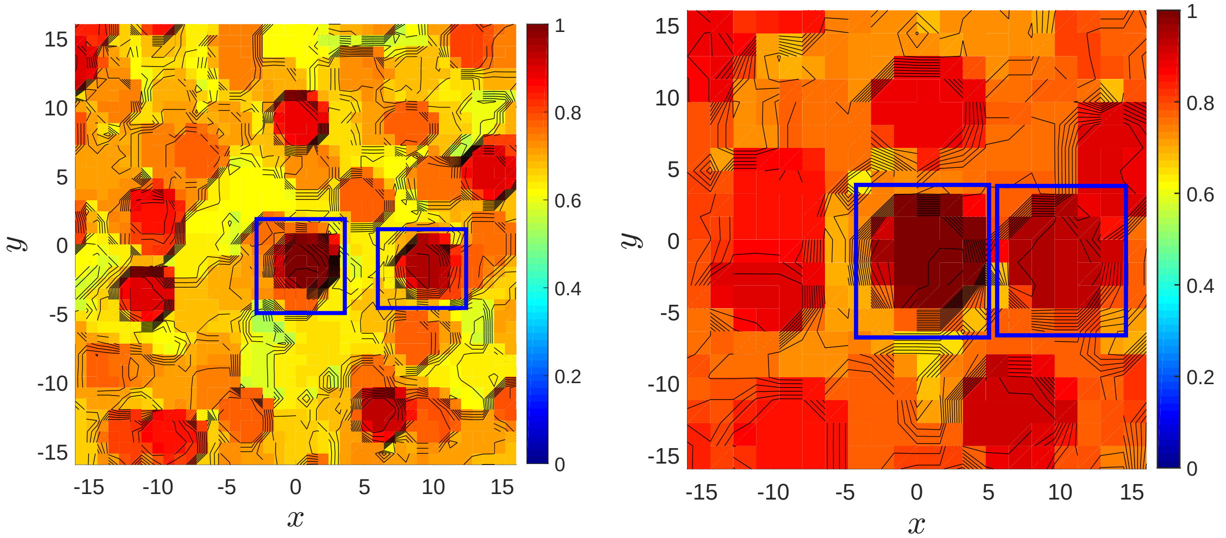

(c) $L_{SVE} = 4$ mm **(d)** $L_{SVE} = 8$ mm

Figure 41: The measure of anisotropy, A_N, for the anisotropic domain for different SVE sizes

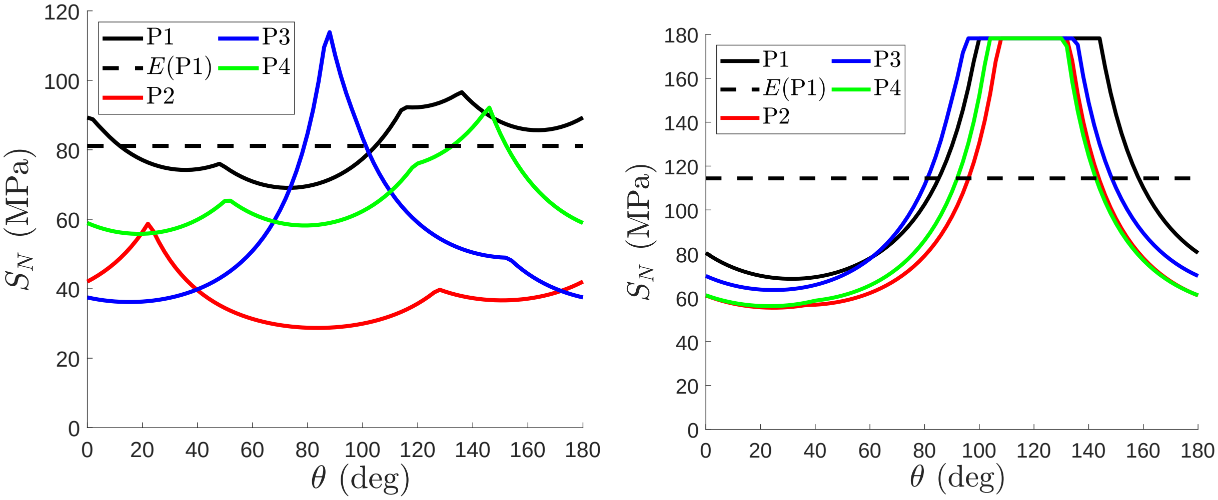

(a) Isotropic Domain **(b)** Anisotropic Domain

Figure 42: $S_N(\theta)$ for four $L_{SVE} = 1$ mm SVEs with different measures of anisotropy A_N, $\theta = [0, 180]$ degrees

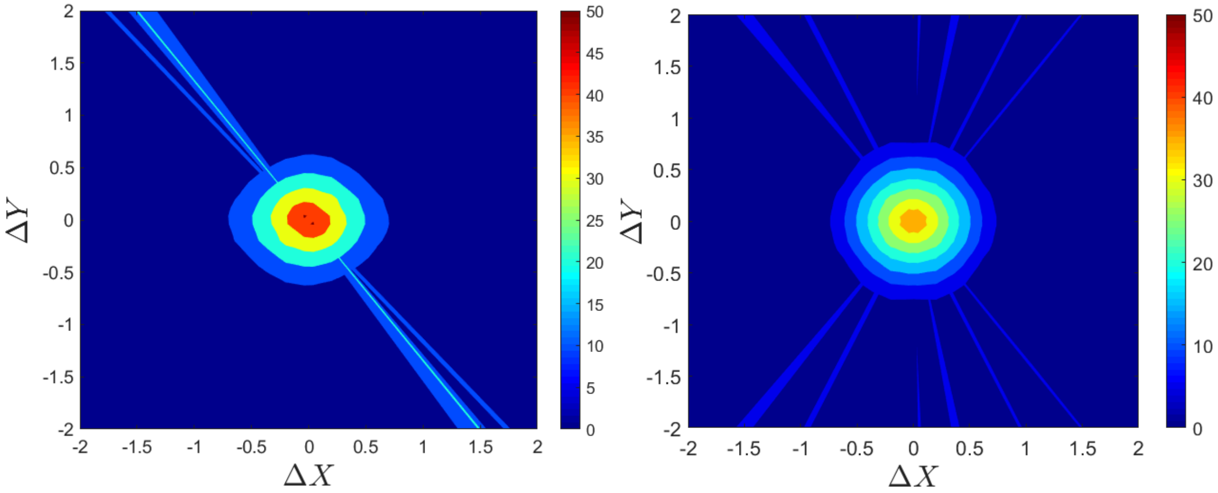

(a) Isotropic domain **(b)** Anisotropic domain

Figure 43: Spatial covariance function for strength field S_N, $\text{cov}_{\mathbf{X}N}$

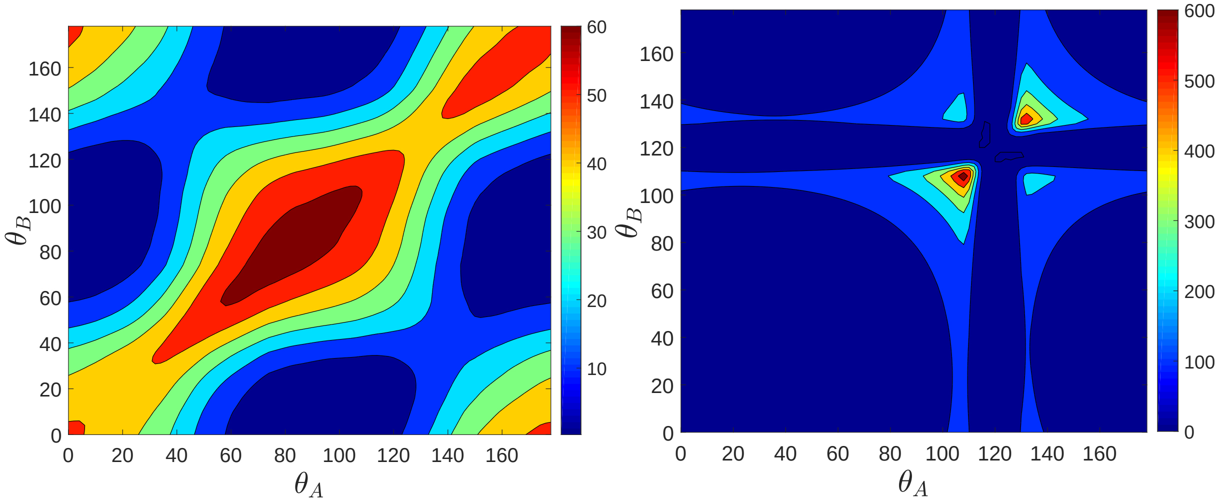

(a) Isotropic domain **(b)** Anisotropic domain

Figure 44: Angular covariance function for strength field S_N, $\text{cov}_{\theta N}$

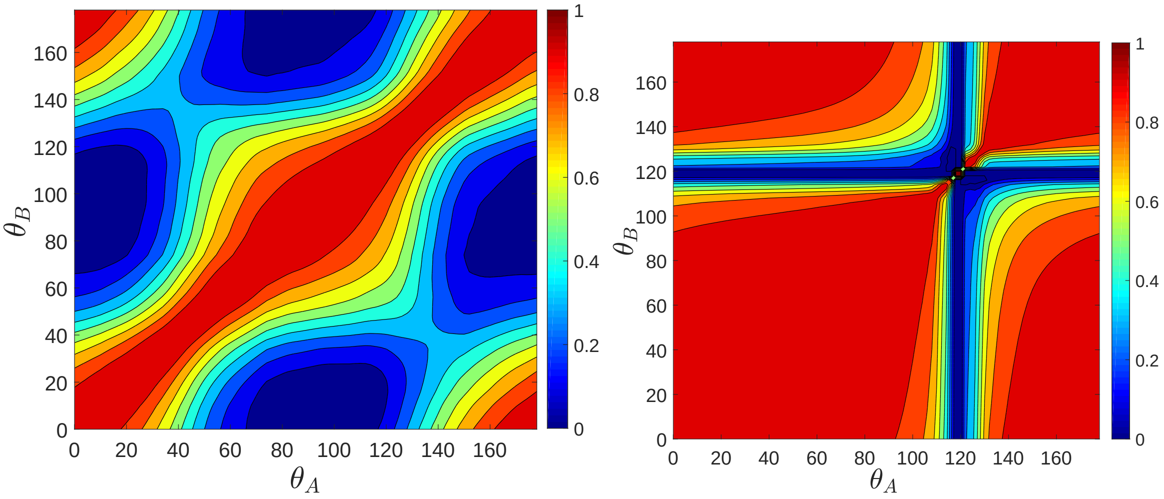

(a) Isotropic domain **(b)** Anisotropic domain

Figure 45: Angular correlation function for strength field S_N

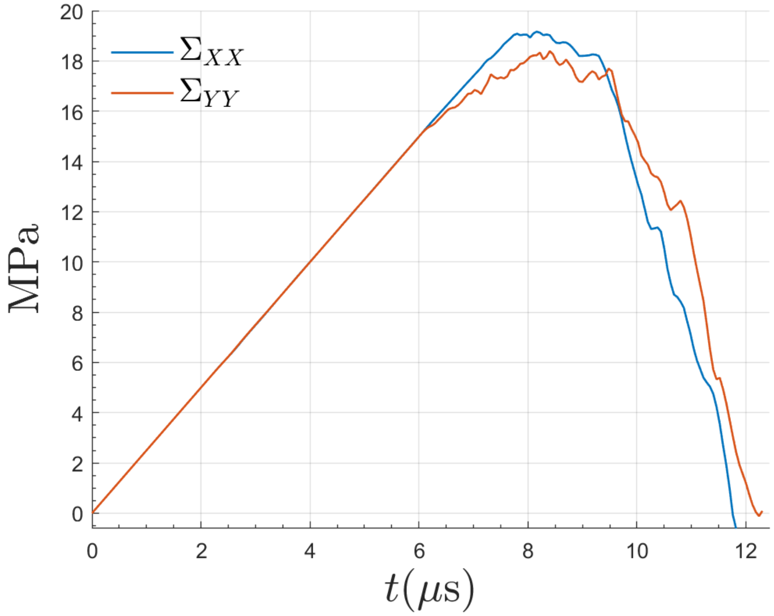

(a) Isotropic domain

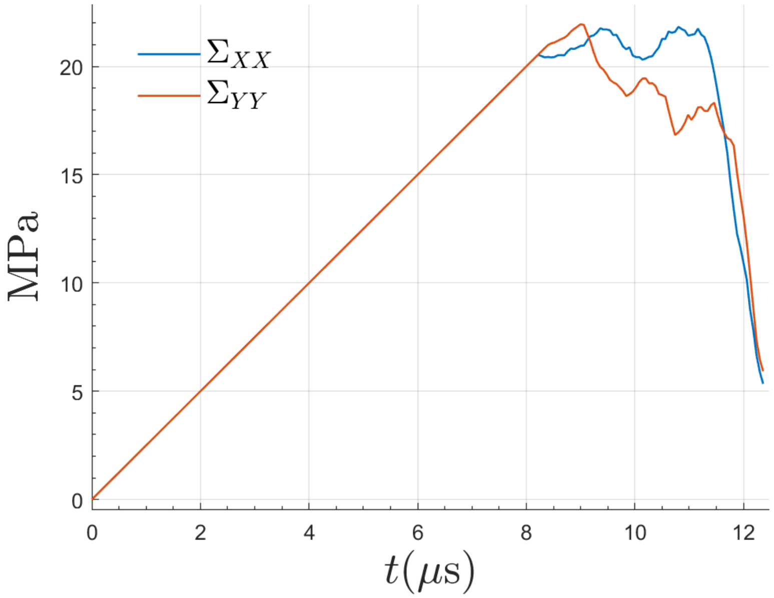

(b) Anisotropic domain

Figure 46: Macroscopic tensile strain-stress response in x and y directions

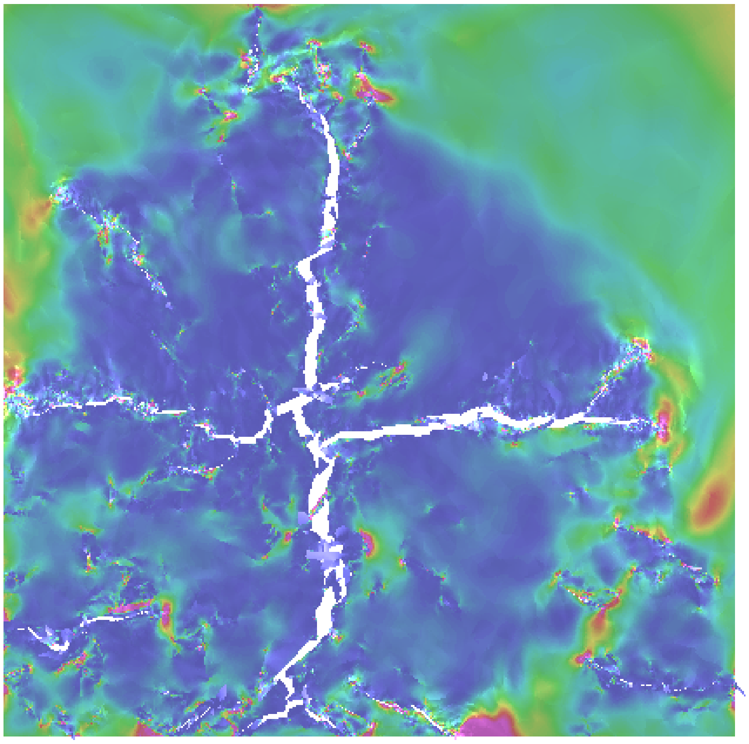

(a) Isotropic domain

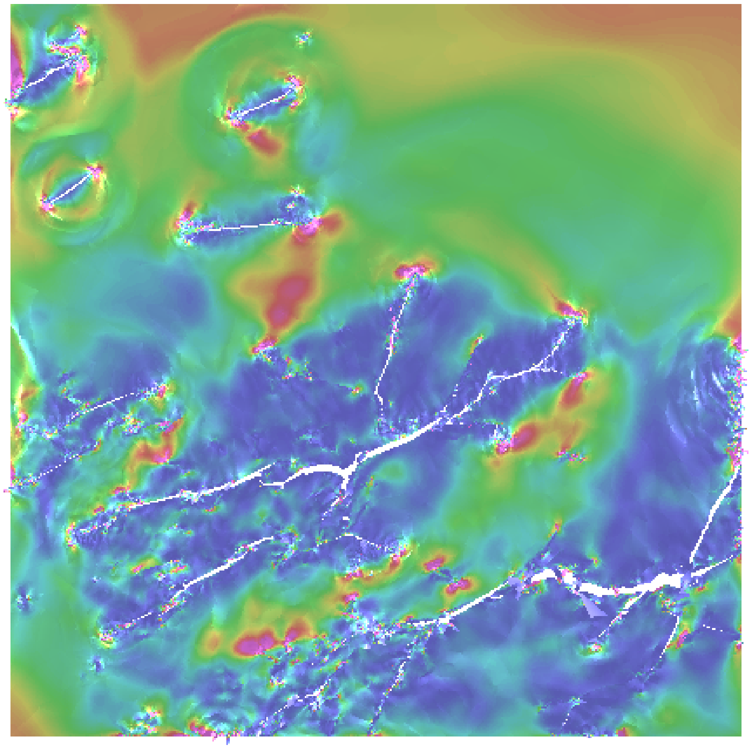

(b) Anisotropic domain

Figure 47: Strain and kinetic energy densities at $t = 12$ μs

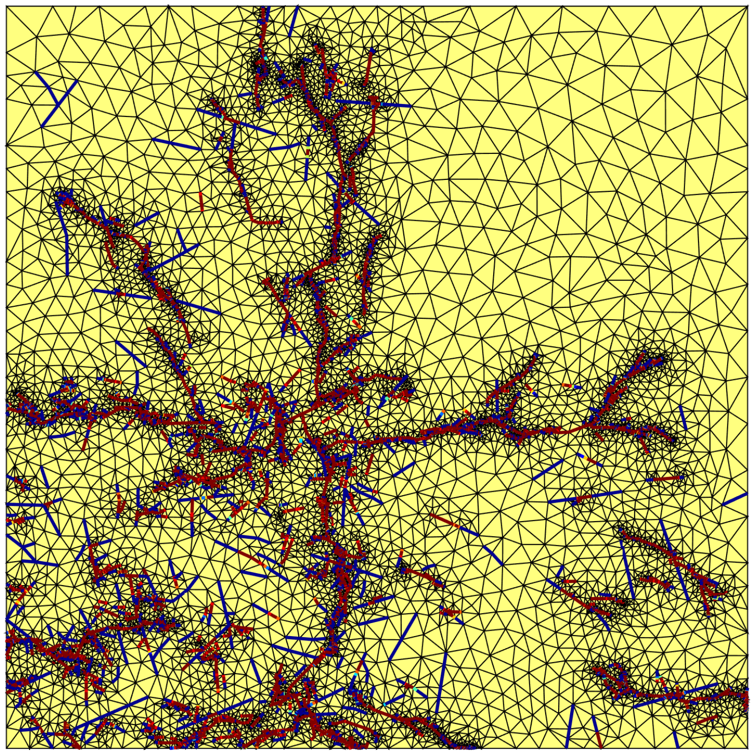

(a) Isotropic domain

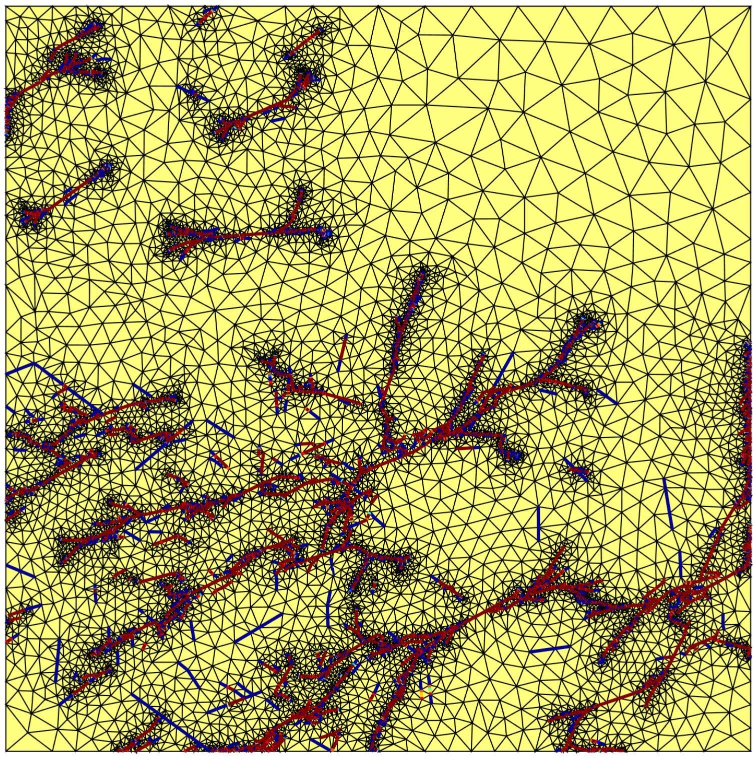

(b) Anisotropic domain

Figure 48: aSDG front mesh at $t = 12\ \mu$s

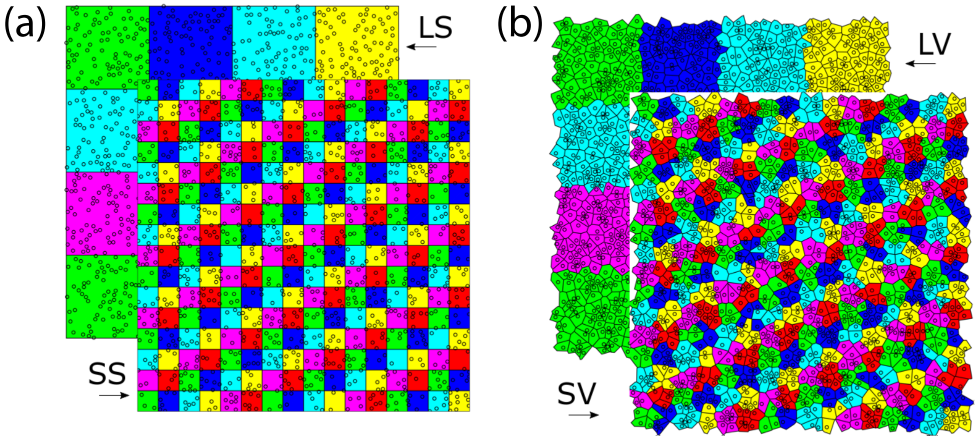

Figure 49: (a) Large Square regular (LS) and Small Square regular (SS) and (b) Large square Voronoi (LV) and Small square Voronoi (SV) RVE partitioning. Each separately colored region represents an SVE. Here, larger partition sizes have $\delta = 25$, smaller sizes $\delta = 6.25$.

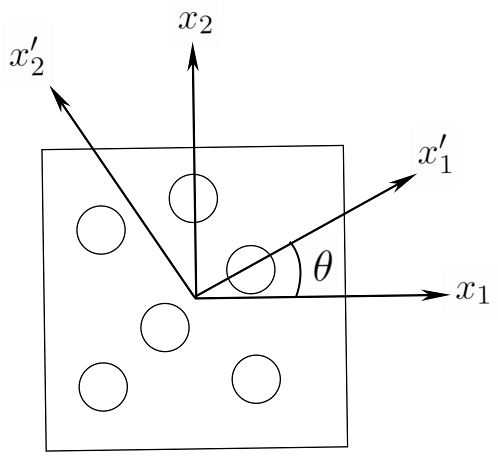

Figure 50: Rotation of SVE from global coordinate system (x_1, x_2) to arbitrary coordinate system (x'_1, x'_2) by angle θ

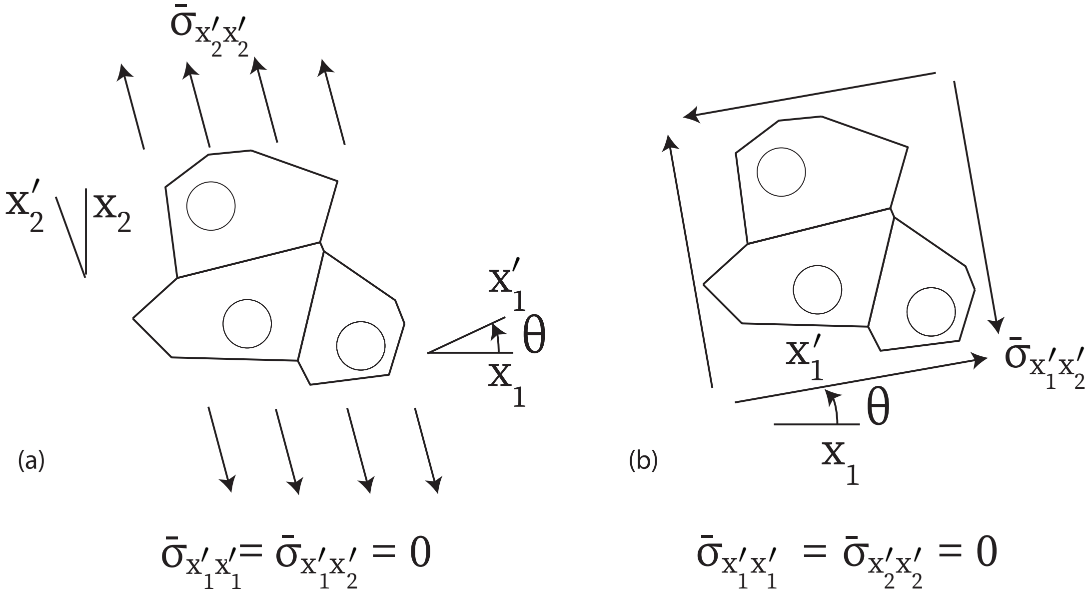

Figure 51: Sample SVE under uniaxial and shear loading conditions

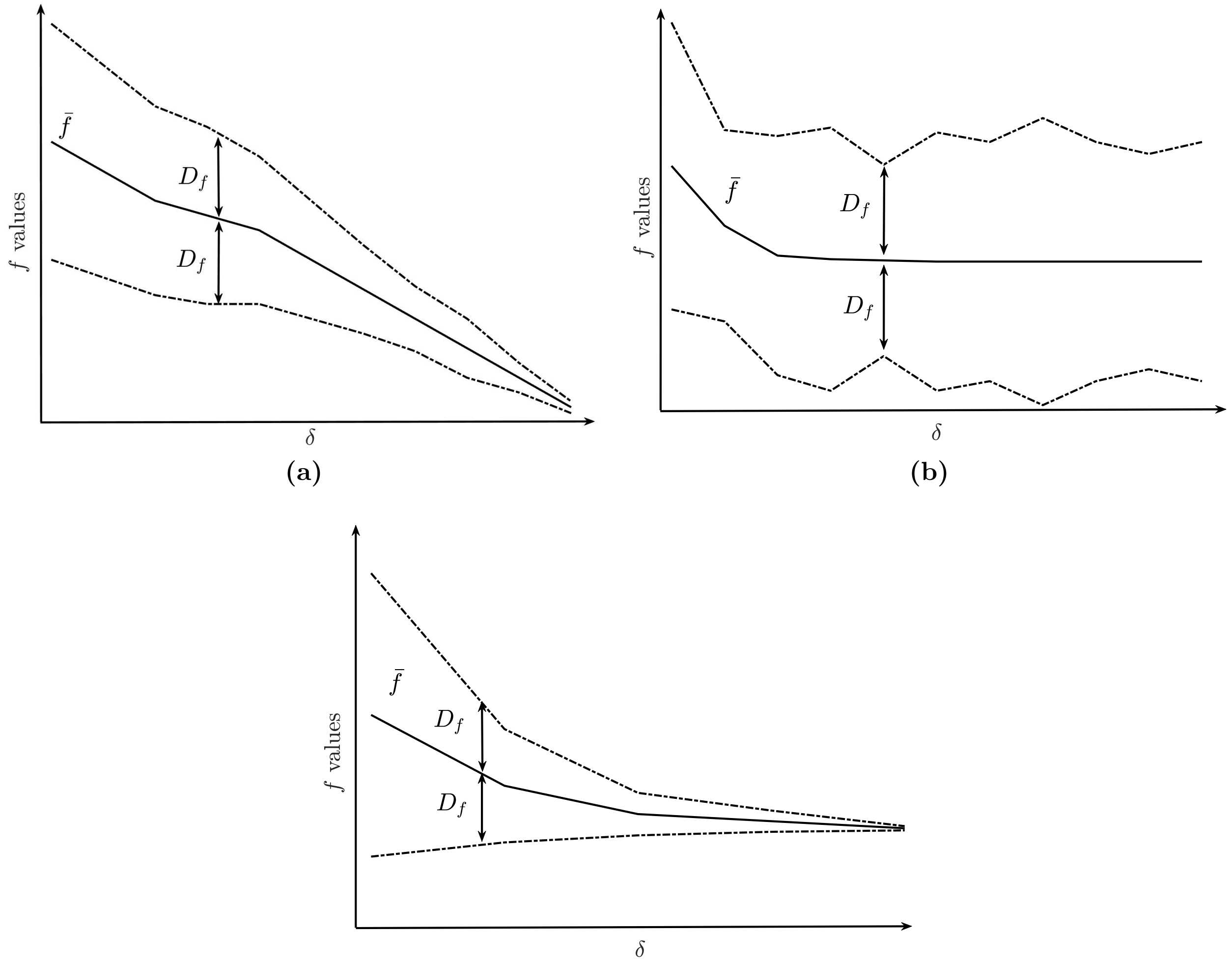

(a) **(b)**

(c)

Figure 52: In each schematic diagram, f represents any scalar material property field. This figure depicts three potential cases for RVE convergence (a) shows an unstable mean $\bar{f}$ with a converged variation D_f (b) shows $\bar{f}$ reaching a terminal value with an unstable, large D_f (c) is the most conservative case with the mean $\bar{f}$ reaching a terminal value and the variation D_f diminishing as δ increases.

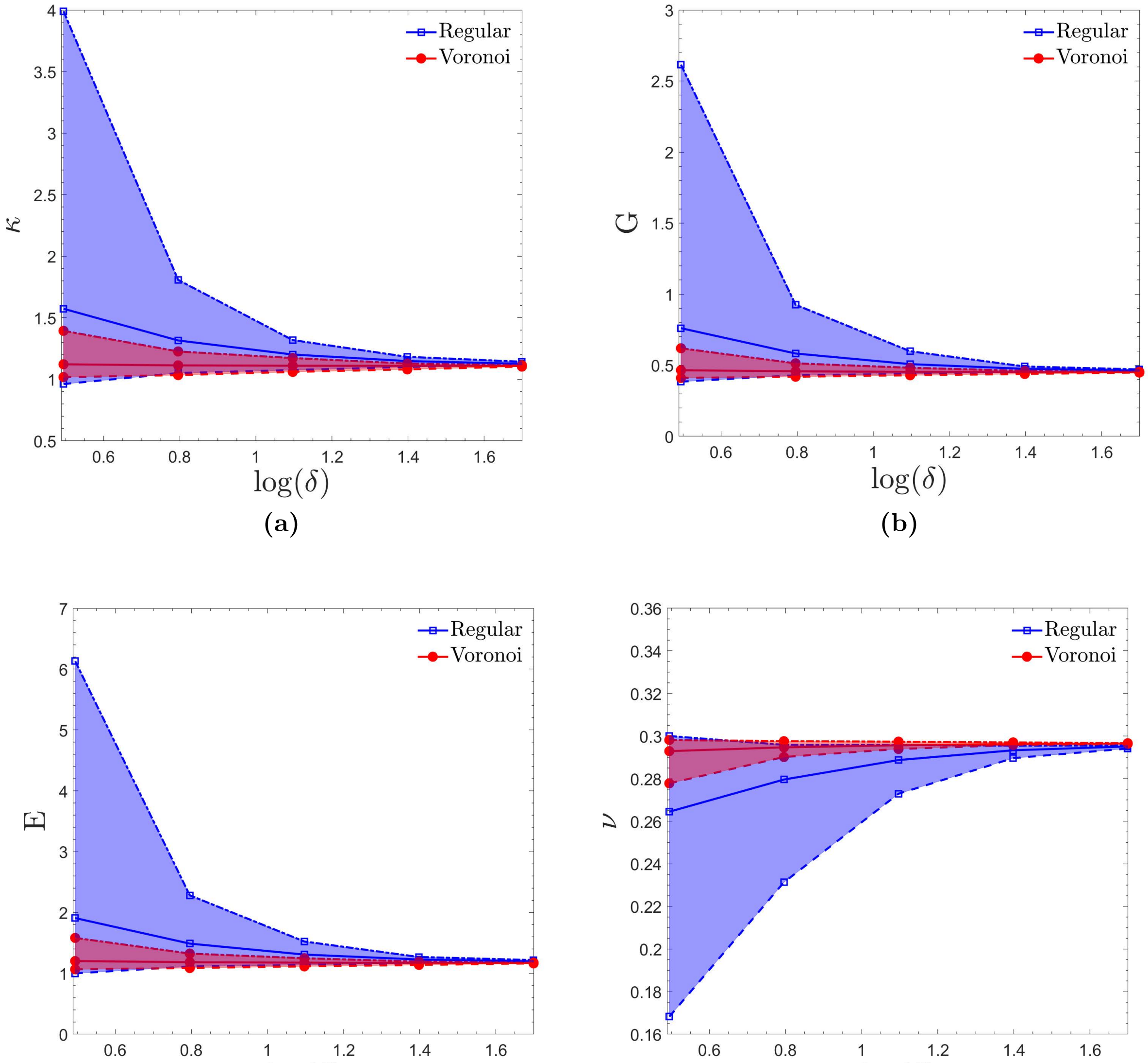

(a) **(b)**

(c) **(d)**

Figure 53: Mean, maximum, and minimum values for elastic properties κ, G, E, and ν for different δ sizes

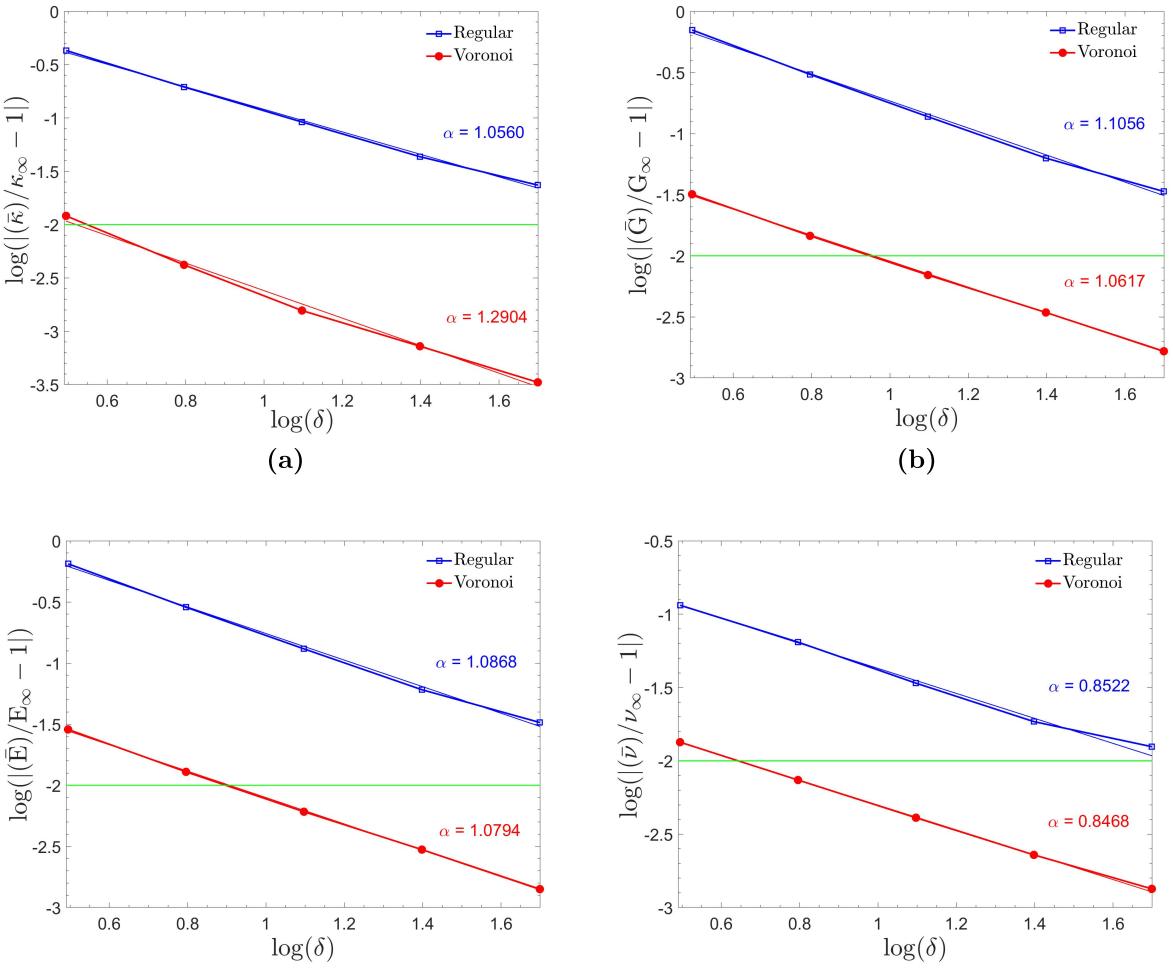

(a) **(b)**

(c) **(d)**

Figure 54: Convergence of VE size to $\Delta^{\bar{f}}$ for elastic properties κ, G, E, and ν

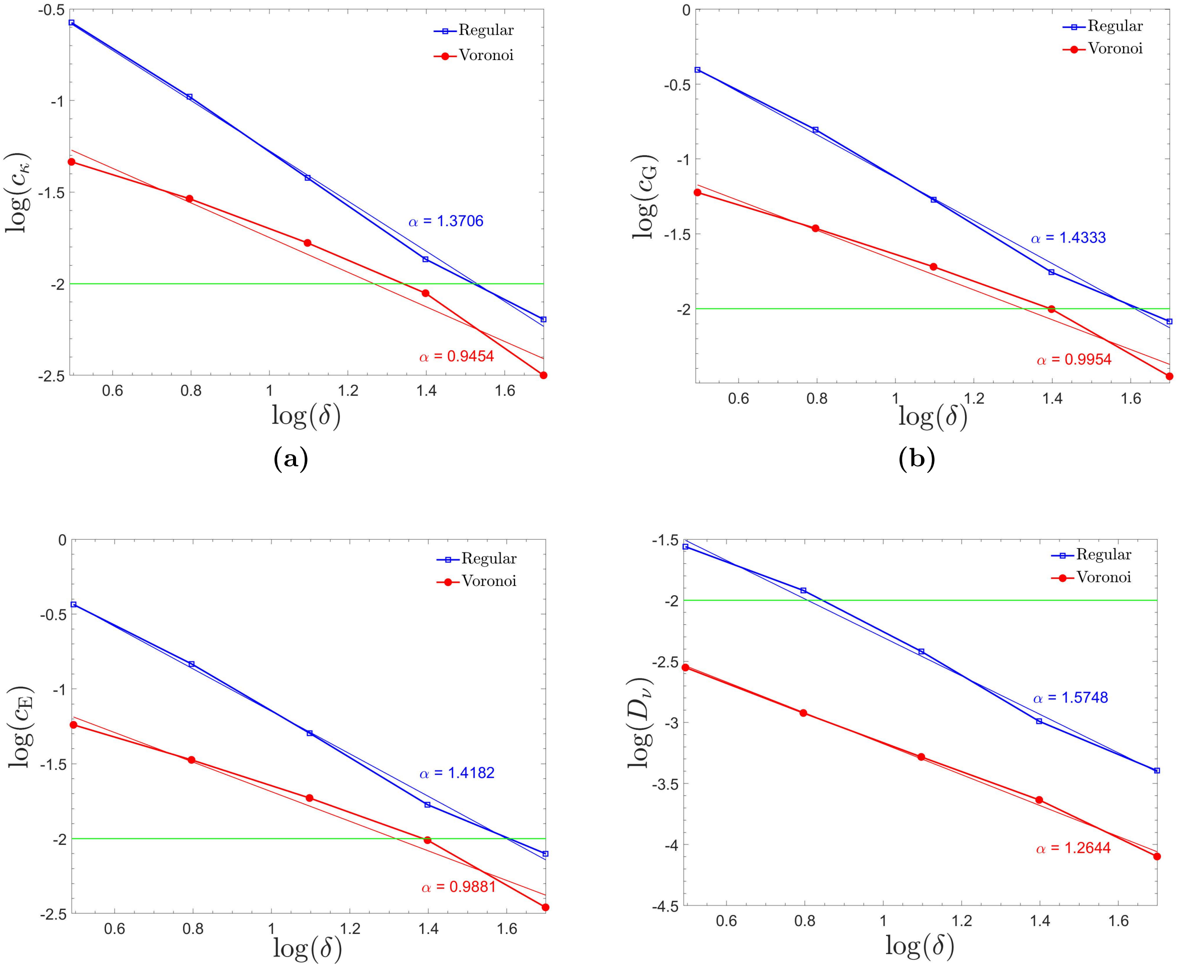

(a) **(b)**

(c) **(d)**

Figure 55: Convergence of VE size to Δ^{c_f} for elastic properties κ, G, E, and ν.

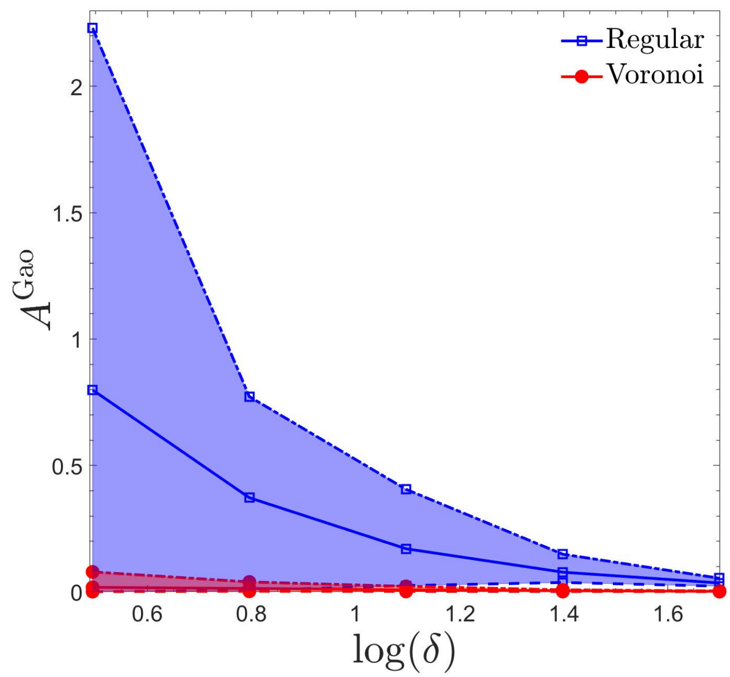

Figure 56: Mean, minimum, and maximum values for elastic anisotropy measure A^{Gao} for different δ sizes

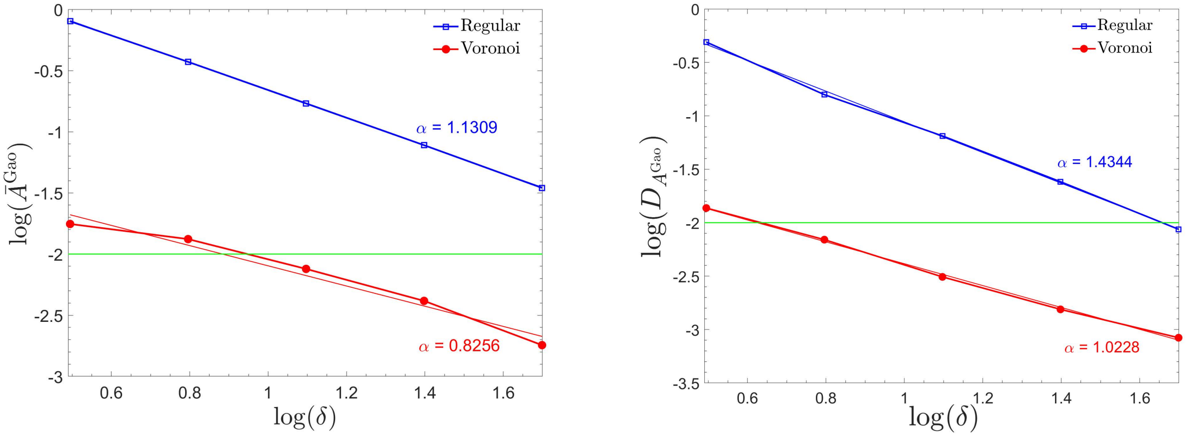

(a) $\Delta^{\bar{A}^{\text{Gao}}}$ **(b)** $\Delta^{D_{A^{\text{Gao}}}}$

Figure 57: Convergence of VE size to $\Delta^{\bar{A}^{\text{Gao}}}$ and $\Delta^{D_{A^{\text{Gao}}}}$ for elastic anisotropy measure A^{Gao}.

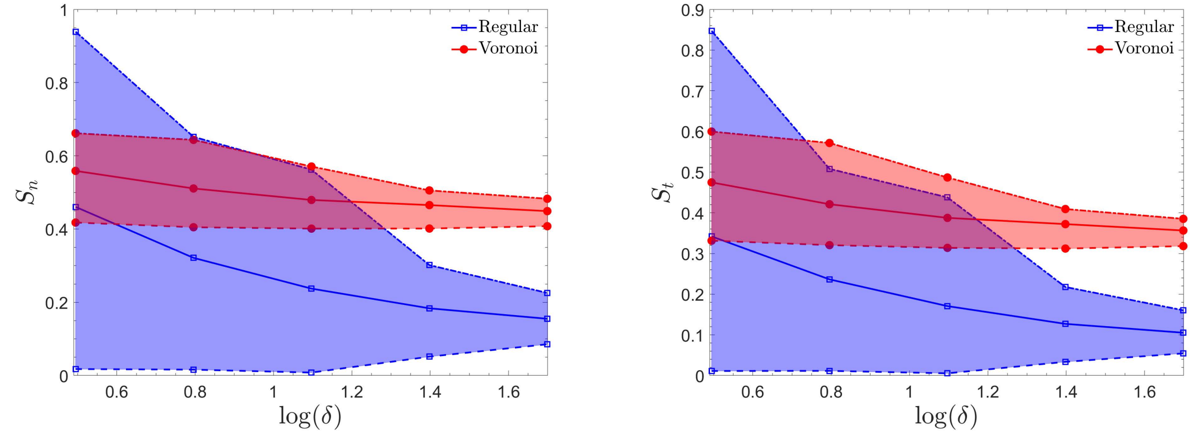

(a) S_n **(b)** S_t

Figure 58: Mean, maximum, and minimum values for fracture properties S_n and S_t for different δ sizes

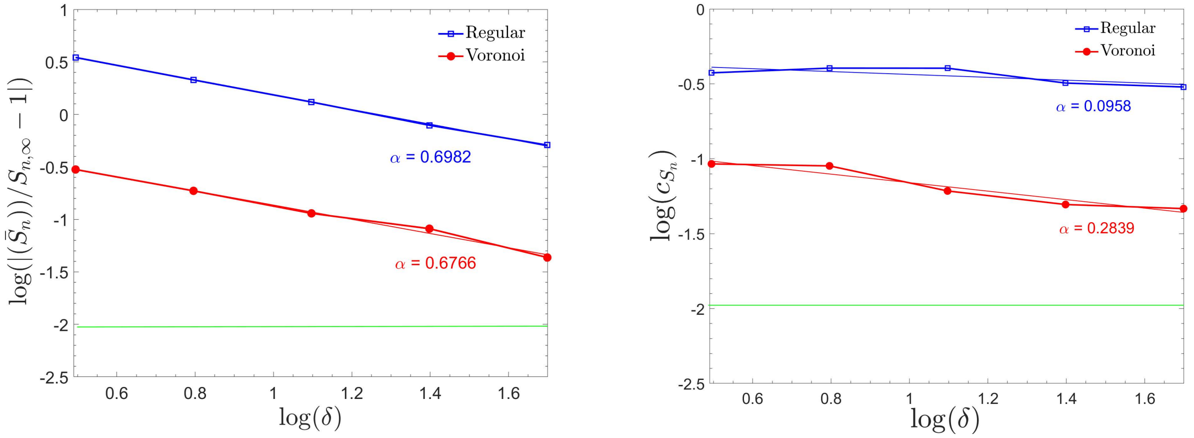

(a) $\Delta^{\bar{S}_n}$ **(b)** $\Delta^{c_{S_n}}$

Figure 59: Convergence of VE size to $\Delta^{\bar{S}_n}$ and $\Delta^{c_{S_n}}$ for fracture property S_n.

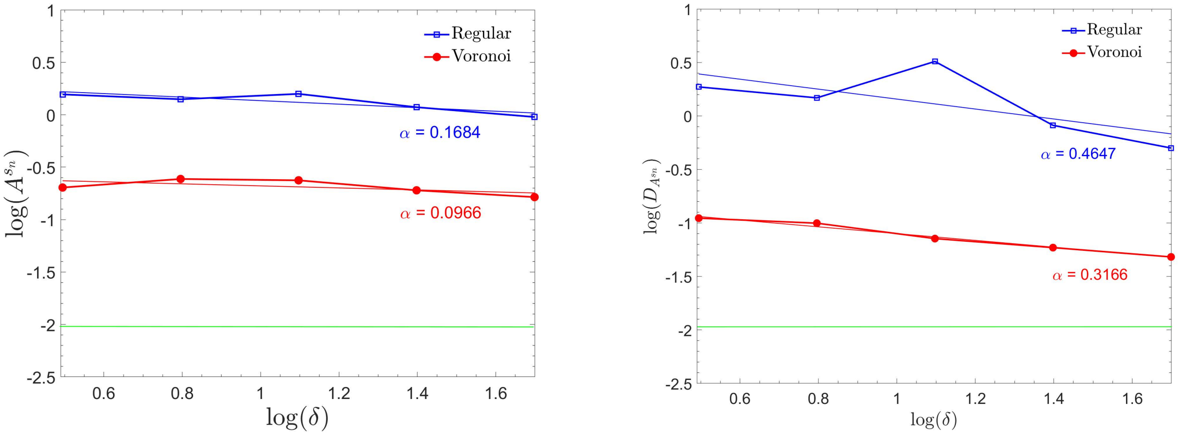

(a) $\Delta^{\bar{A}^{s_n}}$ **(b)** $\Delta^{D_{A^{s_n}}}$

Figure 60: Convergence of VE size to to $\Delta^{\bar{A}^{s_n}}$ and $\Delta^{D_{A^{s_n}}}$ for fracture anisotropy measure A^{s_n}.

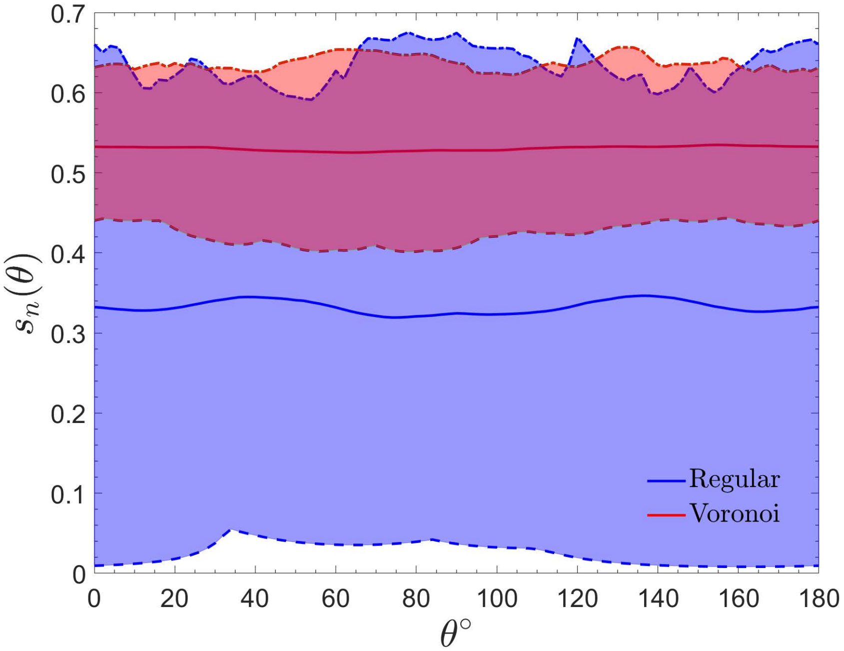

Figure 61: Mean, minimum, and maximum fracture strength $s_n(\theta)$ at different loading angles θ and SVE types for $\delta = 12.5$.

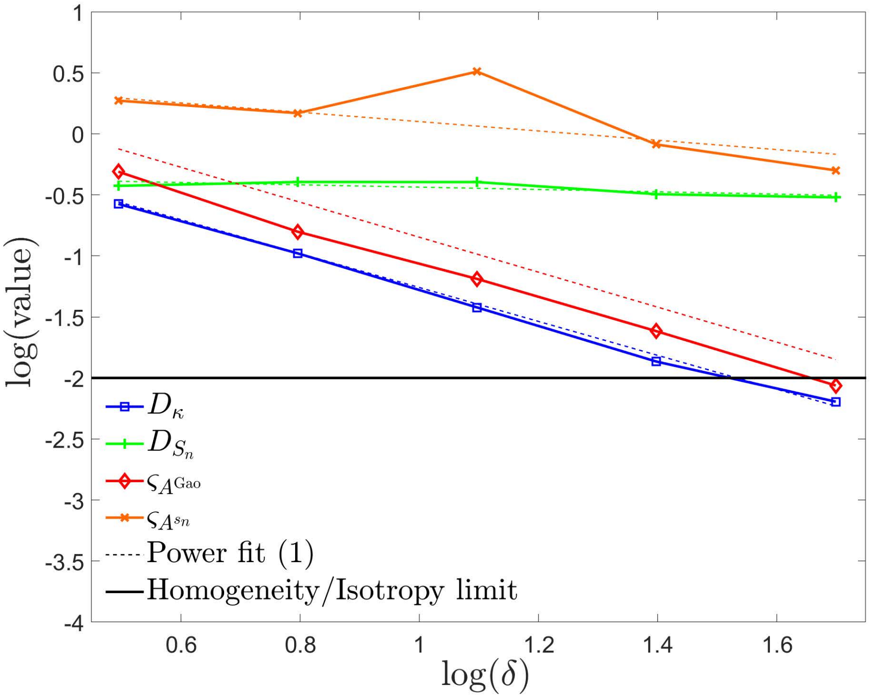

(a) Regular

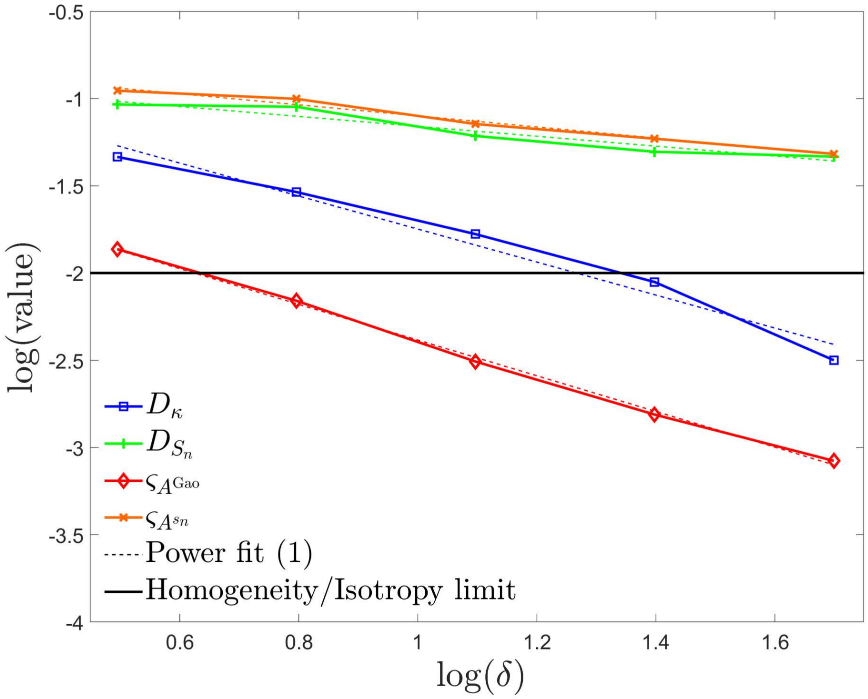

(b) Voronoi

Figure 62: Convergence of SVEs to RVE size for elastic and fracture properties for regular and Voronoi SVEs.

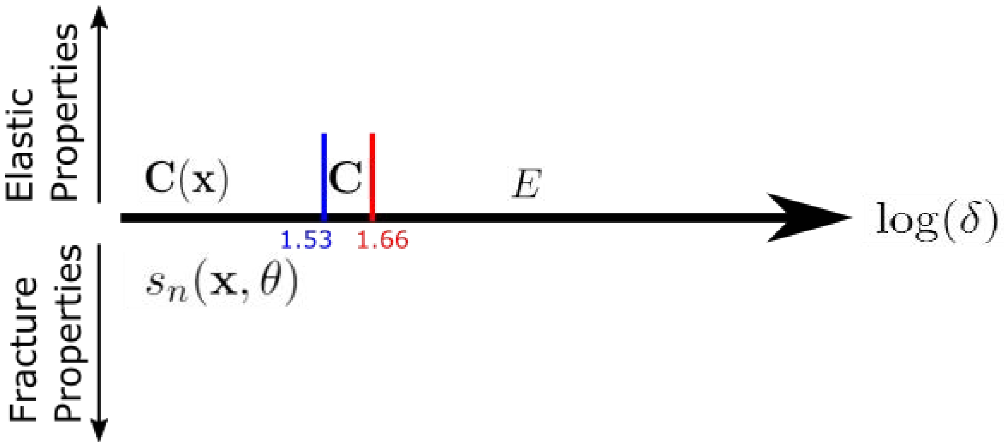

(a) Regular

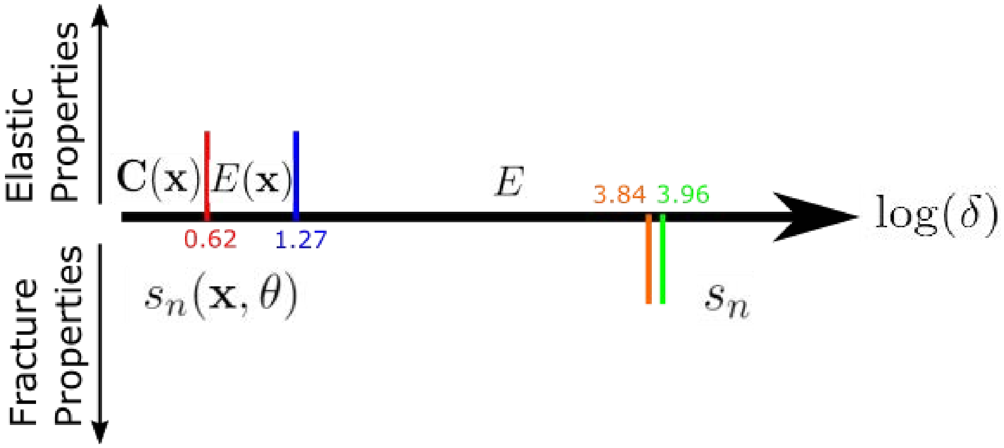

(b) Voronoi

Figure 63: Summary of Convergence to the Homogeneous and Isotropic Δ limits for regular and Voronoi SVE types. Regular SVEs converge slowly from inhomogeneous/anisotropic $\mathbf{C}(\mathbf{x})$ elastic field to anisotropic/homogeneous $\mathbf{C}$ before reaching ideal homogeneous/isotropic E, while fracture remains inhomogeneous/anisotropic throughout. Voronoi converges faster from $\mathbf{C}(\mathbf{x})$ to inhomogeneous elastic modulus $E((\mathbf{x}))$. For all reasonable sizes δ strength remains inhomogeneous/anisotropic even for Voronoi. Figure colors match the given properties in Figure 62.

B Tables

Table 1: Sample S19 material properties taken from [159]

ρ (kg/m^3)	ν	E (GPa)	$2a$ (mm)	a' (mm)	ε_0	z	q^*V_0
2727	0.25	34.65	0.141	0.0075	0.243	2.017	0.007

Table 2: Important quantities of macroscopic tensile strain-stress response in y direction

	m	$\frac{1}{2}$	1	2	4
Initiation of nonlinear response	$\tilde{t}_i$ (μs)	46	110	130.8	197.2
	$\tilde{E}_i$	6.44×10^{-5}	1.54×10^{-4}	1.83×10^{-4}	2.76×10^{-4}
	$\tilde{\Sigma}_i$ (MPa)	**4.60**	**11.0**	**13.1**	**19.7**
	$\tilde{\psi}_i$ (J/m^3)	148	847	1199	2719
Maximum stress	$\tilde{t}_m$ (μs)	67.2	111.2	148.8	198
	$\tilde{E}_m$	9.41×10^{-5}	1.56×10^{-4}	2.08×10^{-4}	2.77×10^{-4}
	$\tilde{\Sigma}_m$ (MPa)	**6.0**	**11.1**	**14.9**	**19.8**
	$\tilde{\psi}_m$ (J/m^3)	351	921	1666	2832
Failure	$\tilde{t}_f$ (μs)	76.7	117.2	156.4	203.0
	$\tilde{E}_f$	1.07×10^{-4}	1.64×10^{-4}	2.19×10^{-4}	2.84×10^{-4}
	$\tilde{\psi}_f$ (J/m^3)	**530**	**1124**	**2210**	**3297**
Brittleness factors	$\tilde{t}_i/\tilde{t}_f = \tilde{E}_f/\tilde{E}_i$	0.60	0.94	0.84	0.97
	$\tilde{\psi}_i/\tilde{\psi}_m$	0.42	0.92	0.72	0.96
	$\tilde{\psi}_m/\tilde{\psi}_f$	0.66	0.82	0.75	0.86

Table 3: Selected SVE Location, Measures of Anisotropy A_N, and Mean Strengths $\bar{s_N}$

Points	X	Y	$A_{N,Iso}$	$A_{N,Aniso}$	$\bar{S}_{N,Iso}$	$\bar{S}_{N,Aniso}$
P1	-5.4	-13.8	0.093	0.401	81.1	114.4
P2	0.6	-1.4	0.457	0.964	37.5	93.5
P3	11.6	14.4	0.701	0.539	54.6	109.2
P4	-14.2	9.4	0.800	0.406	65.7	96.0

Table 4: Pearson correlation coefficients for angle-independent strength fields for the isotropic domain

S_{NH}	S_{NH}	$\bar{S}_N$	$\bar{S}_S$	$\bar{S}_C$	$m(S_N)$	$m(S_S)$	$m(S_C)$
S_{NH}	1	0.917	0.939	0.847	1	1	1
$\bar{S}_N$	0.917	1	0.993	0.950	0.917	0.917	0.917
$\bar{S}_S$	0.939	0.993	1	0.950	0.939	0.939	0.939
$\bar{S}_C$	0.847	0.950	0.950	1	0.847	0.847	0.847
$m(S_N)$	1	0.917	0.939	0.847	1	1	1
$m(S_S)$	1	0.917	0.939	0.847	1	1	1
$m(S_C)$	1	0.917	0.939	0.847	1	1	1

Table 5: Pearson correlation coefficients for angle-independent strength fields for the anisotropic domain

S_{NH}	S_{NH}	$\bar{S}_N$	$\bar{S}_S$	$\bar{S}_C$	$m(S_N)$	$m(S_S)$	$m(S_C)$
S_{NH}	1	0.995	0.993	0.967	1	1	1
$\bar{S}_N$	0.995	1	0.997	0.979	0.995	0.995	0.995
$\bar{S}_S$	0.993	0.997	1	0.990	0.993	0.993	0.993
$\bar{S}_C$	0.967	0.979	0.990	1	0.967	0.967	0.967
$m(S_N)$	1	0.995	0.993	0.967	1	1	1
$m(S_S)$	1	0.995	0.993	0.967	1	1	1
$m(S_C)$	1	0.995	0.993	0.967	1	1	1

Table 6: Definition of Homogeneous and Isotropic RVE Limit

	Homogeneity	Isotropy
Elastic	$\Delta^{\kappa} = \max(\Delta^{c_{\kappa}}, \Delta^{\bar{\kappa}})$	$\Delta^{A^{\mathrm{Gao}}} = \max(\Delta^{D_{A^{\mathrm{Gao}}}}, \Delta^{\bar{A}^{\mathrm{Gao}}})$
Fracture	$\Delta^{S_n} = \max(\Delta^{c_{S_n}}, \Delta^{\bar{S}_n})$	$\Delta^{A^{sn}} = \max(\Delta^{D_{A^{sn}}}, \Delta^{\bar{A}^{sn}})$

Table 7: Convergence and power law fit data for elastic fields κ, G, E, and ν for regular (R) and Voronoi (V) SVE types.

[a] The expression (-) correspond to the minus sign choice in Equation (4.16).

[b] κ is highlighted as this property is used to represent the elastic convergence to Δ.

f	Type	$\bar{f}_{\infty}$	$\delta_{\bar{f}}$ [a]	$\alpha_{\bar{f}}$	δ_{c_f}	α_{c_f}	$\Delta^{\bar{f}}$	Δ^{c_f}	Δ
κ [b]	R	1.101	1.348	1.056	0.432	1.371	105.6	33.8	105.6
κ [b]	V	1.109	0.042	1.290	0.236	0.945	3.3	18.5	18.5
G	R	0.447	1.783	1.106	1.640	0.520	139.6	40.8	139.6
G	V	0.451	0.116	1.062	0.270	0.995	9.1	21.2	21.2
E	R	1.158	1.771	1.087	0.507	1.418	138.8	39.7	138.8
E	V	1.169	0.103	1.079	0.265	0.988	8.1	20.8	20.8
ν	R	0.299	(-)0.599	0.852	0.344	1.575	54.9	6.4	54.9
ν	V	0.297	(-)0.047	0.847	0.031	1.264	4.4	1.2	4.4

Table 8: Convergence and power law fit data for elastic anisotropy field A^{Gao} for Regular (R) and Voronoi (V) SVE types.

Type	$\delta_{\bar{A}^{\mathrm{Gao}}}$	$\alpha_{\bar{A}^{\mathrm{Gao}}}$	$\delta_{D_{A^{\mathrm{Gao}}}}$	$\alpha_{D_{A^{\mathrm{Gao}}}}$	$\Delta^{\bar{A}^{\mathrm{Gao}}}$	$\Delta^{D_{A^{\mathrm{Gao}}}}$	Δ
R	2.590	1.131	1.833	1.434	152.0	45.4	152.0
V	0.029	0.826	0.047	1.023	7.7	4.2	7.7

Table 9: Convergence and power law fit data for fracture strength fields S_n and S_t for Regular (R) and Voronoi (V) SVE types, where NC indicates non-convergence.

f	Type	$\bar{f}_\infty$	$\delta_{\bar{f}}$	$\alpha_{\bar{f}}$	δ_{c_f}	α_{c_f}	$\Delta^{\bar{f}}$	Δ^{c_f}	Δ
S_n	R	0.103	172.5	0.699	2.56E15	0.096	13520.7	NC	NC
S_n	V	0.430	6.1	0.677	116.7	0.284	477.5	9139.0	9139.0
S_t	R	0.060	385.9	0.669	1.42E19	0.080	30233.0	NC	NC
S_t	V	0.339	6.4	0.728	70.1	0.341	498.9	5490	5490

Table 10: Resulting RVE Size for homogeneous and isotropic RVE limit of the composite considered.

Field	Type	Homogeneity RVE Size	Isotropy RVE Size
Elastic	R	$\Delta^{\kappa} = \max(\Delta^{\bar{\kappa}}, \Delta^{c_\kappa}) = 105.6$	$\Delta^{A^{\mathrm{Gao}}} = \max(\Delta^{\bar{A}^{\mathrm{Gao}}}, \Delta^{D_{A^{\mathrm{Gao}}}}) = 152.0$
Elastic	V	$\Delta^{\kappa} = \max(\Delta^{\bar{\kappa}}, \Delta^{c_\kappa}) = 18.5$	$\Delta^{A^{\mathrm{Gao}}} = \max(\Delta^{\bar{A}^{\mathrm{Gao}}}, \Delta^{D_{A^{\mathrm{Gao}}}}) = 7.7$
Fracture	R	$\Delta^{S_n} = \max(\Delta^{\bar{S}_n}, \Delta^{c_{S_n}}) = \mathrm{NC}$	$\Delta^{A^{sn}} = \max(\Delta^{\bar{A}^{sn}}, \Delta^{D_{A^{sn}}}) = \mathrm{NC}$
Fracture	V	$\Delta^{S_n} = \max(\Delta^{\bar{S}_n}, \Delta^{c_{S_n}}) = 9139$	$\Delta^{A^{sn}} = \max(\Delta^{\bar{A}^{sn}}, \Delta^{D_{A^{sn}}}) = 6978$

Vita

Justin Garrard was born in Murfreesboro, TN on November 21, 1988. Justin grew up in Manchester, TN, and graduated from Coffee County Central High School in May 2007. In August 2007, he entered Tennessee Technological University in Cookeville, TN and subsequently received the degree of Bachelor of Science in Mechanical Engineering in December 2010. He began working at Arnold Engineering Development Complex, Arnold AFB, TN, and in August 2011 began his studies at the University of Tennessee Knoxville/Space Institute. Justin received a Master of Science degree in Mechanical Engineering in May 2014. He has since continued his studies at the University of Tennessee Knoxville/Space Institute pursing a Ph.D. in Mechanical Engineering with a research concentration of Applied Mechanics and Computational Mechanics under the pupilage of Dr. Reza Abedi.